NAS8-32475
DPD541
DR MA-04

SD 78-AP-0023-4

(NASA-CR-150683) SATELLITE POWER SYSTEMS (SPS) CONCEPT DEFINITION STUDY. VOLUME 4: SPS POINT DESIGN DEFINITION Final Report (Rockwell International Corp., Downey, Calif.) 220 p HC A10/MF A01 CSCL 22B G3/15

N80-12106

Unclas
41129

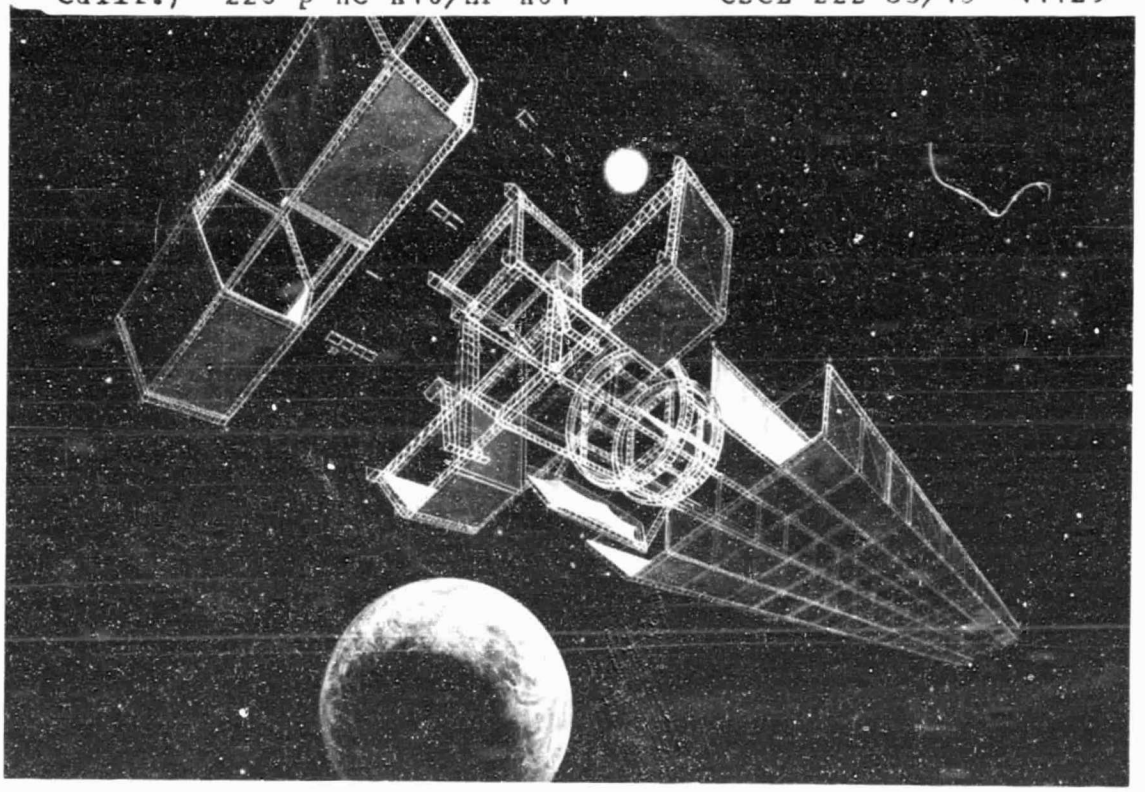

Satellite Power Systems (SPS) Concept Definition Study

FINAL REPORT
VOLUME IV

SPS POINT DESIGN DEFINITION

April 1978

Rockwell International
Space Division
12214 Lakewood Boulevard
Downey, California 90241

SD 78-AP-0023-4

Satellite Power Systems (SPS) Concept Definition Study

FINAL REPORT

VOLUME IV

SPS POINT DESIGN DEFINITION

CONTRACT NAS8-32475
DPD 541 MA-04

April 1978

Submitted by

G. HANLEY
Program Manager

Approved

C.H. GUTTMAN
SPS Study Team Manager, NASA/MSFC

Prepared for:

National Aeronautics and Space Administration
George C. Marshall Space Flight Center

Marshall Space Flight Center
Alabama 35812

Rockwell International
Space Division
12214 Lakewood Boulevard
Downey, California 90241

FOREWORD

This document, *SPS Point Design Definition*, is Volume IV of the SPS Concept Definition Study (Contract NAS8-32475), Exhibits A and B, and also incorporates results of NASA/MSFC in-house effort Other volumes of the final report that provide additional detail are listed below.

Volume	
I	Executive Summary
II	SPS System Requirements
III	SPS Concept Evolution
V	Transportation and Operations Analysis
VI	SPS Technology Requirements and Verification
VII	SPS Program Plan and Economic Analysis

CONTENTS

ILLUSTRATIONS

TABLES

1.0 INTRODUCTION

This volume describes the SPS system point design concept selected as a result of the trade studies conducted on the concepts described in Volume III, SPS Concept Evolution. The concept definition includes satellite, ground and space systems and their relationship as shown in Figure 1.0-1. The transporta- and operations analysis are described in Volume V.

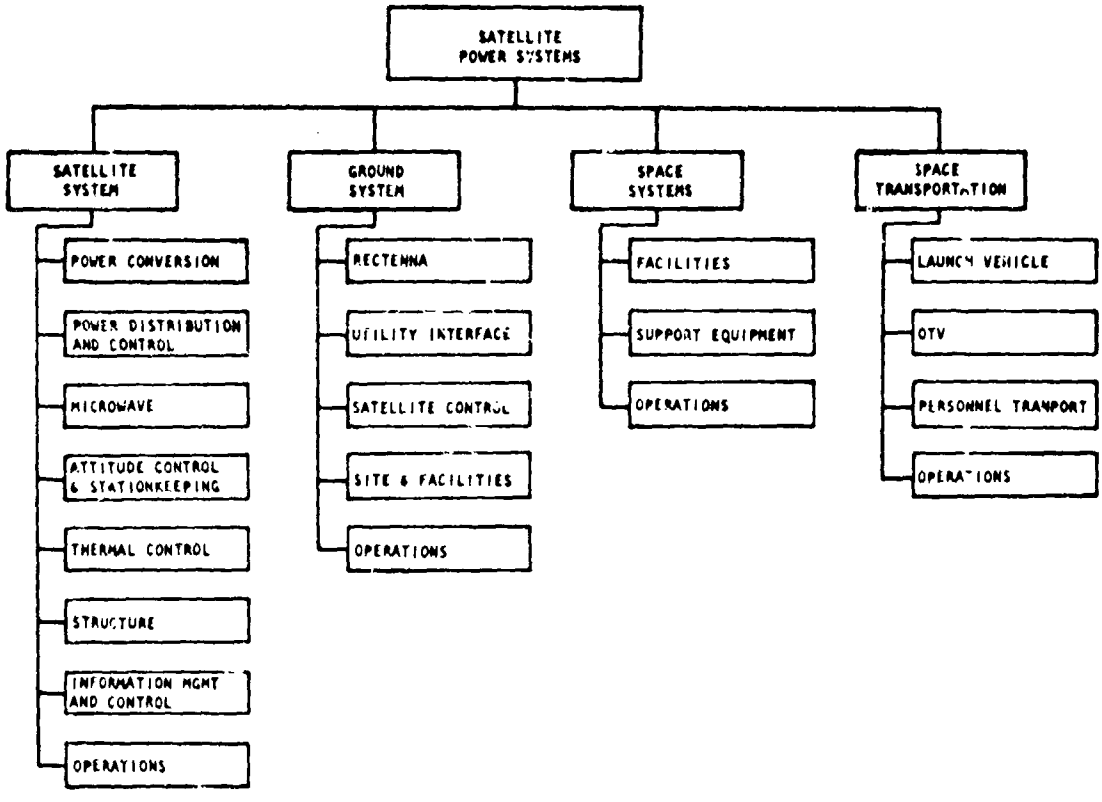

Figure 1.0-1. SPS System Relationships

Major emphasis during this study has been placed on definition of the GaAlAs photovoltaic satellite system which has been recommended by MSFC as the preliminary baseline concept. The Solar Thermal Concept has also been defined (to a lesser detail) as an alternate concept to the Solar Photovoltaic Concept. The primary purpose of this documentation is to provide sufficient detail on these two concepts to support MSFC in its recommendations to NASA HQ/DOE of preferred baseline SPS concept(s) by CY 1981 as a basis for subsequent technology advancement and verification activities in the CY 1981-1987 time period.

Program ground rules followed in development of point design definition is listed below:

- IOC Date: 1998
- Maximum Program Size: 2005 - 170 GW
  2025 - 600 GW
- Minimum Program Size: 2005 - 40 GW
  2025 - 140 GW
- System Life: 30 years
- Cost: 1977 constant dollars (7.5% discount rate)
- Systems Available in the 1980's:

Shuttle	1980
IUS	1981
OTV	1987

This volume covers the major subsystems of the satellite system including power conversion, power distribution and control, microwave, attitude control and stationkeeping, thermal control, structures, and information management and control. In addition, ground and space systems are described covering the rectenna, utility interface, orbital and ground support systems and satellite control.

2.0 SUBSYSTEM ANALYSIS

The results of the design studies, analyses and evaluation for the point design subsystem concepts are presented in the following sections. The major subsystems consists of the solar photovoltaic and solar thermal power conversion subsystems, power distribution and control subsystem, structural subsystem, attitude control and stationkeeping subsystem, microwave power transmission subsystem and the thermal control subsystem.

2.1 PHOTOVOLTAIC POWER CONVERSION SUBSYSTEM

The point design photovoltaic concept is shown in Figure 2.1-1 and was designed to supply 5 GW of electrical power to the utility grid on the ground. The SPS is a three trough configuration having reflective membranes at a 60° slant angle. It has a single microwave antenna, located in the center of the configuration. The overall dimensions of the SPS are approximately

- Length - 21.3 km
- Width - 3.85 km
- Depth - 1.75 km.

The mass in order of the SPS is 36.6×10^6 and includes a 30% growth factor. In geosynchronous orbit the longitudinal axis of the SPS is oriented perpendicular to the orbital plane. The SPS design is based on construction in GEO.

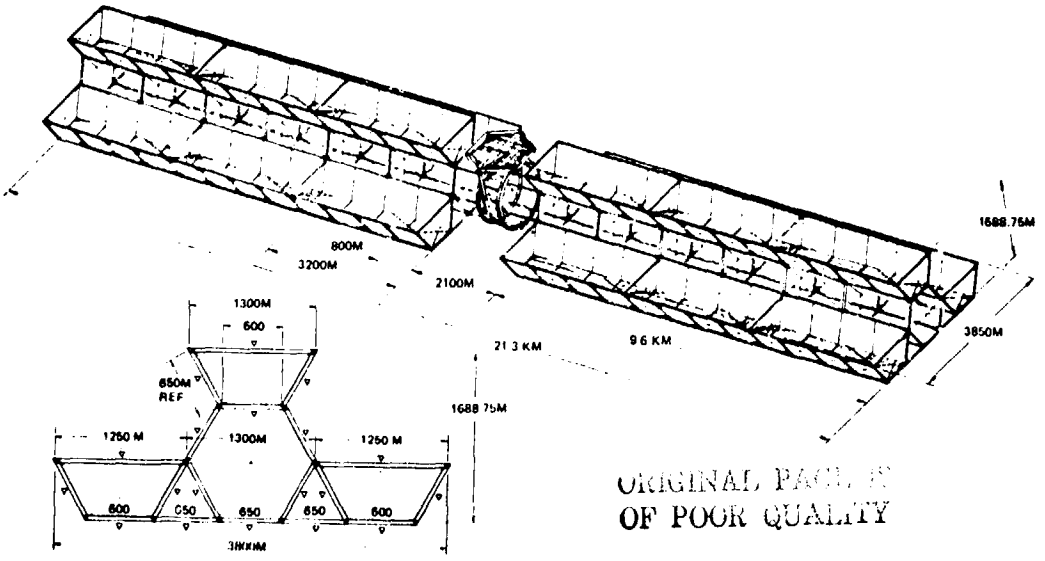

Figure 2.1-1. 5 GW Photovoltaic SPS CR-2

Subcontracts were also issued for support of the SPS photovoltaic GaAlAs point design effort in the major areas of cell performance characteristics, manufacturing and production techniques, effects of radiation damage on cell performance, and cost and weight estimates. The organizations that contributed to the study are listed below:

- Electronics Research Division - Rockwell International
- Hughes Aircraft Company - Space and Communications Group
- Science Center - Rockwell International

The solar photovoltaic power subsystem consists of the solar cells, blankets, attachment devices, and for the concentrator-type system, includes the reflector membranes and attachment devices. Gallium aluminum arsenide (GaAlAs) cells have been selected as the point design solar cell. The cell is fastened to a thin-film Kapton substrate with an FEP adhesive. The photovoltaic power conversion subsystem is designed for a geometric concentration ratio of 2.

The functional requirements for the photovoltaic power subsystems are listed in Tables 2.1-1 and 2.1-2. The system efficiency block diagram is shown in Figure 2.1-2. Shown in the figure are power levels, efficiencies, temperatures, degradation factors and solar cell area requirements. A simplified integrated block diagram for the CR-2 point design concept is presented in Figure 2.1-3. The major assemblies and components that are required for the photovoltaic subsystem are shown in Figure 2.1-4.

2.1.1 SOLAR CELLS

The solar cell used in the SPS design is a GaAlAs cell having an efficiency of 20 percent at Air Mass Zero (AM0) and 28°C. The cell consists of the GaAlAs junction, GaAlAs window, cover/substrate, current collectors, and an anti-reflection coating. The basic cell design is the inverted GaAs/sapphire design having a weight of 0.252 kg/m^2. The various cell designs that were investigated and the selected design are shown in Figure 2.1-5. The point design cell has a 20-μm sapphire substrate upon which is grown a 5-μm single crystal GaAs junction. A 500-Å GaAlAs window is then deposited on the 5-μm junction. The voltage and current characteristics of the cell as a function of operating temperature are shown in Figure 2.1-6.

2.1.2 SOLAR BLANKET

The solar blanket consists of a 25-μm Kapton membrane upon which the cells are fastened with a thermosetting FEP adhesive. Also included in the blanket are the interconnects, transparent thermal coating required for thermal control, attachments, tensioning devices, and sensors. The solar cell blankets will be manufactured in blanket form and the solar cells attached. This assembly will then be rolled up on a drum type canister. It is postulated that the blankets will be 25 m wide by approximately 750 m in length. The canisters are then transported to orbit where the blankets are deployed via a roll-out deployment-type operation.

Table 2.1-1. Point Design Solar Array Functional Requirements

PROCRAMMATIC	
ENERCY SOURCE	SOLAR
CAPACITY	5 GW DELIVERED TO UTILITY NETWORKS
LIFETIME	30 YEARS WITH MINIMUM PLANNED MAINTENANCE (SHOULD BE CAPABLE OF EXTENDED LIFE BEYOND 30 YEARS WITH REPLACEMENT)
IOC DATE	1998
OPERATIONS	GEOSYNCH ORBIT; 0-DFG INCLIN, CIRCULAR (35,786 km ALTITUDE)
RESOURCES	MINIMUM USE OF CRITICAL RESOURCES
COMMERCIALIZATION	COMPATIBLE WITH U.S. UTILITY NETWORKS
DEVELOPMENT	EVOLUTIONARY WITH PROVISIONS FOR INCORPORATING LATER TECHNOLOGY
TECHNOLOGY	
OUTPUT POWER	POWER LEVEL IS DEFINED AS CONSTANT POWER LEVEL (EXCEPT DURING SOLAR ECLIPSE
WEIGHT GROWTH	30%
ENERGY STORAGE	TO SUPPORT ON-BOARD SATELLITE SYSTEM OPERATIONS ONLY
FAILURE CRITERIA	NO SINGLE POINT FAILURE MAY CAUSE TOTAL LOSS OF SPS FUNCTION
ENERGY PAYBACK	LESS THAN 3 YR
COST	COMPETITIVE WITH GRND-BASED PWR GENERATION WITHIN LIFETIME OF SPS PROJECT
STORAGE	ONE YEAR ON BOARD WITHOUT RESUPPLY

Table 2.1-2. Point Design Solar Array Functional Requirements - Operations

MODE	ASSEMBLY	FUNCTIONS
CONSTRUCTION	SUBSYSTEM	NONE
INTER-ORBIT TRANSFER	SUBSYSTEM	NONE
OPERATIONS	SUBSYSTEM REFLECTOR	STEADY-STATE OPERATION SIZED FOR EOL POWER RATING
ECLIPSE	SUBSYSTEM BATTERIES	SHUT DOWN BEFORE ENTERING ECLIPSE STANDBY (ZERO POWER) TURN ON AFTER LEAVING ECLIPSE & ARRAYS REACH EQUILIBRIUM TEMPERATURE SUPPLY POWER FOR ESSENTIAL FUNCTIONS
FAILURE/ MAINTENANCE	SUBSYSTEM PWR MODULE*	REDUNDANT OPERATION, AUTO SHUTDOWN, MANUAL STARTUP SHUT DOWN & ISOLATE FAILED MODULE, REPLACE SOLAR CELL BLANKET AND/OR REFLECTOR
CHECKOUT	SUBSYSTEM	FAIL-SAFE CHECKS; CONTROL RESPONSE

*SOLAR CELL/BLANKET/REFLECTOR MODULE

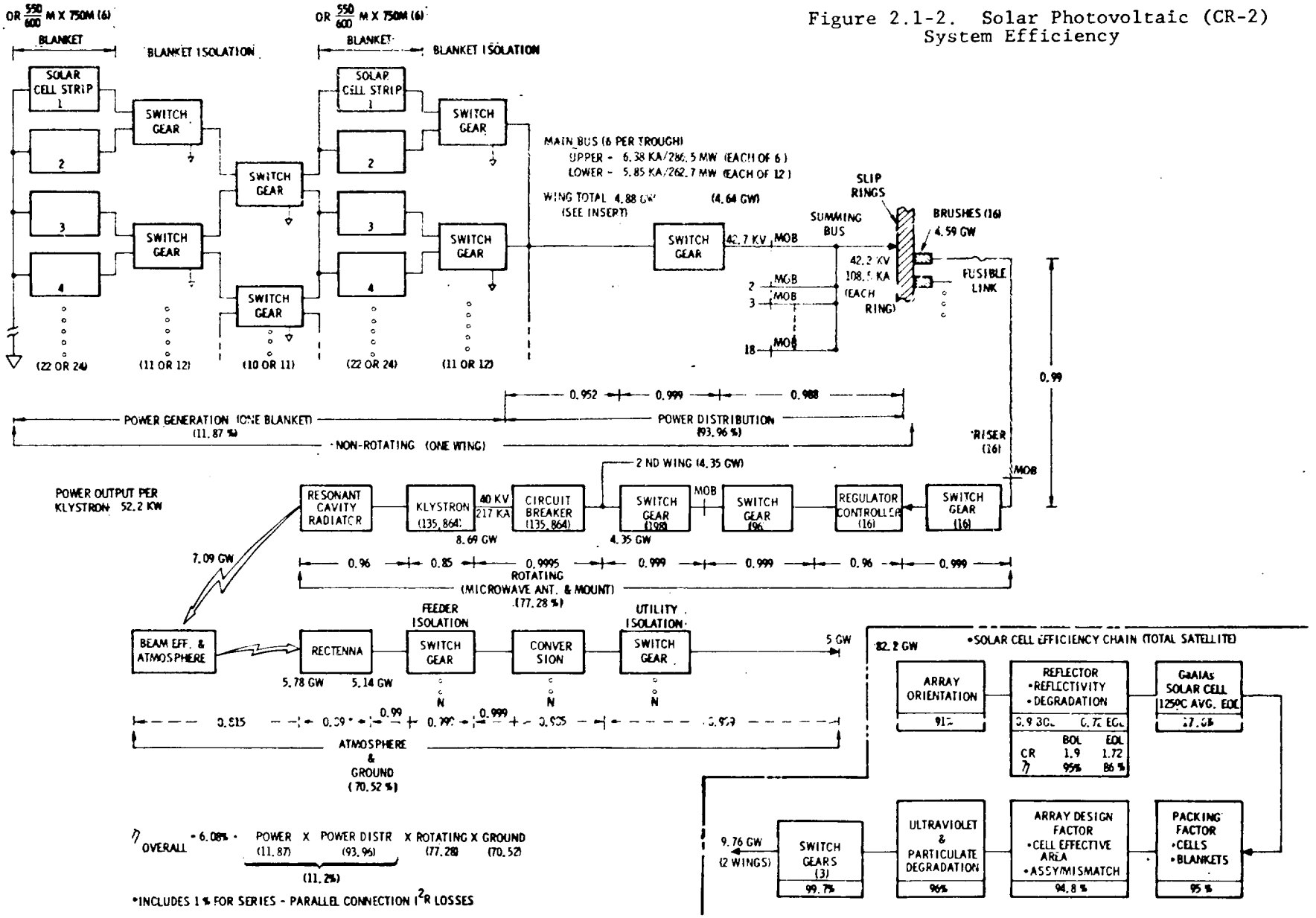

Figure 2.1-2. Solar Photovoltaic (CR-2) System Efficiency

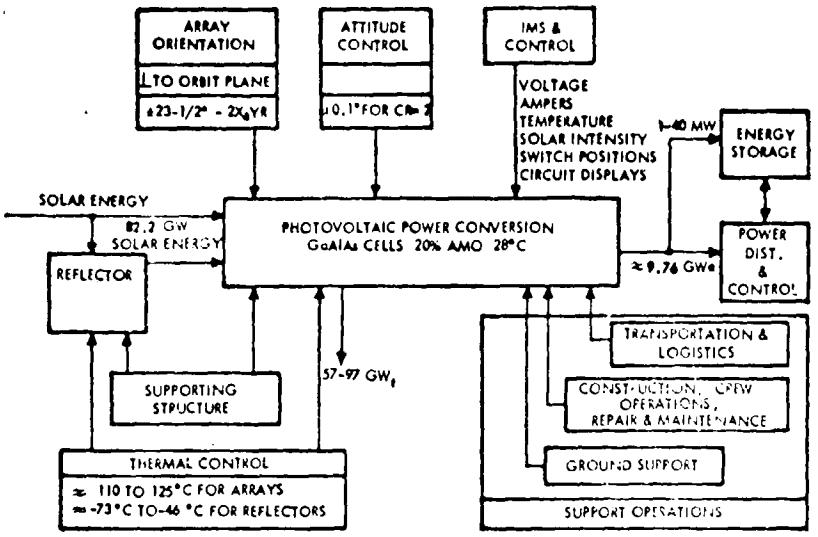

Figure 2.1-3. Simplified Integrated Block Diagram - Photovoltaic (CR-2)

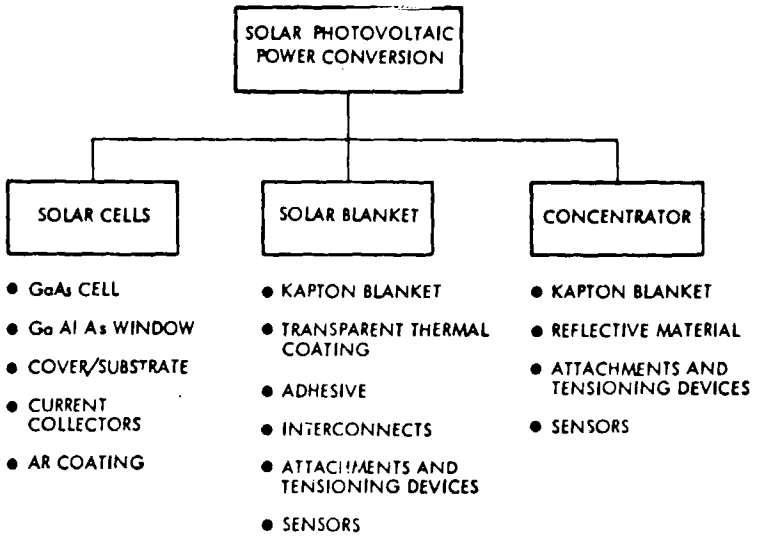

Figure 2.1-4. Assembly Tree

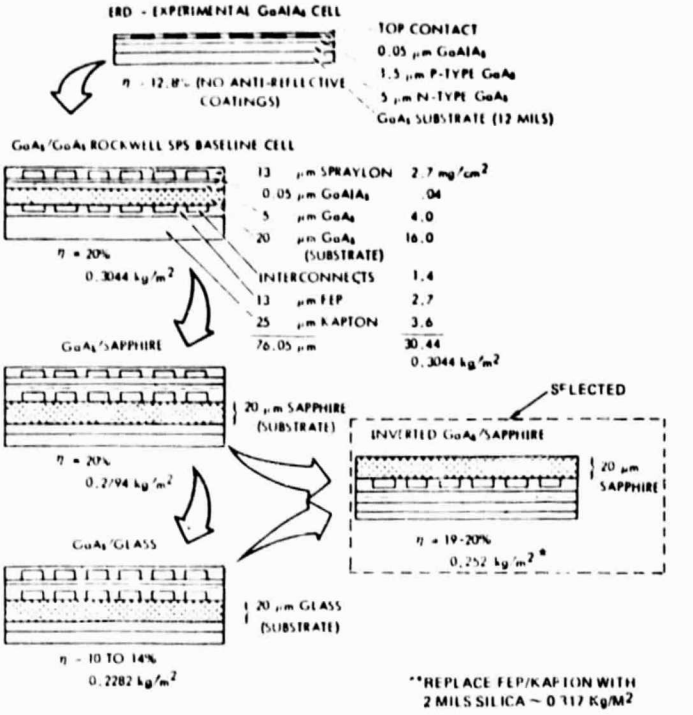

Figure 2.1-5. Solar Cell Design

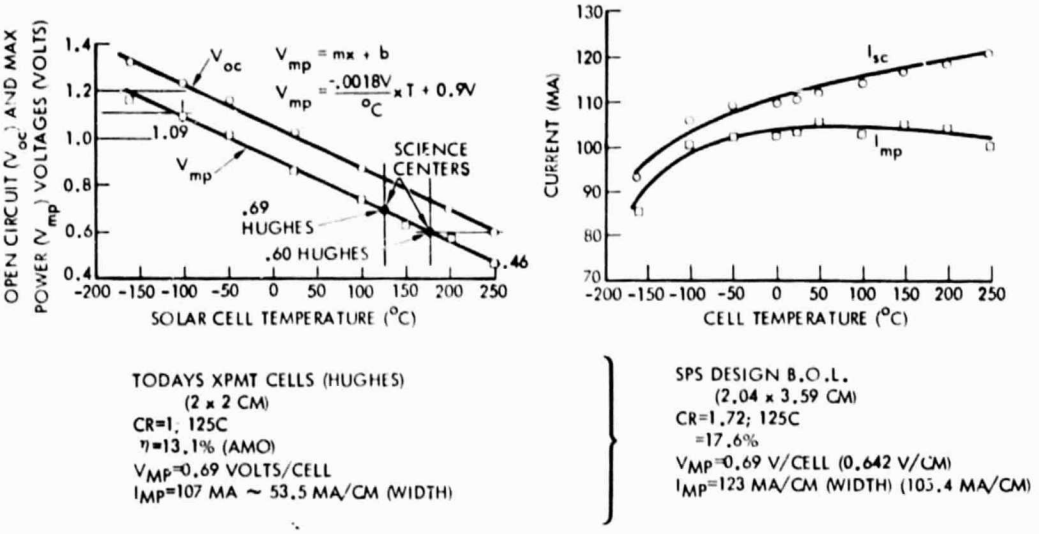

TODAYS XPMT CELLS (HUGHES)
(2 x 2 CM)
CR=1, 125C
η=13.1% (AMO)
V_{MP}=0.69 VOLTS/CELL
I_{MP}=107 MA ~ 53.5 MA/CM (WIDTH)

SPS DESIGN B.O.L.
(2.04 x 3.59 CM)
CR=1.72; 125C
=17.6%
V_{MP}=0.69 V/CELL (0.642 V/CM)
I_{MP}=123 MA/CM (WIDTH) (105.4 MA/CM)

( ) = EOL

Figure 2.1-6. GaAlAs Solar Cell Voltage and Current Characteristics

The solar blanket layout for the GaAlAs point design configuration is shown in Figure 2.1-7. The solar panel in the top trough (effective cell area) measures 600×750 m × 2 for 900,000 m^2. Twelve panels are required for the top trough. The panels for the two lower troughs are slightly smaller in width and measure 550×750 m × 2 for 825,000 m^2 (effective cell area). Twenty-four panels are required for the bottom troughs. The total deployed solar area for the SPS is 30.6×10^6 m^2 which is comprised of 10.8×10^6 m^2 in the top troughs and 19.8×10^6 m^2 in the bottom troughs.

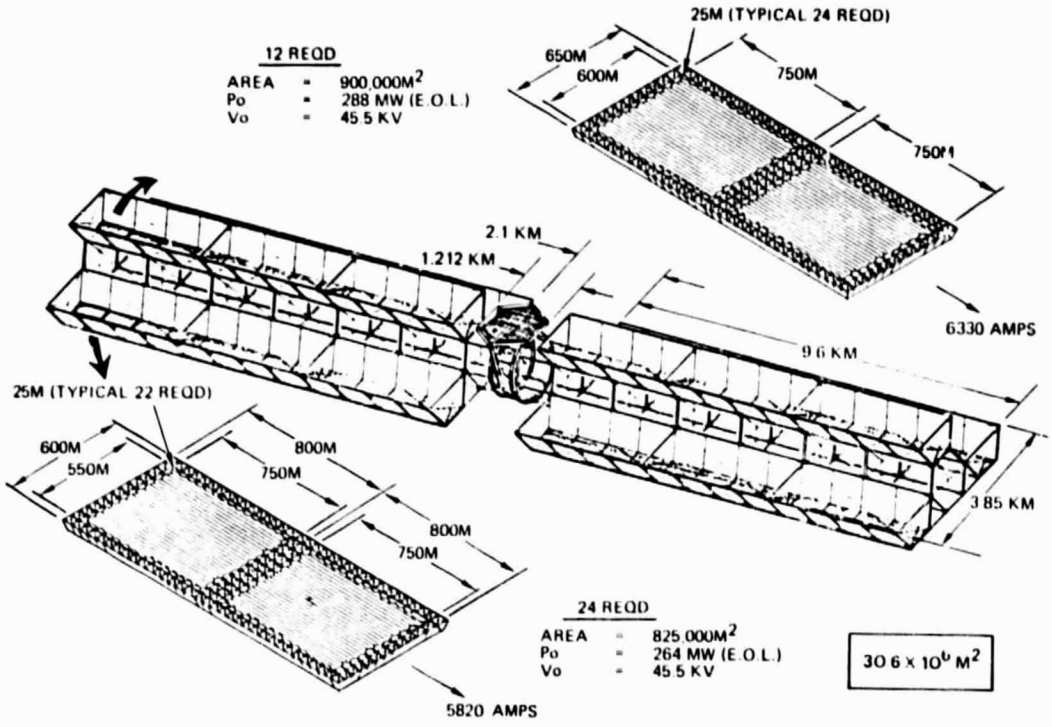

Figure 2.1-7. Solar Blanket Concept

The cell arrangement on the solar panel is illustrated in Figure 2.1-8. The basic building block is a 1 m^2 module configuration and the cells are connected together in a series parallel arrangement. The voltage output of each 1 m^2 module is 30.3 V with a current of 10.54 amps. The module output is calculated to be 320 W/m^2 at the end of life. The cell characteristics and cell design used to form a submodule for the solar blanket is shown in Figure 2.1-9.

2.1.3 SOLAR CELL DEVELOPMENT AND PRODUCTION

The Electronics Research Division (ERD) of Rockwell has been actively engaged in the analysis design, and development of GaAlAs cells. ERD has investigated the development and mass production requirements of the GaAlAs cells for the SPS mission and a summary of their study results are presented in the following subsections.

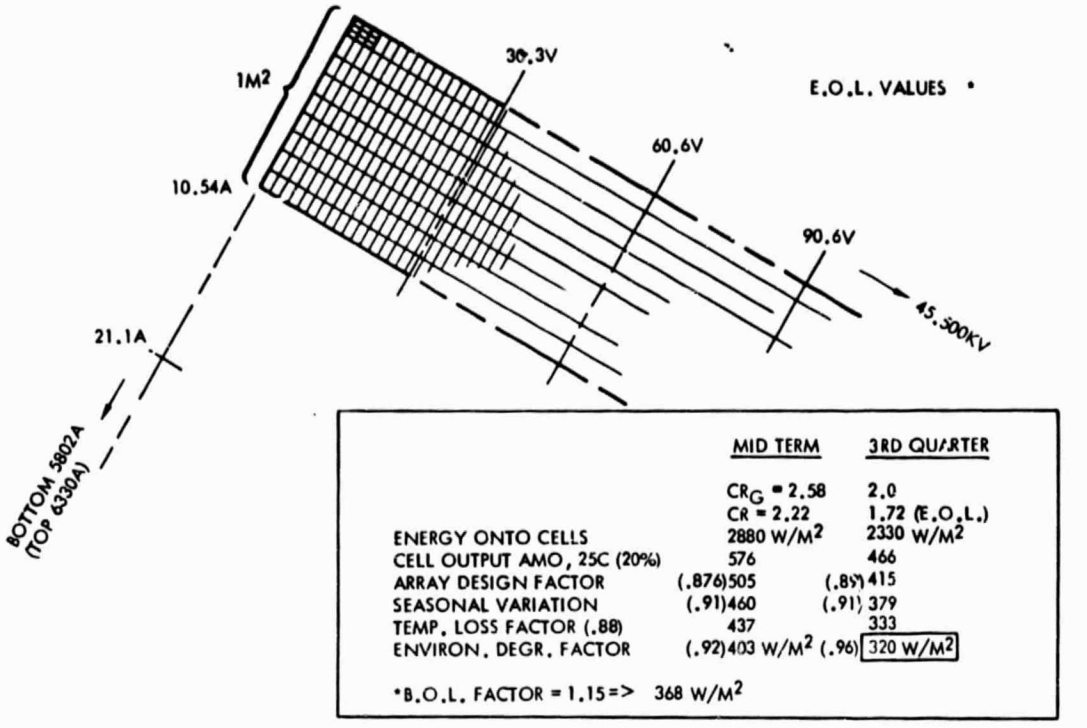

	MID TERM	3RD QUARTER
	CR_G = 2.58	2.0
	CR = 2.22	1.72 (E.O.L.)
ENERGY ONTO CELLS	2880 W/M²	2330 W/M²
CELL OUTPUT AMO, 25C (20%)	576	466
ARRAY DESIGN FACTOR	(.876)505	(.89)415
SEASONAL VARIATION	(.91)460	(.91)379
TEMP. LOSS FACTOR (.88)	437	333
ENVIRON. DEGR. FACTOR	(.92)403 W/M²	(.96) 320 W/M²

*B.O.L. FACTOR = 1.15 => 368 W/M²

Figure 2.1-8. Solar Panel Power Output ~ Watts/m^2

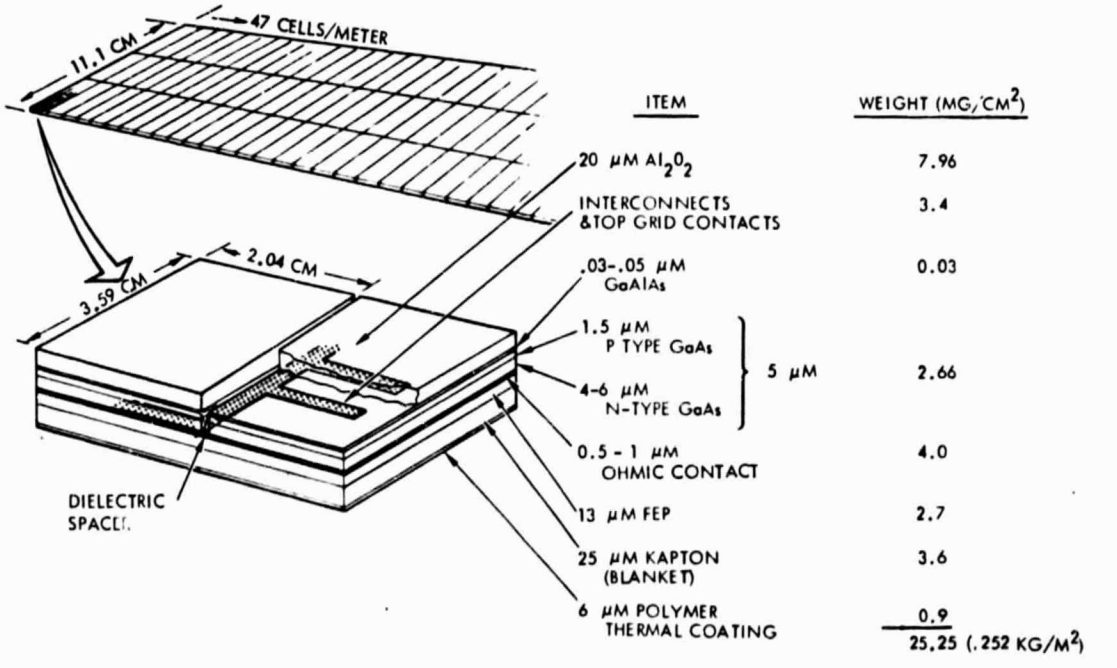

ITEM		WEIGHT (MG/CM²)
20 μM Al_2O_2		7.96
INTERCONNECTS &TOP GRID CONTACTS		3.4
.03-.05 μM GaAlAs		0.03
1.5 μM P TYPE GaAs	5 μM	2.66
4-6 μM N-TYPE GaAs		
0.5 - 1 μM OHMIC CONTACT		4.0
13 μM FEP		2.7
25 μM KAPTON (BLANKET)		3.6
6 μM POLYMER THERMAL COATING		0.9
		25.25 (.252 KG/M²)

Figure 2.1-9. GaAlAs Solar Cell Blanket Cross Section

The performance curve of an experimental type GaAlAs/GaAs cell that was developed at Rockwell using metal oxide - chemical vapor deposition (CVD) process is shown in Figure 2.1-10. The cell did not have an antireflective coating but corrected for AMO conditions and with a coating, efficiencies of up to 17% were calculated. Liquid phase epitaxy cells developed at Rockwell were tested with efficiencies of approximately 17.2%. The major component/ regions of the cell are listed in Table 2.1-3. The invested cell configuration as shown in Figure 2.1-5 in conjunction with the CVD process offers the potential for high production capabilities. The technical problems that have to be solved for the successful demonstration of laboratory type invested cell GaAlAs structure cells having high efficiency and good yields consist of determining the optimum surface preparation, characterize the interface region, establish growth parameters, develop reliable contacts and AR coatings.

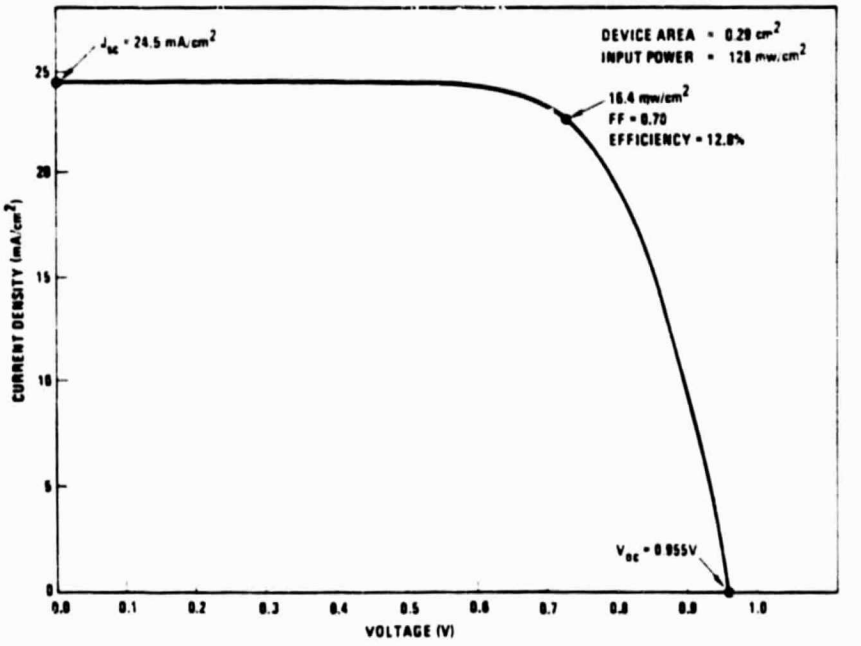

Fourth Quadrant of I-V Characteristic of MO-CVD GaAlAs/GaAs Heterostructure Solar Cell under 128 mw/cm^2 Illumination (uncorrected for contact area or reflection from uncoated GaAlAs window).

Figure 2.1-10. I-V Characteristic for Illuminated (AMO) Cell

A proposed cell configuration for laboratory demonstration is shown in Figure 2.1-11. The cell design is similar to that of conventional window type GaAlAs cells and shows an insulating substrate which requires etching of the mesa structure for producing the contacts. Etched cells of the type shown in Figure 2.1-11 have been developed at the Rockwell Electronics Research Center and a typical cell is shown in Figure 2.1-12. The white surface shown in Figure 2.1-12 is the base sapphire substrate that the cell is grown on and also shown is the cell and grid pattern.

Table 2.1-3. Experimental GaAlAs/GaAs Cell Component Listing

	EXPERIMENTAL ALL-EPITAXIAL 3-LAYER GaAlAs/GaAs CELL	
COMPONENT/REGION OF BASIC CELL	MATERIAL	THICKNESS (μm)
1. Substrate	GaAs (single-crystal n-type Si-doped wafer)	375
2. Base Region Contact	Au-12% Ge alloy layer (full coverage, on underside of substrate wafer)	0.2
3. Active Base Region	GaAs film (n-type, Se-doped)	5.
4. Front Layer of Cell	GaAs film (p-type, Zn-doped)	1.5
5. Window Layer	$Ga_{0.2}Al_{0.8}As$ film (p-type, Zn-doped)	0.05
6. Front Contact	Au-Zn-Au (2% Zn) square grid (10% area coverage)	~0.4
7. Antireflection Coating (optional)	TBD	TBD

NOT TO SCALE

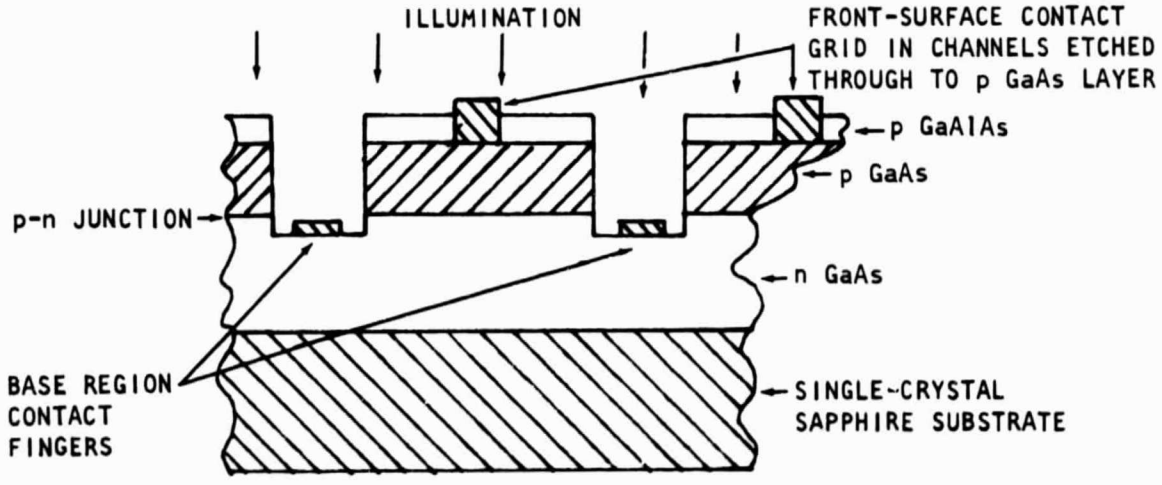

Figure 2.1-11. Experimental Model of Conventional - Structure GaAlAs/GaAs Cell on Sapphire

Rockwell International

PHOTOGRAPH SHOWS EARLY CONVENTIONAL EXPERIMENTAL CELL CONFIGURATION (BASED ON FIGURE 2.1-11 CONFIGURATION) GROWN ON 1½-INCH DIAM. SAPPHIRE SINGLE-CRYSTAL SUBSTRATE (mm GRID BACKGROUND IN PHOTO)

Figure 2.1-12. Rockwell Typical Cell

To meet the SPS requirements for cell development a laboratory model of scaled-up prototype inverted structure CVD GaAlAs/sapphire single crystal solar cell technology should be completed by the end of CY 1979. The proposed cell development will center on developing high efficiency single crystal cells utilizing large area sapphire substrates. By the end of 1980, the preliminary design of large area inverted structure CVD GaAlAs sapphire high efficiency single crystal solar cells utilizing large scale continuous manufacturing techniques and processes should be established. The conceptual design of a production type, large substrate for continuous ribbon manufacturing capability is shown in Figure 2.1-13.

The production of pilot line manufactured quantity cells for SPS as proposed, is estimated to be demonstrated in mid 1982. The major objectives of the pilot line production program are to fabricate and test pilot line quantities of production prototype inverted structure cell using selected high output procedures and process based on the concepts selected from the laboratory apparatus test and development effort. A simplified schematic of the CVD process is shown in Figure 2.1-14 and a photograph of the working laboratory CVD equipment in used at Rockwell is shown in Figure 2.1-15.

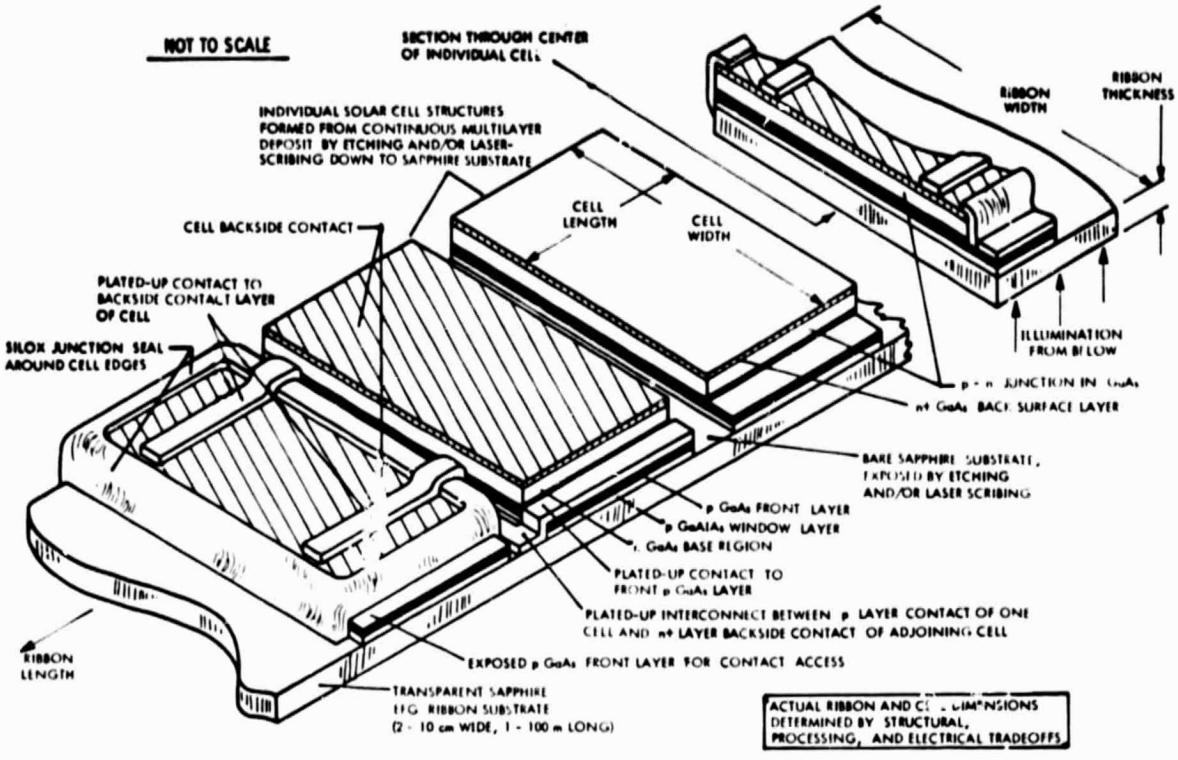

Figure 2.1-13. Conceptual Design of Possible Production Model of Conventional-Structure GaAs/Sapphire Continuous-Ribbon Solar Cell Array

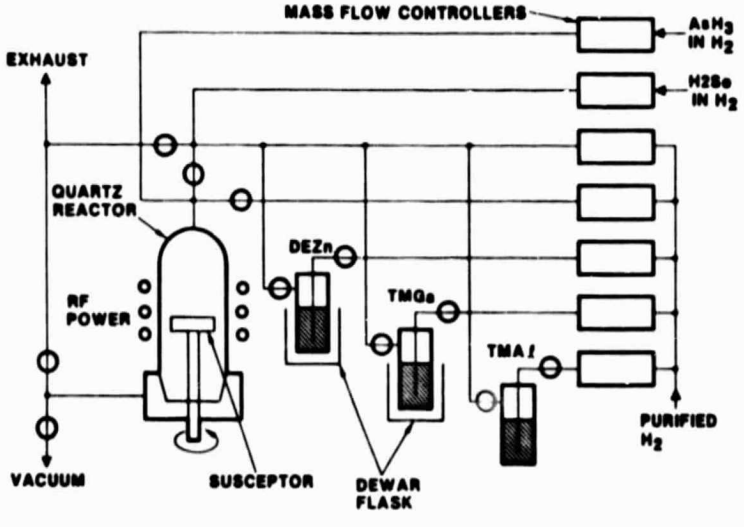

Figure 2.1-14. Simplified Schematic Diagram of Laboratory-Type MO-CVD Apparatus for Growth of GaAs and GaAlAs

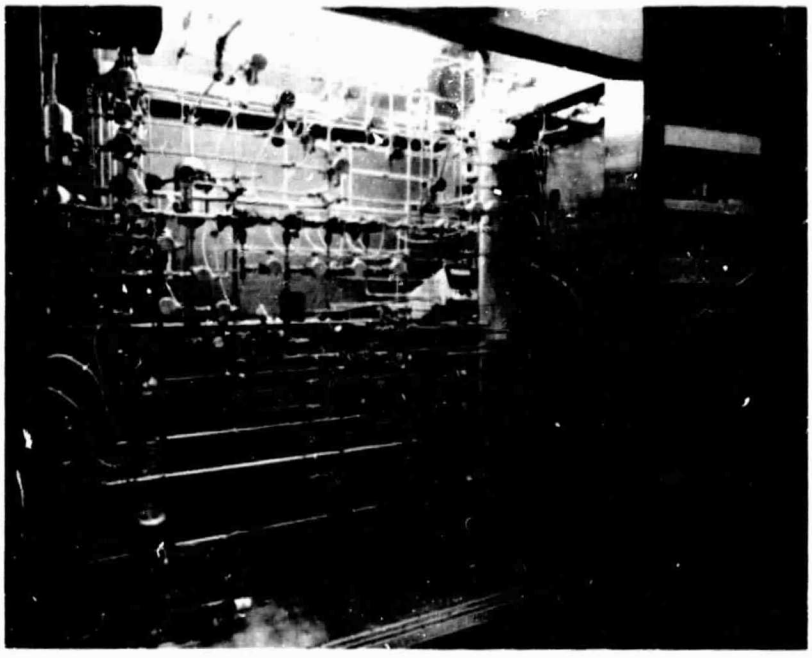

Figure 2.1-15. Laboratory Apparatus Used for GaAlAs MO-CVD Development

Large scale production should occur in the post 1985 time period. A line diagram of a tentative production line facility is shown in Figure 2.1-16. Figure 2.1-17 illustrates the design of the individual MO-CVD film growth furnace that is used in the production line. Depending on chamber size, and production rate, multiple furnaces and production lines will be required.

2.1.4 REFLECTORS

Thin reflector membranes are used on the SPS to reflect the sun onto the solar cell surfaces and obtain a nominal concentration ratio of 2. The reflector is made of 12.5 μm (0.5 mil) aluminized Kapton. Reflectivity of the reflector was taken at 0.9 BOL and 0.72 EOL. The reflector membrane has a mass of 0.018 kg/m^2. The reflective membranes are mounted on the structure using attachments and tensioning devices. Tensioning based on structural limit of the existing beam design (with safety factor of 1.5) indicates that tensioning of up to 75 psi can be used.

Reflectivity values for coated metal reflectors and thin film membranes are illustrated in Table 2.1-4. The thin film membranes utilizing an Aℓ coating has the potential of low weight and cost with high reflectivity. The table indicates that an aluminized film of at least 200 Å is required for a reflectivity of 0.90. In the study, a 700 Å coating was used on the Kapton film. The major parameters that effect the reflectivity of the surface are presented in Table 2.1-5. Long term and on-orbit testing is required to verify the actual reflectivity values to use for the design of

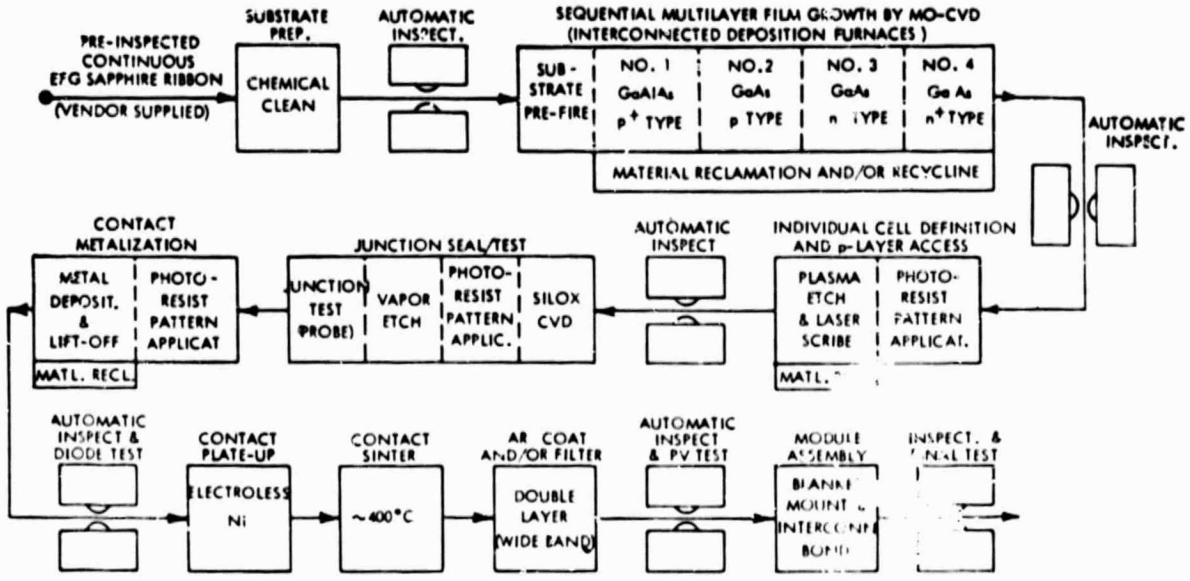

Figure 2.1-16. Tentative Process Flow Chart for Manufacturing Facility for GaAs/Sapphire Continuous-Ribbon Inverted-Structure Solar Cell

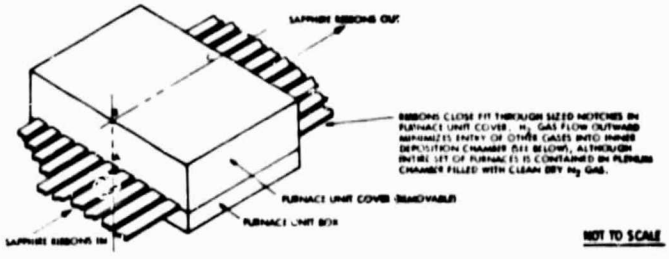

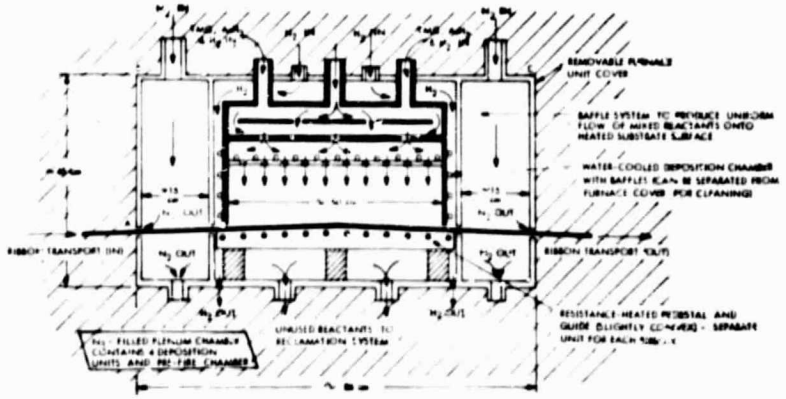

Figure 2.1-17. Possible Design of Individual MO-CVD Film Growth Furnace for Use in Continuous Fabrication of GaAs/Sapphire Ribbon-Type Solar Cells

Table 2.1-4. Reflectivity

COATED METAL REFLECTORS	
COATING	SOLAR REFLECTANCE
SODIUM	0.990
SILVER	0.954
ALUMINUM	0.920
GOLD	0.794
RHODIUM	0.[illegible]13

THIN ALUMINUM FILM		
FILM THICKNESS		SOLAR REFLECTANCE
μm	Å	
0.005	50	0.22
0.010	100	0.68
0.015	150	0.85
0.020	200	0.90

Table 2.1-5. Reflector Degradation

1. OXIDATION OF FILM DURING MANUFACTURE, STOWAGE, STORAGE, AND LAUNCH
2. MECHANICAL WEAR OF FILM DUE TO WINDING AND UNWINDING, AIR CURRENTS, AND PARTICULATE CONTAMINANTS
3. SPACE ENVIRONMENT
   - IONIZED RADIATION EFFECTS
   - DEPOSITS ON FILM FROM SPACE PARTICLES AND EXHAUST PRODUCTS OF SATELLITE
   - CHEMICAL REACTION OF DEPOSITS ON FILM
   - METEOROIDS
4. SELECTED DESIGN VALUES

   R_{BOL} = 0.9

   R_{EOL} = 0.72

NOTE: ECHO SATELLITES (12.5 μm MYLAR WITH 0.22 μm Al COATING) FLEW IN INTENSE REGIONS OF THE VAN ALLEN RADIATION BELTS WITH APPARENTLY LITTLE DEGRADATION.

the SPS reflectors. The Kapton film properties such as ultimate strength, coefficient of thermal expansion and dielectric strength as a function of temperature are shown in Figures 2.1-18 and 2.1-19.

Results of analysis show weight savings with the utilization of concentrators. The selected design concept for the point design is the 60° Vee trough configuration. Weight, cost, on-orbit assembly and fabrication and design complexity were used in the selection of the 60° Vee point design configuration. Weight comparisons showed that penalties for ±1 degree misorientation in reflector oversizing at concentration ratios of 5 and penalties for 1000 psi tensioning are prohibitive. It appears that attitude control errors are controllable and that high membrane tensioning may not be a real requirement. Preliminary radiation tests indicate insignificant reflectivity degradation for aluminized thin film Kapton, e.g., MSFC tests at 10^{15} proton/cm^2

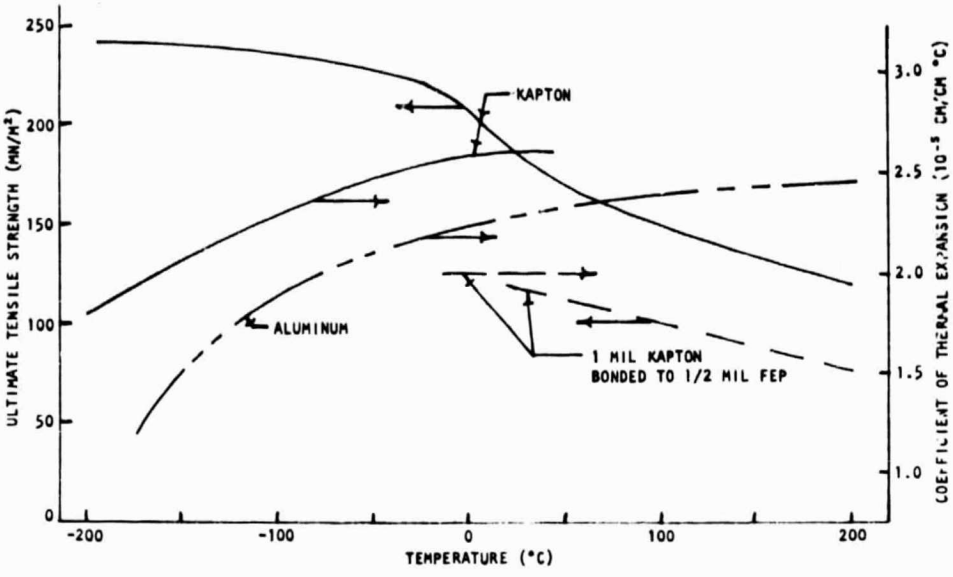

Figure 2.1-18. Kapton Type H Ultimate Tensile Strength and Coefficient of Thermal Expansion

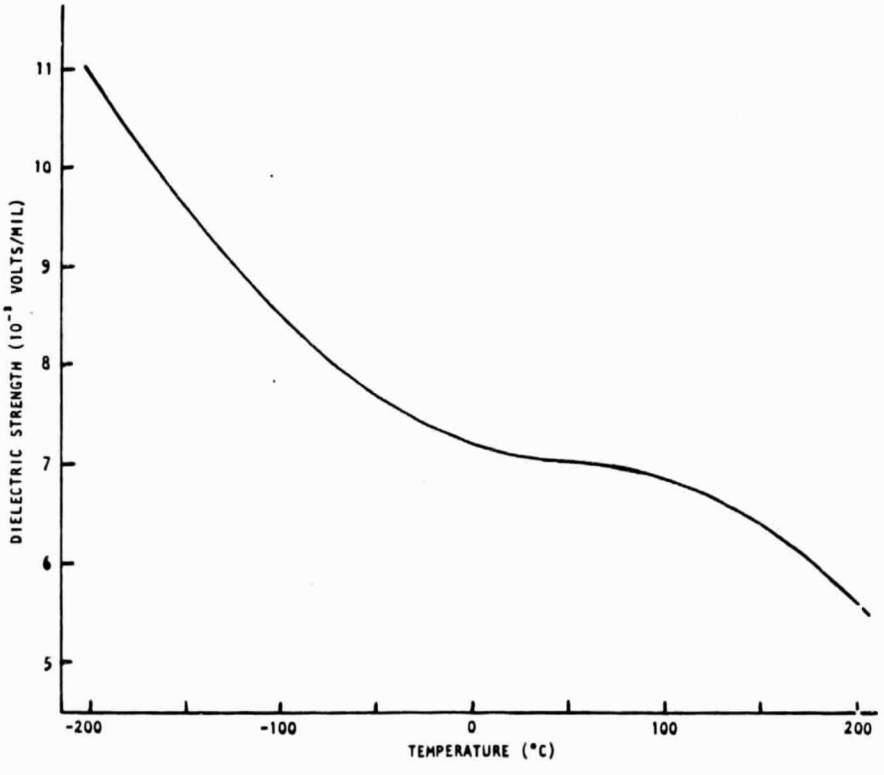

Figure 2.1-19. Kapton Type H Dielectric Strength

(2 MeV) and Rockwell tests at 10^{15} protons/cm^2 (0.7 MeV). Additional tests are planned at 0.1 MeV. There is a potential for an area savings ~9% compared to the point design. The point design solar array sizing model allows for 20% reflectivity degradation over 30 years which in view of some of the newer test data appears to be extremely conservative.

2.1.5 SOLAR PHOTOVOLTAIC POWER CONVERSION MASS AND CHARACTERISTICS

The mass of the solar cells, solar blanket, and concentrator for the SPS are shown in Table 2.1-6. The mass of each component of the three major assemblies is defined. The total mass is 8.83×10^6 kg, excluding the mass of the attachments and tensioning devices for the solar blanket and the concentrator, i.e., ~0.89×10^6 kg additional mass required for attachments and tension devices accounted for in secondary structure.

Table 2.1-6. Solar Photovoltaic Power Conversion Mass

		MASS (KG x 10^{-6})		
● SOLAR CELLS				
COMPONENT				
GaAs CELL		0.814		
GaAlAs WINDOW		0.009		
SAPPHIRE (COVER/SUBSTRATE)		2.436		
CURRENT COLLECTORS		1.836		
AR COATING		0.002		
	SUBTOTAL		5.091	
● SOLAR BLANKET				
KAPTON BLANKET		1.102		
TRANSPARENT POLYMER-THERMAL COATING		0.275		
ADHESIVES		0.826		
INTERCONNECTS		0.428		
	SUBTOTAL		2.631	(7.722)
● CONCENTRATOR				
KAPTON BLANKET		1.102		
REFLECTIVE MATERIAL		0.006		
	SUBTOTAL		1.108	
TOTAL WT: 8.83×10^6 KG				

The GaAlAs solar cell arrays are designed to generate the electrical power for the SPS. The system is capable of delivering 5 GW of electrical power to the utility user on the ground. The end-of-life (EOL) output of the array is 9.52 GW, delivered to the distribution system. The overall system efficiency of the SPS is 6.1%. The solar cells are fastened on a 25-μm (1-mil) Kapton membrane which is mounted by tensioning devices or straps to the main structural members of the SPS. The array design parameters, efficiencies, materials of construction, area requirements, and mass are presented in Table 2.1-7.

Table 2.1-7. GaAlAs Solar Cell and Blanket Design and Performance Characteristics

Item	Characteristic
Array intercepted energy	82.20 GW
Cell η at 28°C, AMO	20%
Cell η at 125°C, AMO	17.6%
Array output to distribution bus EOL	9.76 GW
Array output voltage	45 kV
Cell output voltage at 125°C	0.69 V
Cells in series	65,217
Solar cell subpanel size	
Top 24	600×750 m
Bottom 48	550×750 m
Number of bays per SPS	72
Array design factors	
Assembly and mismatch	97.7%
Interconnect and fatigue	97%
Packing factor	
Cells	96%
Blanket	99%
Reflectivity and degradation	0.90 BOL, 0.72 EOL
Concentration ratio	
Geometric	2
BOL	1.9
EOL	1.72
Solar cell construction	
Cover	20 μm sapphire
Cell	5 μm GaAlAs
Interconnect	12.5 μm silver mesh
Substrate	
Adhesive	12.5 μm FEP
Film	25 μm Kapton
Transparent thermal coating	6 μm polymer
Specific weight	0.2525 kg/m^2 (0.0516 lb/ft^2)
Deployed cell and blanket area planform	61.2 km^2
Solar cell area	30.6 km^2
Reflector surface area	61.2 km^2
Weight (kg)	
Solar cells	$7.722 \cdot 10^6$
reflectors	1.108×10^6
Total weight	8.83×10^6 kg

Thin reflective membranes are used on the SPS to reflect the sun onto the solar cell surface and obtain a nominal concentration ratio of 2. The reflector is made of 12.5 μm (0.5-mil) aluminized Kapton. The reflectors are mounted on the main structural members at a 60° angle with respect to the solar blanket. The reflector design parameters, operating temperatures, area, and mass are presented in Table 2.1-8.

Table 2.1-8. SPS Reflector Design and Performance Characteristics

Item	Characteristic
Material	Aluminized Kapton
Kapton thickness	12.5 μm
Kapton specific gravity	1.42 (0.018 kg/m^2)
Aluminized coating thickness	400 angstrom units
Weight of aluminized coating	96 kg/km^2
Reflector surface protective film coating	Quartz or calcium fluoride
Reflector subpanel size	
Top 24	600×750 m
Bottom 48	550×750 m
Number of reflector panels	144
Reflector reflectivity/degradation	0.90 BOL, 0.72 EOL
Concentration ratio geometric	2.0
Concentration ratio	1.9 BOL, 1.72 EOL
Reflector slant angle from horiz.	60 degrees
Operating temperature	
Top reflectors	-52°C
Inboard bottom reflectors	-46°C
Outboard bottom reflectors	-73°C
Total area of reflectors	61.2×10^6 m^2
Total weight of reflectors	1.012×10^5 kg

Solar array switch gears as shown in Figure 2.1-2 are provided at each end of a string of solar cells for isolation and maintenance. Voltage regulation of the solar array, power output, and beginning-of-life (BOL) excess power dissipation will be controlled by selective switching of isolation switch gears on array submodules. (Note: These switch gears are part of solar array assembly.) Optimum power output will be assured at all times by proper sizing and design of the submodules, their associated switch gear and IMCS control of the switching, in addition to control of the various loads. Voltages and currents being handled by the switch gears will be monitored by the IMCS to determine their status and to establish a need for the opening and closing of these switches. The switch gear and control are discussed in the power distribution and control and the IMCS sections of this report.

2.2 SOLAR THERMAL POWER CONVERSION SUBSYSTEM

The solar thermal system generates power by concentrating sunlight (solar energy) upon a thermal absorber. The absorber consists of a series of tubular passages containing a pressurized fluid that is heated to an elevated temperature which, in turn, is used to drive a cesium/steam Rankine turbine/generator set. Cycle efficiency for this form of power generation is approximately 50%. Waste heat from the turbine exhaust is dissipated to space by means of a radiator subsystem (part of the thermal subsystem network), after which the working fluid is returned to absorber pressure by means of a pump/compressor. Based on the results of the trade studies, the following basic requirements have been established for the solar thermal point design:

1. Satellite power size - 5 GW (at utility)
2. Satellite orientation - P.O.P.
3. Generated power - 9.78 GW, 46.7 kV dc
4. Concentrator configuration - inflatable, continuous
5. Absorber configuration - open disc, refractory metal
6. Power cycle - cesium/steam Rankine
7. Optimization criteria - minimum overall SPS cost

In performing the solar thermal point design study the following subcontractors provided design analysis and feasibility studies in support of the study effort:

Sheldahl, Inc. - Solar concentrator

Westinghouse Electric Corporation - Generator and turbines

Vought Corporation - Radiator

Rocketdyne Division (Rockwell) - Absorber, condenser, turbines

Atomics International Division (Rockwell) - Liquid metal pumps, refractory metals, high-temperature corrosion, development test facilities

2.2.1 SATELLITE CONFIGURATION

Various configurations were analyzed, in which the number of solar concentrator modules varied from 1 to 10. Figure 2.2-1 shows a 4-module design that achieves equal moments of inertia about all three axes thereby eliminating gravity gradient torques and large attitude control propellant requirements. The same can be achieved with any other number of modules, but in all cases, two microwave antennas and rotary joints are needed to achieve balancing. This imposes a substantial penalty in that:

1. Extra support structure is needed for the antennas
2. Antenna specific mass is greater in small power sizes
3. Phasing of two antennas for one rectenna introduces complexity in the microwave system

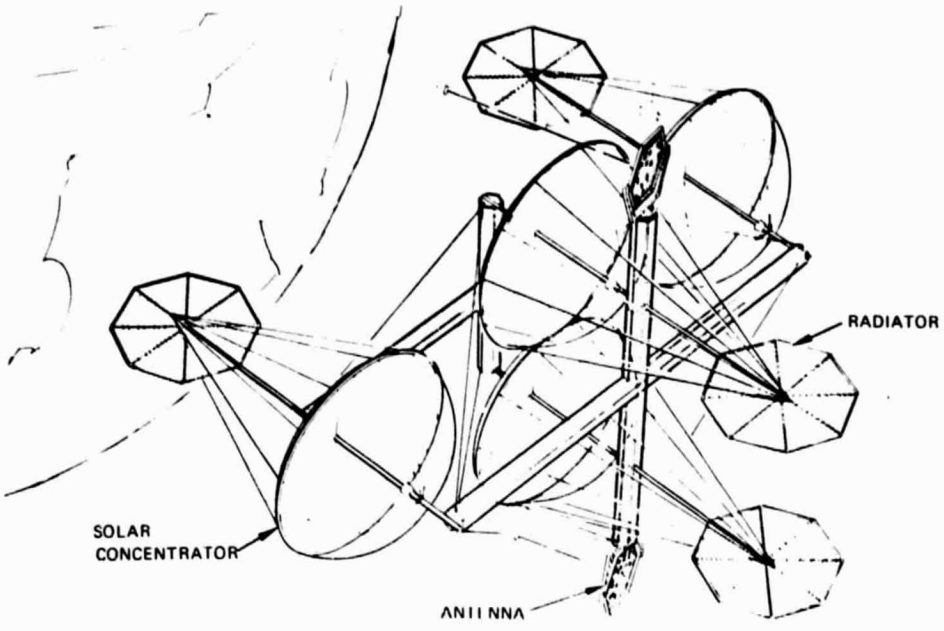

Figure 2.2-1. 4-Module Solar Thermal Satellite

In the case of Figure 2.2-1, additional length between the concentrator focal point and the radiator also imposes a severe mass penalty in terms of fluid lines. The optimum configuration was determined to be a 2-module design with a single antenna mounted between, as shown in Figure 2.2-2. Equal moments of inertia are achieved about only one axis but the other two are earth-oriented in such a way that their gravity gradient torques are always in balance. This is made possible by hinging the concentrator/radiator modules at the ends of the main satellite frame to allow seasonal tracking of the sun without tilting the long dimension of the satellite into the earth's gravity gradient (Figure 2.2-3). As shown in Figure 2.2-3, the main frame girder is offset to locate the rotary joint as the satellite C.G. for mounting ion-thrusters. Thus, they can be earth-oriented for satellite self-transport while the solar concentrator modules are sun-oriented to produce power for the thrusters. Due to the relative compactness of the solar thermal structure, its frequency response is high and there are no attitude control problems or scar weight penalties associated with construction in LEO or self-transport to GEO. Since, no significant degradation of concentrator reflectivity is expected in the Van Allen belt, it appears advantageous to use LEO construction for the entire satellite.

2.2.2 ABSORBER POINT DESIGN

Rocketdyne Division (Rockwell) supported this design with analysis and technology derived from in-house, ground-based solar absorber projects ("tower power" boilers).

Configuration

As discussed in the trade studies, the optimum configuration for a Rankine absorber is an open-disc design occupying the minimum sized aperture.

No benefit is gained by forming a cavity behind the aperture because reradiation losses are not materially lowered. The problem of protecting the exposed, underside of the absorber tubes from meteorite puncture proved to be a dominant driver in optimizing the entire power loop and sizing the SPS structure. This is because heavy armor (~1 cm) is required on the bottom side of the tubes to limit lost absorber area to a reasonable value (assumed to be 10% over 30 year life). It became optimum therefore, to utilize the full strength of the tube wall provided by the armor, to raise the absorber outlet temperature and pressure to the limit of the wall material. This improves power cycle efficiency and reduces the size of the concentrators, absorbers, turbines, radiators and SPS structure. If it were not for the heavy armor requirement, the absorber outlet temperature might optimize at a lower value.

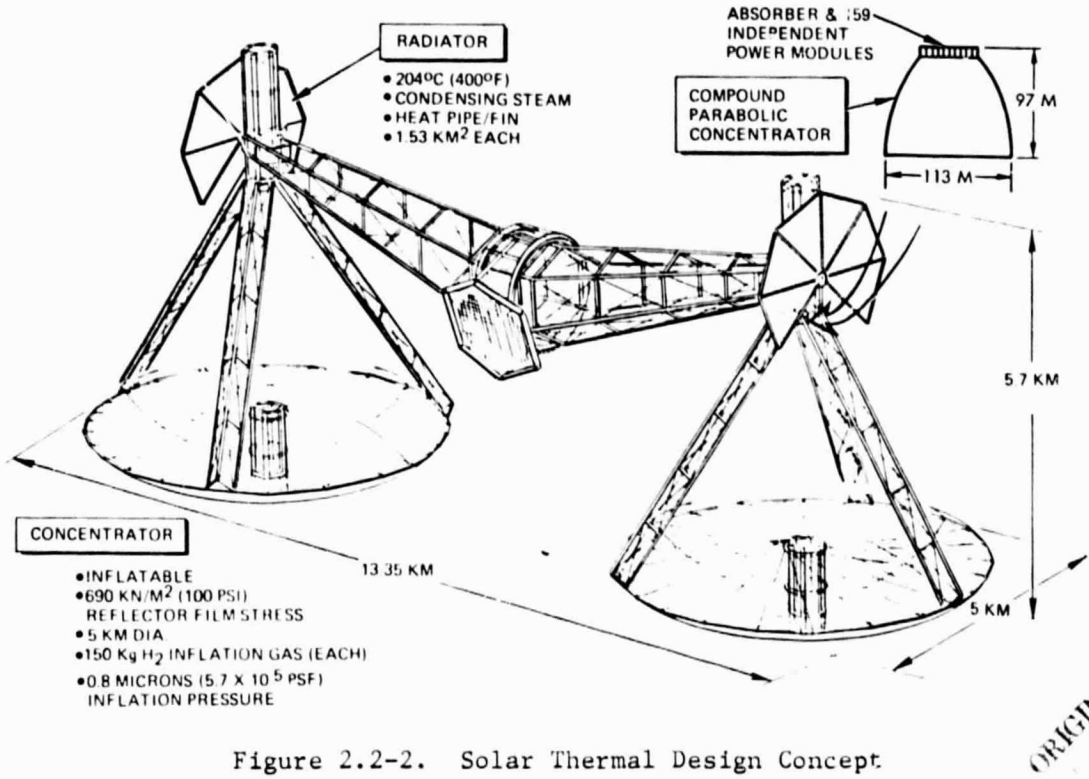

Figure 2.2-2. Solar Thermal Design Concept

Materials

Minimum absorber disc diameter is constrained by: 1) excessive "spillover" losses at the aperture, and 2) the melting temperature of a dry tube. The latter constraint proved to be the most critical because of the limited absorber materials available. Among the various refractory metals, molybdenum and its alloy TZM appeared to have the best combination of characteristics, as listed below:

1. Creep strength - Excellent
2. Melting point - 2620°C (4750°F)
3. Thermal conductivity - 100 W/m-°C (58 B/hr-ft-°F) (at 2000°F)

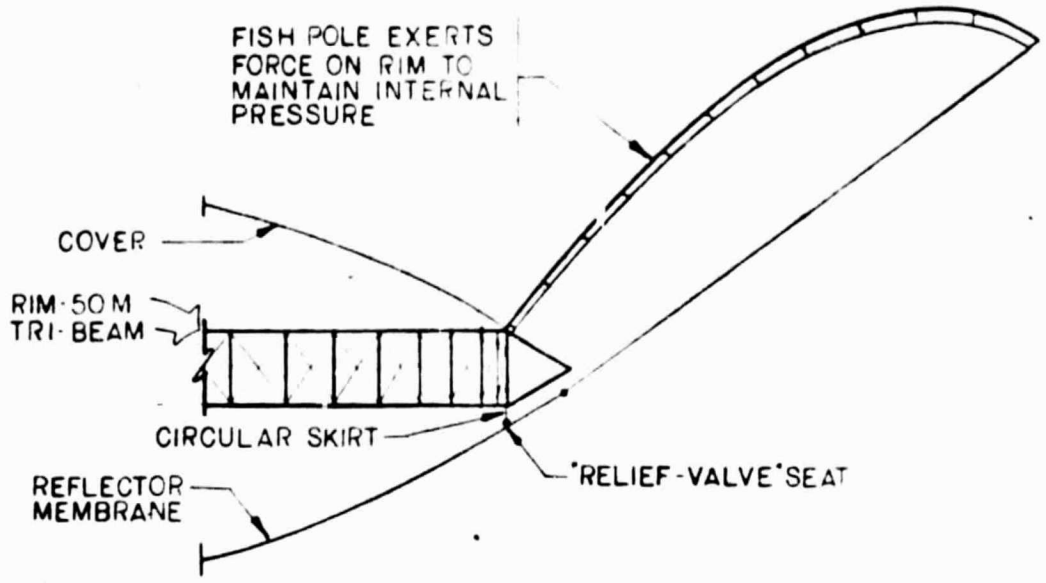
FISH POLE EXERTS FORCE ON RIM TO MAINTAIN INTERNAL PRESSURE
COVER
RIM-50 M TRI-BEAM
CIRCULAR SKIRT
"RELIEF-VALVE" SEAT
REFLECTOR MEMBRANE

W

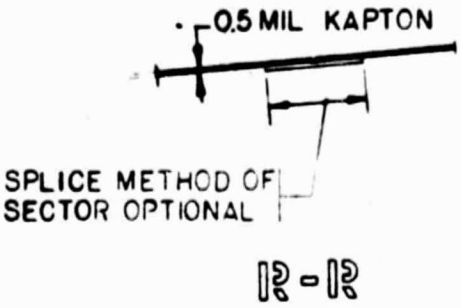

R-R

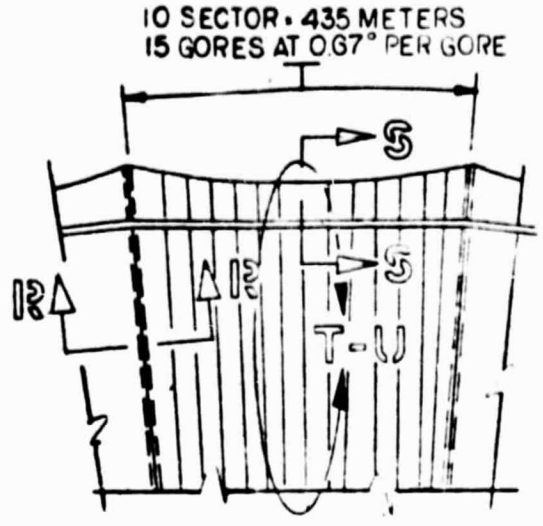

N

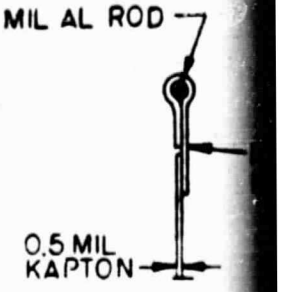

S-S

EACH SECTOR PREFABRICATED ON EARTH & DELIVERED TO ORBIT WHERE
•36 SECTIONS ARE ASSEMBLED TO MAKE A PARABOLIC REFLECTOR

•UP TO 9 SECTORS CAN BE JOINED ON EARTH & DELIVERED TO ORBIT.

MAXIMUM PAYLOAD 90,000 KG (200,000 LB) CARGO BAY 6M X 6M X 30M

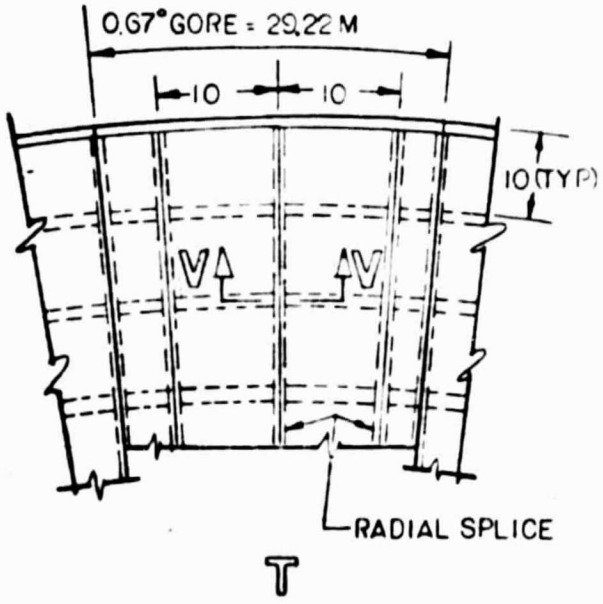

T

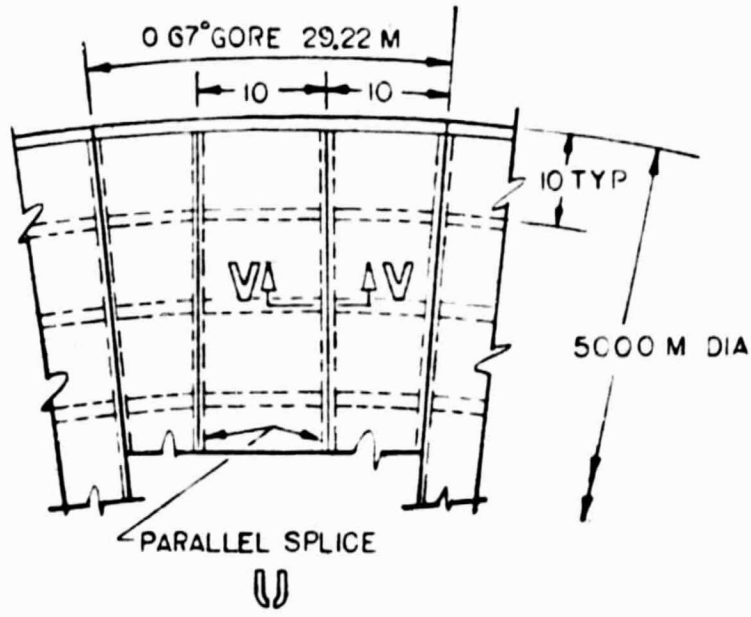

U

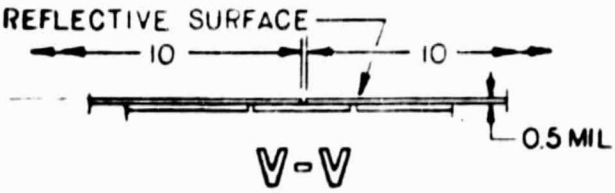

V-V

FOLDOUT FRAME 2

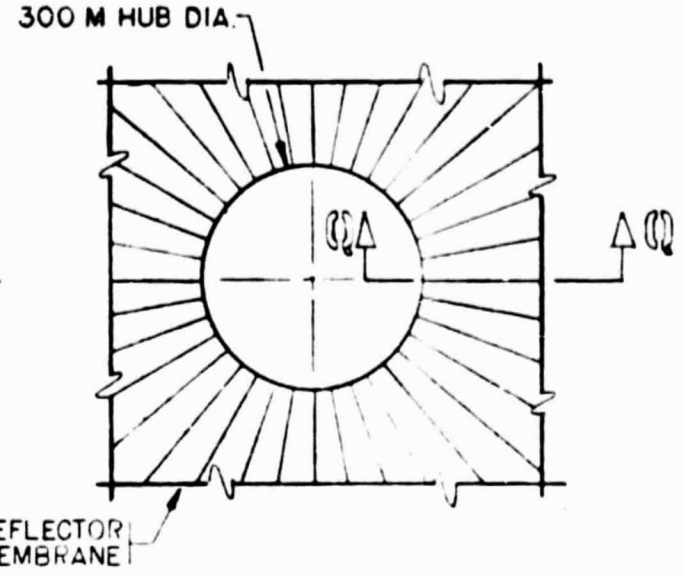

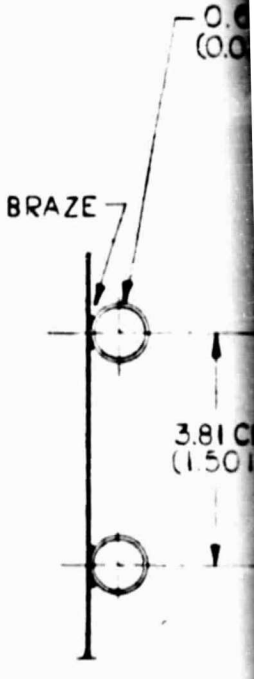

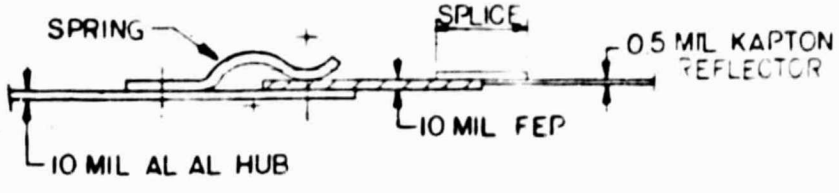

FOLDOUT FRAME 3

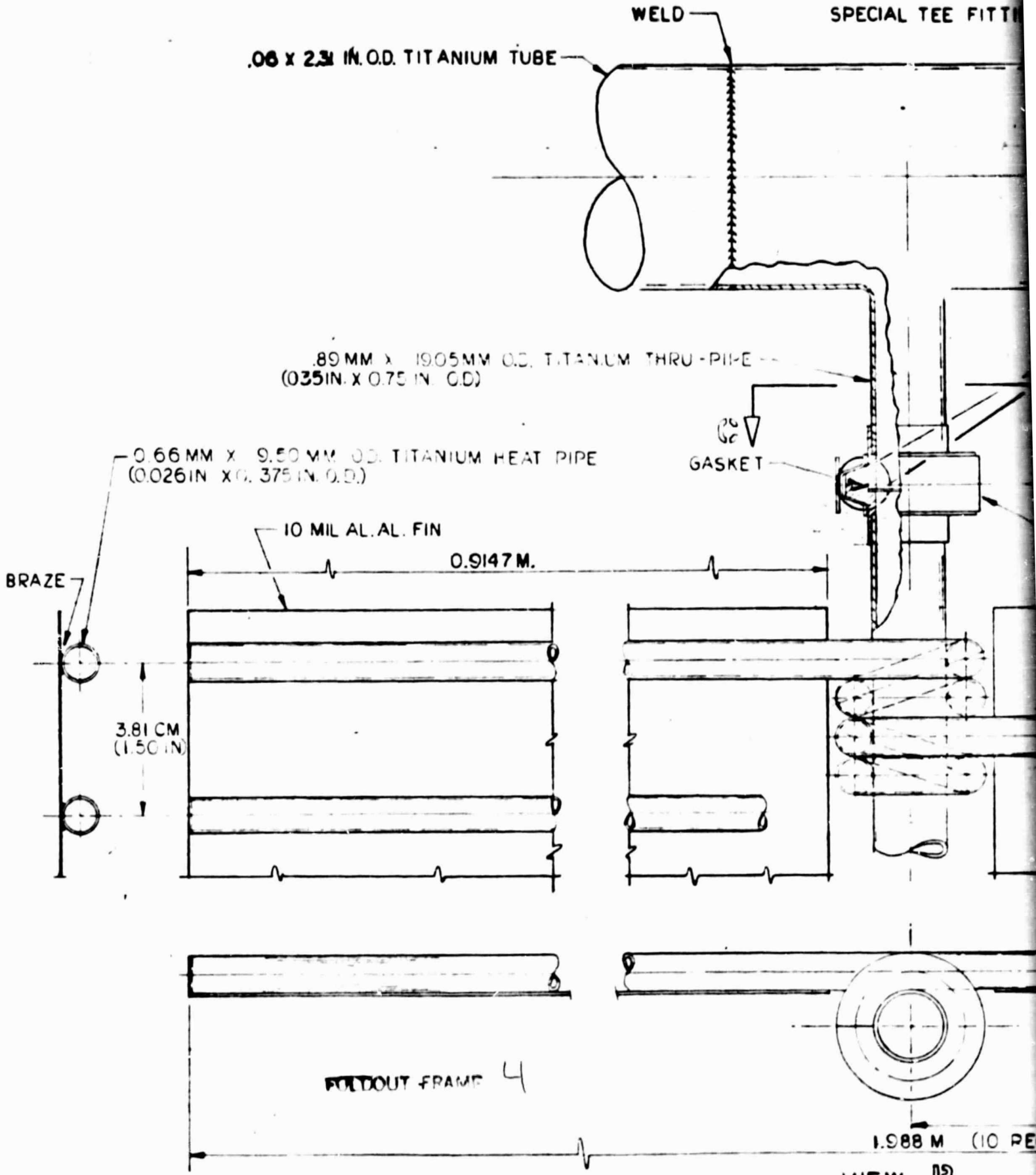

VIEW B

RADIATOR FIN DETAIL AND JOINT ASS

SCALE: NONE

SPECIAL TEE FITTING

THE FUSTO-CONICALLY SHAPED GASKET RESTS BETWEEN THE MATING FLANGES PRIOR TO ASSEMBLY. AS THE FLANGES ARE MOVED TOGETHER UNDER AXIAL LOAD, THE GASKET IS LOADED RADIALLY AGAINST THE MATING FLANGE SEALING EDGE.

AS THE FLANGES CONTINUE AND MOVING TOGETHER THE GASKET ACTS AS A SPRING AND A PLASTIC FLOW CONDITION IS MECHANICALLY INDUCED AT ITS SEALING EDGES. THE SHAPE OF THE GASKET IS TYPICAL OF THE SPRING ACTION. THIS PLASTIC FLOW CONDITION INSURES INTIMATE INTERMESHING OF THE SURFACE FINISHES AT THE SEALING AREA, PROVIDING A FULL CIRCUMFERENTIAL METAL-TO-METAL RADIAL SEAL. THIS IS DONE WITHOUT THE GASKET BRINNELLING OF THE SURFACE AREA OF THE FLANGE. THE METAL OF EACH FLANGE IS HARDER THAN THE GASKET MATERIAL - A CONDITION ESSENTIAL TO PLASTIC FLOW INTERMESHING.

WHEN THE FLANGES ARE CLOSED THE RADIAL COLUMN LOAD ON THE GASKET PROVIDES A SPRING EFFECT. THIS SPRING ASSURES THAT RADIAL CONTACT IS MAINTAINED WHEN THE FLANGES MOVE DUE TO THERMAL CYCLING.

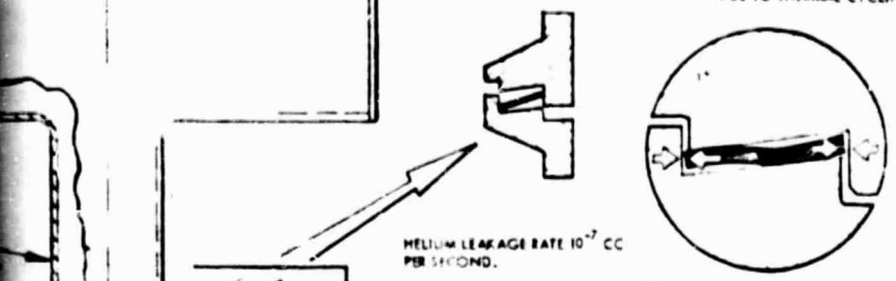

C-C

JOINT ASSY. IN SPACE

HELIUM LEAKAGE RATE 10^{-7} CC PER SECOND.

C C

SPACE ASSY. JOINT

MARMAN CONOSEAL CLAMP OR WELD OPTIONAL (TYPICAL FOR VALVE AND PUMP CONNECTIONS)

19.62 M

19.85 M ON EARTH RADIATOR ASSY.

0.994 M

1.988 M (10 REQ PER PANEL)

VIEW B

D JOINT ASSEMBLY

LE: NONE

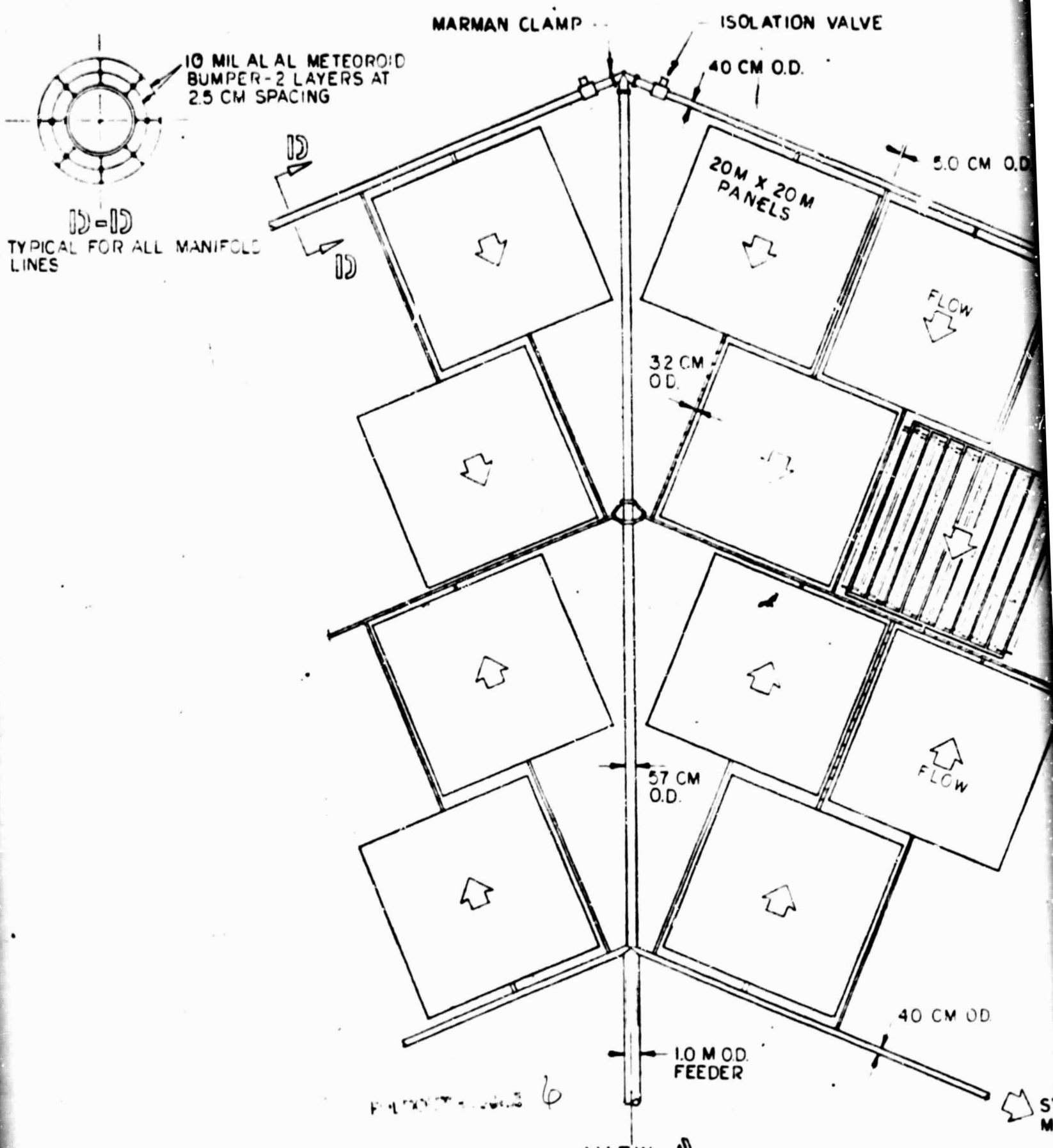

VIEW A
PANEL INSTALLATION
SCALE 1:250

TION VALVE

O.D.

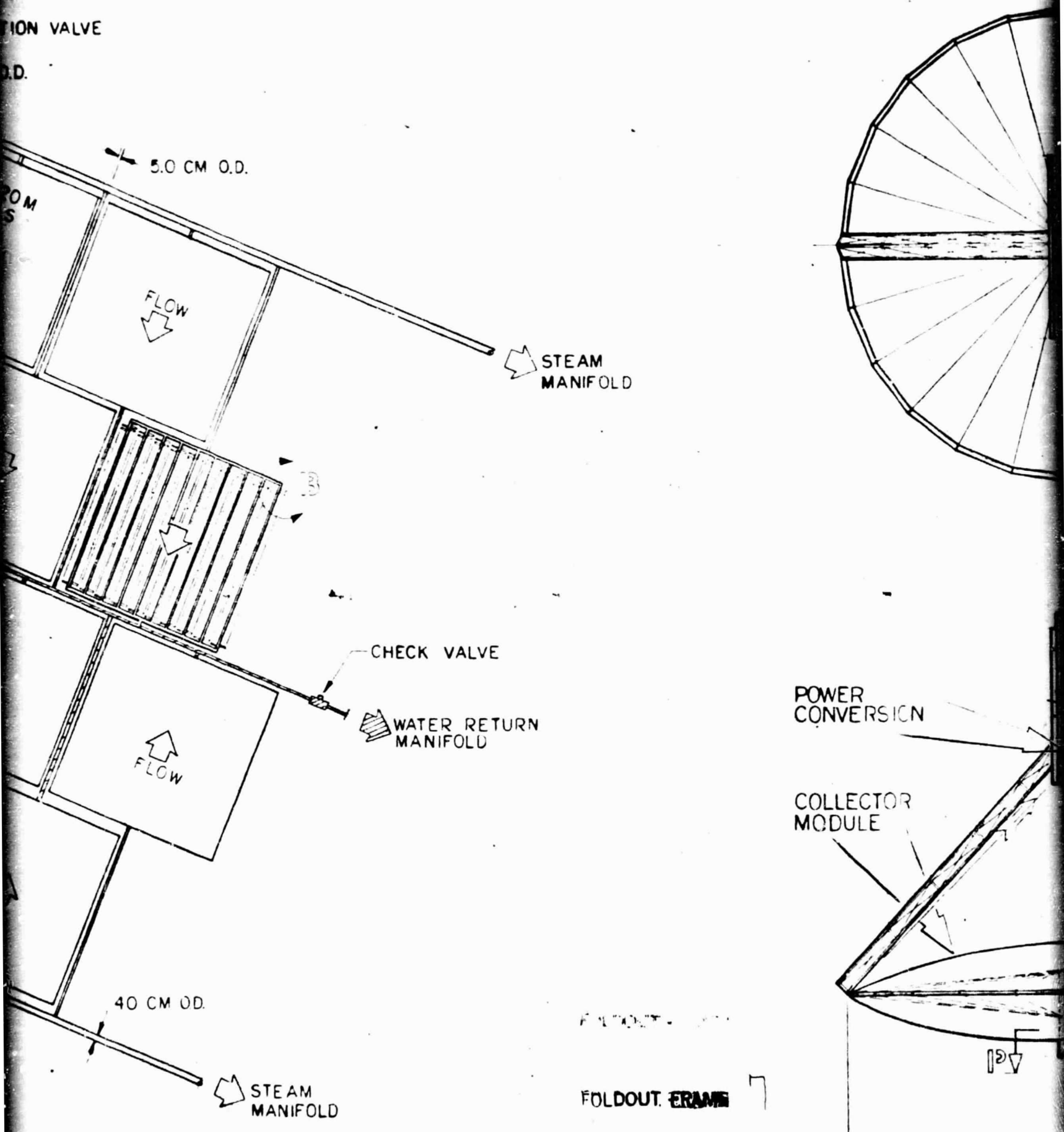

FOLDOUT FRAME

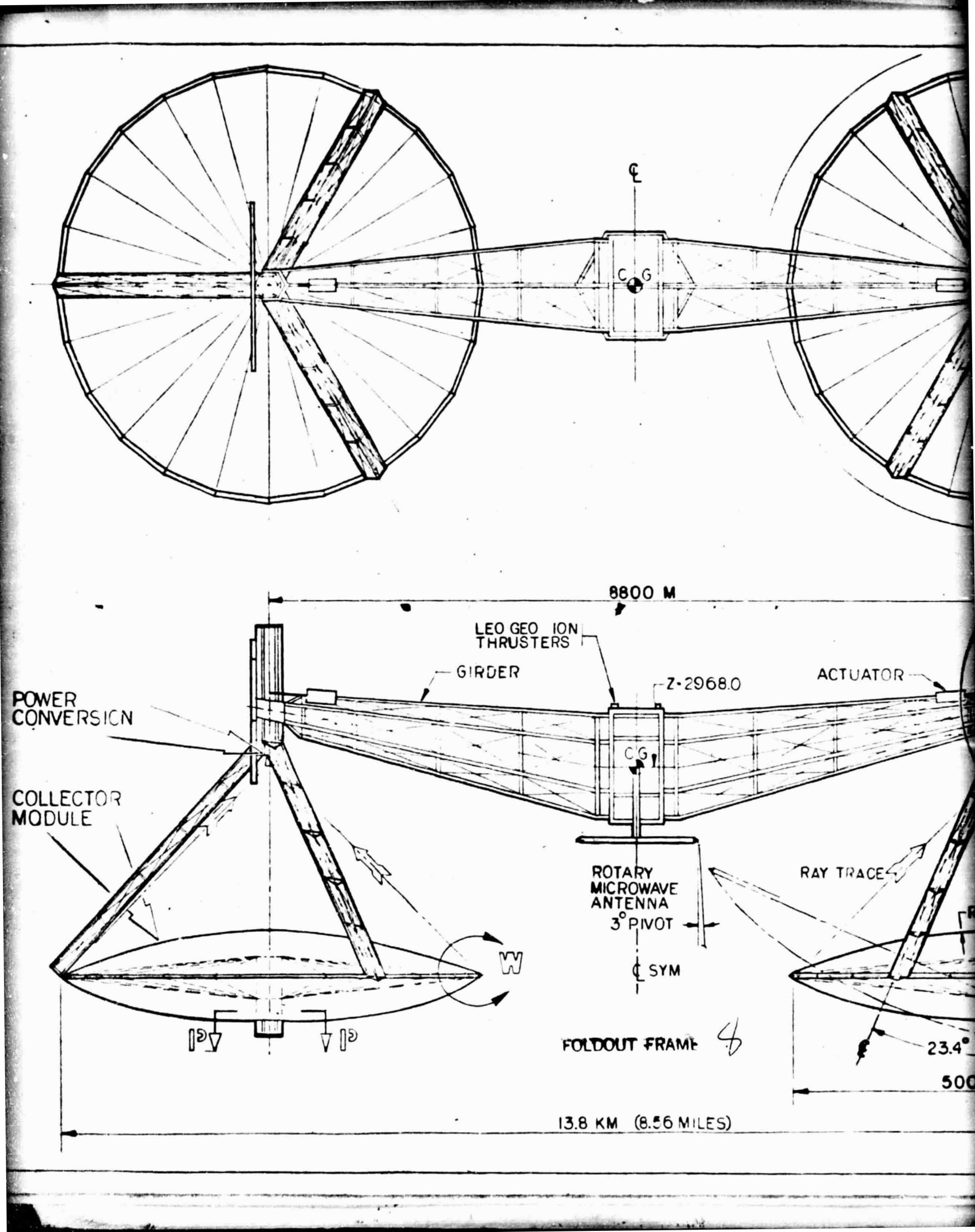
8800 M
LEO GEO ION THRUSTERS
GIRDER
Z-2968.0
ACTUATOR
POWER CONVERSION
COLLECTOR MODULE
C G
ROTARY MICROWAVE ANTENNA
3° PIVOT
℄ SYM
RAY TRACE
W
FOLDOUT FRAME
23.4°
500
13.8 KM (8.56 MILES)

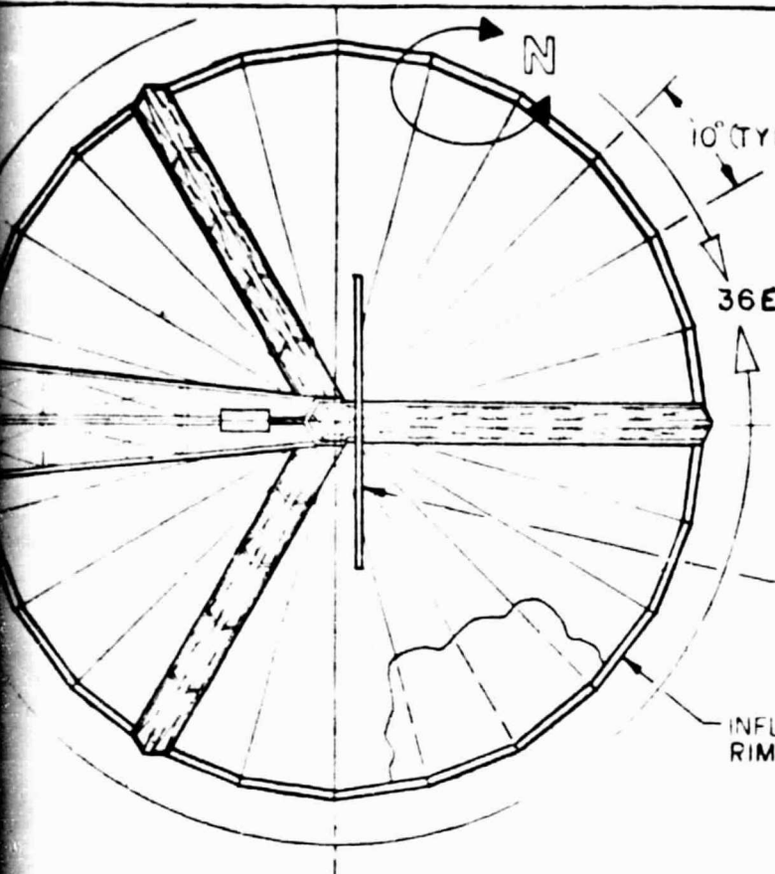

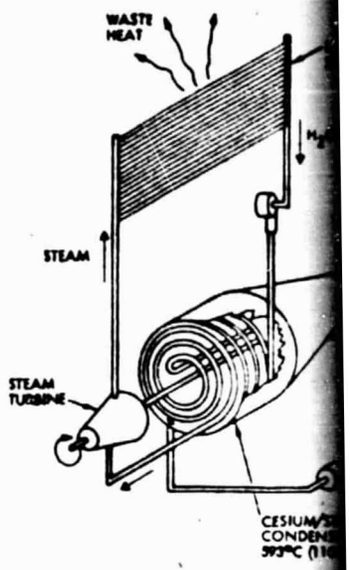

CESIUM/

THE MAIN HARDWARE ELEMENTS OF
IN SCHEMATIC RELATIONSHIP. CO
BOILER PANEL PROVIDES CESIUM VA
EXHAUST FROM THE TURBINE CONDE
OF THE STEAM LOOP, THEREBY UTILI
DRIVE THE STEAM TURBINE WHICH IS
CESIUM TURBINE AND ELECTRICAL G
CONDENSES DIRECTLY IN A LIGHTW

BOLDOUT FRAME 9

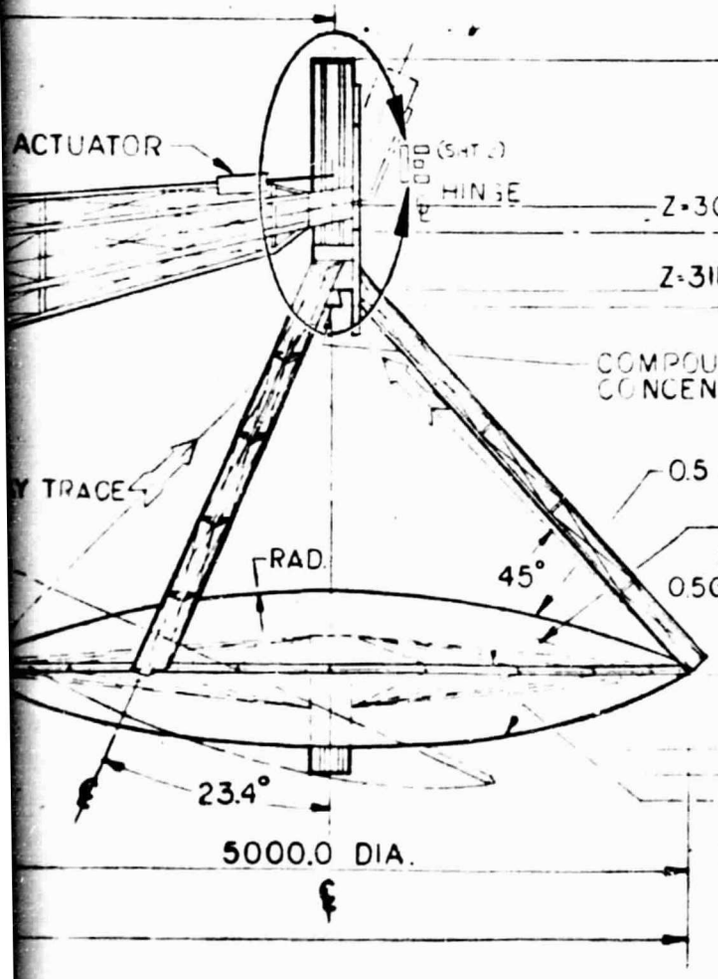

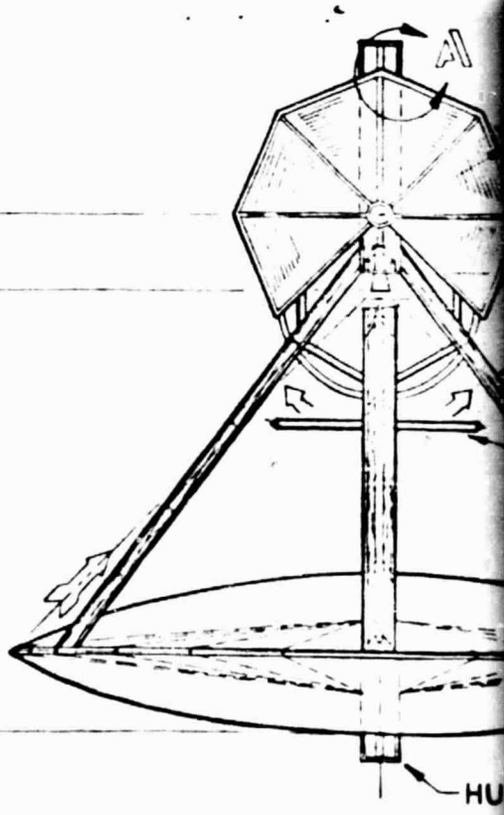

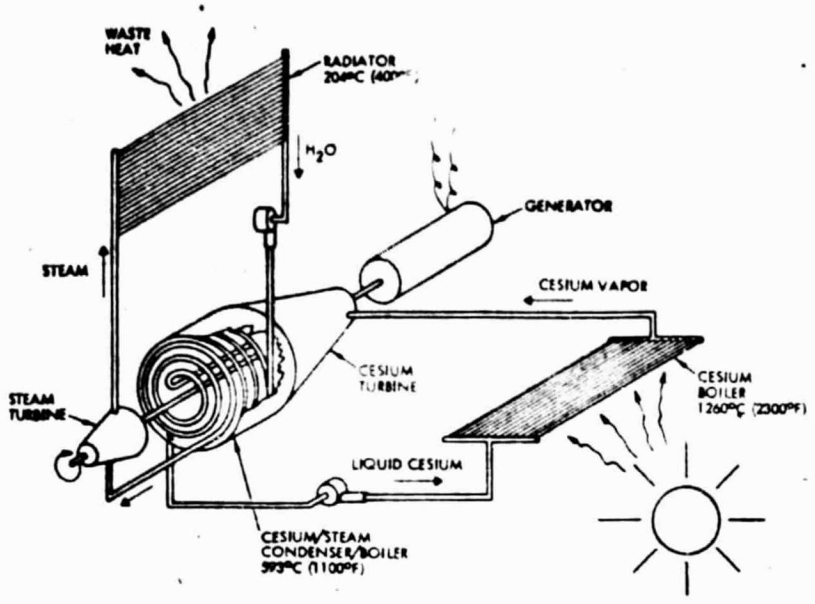

CESIUM/STEAM POWER LOOP

THE MAIN HARDWARE ELEMENTS OF THIS RANKINE CYCLE POWER LOOP ARE SHOWN IN SCHEMATIC RELATIONSHIP. CONCENTRATED SOLAR FLUX IMPINGING ON THE BOILER PANEL PROVIDES CESIUM VAPOR AT 1260°C (2300°F) TO THE CESIUM TURBINE. EXHAUST FROM THE TURBINE CONDENSES ON THE BOILER AND SUPER-HEATER TUBES OF THE STEAM LOOP, THEREBY UTILIZING WASTE HEAT FROM THE CESIUM LOOP TO DRIVE THE STEAM TURBINE WHICH IS MOUNTED ON A COMMON SHAFT WITH THE CESIUM TURBINE AND ELECTRICAL GENERATOR. EXHAUST FROM THE STEAM TURBINE CONDENSES DIRECTLY IN A LIGHTWEIGHT RADIATOR (HEAT PIPES NOT SHOWN).

SOLAR THERMAL SATELLITE DESIGN CHARAC

1. OVERALL DESCRIPTION

   A. 5-GW POWER TO UTILITY INTERFA
   B. GEOSYNCHRONOUS CONSTRUCTI
   C. SINGLE MICROWAVE ANTENNA
   D. GEOSYNCHRONOUS EQUATORIAL

2. SOLAR THERMAL DESIGN CONCEPT

   A. TWO SEPARATE COLLECTOR MODU
      GRADIENT BALANCING (WITH A S
      ROTARY JOINT TO BE LOCATED A
      THE LEO/GEO ION THRUSTERS, E
      THE STRUCTURE TO PERMIT SEASO
      AFFECTING GRAVITY-GRADIENT
      INDEPENDENT POWER MODULES U
      WASTE HEAT IS REJECTED TO A CO
      AND FINS).

3. SUBSYSTEMS

   A. POWER CONVERSION
      . CESIUM/STEAM RANKINE CY
   B. ATTITUDE CONTROL/STATIONKEEP
      . Y-POP
      . ARGON THRUSTERS
   C. POWER DISTRIBUTION
      . 60 KV DC
   D. MICROWAVE ANTENNA
      . GAUSSIAN BEAM
      . 2.45-GHz FREQUENCY
   E. STRUCTURE
      . ALUMINUM (GRAPHITE/THER
      . BEAM MACHINE CONSTRUCT
   F. INFORMATION MANAGEMENT
      . DISTRIBUTED
   G. ARTICULATED, SUN-POINTING RE
   H. STRUCTURE/WIRING NOT INTEGRA
   I. RCR WAVEGUIDE PANELS
   J. TENSION-WEB, COMPRESSION-FRA

4. ROTARY ANTENNA IS IDENTICAL TO PH
   NO. 77086-12 SHEET 2 FOR STRUCTURAL

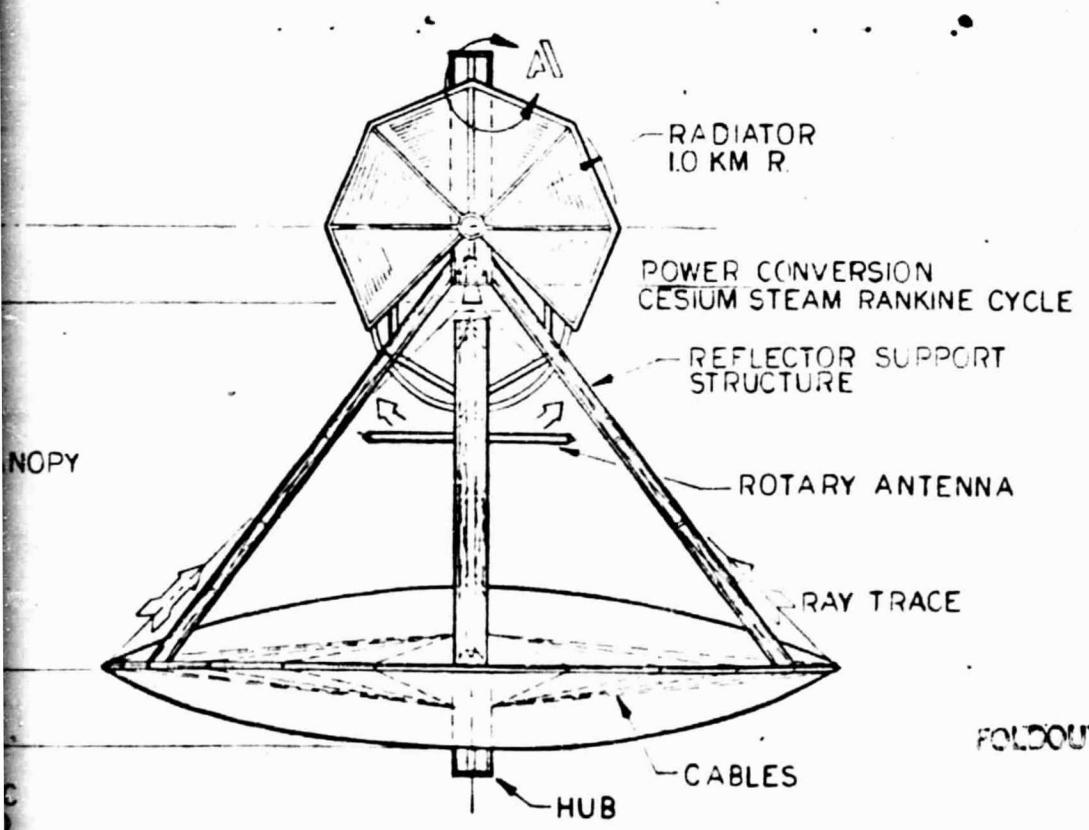

FOLDOUT FRAME 10

Figure 2.2-3. Main Frame Details

FOLDOUT FRAME

SOLAR THERMAL SATELLITE DESIGN CHARACTERISTICS

1. OVERALL DESCRIPTION

   A. 5-GW POWER TO UTILITY INTERFACE
   B. GEOSYNCHRONOUS CONSTRUCTION LOCATION
   C. SINGLE MICROWAVE ANTENNA
   D. GEOSYNCHRONOUS EQUATORIAL OPERATIONAL ORBIT

2. SOLAR THERMAL DESIGN CONCEPT

   A. TWO SEPARATE COLLECTOR MODULES ARE USED TO (1) FACILITATE GRAVITY-GRADIENT BALANCING (WITH A SINGLE ANTENNA), AND (2) ALLOW THE ROTARY JOINT TO BE LOCATED AT THE SATELLITE c.g. FOR MOUNTING THE LEO/GEO ION THRUSTERS. EACH COLLECTOR MODULE IS HINGED TO THE STRUCTURE TO PERMIT SEASONAL TRACKING OF THE SUN WITHOUT AFFECTING GRAVITY-GRADIENT BALANCE. EACH ABSORBER HAS 159 INDEPENDENT POWER MODULES UTILIZING A CESIUM/STEAM RANKINE CYCLE. WASTE HEAT IS REJECTED TO A CONDENSING STEAM RADIATOR (HEAT PIPES AND FINS).

3. SUBSYSTEMS

   A. POWER CONVERSION
      . CESIUM/STEAM RANKINE CYCLE
   B. ATTITUDE CONTROL/STATIONKEEPING
      . Y-POP
      . ARGON THRUSTERS
   C. POWER DISTRIBUTION
      . 40 KV DC
   D. MICROWAVE ANTENNA
      . GAUSSIAN BEAM
      . 2.45-GHz FREQUENCY
   E. STRUCTURE
      . ALUMINUM (GRAPHITE/THERMAL PLASTIC COMPOSITE ALTERNATIVE AS NEEDED)
      . BEAM MACHINE CONSTRUCTION
   F. INFORMATION MANAGEMENT
      . DISTRIBUTED
   G. ARTICULATED, SUN-POINTING REFLECTORS
   H. STRUCTURE/WIRING NOT INTEGRATED
   I. RCR WAVEGUIDE PANELS
   J. TENSION-WEB, COMPRESSION-FRAME STRUCTURE

4. ROTARY ANTENNA IS IDENTICAL TO PHOTOVOLTAIC SYSTEM. REFER TO DRAWING NO. 77016-12 SHEET 2 FOR STRUCTURAL ARRANGEMENT.

FOLDOUT FRAME //

ORIGINAL PAGE IS
OF POOR QUALITY

4.	Weldability	-	fair (electron beam)
5.	Forming	-	rolling, extruding, forging
6.	Density	-	10.2 gm/cc (0.37 lb/in^3)
7.	Machinability	-	acceptable
8.	Availability	-	good
9.	Cost	-	relatively low
10.	Toughness	-	acceptable, above room temperature
11.	Cesium compatibility	-	excellent (if no oxygen contaminants)

By comparison, columbium and hafnium alloys have inferior creep strength above 1260°C (2300°F), while tantalum is both scarce and heavy. Tungsten is the heaviest of the group and difficult to extrude, weld and machine. The biggest drawback of molybdenum is its brittleness at room temperature, especially in the recrystallized or welded state. The absorber, however, is not required to withstand impact loads in service. As with brittle ceramics, which have been routinely recommended for heat exchanger tubing in both spaceborne and ground thermal power systems, reasonable care must be exercised in handling and shipping. With proper equipment, molybdenum and TZM can be extruded quite well into 4 ft long tubes although TZM is more difficult. The price of TZM in ingot form is quoted by AMAX Corporation at ~$8/lb while the estimate for extruded tubing in very large production quantities is ~$25/lb.

Based on the use of molybdenum or TZM alloy, the minimum absorber diameter required to prevent melting of a dry tube in a 20% over-flux hot spot was found to be 80 m. This corresponds to an average flux impinging on the absorber disc of 2250 suns, in which a dry tube would reach an equilibrium reradiation temperature of 2480°C (4500°F) vs a melting point of 2620°C (4750°F). This is well above the recrystallization temperature 1316°C (2400°F) which causes growth of large grains in the metallurgical structure. Recrystallization raises the upper brittle boundary temperature to ~100°C (212°F) but does not seriously affect toughness, creep or strength properties at working temperature (reference Figure 2.2-4). As discussed below, the average service temperature ofthe tube wall is ~1316°C (2400°F) so that in time, all the tubes would be essentially recrystallized anyway. A "dry-tube" condition could result from either a meteorite puncture, inadvertant shutdown, or planned shutdown of the cesium flow in a boiler panel. In either case, no significant internal pressure would be present at the time of reaching a high over-temperature condition. The cesium would either be vented externally or condensed by the interfacing steam boiler at a low vapor pressure.

Panels

To minimize absorber weight, it was decided not to use a heavy central manifold system for collecti' g liquid from and distributing vapor to the individual turbines. The absorber disc was divided into 159 individual, rectangular boiler panels (4.25 m × 7.2 m) as shown in Figure 2.2-5. Each panel is assigned to a single turbine mounted on the insulated, top side of the panel. This also gives a high degree of redundancy for isolating meteorite failures. Figure 2.2-6 shows the interconnecting plumbing for sharing

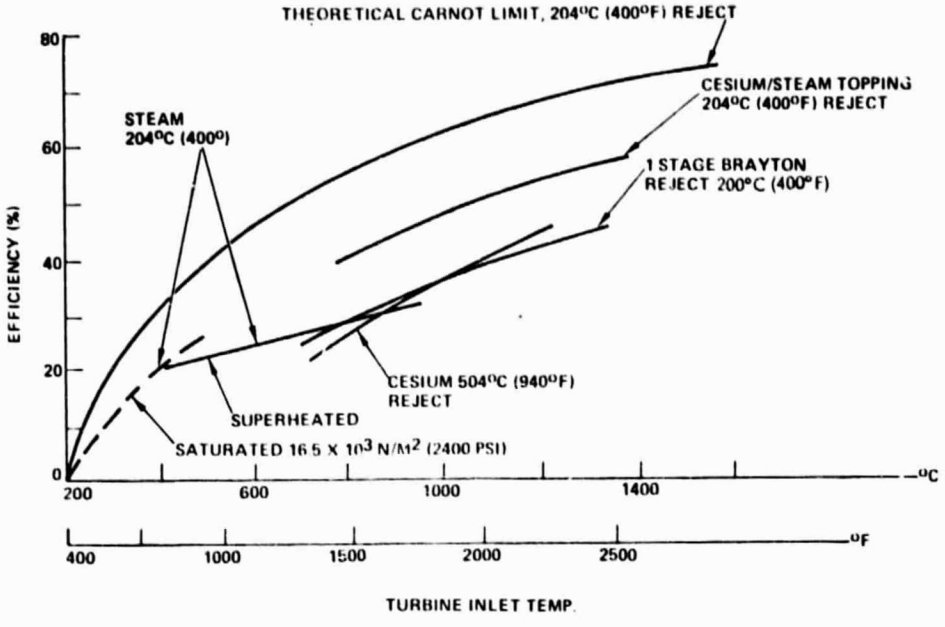

Figure 2.2-4. Dynamic Conversion Efficiencies

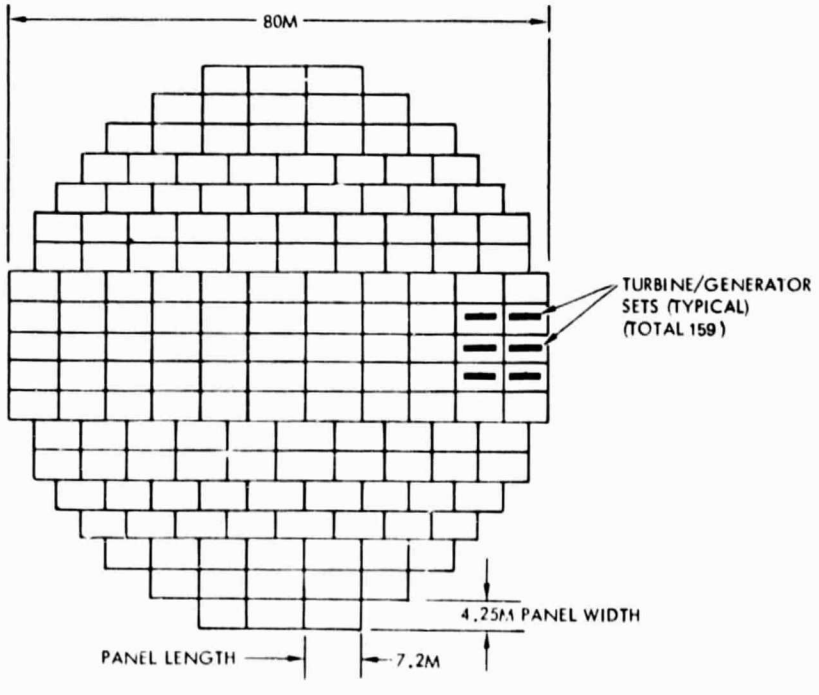

Figure 2.2-5. Solar Absorber Panel Matrix

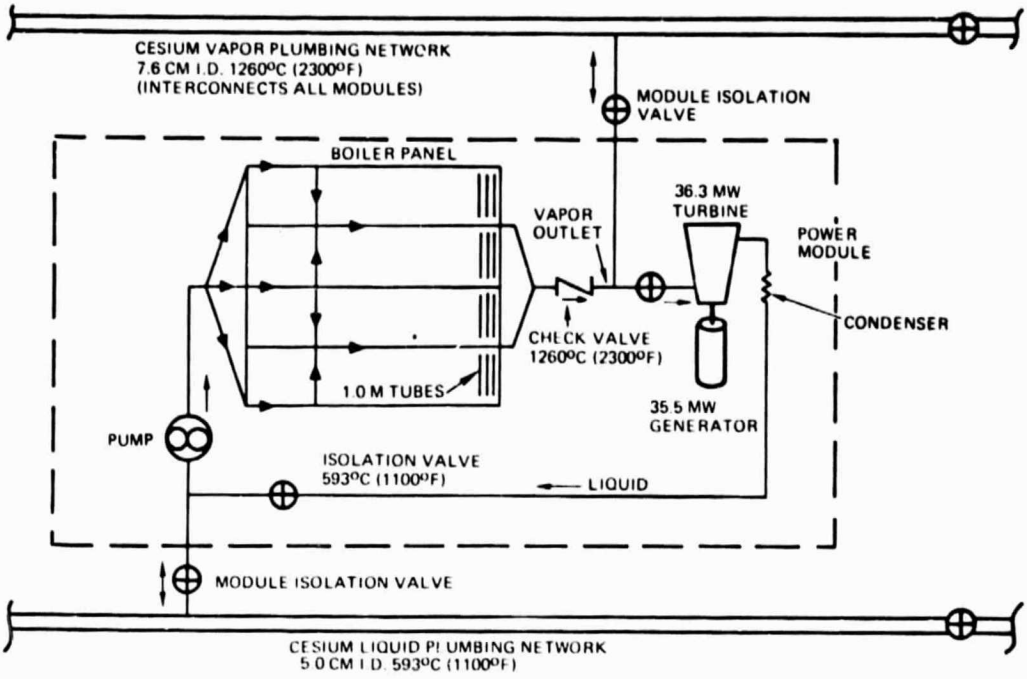

Figure 2.2-6. Cesium Loop Isolation Circuitry

flow between adjacent power loops in the event of a turbine or panel failure. It was determined that a quantity of 159 panels was best for minimizing lost corner area at the edge of the disc and staying within the optimum turbine/generator size of 30-40 MW. Although gyroscopic forces from the turbines and generators are very low at the design flight control acceleration (10^{-4} g), adjacent units will rotate in opposite directions to cancel out such forces.

Meteorite Protection

Determination of the required armor thickness for the boiler tubes was based on use of a 45° compound parabolic reflector skirt as shown in Figure 2.2-7. The reflector panels of 0.025 cm (10 mil) polished nickel increase the solar capture area and serve as bumpers to break up most of the heavier meteorites into harmless particles. Only meteorites entering within an effective cone angle of ±30° can avoid the bumper. On the basis of puncturing 10% of the individual boiler panels in 30 years, the required armor thickness (including the tube wall) came to 1 cm. The plastic membrane of the inflated concentrator intercepts all meteorites which enter within the ±30° cone angle but it is too thin to break up damaging sized particles.

Tube Design

Optimization of the boiler tube length and diameter was based on the following design factors which influence panel mass:

1. Short tube length reduces pressure drop and inlet pressure.

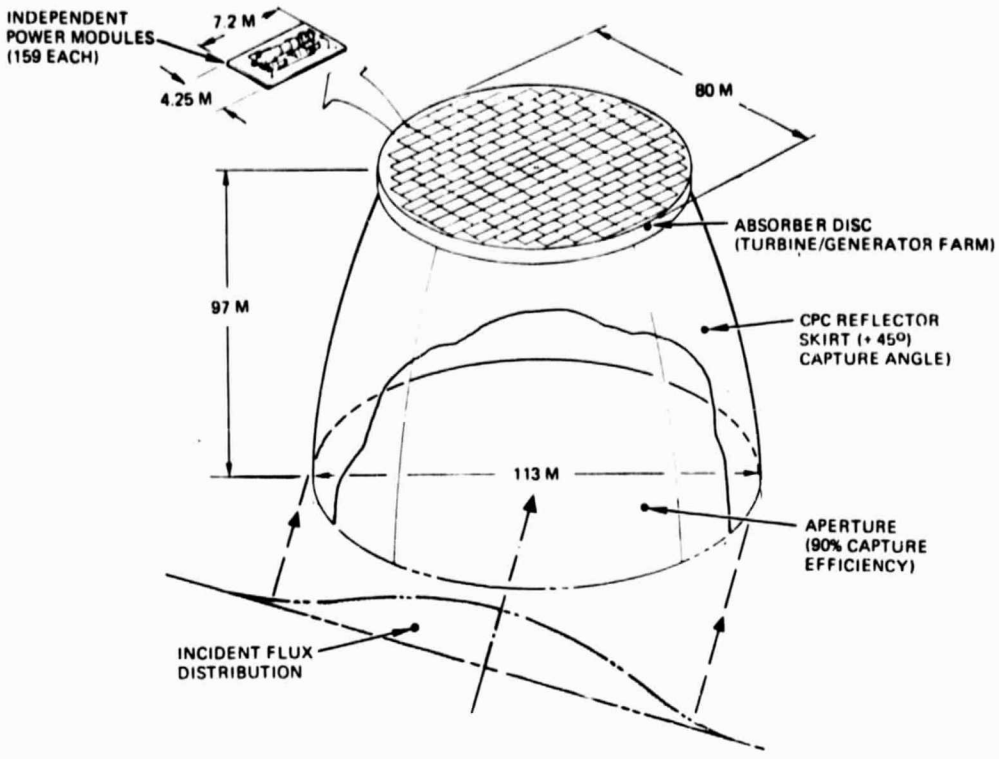

Figure 2.2-7. Solar Absorber Point Design

2. Small inside diameter reduces stress on armor side of tube and reduces required wall thickness on opposite side, for a given pressure level. However, small I.D. also reduces total panel cross-sectional flow area and raises pressure drop and inlet pressure, for a given panel face area.

A minimum tube length of 3.5 ft was selected (Figure 2.2-6) to avoid excessive welding and manifolding. The tube I.D. was then iterated to obtain the maximum cesium outlet temperature and pressure (saturated vapor conditions), as permitted by the creep strength (1% in 30 years) of the armor side of the tube. The thickness of the opposite wall was then calculated, based on a temperature equal to the fluid temperature. Figure 2.2-8 shows the resulting optimum tube cross section dimensions. The creep strength assumed is that for TZM shown in Figure 2.2-9. Some sources of data show that unalloyed molybdenum has a substantially higher creep strength than TZM at temperatures above 1216°C (2200°F) (Reference 2.2-1).

To maximize boiler performance and minimize tube mass, a recirculating design was selected for each boiler panel. A maximum vapor quality of 0.5 was assumed at the tube outlet to insure a high inside heat transfer film coefficient (20,000 Btu/hr/ft^2-°F) and minimize tube wall temperatures. Moisture droplets are extracted from the boiler discharge flow in a "cyclone-type" (solid state) separator and returned to the boiler inlet line. A venturi throat in the inlet line provides a lowered pressure to aspirate the recirculated liquid from the separator. This avoids the need for a high temperature recirculation pump to handle saturated liquid cesium at 1260°C (2300°F).

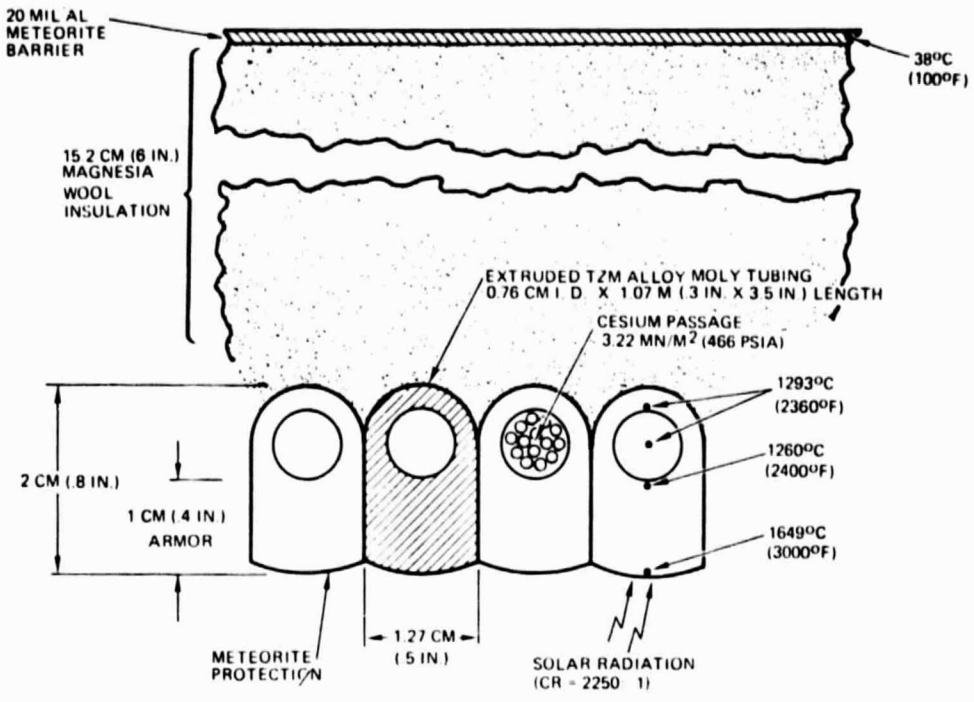

Figure 2.2-8. Cesium Boiler Panel Cross-Section

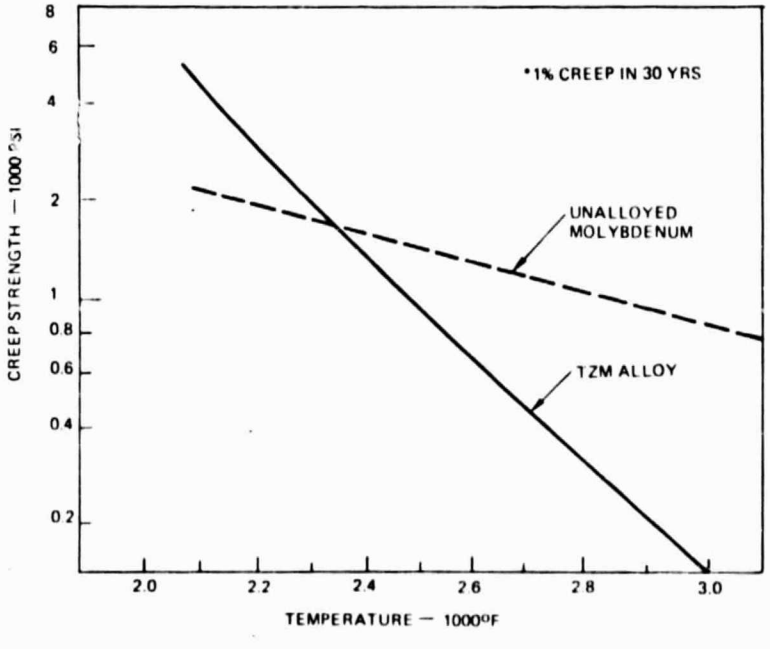

Figure 2.2-9. Refractory Metal Creep Strength*

The critical point along the tube length was found to be the "bubble point" near the inlet end where boiling first starts and the combination of fluid pressure and saturation temperature is the worst. Figure 2.2-8 shows the temperature profile and pressure across the tube walls at this critical point. The pressure drop in the 1.07-m long tube is 386 KN/m^2 (56 psi), which is adequate to prevent 2-phase flow instability. A high absorptivity, vitreous glaze coating ("Pyromark", α = 0.95) was assumed for the sun side of the boiler tubes. Meteorite punctures of the topside of the tubes are virtually eliminated by 0.15 meter of thermal insulation covered with a 0.05 cm (20 mil) bumper sheet. The insulation is sized to give a topside temperature of 38°C (100°F).

Reflector Skirt

Figures 2.2-10 and 2.2-7 show the constructional details of the absorber assembly and reflector skirt. Insulation on the outside of the skirt may be advantageous by raising its inside surface temperature and reducing the overall reradiation losses of the absorber disc, in effect forming a semi-cavity. Another area for further study is installation of a thin quartz window across the bottom of the reflector skirt to act as a meteorite bumper and thermal reradiation barrier, and still admit visible light. This would permit a substantial reduction in the mass of armor on the absorber tubes.

Absorber Characteristics

Table 2.2-1 presents the salient characteristics and performance data for the point design absorber.

2.2.3 CONCENTRATOR POINT DESIGN

Based on results of the trade studies, the following ground rules and requirements were assumed for the point design.

1. Configuration - inflated, continuous surface
2. Number of concentrator modules - 2
3. Effective concentration ratio - 2250:1
4. Emergency defocusing - 10 sec

Special problems considered in the point design were:

1. Meteorite damage and gas leakage
2. Structural frequency response of membranes
3. Static charge buildup
4. Dimensional tolerances
5. Focusing control and absorber hot spots
6. Degradation and maintenance
7. "Space dust"

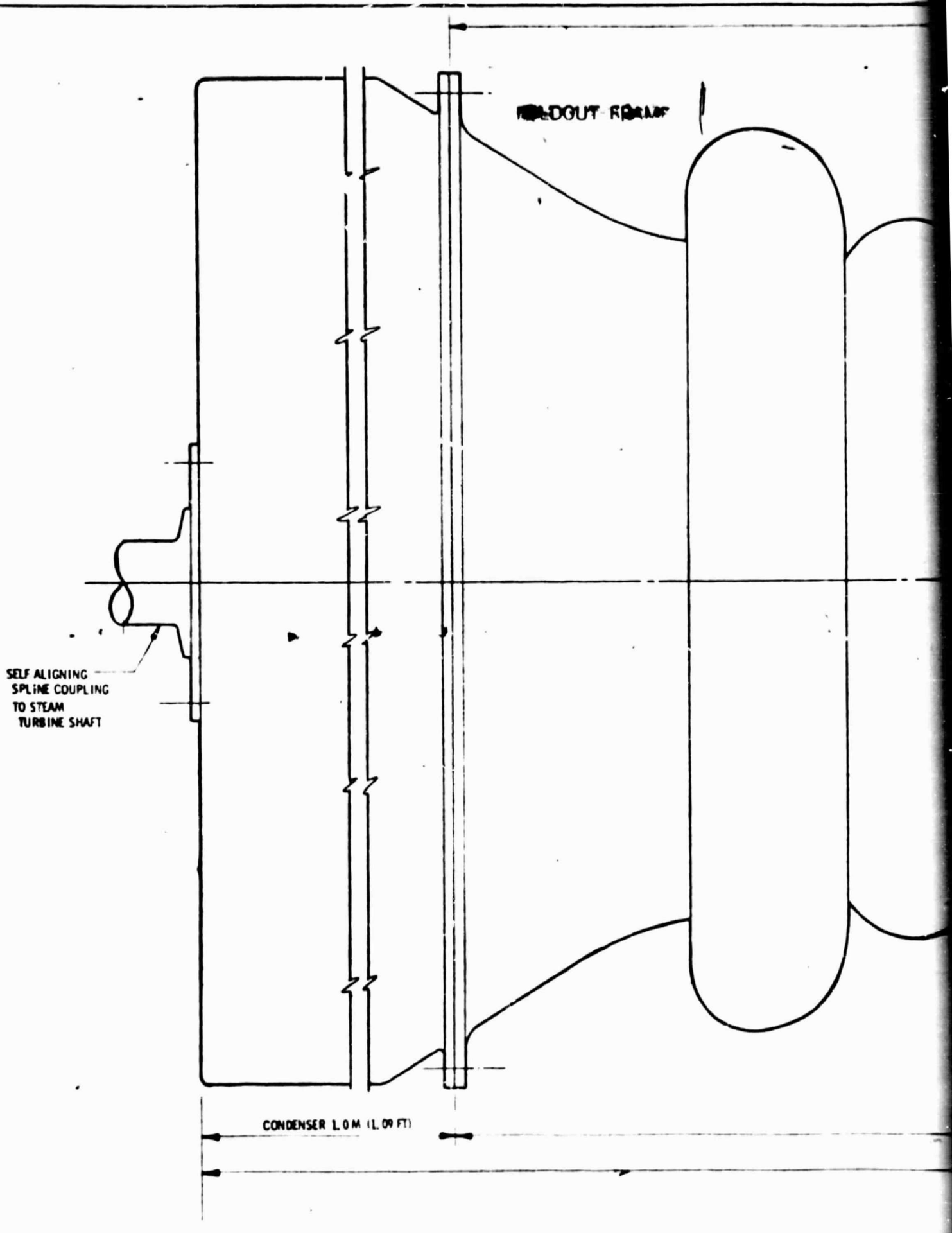
SELF ALIGNING
SPLINE COUPLING
TO STEAM
TURBINE SHAFT
CONDENSER L.O.M. (L.09 FT)

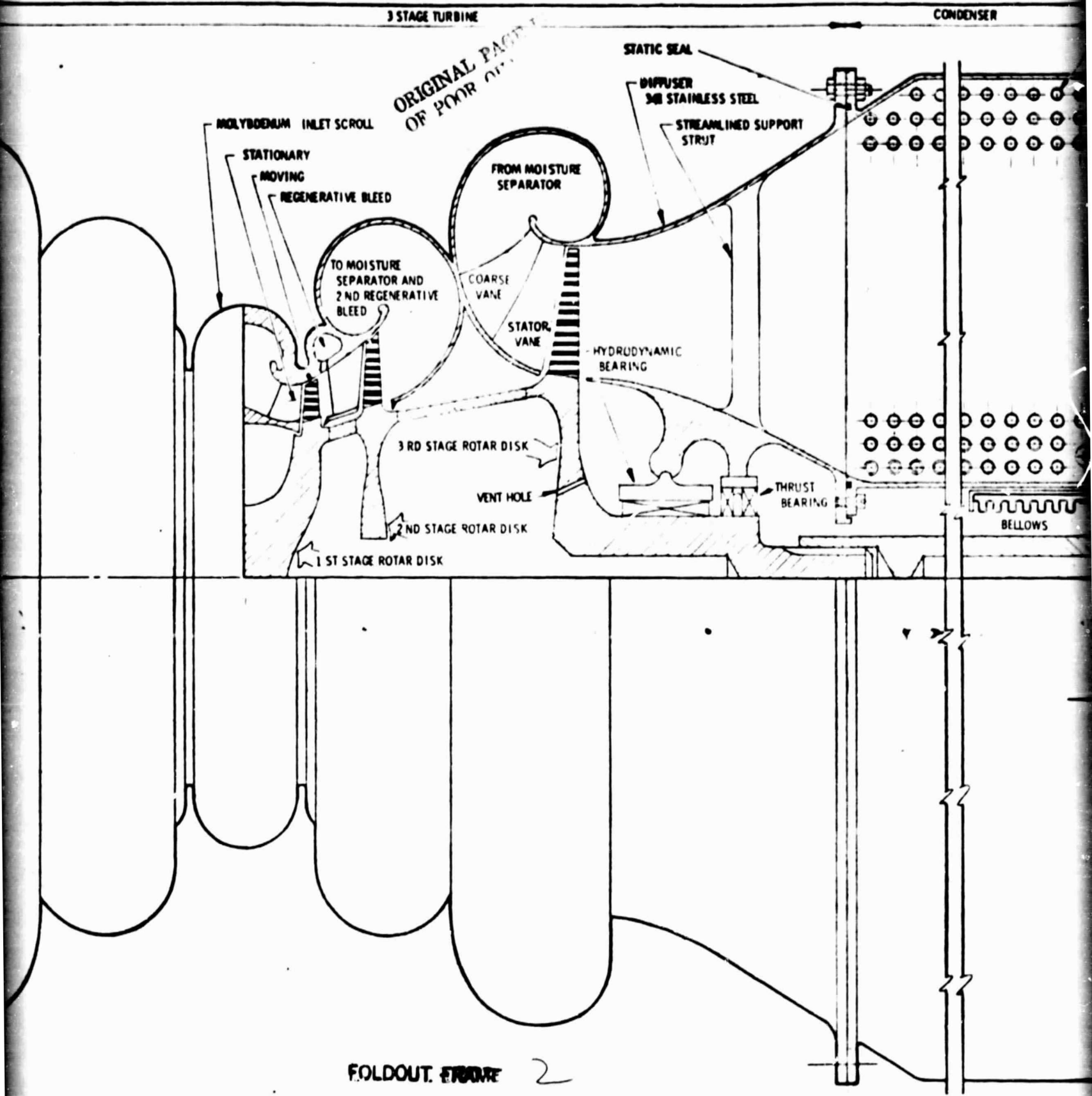

FOLDOUT. FIGURE 2

TURBINE 2.0 M (6.67 FT.)

CONDENSER 1.0 M (1.09 FT)

348 STAINLESS STEEL

OVERALL LENGTH 4.0 M (13.12 FT)

SECTION L-L
SCALE: 1 CM = 4 CM

SPS CESIUM TURBINE

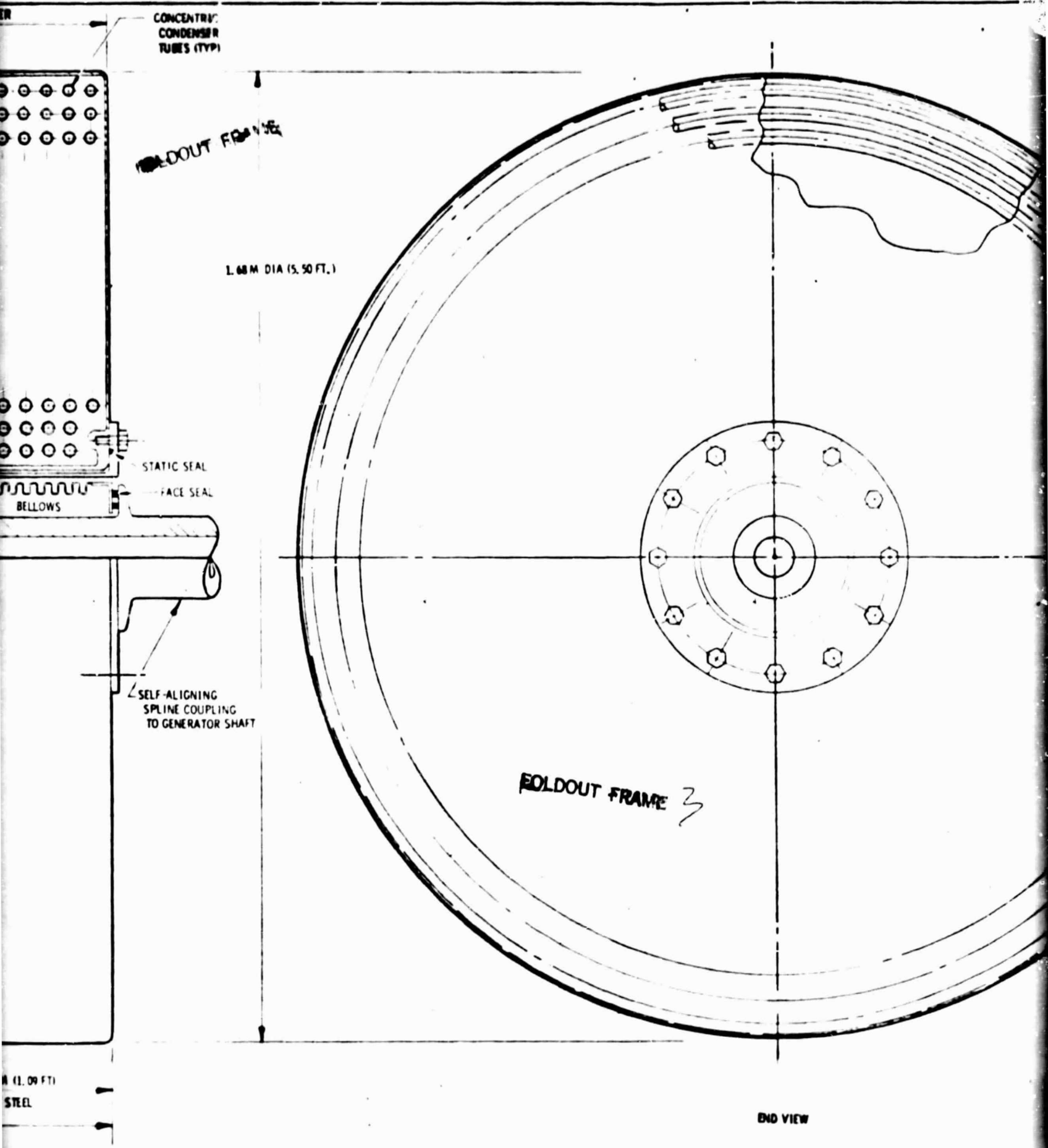
ER
CONCENTRIC CONDENSER TUBES (TYP)
FOLDOUT FRAME 2
1.68 M DIA (5.50 FT.)
STATIC SEAL
FACE SEAL
BELLOWS
SELF-ALIGNING SPLINE COUPLING TO GENERATOR SHAFT
FOLDOUT FRAME 3
M (1.09 FT)
STEEL
END VIEW

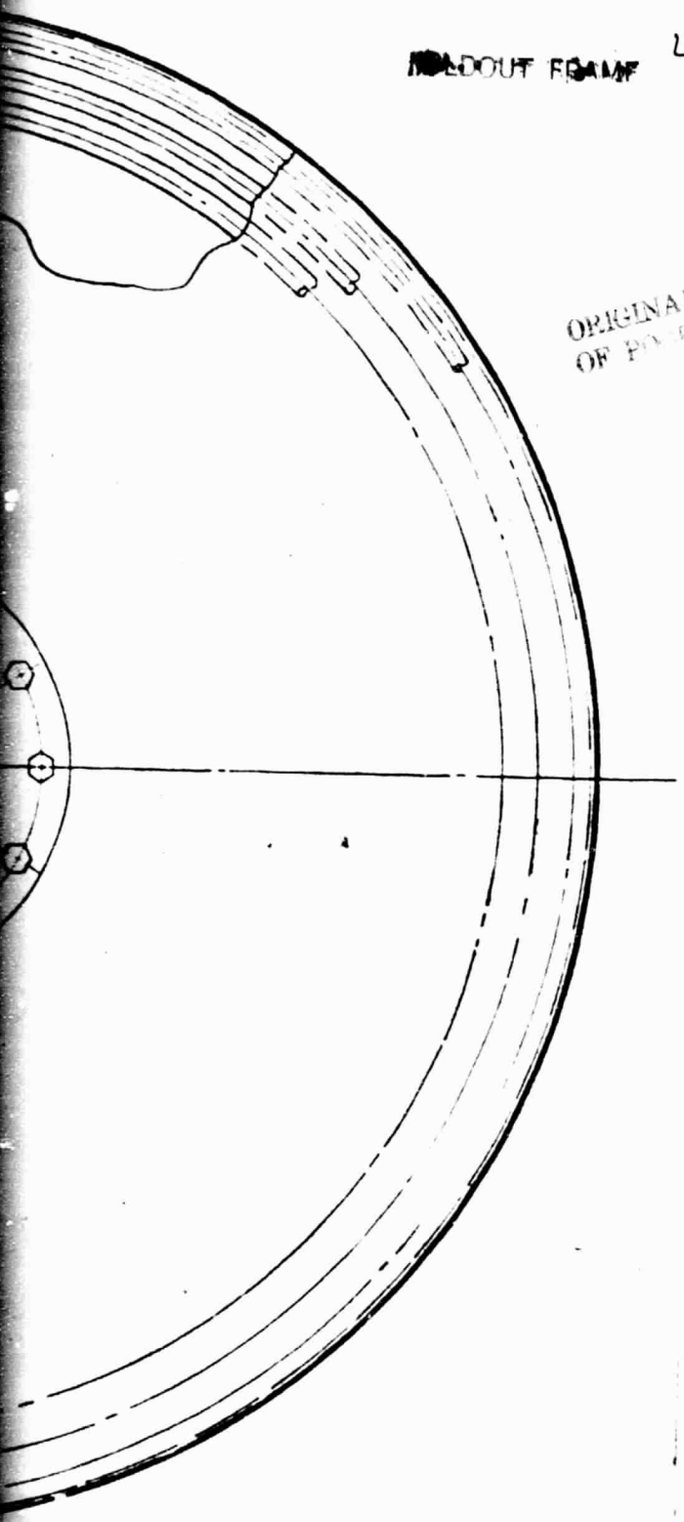

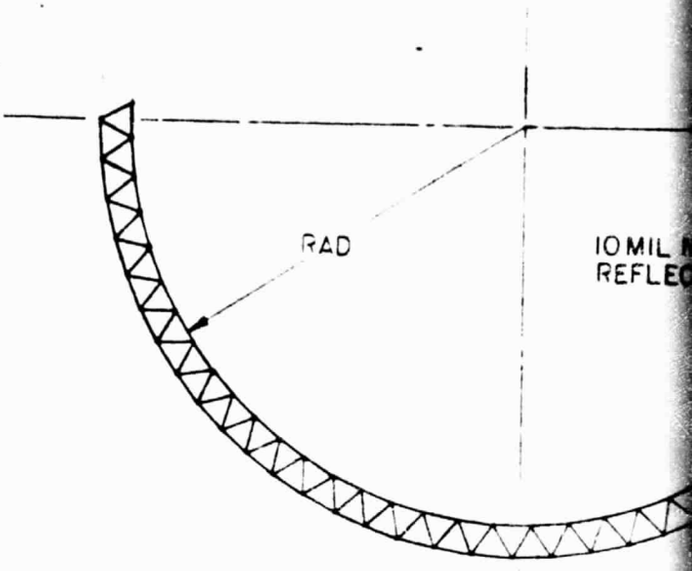

K - K

1 CM = 5M

COMPOUND PARABOLIC REF

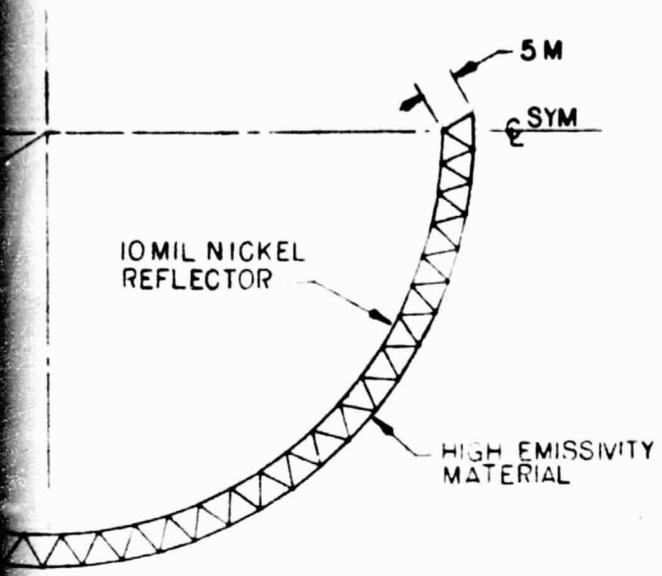

K - K
CM = 5M
PARABOLIC REFLECTOR

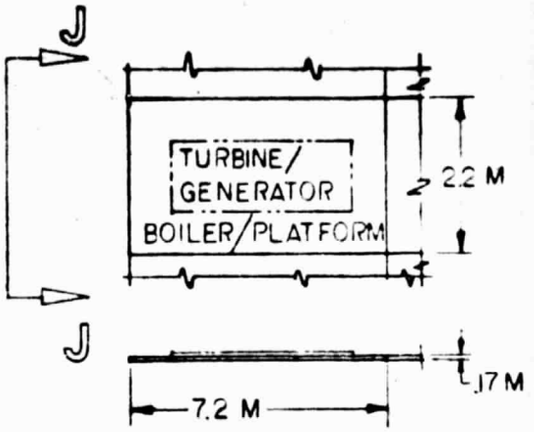

H
1 CM = 1 M
TYPICAL POWER MODULE

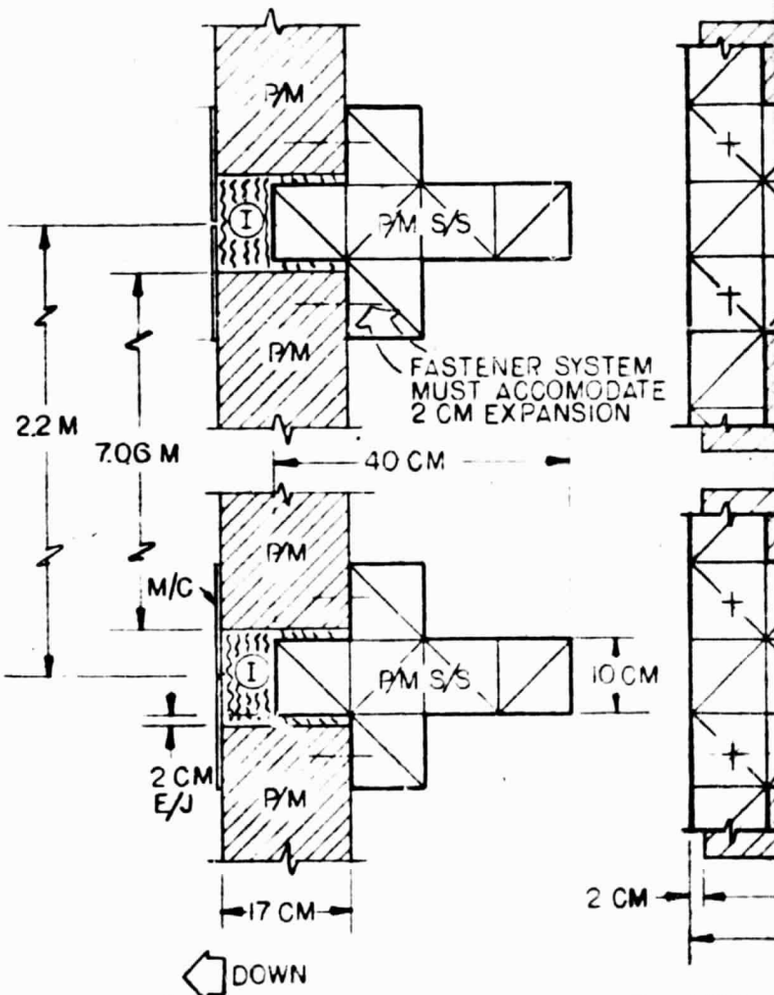

J - J
1 CM = 5 CM
POWER MODULE INSTALLATION

I INSULATI
M/C 10 MIL MO
P/M POWER M
P/M S/S POWER M SUPPORT MACHINE
E J EXPANSIO

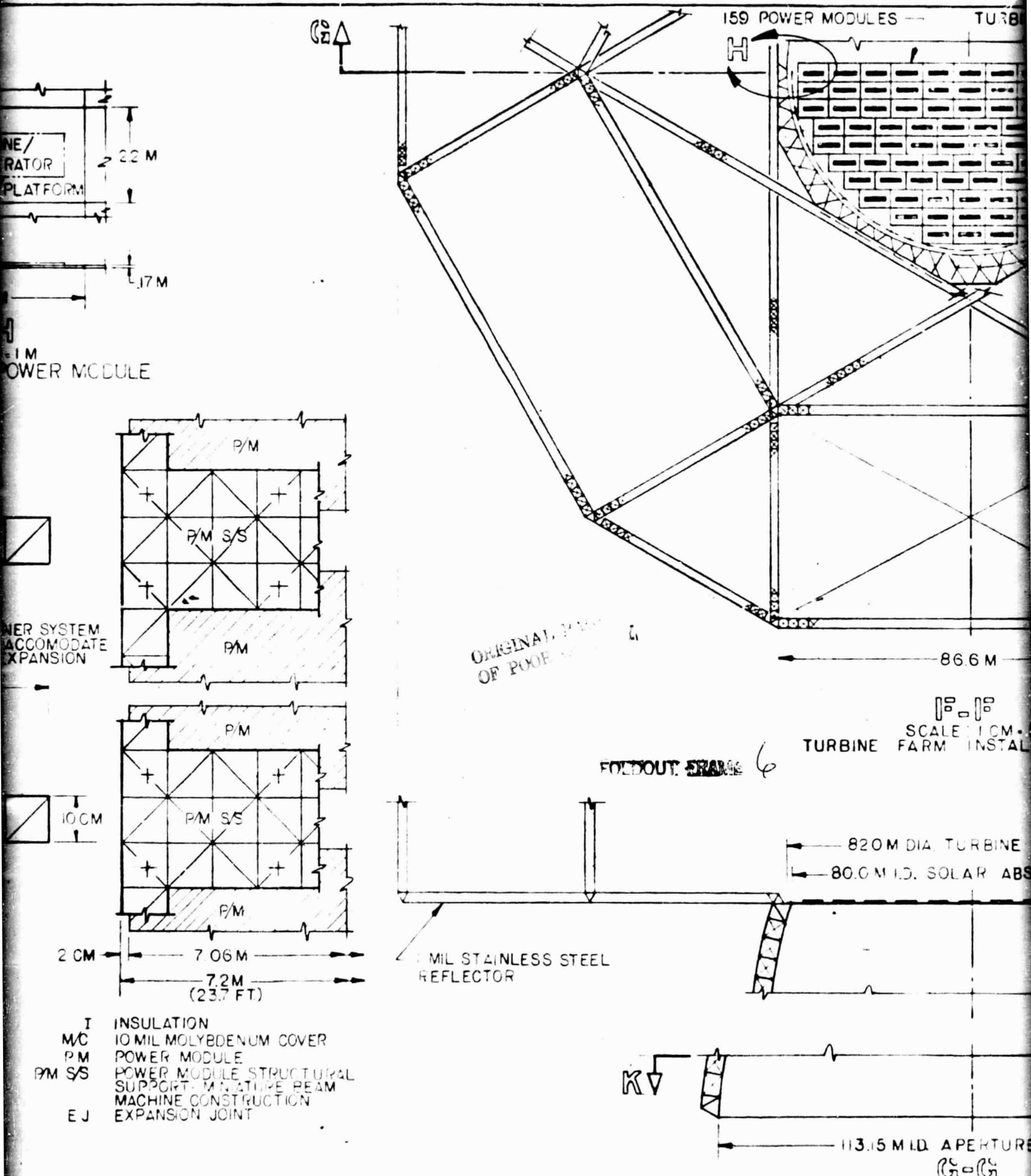

I	INSULATION
M/C	10 MIL MOLYBDENUM COVER
P/M	POWER MODULE
P/M S/S	POWER MODULE STRUCTURAL SUPPORT - MINIATURE BEAM MACHINE CONSTRUCTION
E J	EXPANSION JOINT

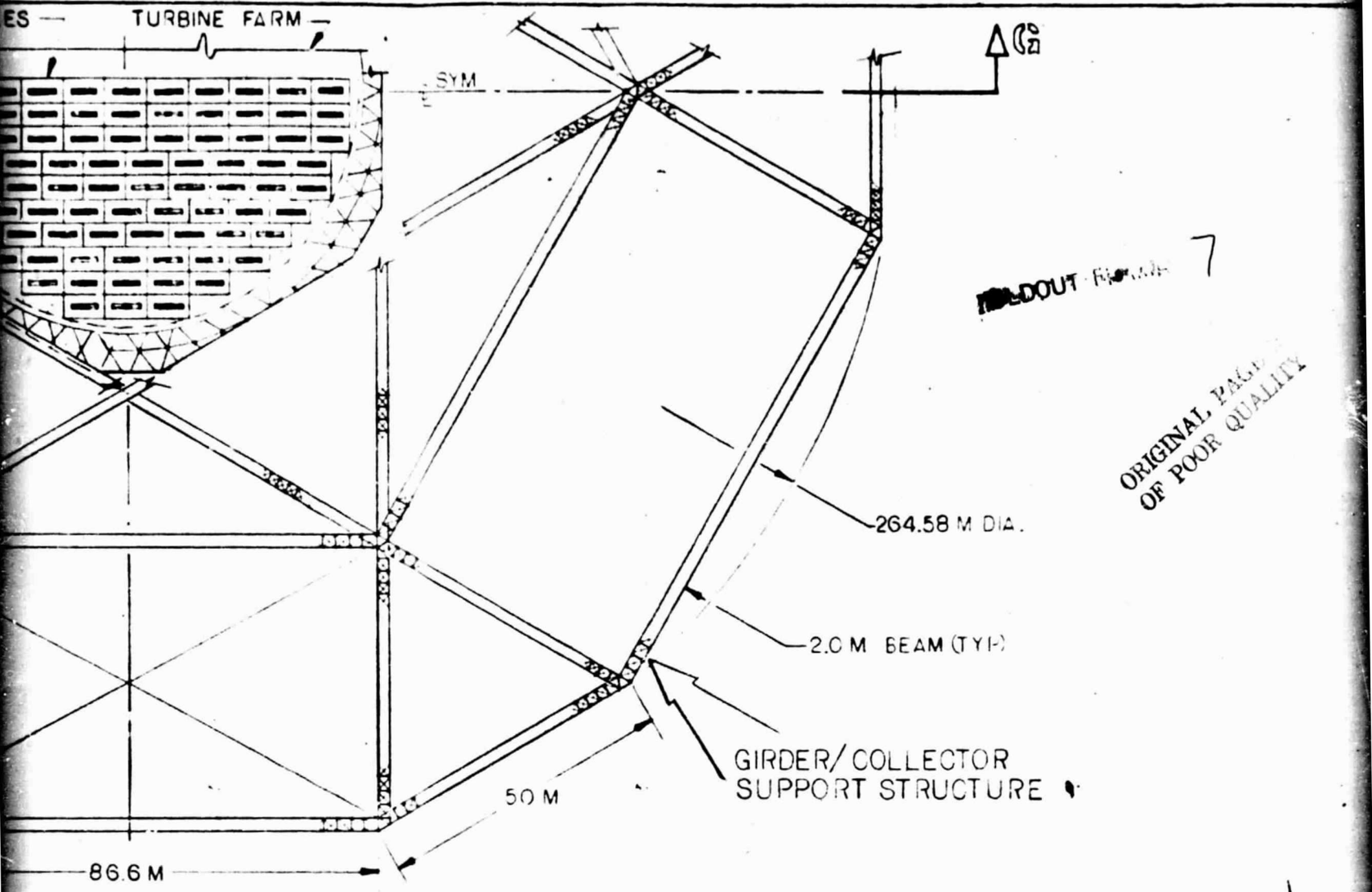

FOLDOUT FRAME 7

ORIGINAL PAGE IS
OF POOR QUALITY

SCALE: 1 CM = 5 M
FARM INSTALLATION

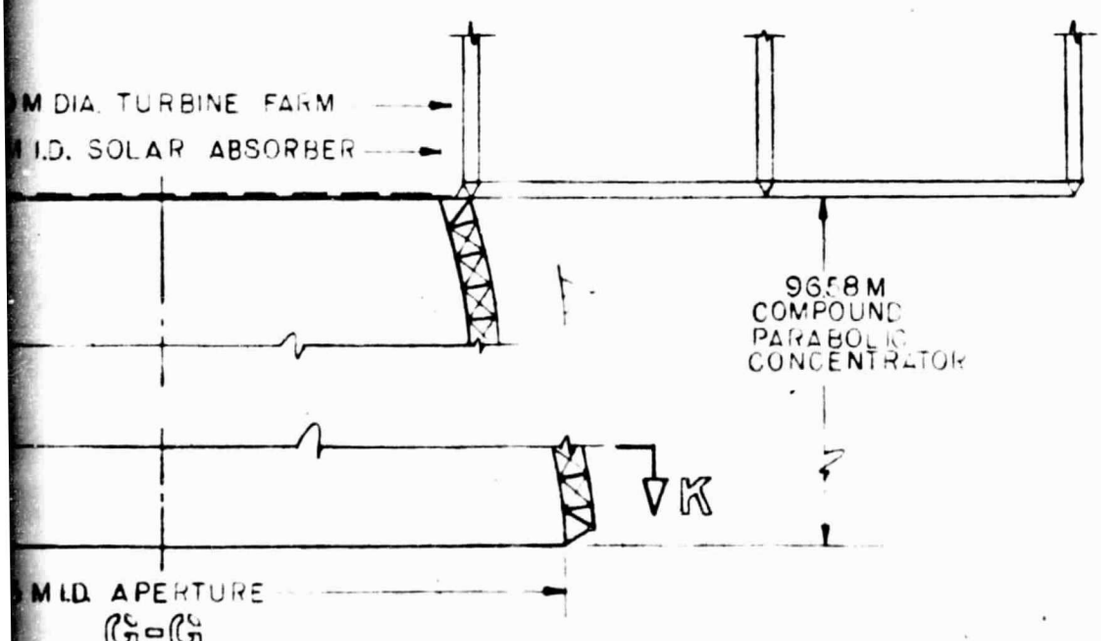

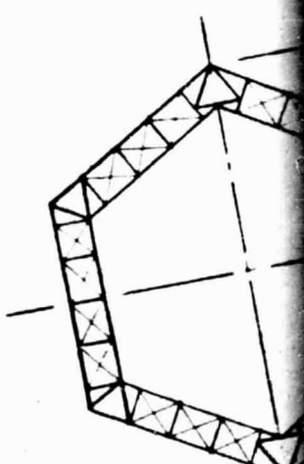

N-

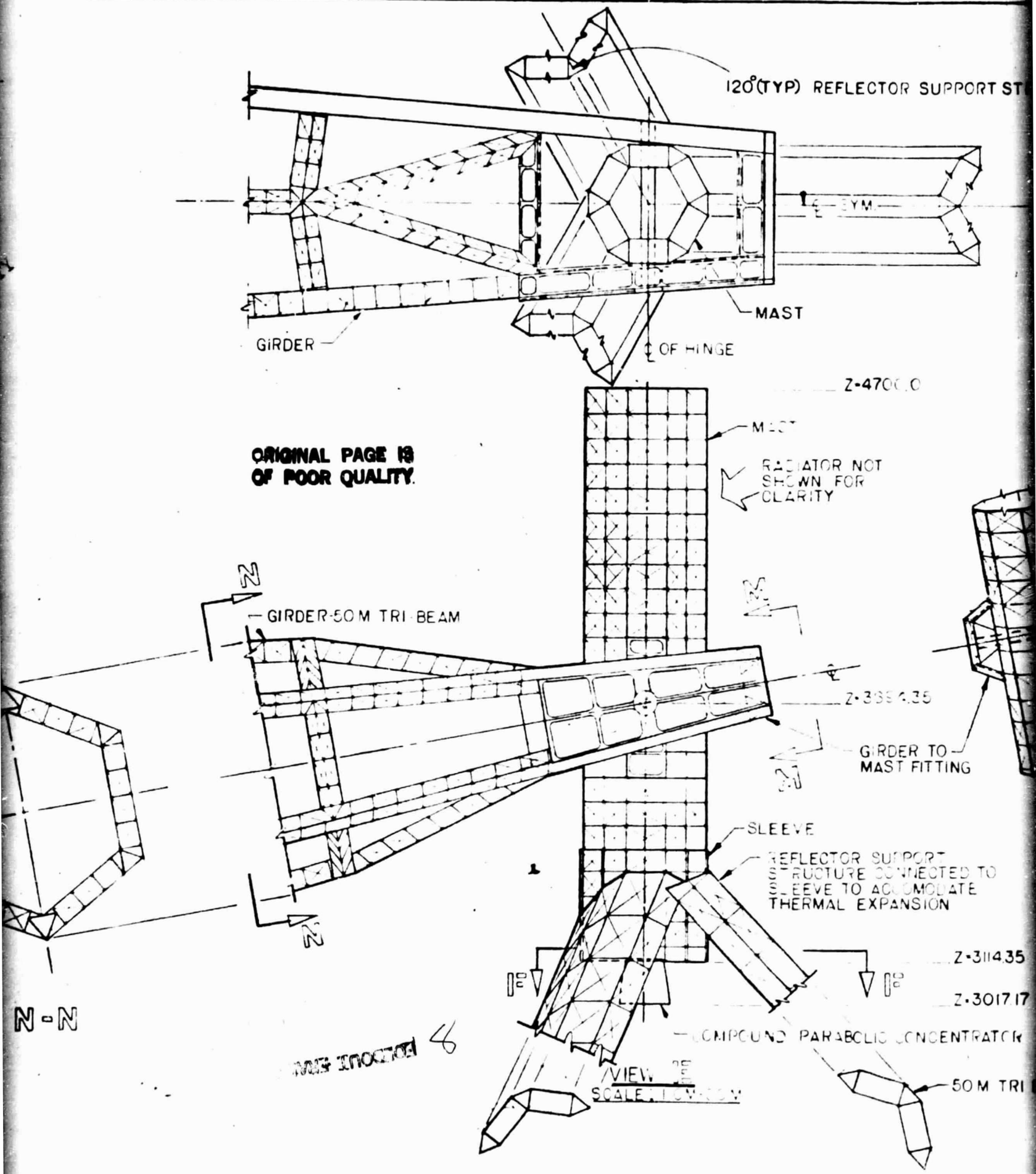

ORIGINAL PAGE IS
OF POOR QUALITY

N - N

MIS INSERT 6

(TYP) REFLECTOR SUPPORT STRUCTURE

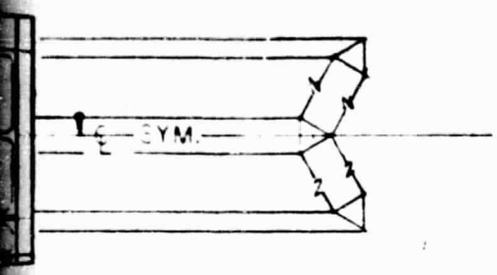

MAST

Z-4700.0

MAST

RADIATOR NOT SHOWN FOR CLARITY

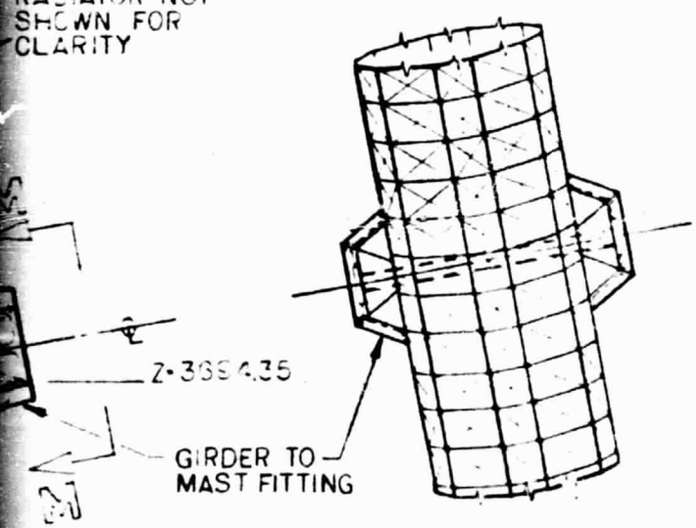

SLEEVE

M-M

REFLECTOR SUPPORT STRUCTURE CONNECTED TO SLEEVE TO ACCOMODATE THERMAL EXPANSION

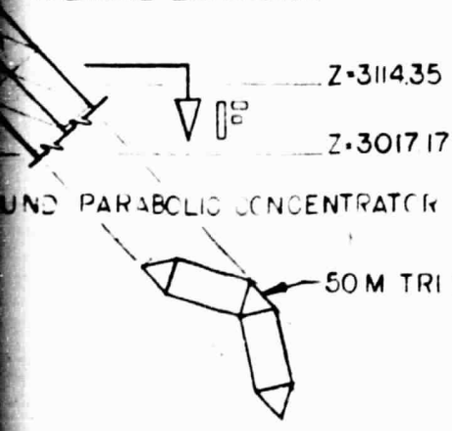

ROUND PARABOLIC CONCENTRATOR

•TURBINE & PLUMBING INSULATION NOT SHOWN
•TOTAL MASS 15,000 KG (33,000 LB)

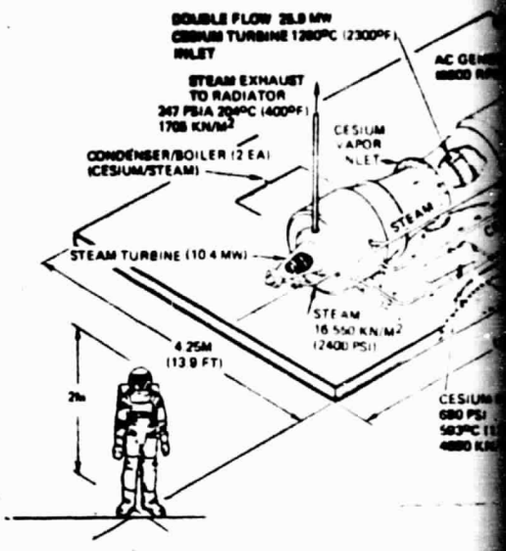

INDEPENDENT POWER

A RELATIVELY SMALL (34 MW) MODULE SIZE WAS S... AND TURBINE SPECIFIC WEIGHT, (2) REDUCE DEVEL... OF MASS PRODUCTION, (4) IMPROVE SPS REDUNDA... ING. THE LOSS IN TURBINE AND GENERATOR EFF... AND SCHIEVES A 65% REDUCTION IN WEIGHT. FU... PIT SPS COST, DUE TO THE ADDED INSTRUMENTATI... MENTS.

EACH POWER MODULE IS COMPLETELY INDEPENDE... AND WATER CONNECTIONS TO A COMMON RADI... "PERFORMANCE TESTS OF THE UNIT TO BE ACCOMP... JOINED SIDE BY SIDE FORM A SINGLE ABSORBER (... LINES PERMIT SHARING OF FLOW BETWEEN NEIGH... THE EVENT OF METEORITE PUNCTURES OR TURBINE... MAINTENANCE (MODULAR COMPONENT REPLACE... UP TO 100% OF THE UNITS CAN BE SHUTDOWN FO... OUTPUT. A COMPLETE POWER MODULE CAN BE RE... AND WITHDRAWING IT THROUGH THE UNDERSIDE ...

SEVEN POWER MODULES MAKE UP A FULL LOAD...

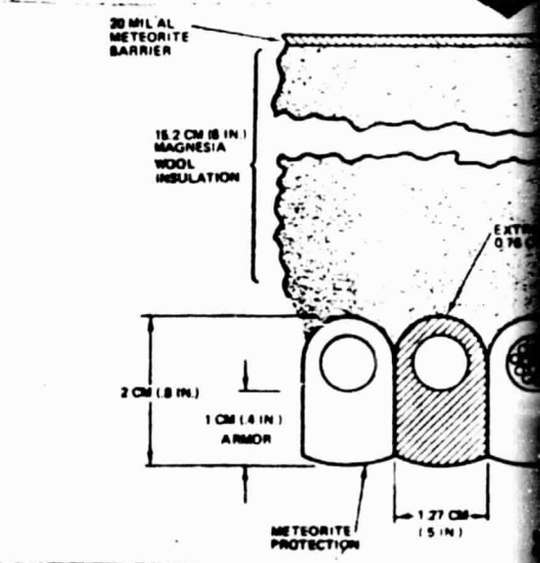

CESIUM BOILER PANEL CROSS ...

THE CESIUM BOILER PANELS ARE MADE UP OF 1.1 M... TZM MOLY TUBES WELDED (ELECTRON BEAM) TO TZ... THICKNESS OF 1 CM (0.4") ON THE TUBE UNDERSID... PANELS TO ~ 10%/30 YRS. A ... 75 CM (0.3") I.D. ... WALL ALLOW A PEAK FLUID TEMPERATURE OF 1293°... POINT, AND 1260°C (2300°F) AT THE OUTLET. THE ... SO THAT A FAILED (DRY) PANEL WILL NOT APPROA... (2600°F) TO ITS MELTING TEMPERATURE.

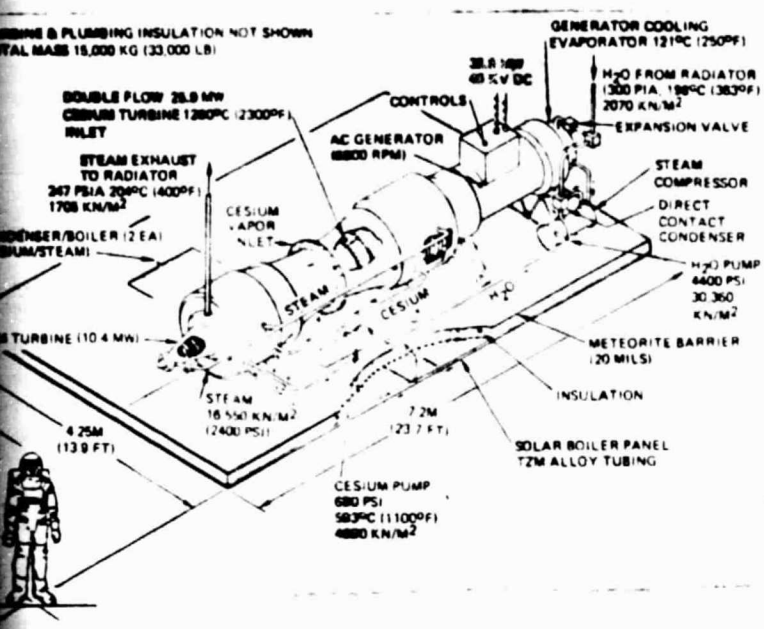

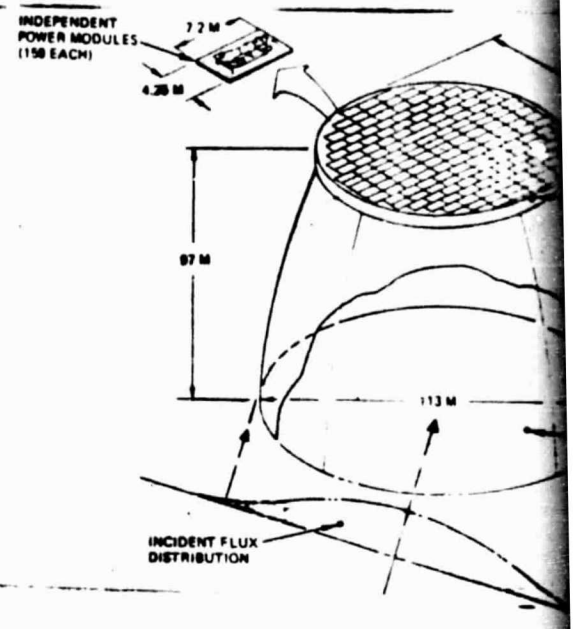

ORIGINAL PAGE IS OF POOR QUALITY

INDEPENDENT POWER MODULES

A RELATIVELY SMALL (34 MW^t MODULE SIZE WAS SELECTED TO (1) MINIMIZE GENERATOR AND TURBINE SPECIFIC WEIGHT, (2) REDUCE DEVELOPMENT COST, (3) PROVIDE ECONOMIES OF MASS PRODUCTION, (4) IMPROVE SPS REDUNDANCY, AND (5) REDUCE BOILER MANIFOLDING. THE LOSS IN TURBINE AND GENERATOR EFFICIENCY (VS 300 MW SIZE) IS ONLY 2% AND SCHIEVES A 65% REDUCTION IN WEIGHT. FURTHER REDUCTION IN SIZE WOULD NOT BENEFIT SPS COST, DUE TO THE ADDED INSTRUMENTATION, CONTROL AND MONITORING REQUIREMENTS.

EACH POWER MODULE IS COMPLETELY INDEPENDENT AND SELF-SUFFICIENT EXCEPT FOR STEAM AND WATER CONNECTIONS TO A COMMON RADIATOR. THIS ALLOWS ALL LEAK CHECKS AND PERFORMANCE TESTS OF THE UNIT TO BE ACCOMPLISHED ON THE GROUND. 159 MODULES JOINED SIDE BY SIDE FORM A SINGLE ABSORBER (BOILER) DISC. INTERCONNECTING CESIUM LINES PERMIT SHARING OF FLOW BETWEEN NEIGHBORING BOILER PANELS AND TURBINES IN THE EVENT OF METEORITE PUNCTURES OR TURBINE/GENERATOR FAILURES. ONLY MINOR MAINTENANCE (MODULAR COMPONENT REPLACEMENT) WILL BE PERFORMED ON STATION. UP TO 100% OF THE UNITS CAN BE SHUTDOWN (MAJOR FAILURES) WITHOUT AFFECTING SPS OUTPUT. A COMPLETE POWER MODULE CAN BE REPLACED BY BREAKING PLUMBING CONNECTIONS AND WITHDRAWING IT THROUGH THE UNDERSIDE OF THE ABSORBER.

SEVEN POWER MODULES MAKE UP A FULL LOAD FOR THE CARGO PLANE

SOLAR ABSORBER DESIGN

TO MINIMIZE WEIGHT, THE SOLAR ABSORBER IS CONSTRUCTED IN [illegible] USING THE SMALLEST DIAMETER POSSIBLE (10 M) WITHOUT REA[illegible] TEMPERATURES IN A DRY TUBE. A COMPOUND PARABOLIC COLLEC[illegible] REFLECTOR SKIRT IS UTILIZED TO INCREASE THE INTERCEPTION OF [illegible] A ± 45° CAPTURE ANGLE PERMITS A RELATIVELY SHORT SKIRT WITH [illegible] REFLECTION LOSSES.

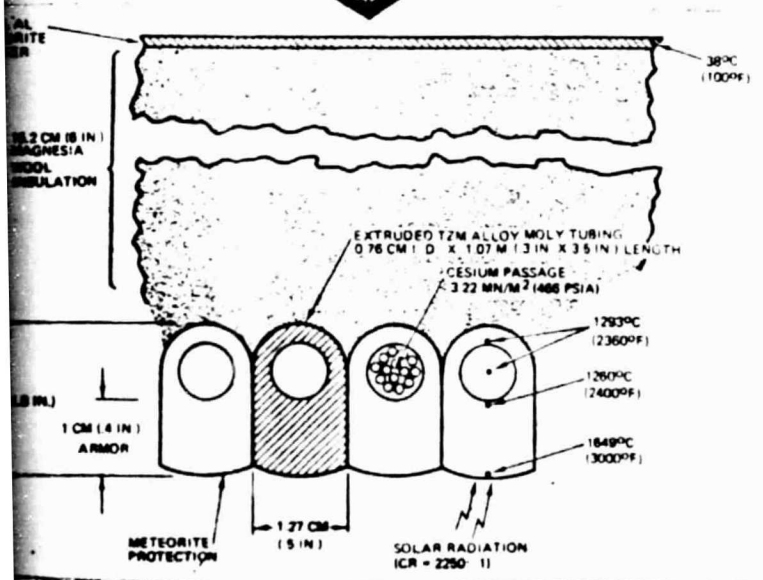

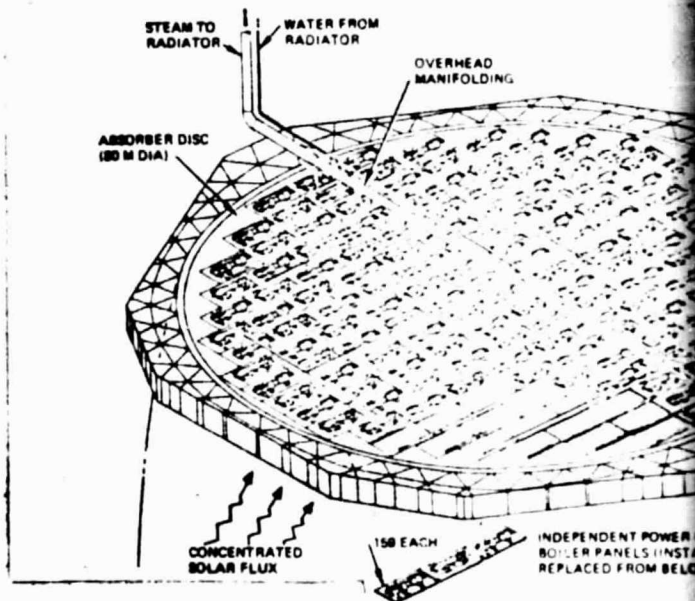

CESIUM BOILER PANEL CROSS SECTION

THE CESIUM BOILER PANELS ARE MADE UP OF 1.1 M (3.5') LONG EXTRUDED TZM MOLY TUBES WELDED (ELECTRON BEAM) TO TZM HEADERS. AN ARMOR THICKNESS OF 1 CM (0.4") ON THE TUBE UNDERSIDE LIMITS LOSS OF BOILER PANELS TO ~ 10%/30 YRS. A 0.75 CM (0.3") I.D. AND 0.25 CM (0.1") WALL ALLOW A PEAK FLUID TEMPERATURE OF 1293°C (2360°F) AT THE BUBBLE POINT, AND 1260°C (2300°F) AT THE OUTLET. THE ABSORBER DISC IS SIZED SO THAT A FAILED (DRY) PANEL WILL NOT APPROACH CLOSER THAN ~ 200°C (360°F) TO ITS MELTING TEMPERATURE.

FOLDOUT FRAME 10

SOLAR ABSORBER PANEL MATRIX

EACH ABSORBER DISC IS COMPOSED OF 159 RECTANGULAR CES[illegible] PANELS (4.25 × 7.2 M) ARRANGED IN A CIRCULAR MATRIX. EA[illegible] IS PART OF AN INDEPENDENT POWER MODULE INCLUDING A T[illegible] GENERATOR SET MOUNTED ON THE TOP SIDE OF EACH PANEL.

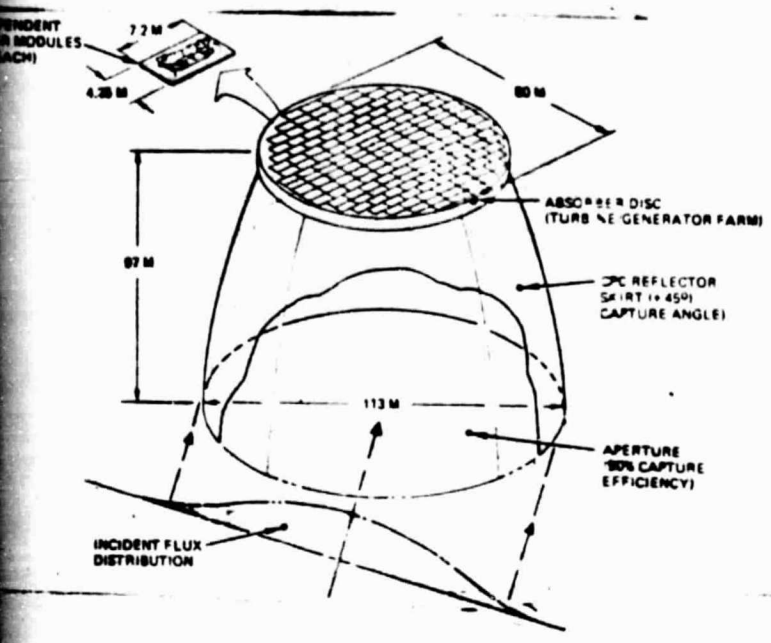

SOLAR ABSORBER DESIGN

TO MINIMIZE WEIGHT, THE SOLAR ABSORBER IS CONSTRUCTED IN A DISC FORM USING THE SMALLEST DIAMETER POSSIBLE (80 M) WITHOUT REACHING MELTING TEMPERATURES IN A DRY TUBE. A COMPOUND PARABOLIC COLLECTOR (CPC) REFLECTOR SKIRT IS UTILIZED TO INCREASE THE INTERCEPTION OF SOLAR FLUX. A + 45° CAPTURE ANGLE PERMITS A RELATIVELY SHORT SKIRT WITH SMALL REFLECTION LOSSES.

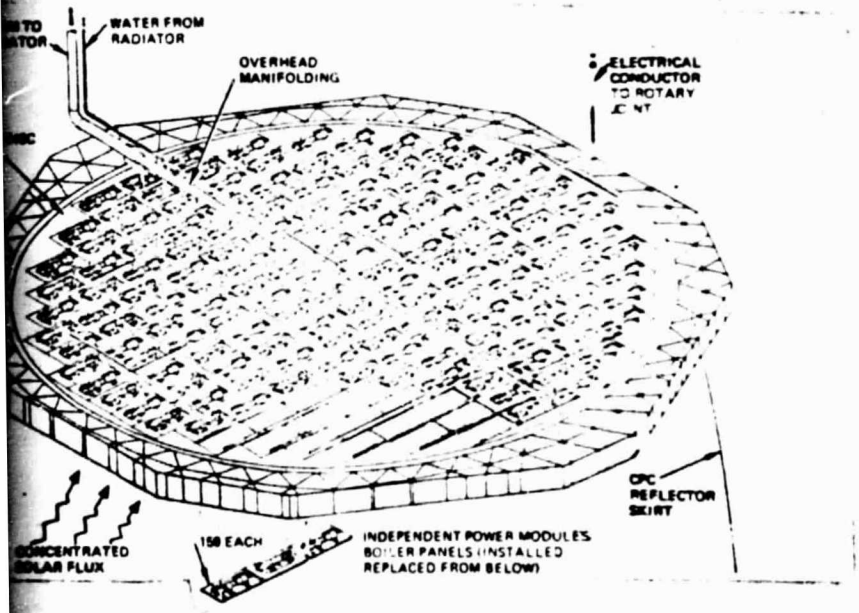

SOLAR ABSORBER PANEL MATRIX

EACH ABSORBER DISC IS COMPOSED OF 159 RECTANGULAR CESIUM BOILER PANELS (4.25 x 7.2 M) ARRANGED IN A CIRCULAR MATRIX. EACH PANEL IS PART OF AN INDEPENDENT POWER MODULE INCLUDING A TURBINE GENERATOR SET MOUNTED ON THE TOP SIDE OF EACH PANEL.

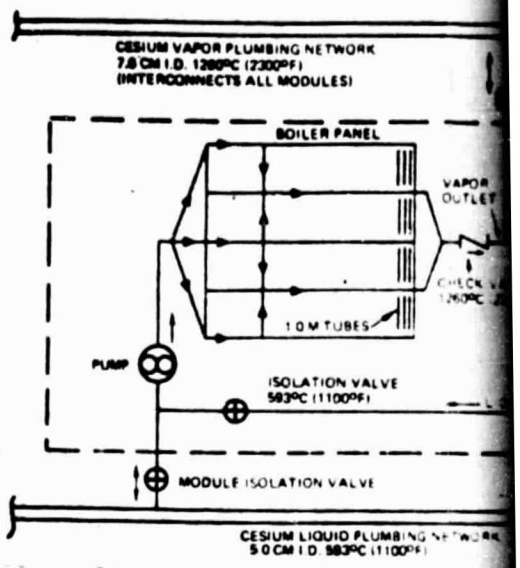

CESIUM LOOP ISOLATION CIRCUITRY

NEIGHBORING POWER MODULES ARE INTERCONNECTED BY A NETWORK TO PERMIT SHARING OF FLOW BETWEEN MODULES. METEORITE PUNCTURES (BOILER PANELS) OR TURBINE GENERATOR THE DEFECTIVE PANELS OR TURBINES ARE ISOLATED BY ALVES THIS DECENTRALIZED MANIFOLD GREATLY REDUCES THE PLUMBING REQUIRED VS. A CENTRALIZED MANIFOLD FOR THE ENTIRE ARRAY

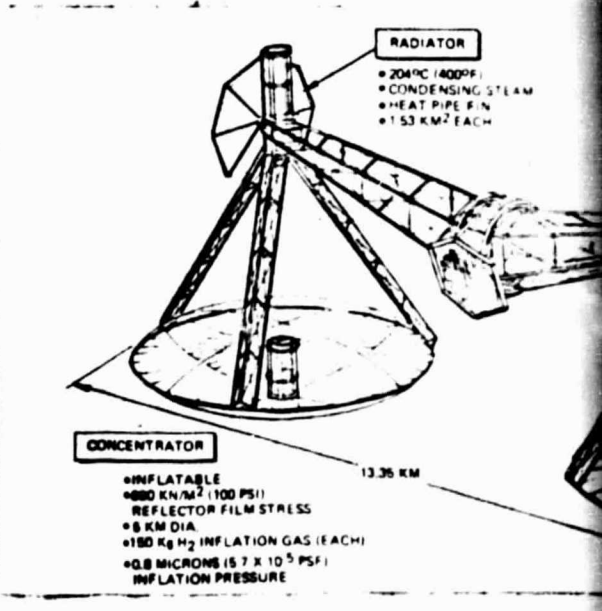

SOLAR THERMAL DESIGN CON

Figure 2.2-10. Construction Details
(Absorber Assembly and Reflector Skirt)

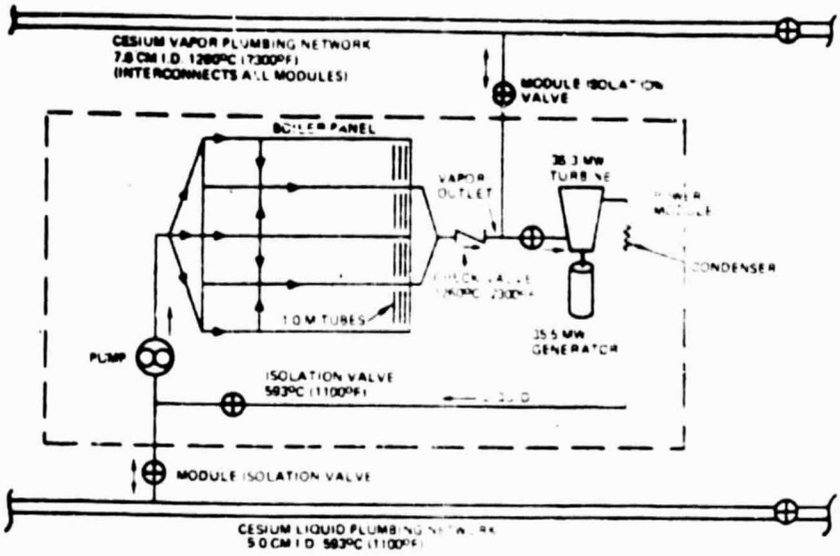

CESIUM LOOP ISOLATION CIRCUITRY

NEIGHBORING POWER MODULES ARE INTERCONNECTED BY A CESIUM MANIFOLD NETWORK TO PERMIT SHARING OF FLOW BETWEEN MODULES IN THE EVENT OF METEORITE PUNCTURES (BOILER PANELS) OR TURBINE-GENERATOR FAILURES. THE DEFECTIVE PANELS OR TURBINES ARE ISOLATED BY VALVING AS REQUIRED. THIS DECENTRALIZED MANIFOLD GREATLY REDUCES THE PLUMBING SIZES REQUIRED VS. A CENTRALIZED MANIFOLD FOR THE ENTIRE ABSORBER DISC.

FOLDOUT FRAME 12

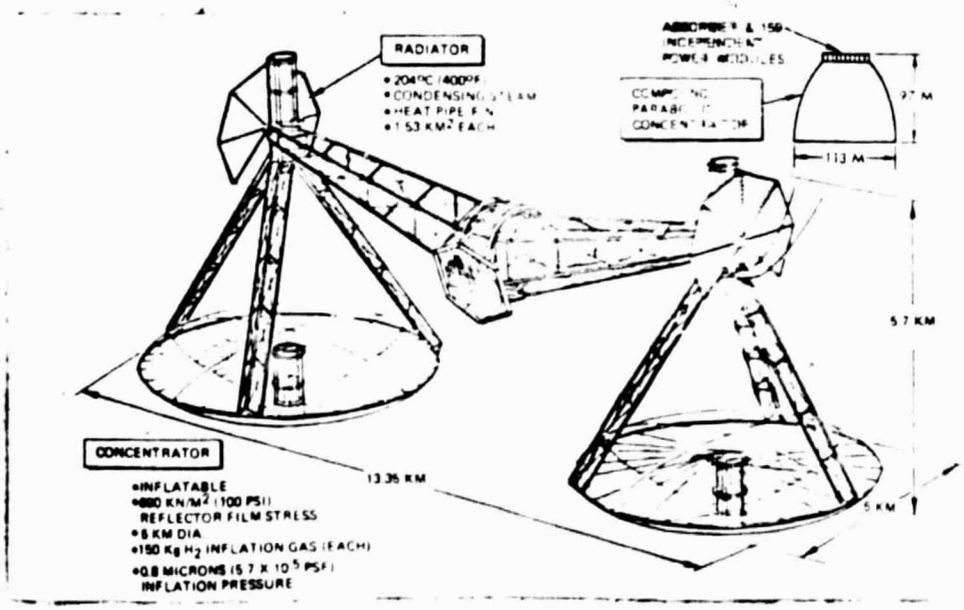

SOLAR THERMAL DESIGN CONCEPT

2-31, 2-32

truction Details
d Reflector Skirt)

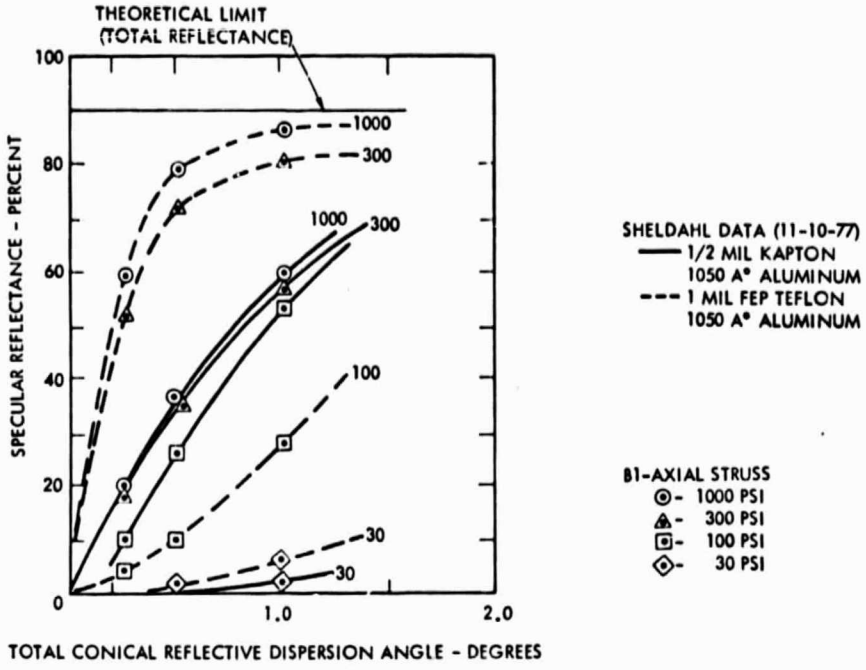

Figure 2.2-11. Specular Reflectance of Aluminized Plastic Film

are expected for SPS production quantities. An alternate coating for Kapton is vapor-deposited silver with an overcoat of silicon dioxide to avoid tarnishing during ground handling. The total reflectivity of silver is 0.96 vs 0.90 for aluminum.

Indications are that no significant degradation of reflectivity of either aluminized or silvered Kapton will occur over a 30 year life span, including self-transportation through the Van Allen belt. Previous tests, which indicated a problem from proton damage that caused bubbling of the Kapton substrate, are now known to have used dosage rates an order of magnitude too high. Some degradation of Kapton strength may occur but it would be insignificant at the low stress levels used.

Mylar is another possible film candidate, which had been eliminated earlier due to reports of severe degradation in radiation environments. Recent data, however, shows that in the absence of air, its mechanical properties actually improve with typical SPS dosages. Limited tests performed by Rockwell tend to confirm these findings, and more conclusive tests are planned for future studies. Mylar's resistance to UV in a vacuum is not presently known but UV is eliminated in the SPS environment by silvering the sun side. Mylar has the advantage of superior reflectivity, toughness, tear strength, and much lower cost, compared to Kapton (presently \$2.30/lb vs \$140/lb). Its slight tendency to creep with time can also result in a lower film stress requirement for achieving high specular reflectance. The minimum film stress requirement to avoid mechanical frequency interactions with the attitude control system is ~69 KN/m^2 (10 psi).

The problem of static charge buildup during eclipse is readily avoided by metallizing the outside surface of the reflector membrane to conduct away such charges. In the case of the transparent canopy, a transparent, conductive coating will be applied.

During eclipse, the average temperature of the reflector and its inflation gas will drop from ~-18°C (0°F) to ~-184°C (-300°F) resulting in a substantially lowered inflation pressure. Thermal response of the membrane and gas is on the order of a 1-minute time constant. Therefore inflation pressure and optical performance of the reflector will essentially recover during the 2-minute period it takes to uncover the sun's disc at the end of the eclipse period. Radial shrinkage of the reflector membrane during eclipse will be accommodated by the flexible "fish pole" attachment on the rim.

Rim Angle Selection. Rim angle is defined as the angle between the axis of the concentrator and a ray reflected from the rim of the concentrator. For a given reflector diameter, a large rim angle decreases the distance to the absorber aperture, thereby providing a larger apparent target (larger subtended angle) and decreasing spillover losses at the aperture. Also the overall satellite length (main girder), required to clear the antenna beam with a 23° seasonal tilt of the concentrator, is reduced. On the other hand, rays reflected from the extreme edge of the reflector see an elliptical aperture opening, which at very large angles gives a smaller overall target. Large rim angles also result in a deep reflector dish which intercepts more meteorite punctures and requires more inflation pressure to achieve a given film stress. On the basis of overall satellite size and mass, the selected rim angle is ~45°. For this angle, an overall reflector diameter of 5 km was calculated, based on statistical summation of the following error sources:

1. Pointing error - ±0.1° (3 sigma)
2. Reflector surface error - ±0.5° deviation from paraboloid (3 sigma)
3. Specular reflectance - per Figure 2.2-11
4. Sun disc diameter - ±0.25°

Inflation Pressure and Makeup Gas. The inflation pressure required to achieve 690 KN/m^2 (100 psi) stress in the reflector is given by the stress formula for a spherical shell:

$$P = \frac{4\ St}{D} = \frac{(4)(100)(0.0005)}{13\times10^3\times39.33} =$$

$$= 0.392\times10^{-6} \text{ psia } (2.7\times10^{-3} \text{ N/m}^2)$$

or $0.565\ 10^{-4}$ psf

or 0.8 microns of Hg

where

P = pressure differential, psi
S = stress, psi
t = film thickness, inches
D = diameter of curvature, inches

This extremely low pressure is in the range of a soft vacuum, such as found at altitudes of 120 km (75 miles). It is due chiefly to the large radius of curvature (6.5 km) of the reflector dish. The entire mass of H_2 gas required to inflate both reflectors is only 300 kg (660 lb).

The leakage area due to meteorite punctures was estimated at 2320 m^2 (0.0027% of total area) for both modules at the end of 30 years. This area is equivalent to half a football field, and is based on the conservative assumption that each meteorite breaks up into 100 fragments after passing through the first membrane and that each of these particles in turn makes a separate hole in the opposite membrane. Thus a 2.8 increase in leakage area is realized vs. the no-breakup case. Meteorite penetration tests show little tendency for the hole area to exceed the cross-section area of the particle.

Because the mean free path of the gas molecules is several meters, which is very large compared to the leakage hole size, leakage flow is in the free molecular regime rather than the viscous regime. The leakage mass flow is consequently reduced by a factor of ~4. Based on the calculated leakage area, the average makeup gas requirement was calculated to be 26,100 kg/yr. This becomes a total of 844,000 kg for a 30 year life or approximately 2.6% of the total satellite mass. The makeup gas would be stored onboard as liquid hydrogen in lightweight cryogenic containers. If the inflation pressure is reduced through use of thinner film or substituting Mylar for Kapton, the makeup gas requirement will be correspondingly reduced.

Previously, it was assumed that makeup gas requirements for a large inflated reflector in a meteorite environment would be prohibitive. This may be the chief reason that inflatable concentrators were not seriously considered in other SPS studies. Actual calculation of pressures, leakage areas, and flow rates, however, show that gas leakage is not a major problem.

Reflector Membrane Design. As shown in Figure 2.2-3, the reflector membrane is composed of 36 tapered gore sections, each in turn composed of 15 sub-gores. The sub-gore edges are curved such that after joining and inflation, they form an accurate paraboloidal surface as required to produce a high concentration ratio. The sub-gores are narrow enough so that elastic deformation at the center of the gores is sufficient to remove puckering along the sub-gore edges when the inflation pressure is raised to its design value. The edge of the reflector membrane is scalloped over each 10° gore sector to accommodate a catenary cable which distributes the radial load evenly into the membrane. Lanyard attach points are at the peaks of each scallop. Figure 2.2-3 shows that each sub-gore is made of straight lengths of film 10-m wide which is assumed to be the optimum (cost effective) width. Present roll widths are ~2.5-m maximum, but the large quantities required for SPS would undoubtedly justify development of machines capable of larger widths. The entire production of Kapton film in 1977 was only 0.5% of the annual rate required for the solar thermal SPS program.

A simple taped, butt joint made with self-curing, pressure-sensitive adhesive was judged to be the cheapest and most satisfactory joining method. Cross tapes are located at 10-m intervals to act as "tear-stops". The tape and its adhesive must have the same coefficient of thermal expansion as the panel to prevent puckering during temperature changes.

Manufacturing and Installation. Based on a reflector surface accuracy of ±0.5 degrees (3 sigma), a dimensional tolerance of ±1 cm on sub-gore width is considered adequate (Reference 2.2-2).

A sub-gore width of 29-m was chosen so that a 90° sector can be fan folded (one sub-gore on top of another) and rolled up on a single 2 ft dia × 30-m mandrel. Thus, an entire 90° sector can fit within the launch vehicle cargo bay (6-m × 6-m × 30-m) and not exceed its payload limit of 200,000 lb.

Assumed manufacturing facilities include film casting machines and metallizing chambers for 10-m fill widths, and 2800-m long × 30-m wide temperature controlled lofting sheds for cutting, seaming, stacking and folding the reflector sectors. Magnetic imprint coding of the panel edges can be used to facilitate accurate automated seaming.

In orbit, the narrow end of the rolled 90° sector will be attached to the reflector hub structure and the whole sector unrolled and strung to the corresponding fish pole lanyard at the reflector rim. Then the accordian folds of sector will be unfurled in a circumferential direction and attached at intervals to the appropriate "fish poles" on the rim and to the attach points on the hub. All four 90° sectors will be strung in this fashion and carefully aligned relative to each other (in a conical shape) prior to joining the edges of the sectors. This joining also can be accomplished with automated equipment, using magnetic code markings on the edge of each sector for accurate alignment. The transparent canopy can be made and assembled in similar fashion, except that accurate dimensional control is not required.

Performance and Characteristics

Table 2.2-2 presents the pertinent performance data and characteristics for the point design solar concentrator.

Table 2.2-2. Point Design Inflatable Concentrator Characteristics

CONCENTRATION RATIO (ACTUAL)	2250
COLLECTOR DIAMETER (KM)	5.0
REFLECTOR MATERIAL	AL KAPTON
FILM STRESS - KN/M^2 (PSI)	690 (100)
FILM THICKNESS - CM (MIL)	0.0012 (0.5)
FILM LIFE, REFLECTIVITY (YR)	30
SPECULAR REFLECTANCE (1.8°), EOL (%)	81
CANOPY LIFE (YR)	15
INFLATION PRESSURE - KN/M^2 (PSF)	2.7×10^{-4} (0.57×10^{-2})
EMERGENCY DEFOCUS (SEC)	5
CANOPY TRANSMISSION, 2-WAY, EOL (%)	80
APERTURE VIEW ANGLE (DEG)	1.8
COLLECTION EFFICIENCY (%)	64.8
MAKEUP GAS - H_2, 30 YR (KG)	0.84×10^4
WORKING TEMPERATURE - °C (°F)	-18 (0)
ECLIPSE TEMPERATURE - °C (°F)	-184 (-300)
INFLATION GAS MASS (KG)	3×10^2
FILM MASS (KG)	1.2×10^4
STRUCTURE MASS (KG)	0.7×10^4
MASS TOTAL (KG)	1.9×10^4

THIS PAGE IS INTENTIONALLY LEFT BLANK.

Technology Advancement and Verification

The chief areas requiring technology advancement are:

1. Material properties data, especially specular reflectance vs. time at tension and radiation dosage.
2. Reduction of film cost.
3. Development of automated techniques for accurate fabrication and assembly of reflector membrane.
4. Development of focusing control techniques.

Technology verification requirements can be satisfied by construction and testing of a subscale concentrator 30-m × 50-m in dia. This would require a large hangar type building with a transparent roof to shield the model from winds and stray air currents. Tests would include focusing control, over-pressure relief, emergency defocusing and optical performance at various levels of film stress.

Design Growth

The chief potential area for design improvement are:

1. Development of ultra-thin films (0.1 mil) to save film weight and reduce inflation pressure, structural loads and makeup-gas requirements.
2. Substitution of Mylar for Kapton to reduce cost and inflation pressure, and improve specular reflectance.
3. Substitution of silver for aluminum reflective coating to improve reflectance.

Development Risk

Assuming the adequate film properties and specular reflectivity can be verified, the only area of significant risk is considered to be achievement of accurate techniques for membrane fabrication and focusing control. Because of the large sizes and dimensional tolerances involved, this risk is considered to be moderate.

2.2.4 POWER MODULE AND GENERATOR POINT DESIGN

Solar thermal power generation is divided among 318 independent turbine/generator/boiler sets or power modules of the type shown in Figure 2.2-12. A entire absorber disc and turbine generator farm is comprised of 159 modules placed together, as shown in Figure 2.2-13.

Subcontractor Engineering Support

Westinghouse Electric Corporation performed feasibility and cost analyses for the point design of the turbogenerator sets. Rocketdyne Division and Atomics International Division of Rockwell assisted Space Division in the

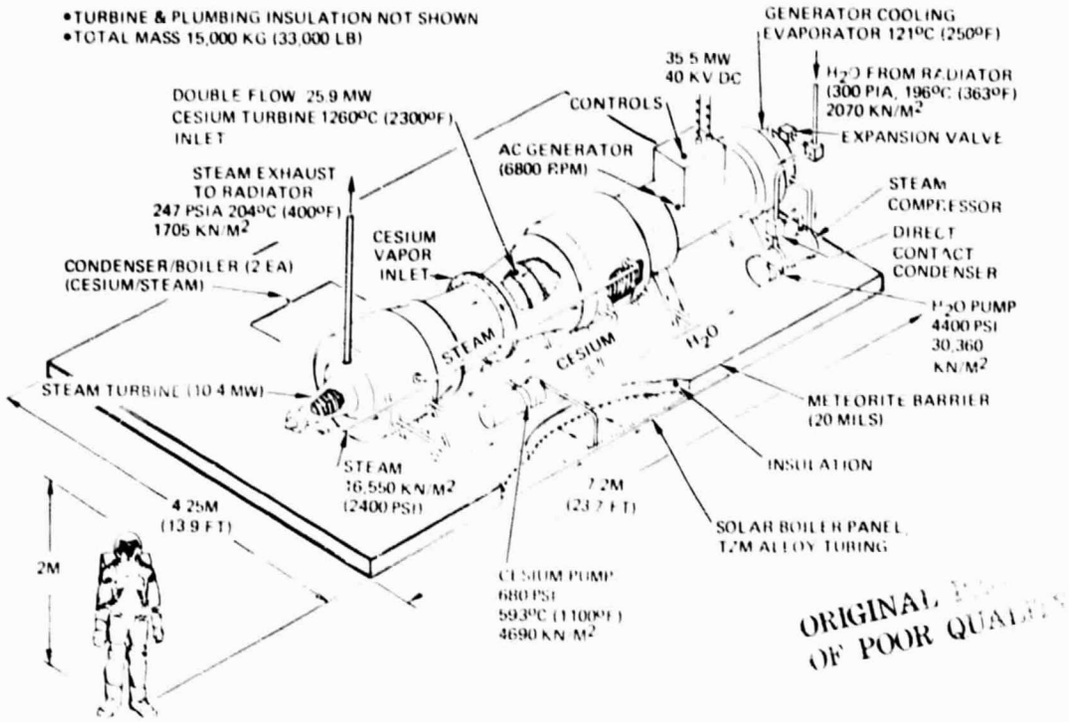

Figure 2.2-12. Independent Power Module

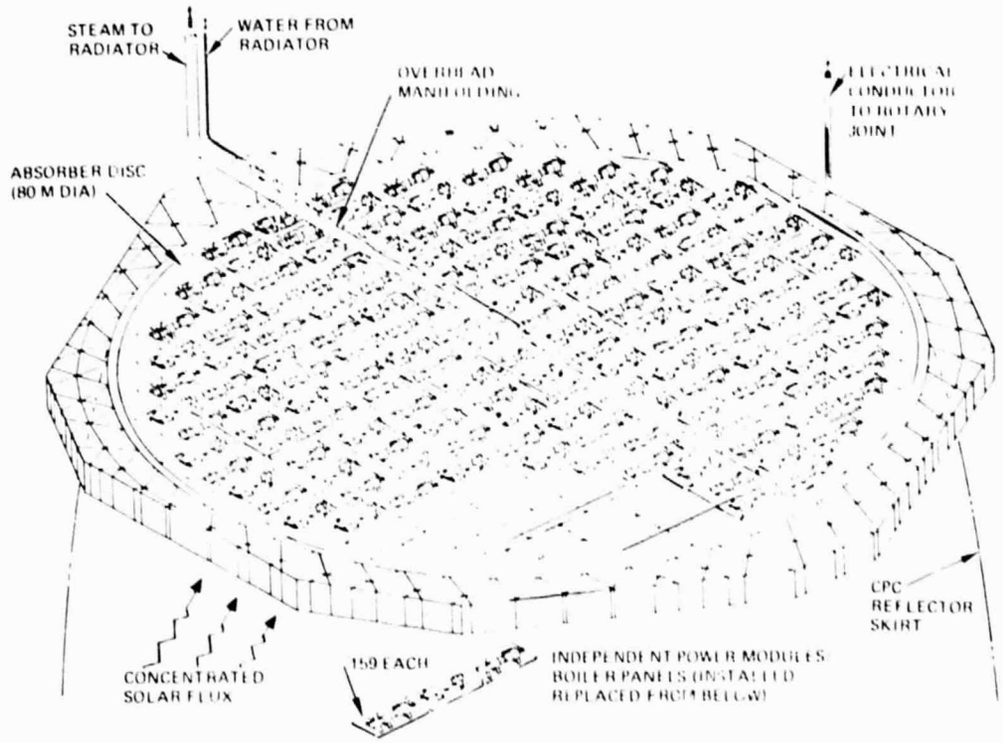

Figure 2.2-13. Turbine/Generator Farm
(1 of 2)

specific areas of turbine design, heat exchanger design, pump technology and materials selection.

Ground Rules and Basic Requirements

Based on results of the trade studies, the following basic requirements were established for the power module point design:

1. Power cycle - cesium/steam Rankine
2. Modularity - completely independent, except for common radiator
3. Power size - optimized for minimum SPS program cost

Point Design Approach

The special problems considered in this design were:

1. Control and monitoring
2. Startup and shutdown
3. Reliability
4. Maintenance
5. Technology verification

Module Size. Module power size was optimized on the basis of minimum SPS program cost. Large module sizes were found to have the following benefits:

1. Less overall complexity
2. Fewer instrumentation and control channels
3. Higher mass efficiency for auxiliary components such as pumps
4. Lower plumbing mass
5. Lower thermal losses (lower surface area to volume ratio)
6. Higher turbine/generator efficiency
7. Lower total parts count, total failure rate, and maintenance

Small module sizes were found to have the following benefits:

1. Higher turbine/generator RPM and lower specific mass
2. Higher redundancy
3. Lower development cost
4. Orbital verification of full-scale module is more feasible
5. Larger production base (lower production cost)

The dominant size factor was found to be the effect of power size on RPM and turbine/generator specific mass. Theoretically, very small sizes would drastically lower system mass according to the relation:

$$M_{SP} \propto \frac{1}{RPM} \propto D_R$$

assuming $V_T = C$

Where:

M_{SP} = specific mass kg/kW

RPM = revolutions/minute

D_R = rotor diameter of generator or turbine

V_T = maximum rotor tip speed (stress limited)

This relation assumes that all linear dimensions of the turbine and generator are scaled proportionately with rotor diameter. In small sizes, this is not possible due to difficulties in accurately manufacturing thin-wall housings, etc. This is reflected in the curves of generator specific weight vs. power shown in Figures 2.2-14 and 2.2-15 (reproduced from Reference 2.2-3). Minimum specific weight is seen to occur in the range of 30-40 MW. This is based on advanced lightweight design of conventional (non-superconducting) generators for airborne application, as shown in Figure 2.2-16. Figure 2.2-15 also shows equivalent data for airborne superconducting generators (Figure 2.2-17), including system mass for the required cryogenic helium refrigeration system. As shown, specific mass is considerably lower for the superconducting concept, especially at very high voltages. For conservatism, it was decided to use the conventional design, since proven, reliable superconducting units may not be available for a design commit date of 1987. They are an important potential means of reducing SPS mass, however, and should be seriously considered when the development status is satisfactory.

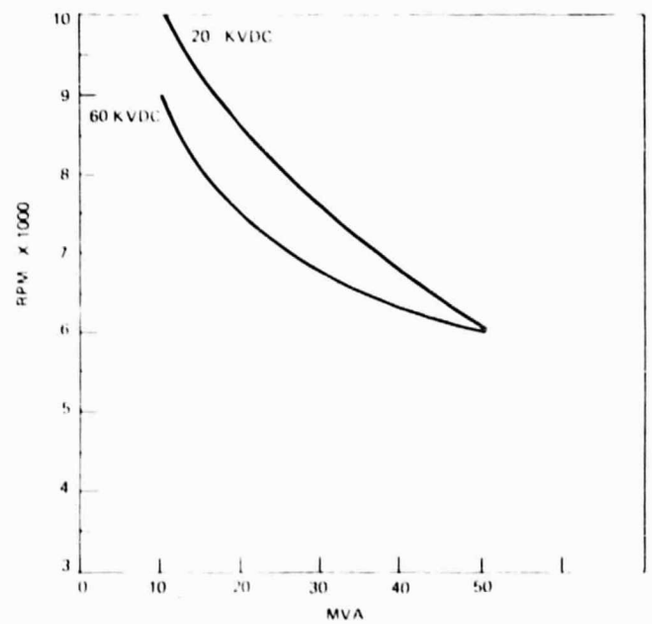

Figure 2.2-14. Conventional Generator RPM Vs. MVA

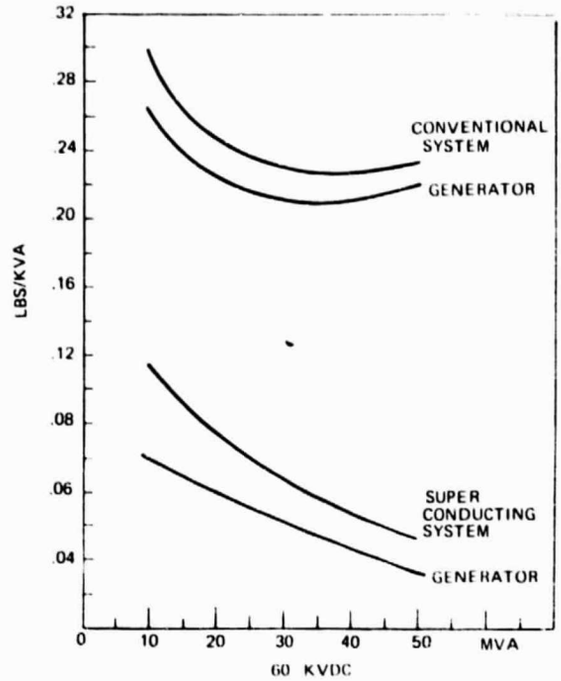

Figure 2.2-15. High Power Study Comparative Highlights - Specific Wt. Versus MVA

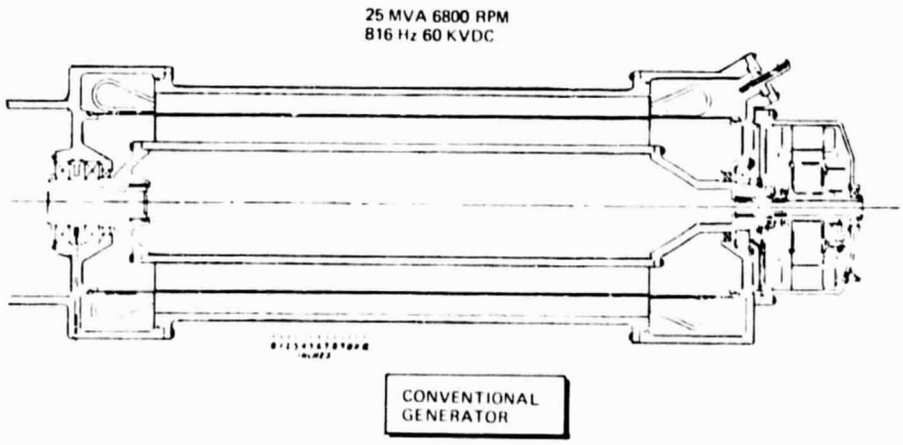

Figure 2.2-16. Conventional Generator Cross-Section

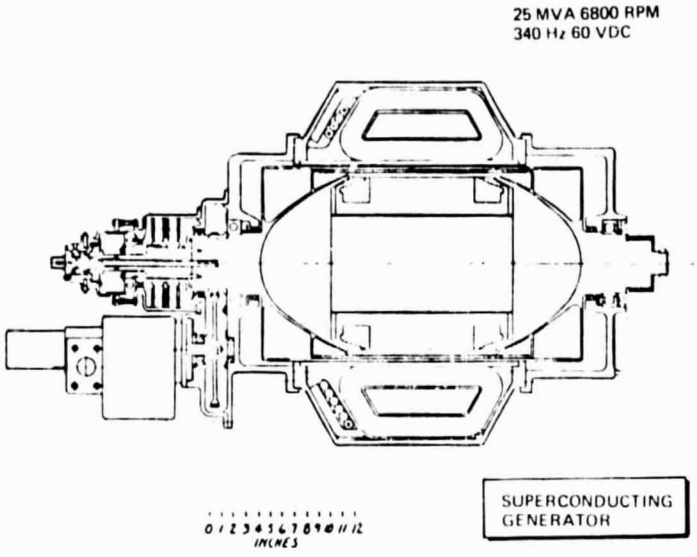

Figure 2.2-17. Superconducting Generator Cross-Section

Specific mass of a cesium/steam turbine, conforming to the generator RPM vs. power curve of Figure 2.2-14, is believed to minimize well below the ideal power size for the generator (30-40 mW). A smaller power size was not used however because of the large number of modules that would result, and associated problems of monitoring, control and maintenance. As discussed under the absorber design, 159 modules per absorber is the optimum number of rectangular modules fitting into a circular field, while yielding a generator size in the desired range (30-40 mW).

A total of 318 modules is not excessive for monitoring and control, and it provides a high degree of redundancy and a high production quantity base, while still providing relatively high efficiencies for the generator (98%), cesium turbine (92%), and the steam turbine (88%). This module is also a convenient size for orbital verification testing (fits in Shuttle cargo bay) and HLLV transport (6 modules comprise a full load). Also, as discussed under cesium turbine design, the full strength of available rotor and blade materials is utilized at this power level. A high utilization of present manufacturing equipment is also provided and the component elements (rotors, windings, blades) are not so small and numerous that total assembly labor is excessive.

Cycle Configuration. Based on earlier trade studies, a first-cut heat rejection temperature of 204°C (400°F) was adapted for the point design. Table 2.2-3 and Figure 2.2-18 present the characteristics of cesium/steam cycles working to this heat rejection temperature, for cesium condensing temperatures of 538°C (1000°F) through 760°C (1400°F). At the lower condensing temperatures, overall cycle efficiency is greater because the average temperature loss across the cesium-condenser/steam-boiler heat exchanger is less at lower values of steam superheat. However, cesium turbine outlet pressure is must lower at low condensing temperatures and requires a much larger turbine (with higher blade stresses) to handle the vapor volume. A cesium condensing temperature of 593°C (1100°F) was chosen as the lowest value which still

Table 2.2-3. Combined Cesium/Steam Cycle Data

CESIUM CONDENSING TEMPERATURE, F		1000	1100	1200	1300	1400
OVERALL CYCLE EFFICIENCY		0.49	0.468	0.447	0.423	0.398
CS:	CYCLE EFFICIENCY	0.341	0.302	0.264	0.226	0.187
	CONDENSING PRESSURE, PSIA	2.9	5.6	10.3	17.5	28
	FLOW RATE/MW, LB/SEC	10.4	10.9	11.4	12.0	12.8
	TURBINE EXIT FLOW/INLET FLOW	0.786	0.814	0.837	0.864	0.894
	TURBINE EXIT QUALITY	0.755	0.785	0.814	0.842	0.87
STEAM:	CYCLE EFFICIENCY	0.227	0.239	0.249	0.255	0.26
	TURBINE INLET TEMPERATURE, F	900	1000	1100	1200	1300
	TURBINE EXIT TEMPERATURE, F	400	445	510	590	660
	FLOW RATE/MW, LB/SEC	1.74	1.84	1.88	1.99	2.09
	TURBINE EXIT FLOW/INLET FLOW	0.75	0.736	0.75	0.746	0.757
	TURBINE EXIT QUALITY	0.983	1	1	1	1

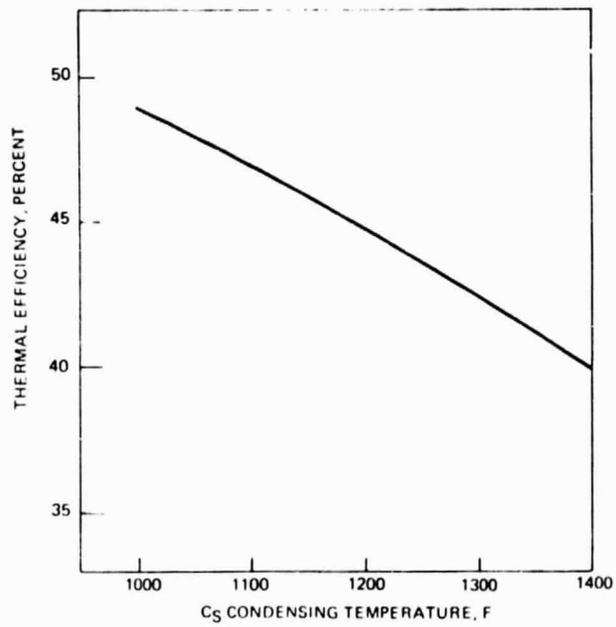

Figure 2.2-18. Cesium/Steam Cycle Efficiency

avoided excessive turbine blade stresses and turbine mass (~5.6% of SPS total). At the turbine inlet temperature of 593°C (2300°F) provided by the absorber design, this provided an overall cycle efficiency of 52% and split the module power at 25.9 MW for the cesium turbine and 10.4 MW for the cesium turbine.

The use of reheat stages for improving cycle efficiency was considered for the cesium and steam turbines but rejected due to the large plumbing mass penalties involved, especially in the absorber (cesium boiler) where meteorite armor is required. Pressure loss is critical in a reheat loop and generous line sizes must be used. Two stages of regenerative turbine bleed were used

in preheating the boiler feed-fluid and thereby raising the cycle efficiency (Figure 2.2-19. Additional bleed stages were not used because of marginal gains in efficiency, and added complexity. In the case of the cesium turbine, additional expansion stages would be needed, resulting in a moderate increase in mass.

Preheaters. As shown in the schematic of Figure 2.2-19, the direct-contact preheaters are of a venturi type which eliminates the need of boost pumps down-stream of each preheater. The high velocity head developed in the throat of the venturi provides the pumping action in the down-stream, pressure recovery section of the venturi. Consequently, the only cesium and water feed-pump required is located in the coolest part of the respective flow circuits. Somewhat higher pump work and discharge pressure is required with the venturi preheaters.

Pumps. The pumps are assumed to be of a high speed, multi-stage, centrifugal design (for minimum specific mass), with hydrodynamic bearings and the drive motors hermetically encased in a side branch of the fluid loop. Non-critical, low performance shaft seals between the motor and pump impeller allow the motor to rotate in a low-viscosity, vapor environment while being cooled with liquid flow in appropriate tubular passages in the stator. External leakage is not possible as long as the hermetic seals of the casing are intact. Canning the motor rotor is an alternate method (Reference 2.2-4). These designs remove the need for an electromagnetic cesium pump which would be considerably more massive and less efficient (20% vs. 75%). Long-life, liquid-metal centrifugal pumps operating at 593°C (1100°F) are practically state-of-the-art. Current development of 30-year life pumps for the nuclear industry is well advanced. The cesium and water pumps (combined) require 3.2% of the generator output.

Generator Cooling. Cooling of the electric generator at 250°F is accomplished by use of a steam compressor to pull a low pressure in the water evaporator coil which contacts cooling oil in the generator assembly (Figures 2.2-12 and 2.2-19). This provides, in effect, a mechanical refrigeration stage which pumps waste heat from the generator at 121°C (250°F) and reclaims it by preheating feed-liquid entering the main water pump at 196°C (384°F). This avoids the need for a separate 121°C (250°F) radiator for cooling the generator. The power required for the steam compressor is ~0.7% of the generator output.

Plumbing, Valves and Connections. As shown in Figures 2.2-6 and 2.2-12, the module is self-contained except for steam connections to a common radiator and cesium connections to adjacent power modules. This permits high integrity leak checks of all other seals and plumbing joints on the ground and minimizes in-orbit installation effort. Sharing of cesium flow between adjacent modules, in the event of boiler and turbine failures, is provided by a plumbing network to minimize resulting loss of power capability.

Design of the boiler panel is covered under the section on absorber point design.

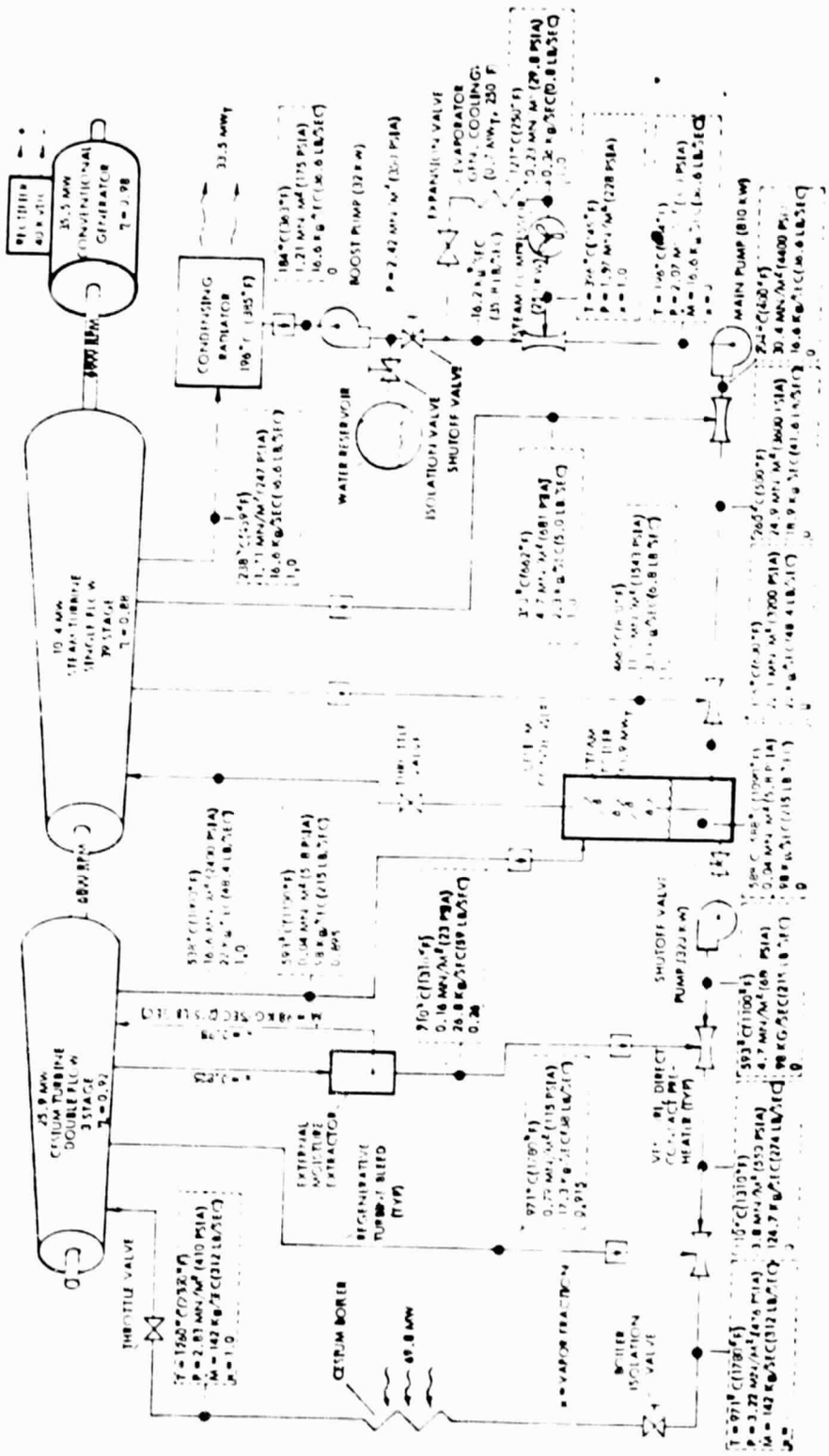

Figure 2.2-19. Cesium/Steam Rankine Cycle Schematic

The most severe valve requirements are imposed by the cesium turbine throttle valve which must operate at 1260°C (2300°F) and 2830 KN/m^2 (410 psi). These conditions can be met with refractory metals such as molybdenum and tungsten. Standard high-temperature design practice, including metal-to-metal seats, long actuating stems, bellows shaft seals and tungsten carbide bearing surfaces should yield an adequate design. The electric motor gear drives for the valves would be isolated from high temperature by long, passively cooled valve stems. Welding is preferred for all plumbing connections except where disconnect capability is required for maintenance and replacement. Figure 2.2-3 shows a lightweight, advanced "Marman Clamp" design which is preferred for such disconnects. It features a radial sealing, metal gasket which achieves a strong wedging action to achieve plastic flow at the metal-to-metal sealing surfaces. This type of connector has been developed in large sizes (over 2-m dia) for the nuclear power industry where reliability and extremely low leakage are mandatory (10^{-7} c.c. of helium per second). Some of the steam radiator mainlines will be of that size. This design also lends itself to single-point latching for quick connection/disconnection without threaded fasteners or tools. Service temperature of the connector is limited only by mechanical properties of the metals used.

Turbines and Condenser. These components are covered fully in the following sections.

Shutdown and Startup Procedures

Automated shutdown procedures will consist of the following steps (refer to Figure 2.2-19):

1. As cesium boiler heat is decreased, gradually unload generator and reduce RPM.
2. Reduce cesium and steam feed pump pressures and flows, and throttle turbine inlets to maintain inlet vapor not more than 100°C (180°F) below turbine temperature.
3. At 3% rated flow, shutoff feed flow to boilers and allow boiler and turbine pressures to cryopump down to condensing pressure.
4. Close turbine inlet valves, isolating dry boilers.
5. Open water reservoir valve and fill with radiator condensate, thereby draining radiator condensing tubes. Allow vapor lines to cryopump down to near vacuum as radiator cools to ~184°C (-300°F). Water will then exist only in large condensate return manifolds which are insulated to prevent freezing.
6. Turbines and cesium condenser will remain near working temperature during entire eclipse period (72 minutes maximum).

Startup procedures will be as follows:

1. Open inlet valves to boilers
2. Open water reservoir valve

3. Apply heat gradually to boilers and increase feed pump flow and pressure.
4. Bypass boiler discharge flow around turbine until its temperature matches the turbine temperature.
5. Gradually open turbine throttle valve, and load generator as RPM increases. Do not exceed a rate of change of turbine temperature over 50°C per minute.
6. Exhaust from steam turbine will quickly thaw any frozen film of water in drained radiator tubes.

Reliability and Maintenance

As discussed in later sections, the bulk of failures are expected to involve small components (sensors, controls, pumps, etc.) which can be readily replaced. It is estimated that major failures which are not practical to repair in service (turbine bearings, generator windings, etc.) would result in less than 10% loss of generating capacity in 30 years. The power modules are 10% oversized to absorb this loss and still meet rated capacity, with some replacement of turbines and generators in later years.

Power Module Characteristics

Table 2.2-4 summarizes performance data and characteristics of the power module point design. Pressure, temperature and mass flow at key points of the system are shown in Figure 2.2-19.

Table 2.2-4. Solar Thermal Power Module
Point Design Characteristics and Mass Summary

THERMAL POWER ABSORBED (MW)	69.8
THERMAL POWER REJECTED (MW)	33.5
GENERATOR POWER (MW)	35.5
CESIUM TURBINE POWER (MW)	25.9
STEAM TURBINE POWER (MW)	10.4
MODULE DIMENSIONS (M)	4.25×7.2
RPM	6800
GENERATOR VOLTAGE (RECTIFIED), KV-DC	40
GENERATOR TYPE	CONVENTIONAL, 3-PHASE
GENERATOR POLES, NUMBER	8
GENERATOR FREQUENCY (HZ)	454 (3-PHASE)
CESIUM TURBINE INLET TEMP, °C (°F)	1260 (2300)
CESIUM CONDESNING TEMP, °C (°F)	593 (1100)
STEAM TURBINE INLET TEMP, °C (°F)	538 (1000)
STEAM CONDENSING TEMP, °C (°F)	204 (400)
CESIUM TURBINE INLET PRESSURE, KN/M^2 (PSI)	2830 (410)
STEAM TURBINE INLET PRESSURE, KN/M^2 (PSI)	16,600 (2400)
REGEN PREHEAT STAGES, CESIUM/STEAM	2/2
OVERALL CYCLE EFFICIENCY	0.52

MASS SUMMARY	KG
BOILER PANEL	4,690
BOILER INSULATION, SHIELD	1,360
GENERATOR, CONTROLS	4,100
TURBINES	3,640
FLUID	330
CONDENSER	910
PUMPS AND COMPRESSOR	455
PLUMBING AND INSULATION	455
TOTAL MODULE MASS	15,940

Technology Advancement and Verification

The chief areas requiring technology advancement are:

1. Material properties data, especially long term creep.
2. Welding of refractory metals (electron beam and laser techniques).
3. High temperature liquid metal pumps.
4. Turbomachinery (see next section).
5. Zero-g condensing (see following section).
6. Reliable, long life electric generators.

Technology verification can be accomplished by subscale and full scale testing of complete modules, both on ground and in orbit. Fire hazard from cesium and air leaks will require elaborate precautions during ground development tests. Ground vacuum chambers or helium purge systems will be required.

Design Growth

Potential areas for design improvement are:

1. Superconducting generators. They offer lower mass, high reliability and higher voltage for power distribution.
2. Compound cesium-condenser/steam-boiler. This transfers heat from cesium to steam at several cesium pressures and temperatures, to reduce average temperature drop across condenser/boiler and improve cycle efficiency. Requires additional stages in cesium turbine.

Development Risk

Considering the present state of refractory metals technology and cesium corrosion data, development risk for the point design power module is considered moderate.

2.2.5 CESIUM TURBINE POINT DESIGN

Engineering support for this effort was provided by Westinghouse Electric Corporation, and the Rocketdyne Division of Rockwell.

Basic Requirements

Based on results of the absorber and power module point designs, the following ground rules and basic requirements were established:

1.	Fluid	- cesium
2.	Power level	- 26 mW
3.	Service life	- 30 years
4.	RPM	- 6800
5.	Load range	- 90-100% of rated

6. Inlet temperature - 1260°C (2300°F)
7. Condensing temperature - 593°C (1100°F)
8. Shutdown/startup cycles - ~100 per year
9. Maximum eclipse duration - 72 minutes

Special Problems. Special problems considered in this design were:

1. Erosion
2. Bearing life
3. Blade fatigue
4. Shutdown/startup
5. Fabrication
6. Materials
7. Shaft seals

Design Approach

The cesium turbine size is based on a 35.5 mW generator which provides minimum generator specific weight with a reasonable efficiency of 0.98. The power split between the cesium turbine and the steam bottoming turbine is 25.9 mW and 10.4 mW respectively, based on the given inlet and condensing temperatures. 6800 rpm is considered to be the highest feasible generator speed (at 35 mW) and sets the rpm for the turbines (direct drive). The minimum specific weight for the cesium turbine may occur at a smaller size and higher rpm but this would probably be offset by its lower efficiency, in addition to the lower efficiencies and higher specific weights for the matching generator and steam turbine. Also specific costs ($/kW) for the smaller sizes (including controls and maintenances) would be higher. At 6800 rpm and the fluid conditions given, a 13 mW single flow cesium turbine is near the limiting size for available material stress levels. Therefore, a double flow (26 mW) design was selected, which also has the advantage of locating both shaft bearings away from the hot inlet fluid.

Three expansion stages and two regenerative bleeds were selected as the minimum number consistent with high efficiency, considering fluid Mach number, percent reaction, expansion ratio per stage, blade angles and regeneration. Four stages may be evaluated in future studies, but the gain in turbine efficiency from the extra regenerative bleed preheat stage would be modest.

Third Stage Design. To minimize exit flow area, turbine size and weight, a high axial exhaust velocity (450 fps) was used in the last stage, with pressure recovery in an annular diffuser (to 150 fps axial velocity), as shown in Figures 2.2-20, 2.2-21, and 2.2-22. Higher axial velocities leaving the rotor would not greatly reduce the required flow area (due to vapor volumetric expansion) but would increase the diffuser losses considerably. A tangential whirl velocity of 100 fps leaving the third stage rotor is used to (1) improve efficiency of diffuser, and (2) sling condensed cesium droplets off the outside of the spiral steam boiler tubes by centrifugal force. These droplets are collected in the condenser shroud under zero "g" conditions by capillary devices and led to the sump outlet supplying the cesium pump. This integral

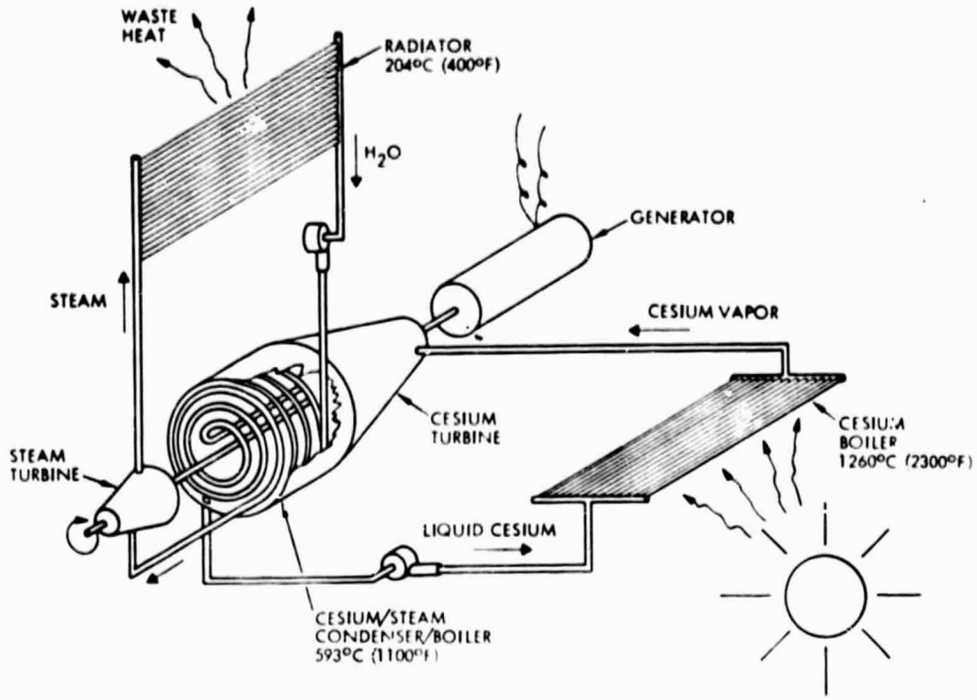

Figure 2.2-20. Cesium/Steam Rankine Cycle

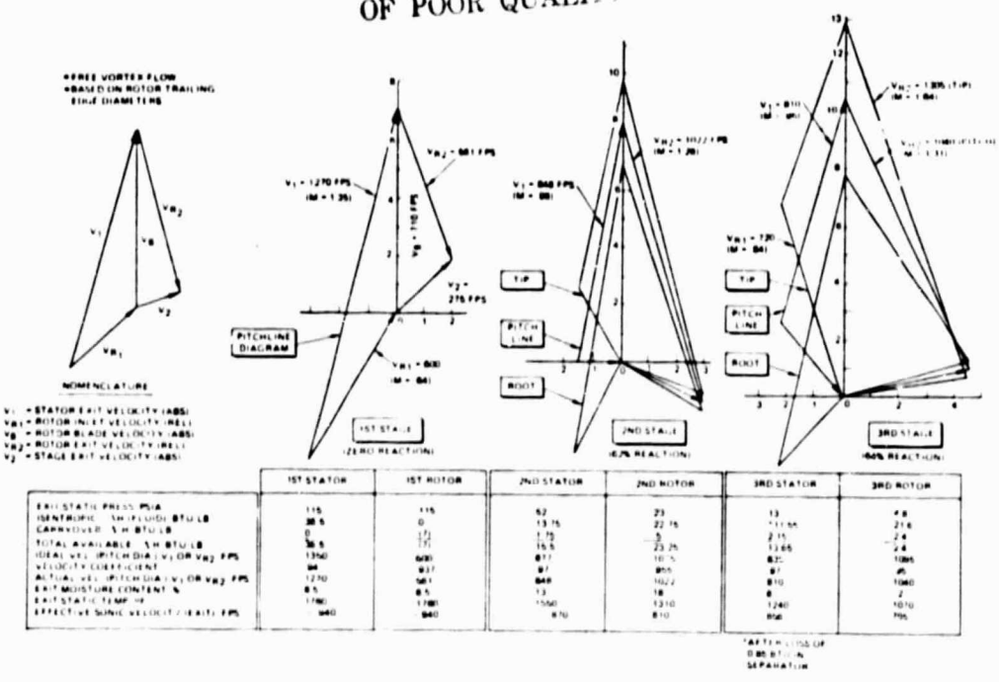

	1ST STATOR	1ST ROTOR	2ND STATOR	2ND ROTOR	3RD STATOR	3RD ROTOR
EXIT STATIC PRESS PSIA	115	115	52	23	13	4.8
ISENTROPIC ΔH FLUID BTU/LB	38.5	0	13.75	22.75	11.55	21.6
CARRYOVER ΔH BTU/LB	0	1.5	1.75	3	2.15	2.4
TOTAL AVAILABLE ΔH BTU/LB	38.5	1.5	15.5	23.25	13.65	24
IDEAL VEL (PITCH DIA) V_1 OR V_{R2} FPS	1360	600	877	1015	825	1085
VELOCITY COEFFICIENT	.94	.937	.87	.905	.87	.95
ACTUAL VEL (PITCH DIA) V_1 OR V_{R2} FPS	1270	561	844	1022	810	1060
EXIT MOISTURE CONTENT %	0.5	0.5	1.5	1.8	8	2
EXIT STATIC TEMP °R	1780	1780	1560	1310	1240	1070
EFFECTIVE SONIC VELOCITY (EXIT) FPS	1640	1640	1570	1510	1540	1395

Figure 2.2-21. Stage Velocity Diagrams

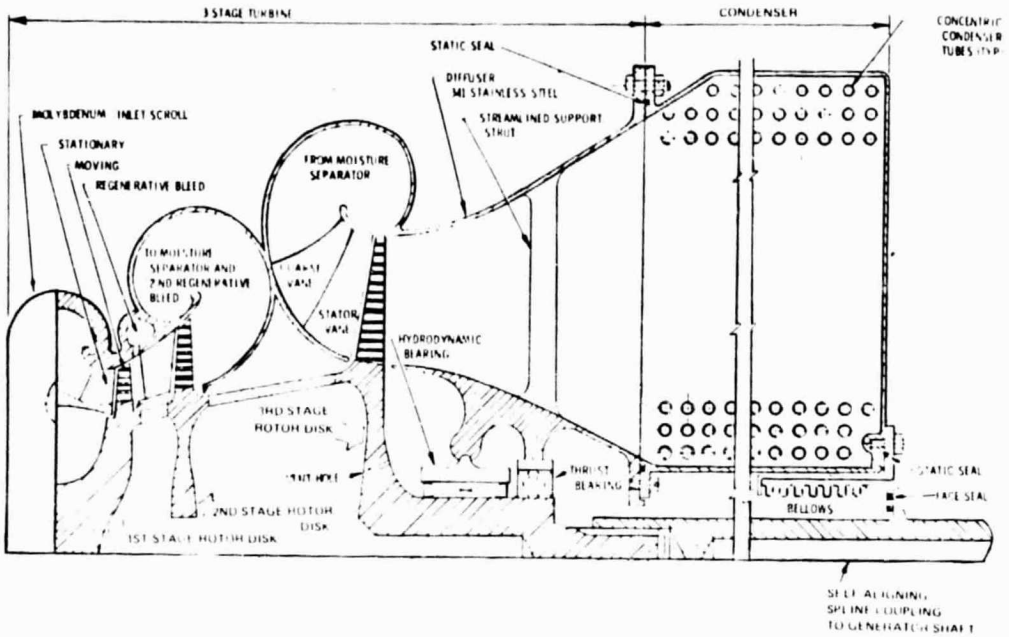

Figure 2.2-22. Quarter-Section of Double-Flow Cesium Turbine

condenser design eliminates the pressure drop and mass of a large turbine exhaust scroll, and ducting to a remote condenser.

A long blade equal to 25% of the pitch dia was selected to minimize rotor tip diameter. A longer blade would have relatively little effect on tip diameter, but would cause excessive blade stress and complicate the blade profile (free vortex flow assumed). The use of regenerative bleed decreases the flow in the 3rd stage to 69% of the 1st stage and correspondingly reduces the flow area required. Due to the high expansion ratio (~2:1) across the rotor, it is not possible to accommodate the change in volumetric flow by flaring the length of a narrow blade. Therefore, the inlet axial velocity to the rotor was reduced to one half the exit axial velocity. This requires the stator nozzle blades to be flared but wide enough to avoid exceeding a 45° flow divergency angle, which is accepted practice in the last stages of large steam turbines. Wide stator blades are preferable to wide rotor blades because the latter increases the centrifugal loads on the rotor disc.

Without external moisture removal, the moisture content leaving the 3rd stage would be ~24%. Cesium fog droplets are not expected to cause blade erosion even at these levels, due to their fine particle size (~0.2 micron). Moisture impinging on blading will be removed by standard suction grooves in the trailing edges of the stator blades and in the rotor housing (Ref. 2.2-5). The low vapor density in the third stage nozzle, however, can allow significant slip of the moisture droplets relative to the accelerating vapor, and resultant efficiency loss. For this reason, external moisture removal in a vortex device is used prior to the 3rd stage, and the enthalpy drop in the 3rd stage is made as small as possible (32% of total) to minimize formation of new droplets. As seen in the velocity diagram of Figure 2.2-21, the stator exit velocity is made as low as possible without exceeding 0.85

relative Mach number at the rotor blade tip inlet. Another benefit of upstream moisture removal is an increase in the sonic velocity of the 2-phase fluid (effective density is reduced). The relative exit Mach number at the rotor blade tip is quite high (~1.6), however, this is common in the last stage of large steam turbines and imposes only a slight loss of efficiency, as opposed to high inlet Mach numbers which cause shock losses in the curved portion of the blade passages.

First and Second Stage Design. Purge impulse (zero reaction) was selected for the 1st stage to:

1. Minimize 1st stage blade and rotor temperatures.
2. Minimize axial temperature gradient along turbine rotor and casing.
3. Eliminate rotor leakage losses which are normally high in 1st stage.

Efficiency considerations also dictate that the second stage have a high degree of reaction with a high enthalpy drop (reaction stages are more efficient). This requires that the pitch diameter of the first stage be considerably smaller than for the second stage, which requires that the mean flow path diverge strongly from the rotor axis between rotors. Selection of 24" and 28" pitch diameters for the first and second stages, respectively, provides a diverging flow path which seems to remain within accepted practice while providing reasonable velocity diagrams, blade angles and efficiencies for the two stages. Tests may show that a wider divergency is permissible. The above pitch diameters result in equal enthalpy drops in the first and second stage (34% each), zero reaction in the first stage, and 62% reaction in the second stage.

Approximately a 1:2 ratio in axial velocity is used across the 2nd stage rotor to accommodate high volumetric expansion across a narrow reaction blade. Blade heights are maximized in the first and second stages (for higher efficiency) by minimizing axial exit velocities, within other design constraints. Full admission in the first stage still permits a good blade length of 2.45" (10% of pitch dia) and avoids vibrational impulses on the rotating blades that would result from partial-admission nozzles. Generous axial spacing is also provided between the stator blades and rotor blades of all stages to minimize vibrational flow impulses which can cause blade fatigue. This spacing also allows fine breakup of any large clinging droplets escaping the suction grooves in the stator trailing edges, before they can strike the rotor blades and cause erosion problems.

Mechanical Design and Assembly. As shown in Fig. 2.2-22, the turbine bearings are assumed to be hydrodynamic (1100°F liquid cesium) tilted-shoe journal bearings fed by either an integral or external liquid pump. An axial thrust bearing is provided at one end of the shaft only. A combination disc-and-drum rotor is provided to reduce rotor stresses at critical points and provide good rotor stiffness. The first-mode rotor natural frequency (beam bending between bearings) is estimated at ~1000 Hz.

The rotor and turbine casing are built up by welding together appropriate discs, rings, cylinders, shafts, blade assemblies and scrolls. The turbine

casing is split horizontally and bolted together with a hollow deformable metal gasket trapped in a flange groove. The cylindrical condenser assemblies are bolted to the ends of the turbine casing along a vertical flange surface with a similar metal gasket. Self aligning splined couplings are used to directly connect the turbine shaft to the generator on one end and the steam turbine on the other. Shaft seals are assumed to be long-life, self-lubricating carbon face seals or equivalent, which are located on the coupling shaft to permit replacement without removing the condenser assembly or opening the turbine casing.

Materials and Corrosion

Working stresses are based on current 1% creep allowables (extrapolated to 30 years) for TZM alloy, pure molybdenum and SU-31 columbium alloy (Figure 2.2-9 and Reference 2.2-6). These materials can be forged, pressed, spun, investment cast; and welded by electron beam, friction welding and probably laser techniques (References 2.2-1 and 2.2-6). SU-31 is a relatively new alloy ($200/lb vs. $8/lb for molybdenum), but price should come down with quantity and the expiration of current patents. Welding of dissimilar metals is considered feasible with use of proper intermetallic diffusion coatings. Getter materials will be incorporated in the cesium loop to absorb oxygen trace impurities in service and eliminate the metal dissolution mechanism.

Characteristics

Performance data and characteristic of the point design are given in Figures 2.2-19 and 2.2-21, and Tables 2.2-5, 2.2-6, and 2.2-7.

Technical Advancement and Verification. The chief technology areas requiring advancement are:

1. Refractory metal properties, especially long term creep
2. Cesium erosion and corrosion data
3. Hydrodynamic bearings
4. Shaft seals
5. Welding techniques for refractory metals (electron beam, laser and friction)

Table 2.2-5. Cesium Turbine Characteristics

FLUID	CESIUM VAPOR
TYPE	DOUBLE FLOW, 3-STAGE
POWER, MW	25.9
RPM	6800
DRIVE	DIRECT
INLET TEMPERATURE, °C (°F)	1260 (2300)
CONDENSING TEMP, °C (°F)	593 (1100)
ADMISSION	100%
BEARINGS	HYDRODYNAMIC (LIQUID CESIUM
MOISTURE EXTRACTION	EXTERNAL BETWEEN STAGES 2 & 3; INTERNAL ON ALL STAGES
REGENERATIVE BLEED STAGES	2
TURBINE EFFICIENCY, %	92
ROTOR NATURAL FREQUENCY, Hz	~1000
INLET MASS FLOW, KG/SEC (LB/SEC)	142 (312)
OUTLET MASS FLOW, KG/SEC (LB/SEC)	98 (215)
DIAMETER HOUSING, M (FT)	1.73 (5.7)
LENGTH, WITHOUT CONDENSERS, M (FT)	2.0 (6.67)
LENGTH, WITH CONDENSERS, M (FT)	4.0 (13.12)
TURBINE MASS, KG (LB)	3220 (7300)
SPECIFIC MASS, KG/KW (LB/KW)	0.128 (0.283)

Table 2.2-6. Cesium Turbine Stage Data

	1st STAGE	2nd STAGE	3rd STAGE	DIFFUSER	CONDENSER
TOTAL INLET TEMP, °C (°F)	1260 (2300)	971 (1780)	707 (1305)	577 (1070)	593 (1100)
INLET PRESSURE, KN/M² (PSIA)	2830 (410)	794 (115)	155 (22.5)	33.1 (4.8)	40 (5.8)
QUALITY, INLET/EXIT	1.0/0.915	.915/.825	.98/.88	.88/.895	.895/0
MASS FLOW, SINGLE FLOW, KG/SEC (LB/SEC)	71 (156)	62.4 (137)	49 (107.5)	49 (107.5)	49 (107.5)
REACTION, %	0	62	64		
REGEN. BLEED, % OF 1st STAGE FLOW	--	12	6		
MOISTURE EXTRACTION, % OF 1st STAGE	MINOR	MINOR	13		
EXIT ANNULUS AREA, M² (FT²)*	0.119(1.28)	0.26 (2.78)	0.62(6.55)		
EXIT SPECIFIC VOLUME, CM³/GM (FT³/LB)	82.8 (1.33)	308 (4.95)	1370 (22)		
PITCH, DIA., CM (IN.)**	61 (24)	72 (28)	89 (35)		
BLADE, HT., CM (IN.)**	6.2 (2.45)	12.2 (4.8)	22.2(8.75)		
TIP DIA., CM (IN.)**	67 (26.45)	83 (32.8)	111(43.75)		
ROOT DIA., CM (IN.)**	55 (21.55)	59 (23.2)	66.7(26.25)		
TIP SPEED, M/SEC (FPS)**	240 (785)	302 (980)	396 (1300)		
PITCHLINE SPEED, M/SEC (FPS)**	216 (710)	255 (832)	317 (1040)		
BLADE MATERIAL	SU-31	TZM	TZM		
BLADE ROOT TEMPERATURE, °C (°F)	1038(1900)	843 (1550)	649 (1200)		
BLADE ROOT STRESS, MN/M² (KPSI)	69 (10)	193 (28)	345 (50)		
ROTOR MATERIAL	SU-31	TZM	TZM		
ROTOR HUB TEMPERATURE, °C (°F)	927 (1700)	788 (1450)	621 (1150)		
ROTOR MAX STRESS, MN/M² (KPSI)	207 (30)	276 (40)	415 (60)		

*BASED ON 0.95 FLOW COEFFICIENT AND 0.15 AREA LOSS FROM TRAILING EDGE THICKNESS.
**AT TRAILING EDGE.

Table 2.2-7. Cesium Turbine Efficiency Data

	1st STAGE	2nd STAGE	3rd STAGE
ISENTROPIC ENTHALPY DROP, J/GM (BTU/LB)	85 (36.5)	85 (36.5	79 (34)*
STANDARD LOSSES (NOZZLE, BUCKET, ROTOR, LEAKAGE, ETC.), %	9.0	8.0	7.0
SUPERSATURATION LOSS, %	4.5	0	0
MOISTURE SLIP LOSS IN NOZZLE, %	0	0.1	0.5
MOISTURE IMPINGEMENT LOSS (5% OF PARTICLES IMPINGE), %	0.5	0.75	0.3
EXTRACTION TP LOSS, %	0	0	2.5
EXIT VELOCITY LOSS (450 FPS), %	0	0	11.7
TOTAL LOSS, J/GM (BTU/LB)	12 (5.12)	7.65 (3.27)	17.5 (7.5)
SHAFT WORK, J/GM (BTU/LB)	73 (31.39)	77.8(33.24)	62 (26.5)
MASS FLOW PER UNIT OF 1st STAGE FLOW	1.0	0.88	0.69
SHAFT WORK, J/GM (BTU/LB) OF 1st STAGE FLOW	73 (31.39)	68.5 (29.3)	42.75(18.3)
AVAILABLE ΔH, J/GM (BTU/LB) OF 1st STAGE FLOW	85 (36.5)	75 (32.0)	49 (21)**

TURBINE EFFICIENCY (WITHOUT REHEAT) = 79 ÷ 89.5 = 0.884

TURBINE EFFICIENCY (WITH REHEAT FACTOR) = 0.884×1.04 = 0.922

SHAFT POWER = $\frac{79 \times 156 \times 3600}{3413}$ = 13,000 KW (SINGLE FLOW), OR 26 MW (DOUBLE FLOW)

*AT ROTOR EXIT PRESSURE (4.8 PSIA)
**AT DIFFUSER EXIT PRESSURE (5.8 PSIA) = 30.5 BTU/LB OF 3rd STAGE FLOW

Technology verification tasks consist of:

1. Subscale component and turbine development testing at over-design conditions. Existing liquid metal flow loops are applicable.
2. Full scale component and turbine development.
3. Extensive accelerated-life, and stress-to-failure testing.
4. In-orbit operation as part of complete power module testing.

The complete cost of cesium turbine development and verification is estimated to be on the order of several hundred millions of dollars. Production costs in SPS quantities are estimated at ~$50/kW.

Design Growth

The potential areas for design improvement include:

1. Additional condensing stages, exhausting to a compound condenser at several levels of temperature and pressure. This allows additional expansion of part of the cesium flow without increasing turbine diameter. The steam can still be heated to the same condition, therefore overall cycle efficiency is substantially increased. Reduces average temperature drop across condenser/boiler.
2. Elimination of external moisture removal, if slip-losses in last stage nozzle prove to be low enough.
3. Increase of turbine inlet temperature, when reliable ceramic components become available (boilers, plumbing, blading, etc.).

Development Risk

Given the fair state of refractory metal technology, cesium corrosion data and hydrodynamic bearing development, the risk in developing a satisfactory cesium turbine is considered moderate. Even if SU-31 alloy should prove unfeasible, TZM and molybdenum would provide a reliable fall-back position although turbine weight would increase somewhat due to the thicker disc and casing sections required.

2.2.6 CONDENSER POINT DESIGN

The chief problem encountered in design of the condenser is the lack of gravity forces to drain the film of condensed cesium away from the surface of the steam boiler. Conventional zero-g designs accomplish condensation within a flowing tube, thereby sweeping the liquid film towards the outlet by vapor drag forces. This method requires a large massive, so-called "compact-type", heat exchanger as shown in Figure 2.2-23 composed of alternate layers of cesium and steam passages brazed into a multi-layer structure, with extensive manifolding and welded seams. These thin-wall welds are vulnerable to cracking from the many thermal cycles (~3000) imposed by eclipse periods. Also a large heavy exhaust scroll and duct is required to convey the cesium vapor from the turbine to the condenser.

The approach finally taken for the point design was to place the condensing surface (in the form of steam boiler tubes) directly in the high velocity vapor exhausting from the cesium turbine. As shown in Figures 2.2-3, 2.2-10, and 2.2-22, spiral banks of boiler tubes are located in an annular shroud at the outlet of the last stage exhaust diffuser where an axial velocity of 45 m/sec (150 fps) and a tangential whirl velocity of 30.5 m/sec (100 fps) impinges on the tubes. The axial velocity must decrease to zero at the far end of the condenser, but a large part of the initial whirl velocity can still exist there. This vapor mass rotating at ~600 rpm sweeps the condensate film along the tubes, thereby creating a centrifugal force which flings the droplets of condensate to the outside of the vapor volume. There, zero-g capillary devices conduct the liquid to a sump area for induction to the cesium feed pump. In effect, this provides an artificial "g" field or centrifuge action without moving parts. The high axial vapor velocity in the upstream banks of tubing also helps to thin out the cesium film on the tubes and fling off the drops. An average film thickness of 0.0025 cm (0.01 inches) was assumed,

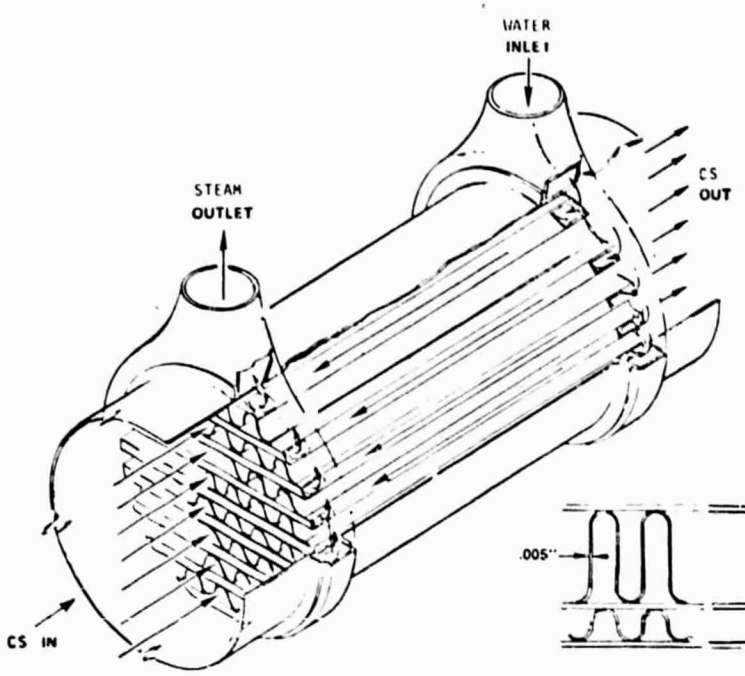

Figure 2.2-23. Plate Fin Type Heat Exchanger

corresponding to a condensing heat transfer coefficient of 20,700 W/sec-m^2-°C (12,000 Btu/hr-ft^2-°F). A supplemental method of collecting the condensate is to provide suction ports on the radial structs which support the tube coils, so as to directly ingest the liquid film being swept along the back side of the tubes. The advantages of these approaches to zero-g condensing are the elimination of pressure drop on the cesium vapor side and a greatly reduced mass (910 kg vs. 5000 kg for the configuration of Figure 2.2-23.

The steam boiler coil configuration at each end of the turbine has 15 banks, each containing 2 coils composed of 6.7 turns of 0.95 cm (0.375 inch) I.D. stainless steel tubing. A high pressure drop (800 psia) was used in the steam coils to achieve very high velocities and high heat transfer film coefficients in the superheat region. The boiling process is essentially supercritical which eliminates any potential problems of flow instability. The resulting increase in pumping power is negligible. Tube wall thickness was 1.15 cm (0.045 inches), resulting in a working stress of 92,000 KN/m^2 (13,300 psi) at the coil inlet (316°C) and 69,000 KN/m^2 (10,000 psi) at the coil outlet (538°C).

The chief problem encountered in any cesium/steam heat exchanger is the possibility of high pressure steam leaking into the cesium system which would cause a spontaneous exothermic reaction (but not a detonation). It could also cause an overpressure condition and extensive corrosion of the refractory metals in the cesium turbine, boiler, and flow loop. An intermediary heat transfer fluid such as molten tin could be used to prevent direct contact of cesium and steam in the event of a leak, but a considerable weight and heat transfer penalty would be involved. Double-walled boiler tubing would impose less of a penalty in these areas. The recommended solution is to use single-walled tubing

which has been proof tested and leak tested to stringent requirements, with all joints of a brazed-sleeve design to avoid the potential cracking problems associated with welded connections in a thermal cycling and vibrational environment. The tubing coils would be supported by streamlined radial struts at appropriate intervals to separate the natural vibration frequencies of the tubing spans from any exciting frequencies in the turbine. In the event of a failure, failed units would be shutdown, drained, and either repaired, replaced or abandoned, as discussed in the maintenance section. Overpressure conditions in the condenser shroud would be prevented by installing a burst-diaphragm with a double-ported vent duct on top of the condenser shroud to achieve thrust-balanced venting of the reaction products (H_2, CeOH, H_2O or Ce) away from adjacent turbo/generator sets.

Characteristics

The chief characteristics and performance data of the point design are given in Table 2.2-8.

Table 2.2-8. Cesium-Condenser/Steam-Boiler Characteristics

DATA FOR ONE OF TWO CONDENSER MODULES PER CESIUM TURBINE	
THERMAL POWER, MW	21.95
BOILER TUBE INSIDE-SURFACE AREA, M^2 (FT^2)	18.2 (196)
TUBE I.D., CM (IN.)	0.95 (0.375)
TUBE WALL THICKNESS, CM (IN.)	0.114 (0.045)
TUBE MATERIAL	SUPERALLOY
COIL LENGTH, M (FT)	20 (66)
PARALLEL COILS	30
COIL PATTERN	SPIRAL, CONICAL
COILS PER BANK	2
NUMBER OF BANKS	15
TUBE CENTER SPACING (RADIAL), CM (IN.)	2.54 (1.0)
TUBE CENTER SPACING (AXIAL), CM (IN.)	5.08 (2.0)
BOILER INLET PRESSURE, KN/M^2 (PSIA)	22,100 (3200)
BOILER INLET TEMPERATURE, °C (°F)	316 (600)
BOILER EXIT PRESSURE, KN/M^2 (PSIA)	16,600 (2400)
BOILER EXIT TEMPERATURE, °C (°F)	538 (1000)
STEAM EXIT VELOCITY, M/SEC (FT/SEC)	113 (370)
CESIUM CONDENSING TEMPERATURE, °C (°F)	593 (1100)
CESIUM CONDENSING PRESSURE, KN/M^2 (PSIA)	40 (5.8)
CESIUM SUBCOOLING, °C (°F)	28 (50)
CESIUM INLET AXIAL VELOCITY, M/SEC (FT/SEC)	46 (150)
CESIUM INLET WHIRL VELOCITY, M/SEC (FT/SEC)	30.5 (100)
CONDENSATE EFFECTIVE FILM THICKNESS, CM (IN.)	0.025 (0.01)
CONDENSATE REMOVAL MECHANISM	VAPOR, ROTATIONAL FLOW
CONDENSATE COLLECTION MECHANISM	CAPILLARY
HEAT TRANSFER COEFFICIENTS, W/M^2-°C (BTU/HR-FT^2-°F)	
WATER, SINGLE PHASE	14,700 (8500)
STEAM, SUPERCRITICAL	8300 (4800)
CESIUM FILM, CONDUCTION	20,700 (12,000)
TUBE WALL, CONDUCTION	4900 (2840)
OVERALL COEFFICIENT	2590 (1500)
LOG MEAN TEMPERATURE DIFFERENCE, °C (°F)	139 (250)
AVERAGE HEAT FLUX, W/M^2 (BTU/HR-FT^2)	3.6×10^5 (3.75×10^5)
TUBE MASS, KG (LB)	173 (380)
SHROUD MASS, KG (LB)	272 (600)
TOTAL MODULE MASS, KG (LB)	445 (980)

Technology Issues

Development and verification of the integrated condenser concept will require subscale and full-scale demonstrations on the ground and in orbit. Ground testing would involve placing the axis of the annular coil bank in a vertical direction, to observe the centrifuging action of the rotating vapor

mass on the cesium condensate without a radial gravitational force component. Development risk is not considered great since additional whirl velocity can be easily provided if needed to obtain required condensing performance. Stress-to-failure testing with over-design pressure, temperature, vibration and corrosion environments would be mandatory.

2.2.7 STEAM TURBINE POINT DESIGN

Rocketdyne provided the computerized analysis and parametric data used for turbine design. Westinghouse Electric Corporation provided engineering support in the areas of steam design practice and operational considerations.

Design Approach

The basic design requirements are listed as follows:

Power level	-	10.4 MW
RPM	-	6800
Inlet temperature	-	538°C (1000°F)
Inlet pressure	-	16,600 KN/m^2 (2400 psia)
Condensing temperature	-	204°C (400°F)
Pressure Ratio	-	6.9

The dominant requirement driving the steam turbine design is a relatively low rpm (6800) relative to power level and condensing pressure. Optimum speeds for those conditions are typically on the order of 30,000 rpm, yielding an efficient turbine with only 6 stages at a specific mass of ~0.0029 kg/kW (0.0063 lb/kW). This very low specific mass relative to large utility steam turbines is derived from a high rpm and a high exhaust vapor density. For the SPS direct drive requirement of 6800 rpm, 39 stages are required and the specific mass becomes 0.022 kg/kW (0.048 lb/km), which still results in a total turbine mass of only 227 kg (500 lb). This is based on a rotor hub-to-tip ratio of 0.9 and a blade pitch-line velocity ratio of 0.5 (zero reaction), yielding a turbine efficiency of 0.88. The large number of stages (39) is within present design practice for large utility steam turbines but is relatively expensive in terms of $/kW for a 10 MW size. This high cost can be largely avoided by use of integral, cast blade-ring assemblies to eliminate the labor required for making and assembling individual blades to the rotors and stators. "Lost-pattern" investment casting techniques, using sulfur instead of wax, lend themselves to accurate, low-cost production operations. The relatively low peripheral speeds, stress levels and temperatures in the turbine permit a wide choice of constructional materials.

The chief operational problem of large steam utility turbines (corrosion and scaling) will be drastically reduced in the SPS design for the following reasons:

1. There is no atmospheric air to leak into the system and promote corrosion.
2. With a very low turbine specific mass, it is economical to use high-alloy stainless steels throughout the design which are corrosion resistant if trace amounts of oxygen are introduced to form a protective oxide film on the surfaces.

3. The high purity metals used will have little tendency to exude contaminants such as silicon which can cause scaling problems.

It is not anticipated that water maintenance or in-service water treatment will be required, if initial descaling runs are made in the steam loop with high ph fluid during production testing of the power module.

Design Characteristics

Tables 2.2-9 and 2.2-10 present the performance and design characteristics of the point design.

Table 2.2-9. Effect of Power Level on Steam Turbine Designs

T_{01} = 1460 R
P_{01} = 2400 psia
PR = 9.72
$(U/C_o)_{STG}$ = 0.5
N = 6500 rpm
DR/DT = 0.2

Power Level, MW	$\dot{W}_{OUT}$, lb/sec	D_{IN}, inches	D_{OUT}, inches	L, inches	wt., pounds	Spec. wt., lb/MW	n, stages	Bearing DN, rpmx10^{-6}	η, %
60	233.6	17.5	31.6	19.7	1120	19	11	0.95	88
30	116.8	13.7	25.0	22.8	800	27	18	0.75	88
15	58.4	10.8	19.7	27.1	580	39	29	0.60	88
10	38.9	9.4	17.1	33.0	500	50	39	0.52	88
7.5	29.2	8.6	15.5	36.7	470	63	47	0.47	88

Table 2.2-10. Steam Turbine Characteristics

POWER (MW)	10.4
TYPE	SINGLE FLOW, 39-STAGE, AXIAL
RPM	6800
DRIVE	DIRECT
INLET TEMP, °C (°F)	538 (1000)
INLET PRESSURE, KN/M² (PSIA)	16,600 (2400)
CONDENSING TEMP, °C (°F)	204 (400)
EXIT PRESSURE, KN/M² (PSIA)	1710 (247)
REGENERATIVE BLEED STAGES	2
TURBINE EFFICIENCY	0.88
HUB-TO-TIP RATIO (ROTOR)	0.9
STAGE VELOCITY RATIO	0.5
PERCENT REACTION	0.0
INLET MASS FLOW, KG/SEC (LB/SEC)	22 (48.4)
OUTLET MASS FLOW, KG/SEC (LB/SEC)	16.6 (36.6)
INLET DIAMETER, HOUSING - CM (IN.)	24 (9.4)
OUTLET DIAMETER, HOUSING - CM (IN.)	43.5 (17.1)
LENGTH, CM (IN.)	84 (33)
MASS, KG (LB)	227 (500)
SPECIFIC MASS, KG/KW (LB/KW)	0.022 (0.048)

Development Risk

Given the moderate inlet temperature of this design and highly advanced state of steam power technology, development risk is considered very low.

2.2.8 RADIATOR DESIGN CONSIDERATIONS

The radiator point design is covered under the thermal control system for an assumed inlet steam condensing temperature of 204°C (400°F). Subsequent power loop optimization studies show that the optimum radiator temperature is approximately 100°C (212°F). Figure 2.2-24 presents the effects of inlet condensing temperature on overall SPS mass, for the point design cesium turbine inlet temperature of 1260°C (2500°F). It is seen that in spite of a larger area requirement, the radiator mass actually minimizes at ~140°C (284°F) because of resulting higher cycle efficiency and a reduced heat rejection load. The overall SPS mass minimizes at a rather low temperature of 65°C (149°F), based on theoretical reductions of plumbing wall thickness with steam pressure. Considerations of minimum practical wall thickness, however, indicate an optimum condensing temperature of ~100°C (212°F). This is still acceptable for the use of water heat-pipes which transport heat from the radiator condensing "through-tubes" to the fins.

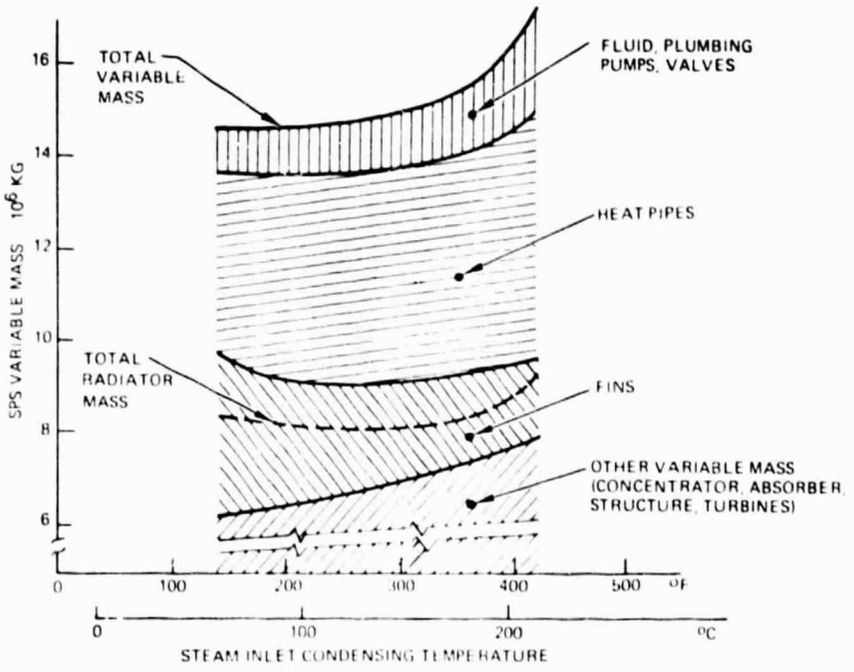

Figure 2.2-24. Steam Radiator Temperature Optimization

Subsequent to finalizing the heat-pipe radiator point design, Vought Corporation, which provided thermal control subcontract engineering support, performed a comparison study which indicates that a straight condensing approach offers ~20% mass reduction and perhaps 70% cost reduction over the water heat pipe design. If a compatible self-sealing additive is developed, the weight reduction would be substantially greater since meteorite bumpers could be eliminated on the many small diameter condensing tubes that replace the heat pipes.

2.2.9 RELIABILITY AND MAINTENANCE

The basic reliability goal for an SPS is uninterrupted production of rated power (excepting eclipse periods), in the most cost-effective manner. This requires determination of the optimum levels of reliability development and operational maintenance. For the point design, a rather high power availability of 90% of total capacity was chosen as a working target. Consequently, each of the 318 power modules was oversized 10%. Achievement of the above target requires the following:

1. Standby repair crews capable of servicing any satellite on 24 hours notice.
2. High inherent component reliability achieved through extensive stress-to-failure testing in development and production samples.
3. Redundant fail-safe system design.
4. Extensive monitoring instrumentation and automated diagnostic/self-shutdown circuitry at the power module level. Typical measurements are system pressures, temperatures, flows, voltages, actuator positions, and vibration signatures of critical rotating units. Summary data from each module is transmitted to the in-orbit and ground control centers.
5. Modularized replacement units at each component level to facilitate rapid maintenance. A boiler feed pump, for instance, could be changed out in 10 minutes, if quick-disconnects are provided for all fluid, electrical and structural connections.

Achievement of a 90% availability (vs. 75% for ground utility power/stations) is also based on the following SPS advantages:

1. No problems of atmospheric air leakage into a sub-atmospheric fluid loop to cause corrosion or degrade condenser performance.
2. Materials in the SPS fluid loop will be highly corrosion resistant. Ground utility boiler tubes and turbine blades are typically low alloy steel. The presence of silica and other metal impurities which cause scaling will be greatly reduced in the SPS.
3. Absence of gravity forces virtually eliminates radial loads on turbine and generator bearings.
4. Shutdown for routine inspection or maintenance will not be used, and will be designed out of the system by fail-safe features, rigorous development and quality control, production burn-in testing, and automated monitoring of turbine/generator vibration signatures.

Failure Rates

The large number of power modules (318) increases the total satellite parts count, but not the failure rate per module. The latter should actually be less in smaller power sizes, since more intensive development can be afforded and the auxiliary systems are usually simpler. Also, the proportion of total satellite capacity unavailable at any one time is reduced, due to higher redundancy.

Although rotating machinery is traditionally expected to have a higher failure rate than solid state equipment, the SPS turbogenerators are expected to require much less replacement than solid state antenna components or specialized components, such as the klystron tubes.

The chief drawback of a small power module size is an increase in the total number of maintenance and repair tasks. Seventy-five percent of the 318 power modules are expected to have at least one failure within their 30 year life. Most of these will be of a minor nature (sensors, wiring, controls, seals, pumps, etc.) that can be quickly repaired or replaced. Major failures of the rotating units such as cracked turbine blades and failed bearings would be much less frequent and would normally be handled by simply shutting down and abandoning the failed unit. Interconnections between power modules permit sharing of cesium flow in such cases. To maintain rated capacity, it may be necessary in the later stages of satellite life to replace entire turbines, generators, and even power modules. These would be refurbished in the orbiting maintenance shop or returned to earth for rebuilding. It is not inconceivable that a power module could be changed out during a 72 minute eclipse period. The connectors involved are 2 cesium, 2 steam, 2 electrical power, 1 electrical control (multi-pin), and 4 structural. In the zero-g environment, a power module is easily removed through the bottom of the absorber disc, away from interference by adjacent plumbing, wiring, etc. Extending the satellite "down-time" several hours, if required, would not be serious since eclipses occur at ground-station midnight when power demand is minimum.

Leakage Problems

The small number of fluid leaks are expected to occur from meteorite punctures of steam and water lines in the two SPS radiator assemblies. Although protected by double bumpers, a certain number of heavier particles will penetrate the lines, perhaps at a rate of 5 or 6 per year per satellite. Fortunately, both steam and cesium are "wet-expanding" fluids; consequently escaping vapors will form a visible plume of moisture droplets or snow. TV cameras set up at strategic points will be used to remotely monitor leaks in the radiators and the turbine farms. "Zoom" capability will enable operators on the ground or in the orbiting control center to pinpoint the leakage source and remotely close appropriate valving to isolate it and prevent excessive loss of fluid. Leaks in the hot absorber disc will be monitored by spectrographic telescopes. Repair techniques such as welding, flame spraying and plasma deposited coating are considered feasible. Even the use of self-sealing additives may be feasible In view of the potential benefits for a condensing tube/fin radiator design, an exhaustive search should be conducted for such additives as part of any further solar thermal SPS development.

Cesium/Steam Interleaks

As discussed under condenser design, the possibility of steam leakage into the cesium loop can be reduced to a small probability, and standard means are available for preventing subsequent over-pressure conditions and cesium contamination in adjacent power modules. This is considered less of a problem than that from the accepted failure rates for turbine blades, generator bearings, etc.

Conclusions

Achievement of a 90% capacity utilization factor for the SPS is considered feasible, although detailed studies may show, that a factor of 85% is more cost-effective. Due to the presence of repair crews, the requirements for component reliability will probably be less stringent than those now used for unmanned satellites.

2.2.10 SATELLITE MASS AND PERFORMANCE CHARACTERISTICS

Figure 2.2-25 identifies the major assemblies comprising the solar thermal subsystem. Figure 2.2-26 contains the overall Solar Thermal SPS block diagram and efficiency chain. Downstream of the switch gear and summing bus, the system is identical with the Photovoltaic SPS, except that the length and mass of electrical conductors leading to the antenna slip rings is less. Table 2.2-11 and 2.2-12 summarizes the major characteristics of the point design.

Overall conversion efficiency including the microwave link is 9.73% as given by the following subsystem efficiencies:

Power generation	-	19.02%
Power distribution	-	93.9%
Rotating	-	77.28%
Ground	-	70.52%
Overall (Product)	-	9.73%

Satellite specific mass is 8.36 kg/kW (18.4 lb/kW) with a potential for reduction to ~6.18 kg/kW, or 31×10^6 kg total mass per satellite.

2.2.11 POTENTIAL DESIGN IMPROVEMENTS

For conservatism, the solar thermal point design did not take advantage of many design improvements that could be available at the assumed design-commit date of 1987, or during the following 30 years of production. The major areas of potential improvement are summarized below. The mass reduction shown do not reflect the 30% growth allowance of Table 2.2-12.

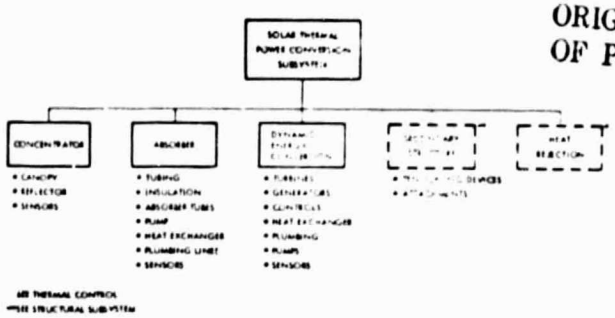

Figure 2.2-25. Assembly Tree

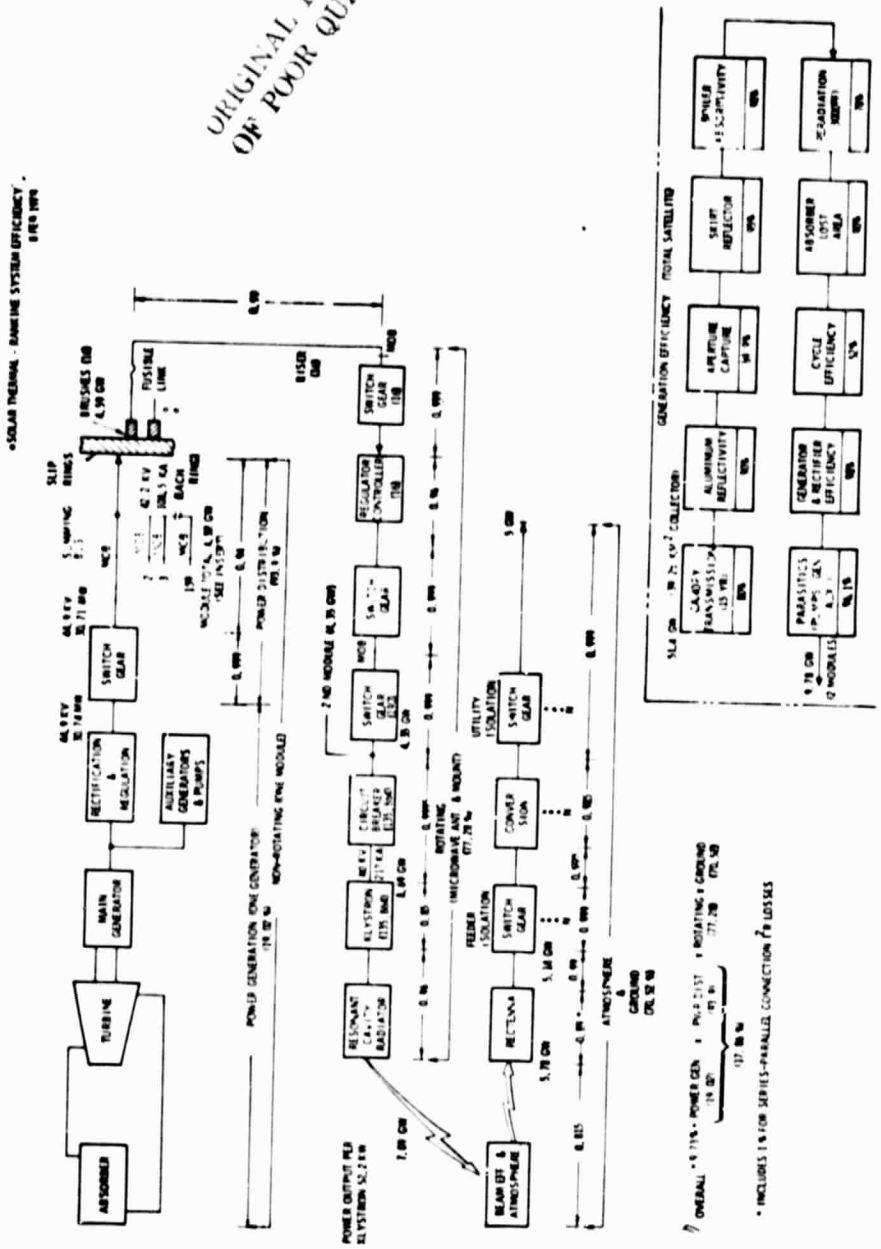

Figure 2.2-26. Solar Thermal Block Diagram and Efficiency Chain

Table 2.2-11. Solar Thermal Power System Characteristics

GENERAL	
POWER TO UTILITY (GW)	5.0
SATELLITE SIZE - LENGTH (KM)	13.8
- DEPTH (KM)	5.7
NUMBER OF MODULES	2
CONCENTRATION RATIO (ACTUAL)	2250
REFLECTOR, TOTAL PLANE AREA (KM²)	39.26
GENERATOR, TOTAL OUTPUT - NET (GW)	9.78
INTERCEPTED SOLAR ENERGY (GW)	51.4
OVERALL SYSTEM EFFICIENCY (%)	9.73
CYCLE EFFICIENCY (%)	52
SYSTEM EFFICIENCY - EXCLUDING POWER CONVERSION (%)	38.9
TOTAL SYSTEM WEIGHT (*)	22.2×10^6
TOTAL SYSTEM WEIGHT (KG)	42.0×10^6
SYSTEM SPECIFIC WEIGHT (KG/GW*)	8.4×10^6
SATELLITE ORIENTATION	PERPENDICULAR TO SUN
LIFETIME (YEARS)	30
IOC DATE	1995
ASSEMBLY ORBIT (KM)	LEO, 435
ASSEMBLY ORBIT INCLINATION (DEG)	0
ELECTRICAL	
GENERATOR SIZE, NOMINAL (MW)	35.5
GENERATORS, QTY	318
GENERATOR TYPE	CONVENTIONAL
NUMBER OF POLES	8
RPM	6800
FREQUENCY (Hz)	454 - 3 Ø
GENERATOR VOLTAGE (KV)	40
POWER DISTRIBUTION	DC
TRANSMISSION VOLTAGE (KV)	40
TYPE OF CONDUCTOR	NON-STRUCT.
BUS MATERIAL	Al
POWER CONVERSION	
WORKING FLUIDS	CESIUM/STEAM
CESIUM TURBINE INLET TEMPERATURE - °C (°F)	1260 (2300)
STEAM TURBINE INLET TEMPERATURE - °C (°F)	538 (1000)
CESIUM TURBINE INLET PRESSURE - KN/M² (PSIA)	2830 (410)
CESIUM TURBINE DISCHARGE PRESSURE - KN/M² (PSIA)	40 (5.8)
STEAM TURBINE INLET PRESSURE - KN/M² (PSIA)	16,600 (2400)
STEAM TURBINE DISCHARGE PRESSURE - KN/M² (PSIA)	1710 (247)
TURBINE REHEAT	NONE
TURBINE TYPE	AXIAL
TURBINE BLADING	REFRACTOR METAL
CESIUM TURBINE SIZE (MW)	25.9
CESIUM TURBINE EFFICIENCY (%)	92
STEAM TURBINE SIZE (MW)	10.4
STEAM TURBINE EFFICIENCY (%)	88
TURBINE SPEED (RPM)	6800
COMPRESSOR/PUMP, TYPE	CENTRIFUGAL
COMPRESSOR/PUMP EFFICIENCY (%)	75/85
REGENERATOR TYPE	DIRECT CONTACT
CESIUM CONDENSING TEMPERATURE - °C (°F)	593 (1100)
STEAM CONDENSING TEMPERATURE - °C (°F)	204 (400)
TURBINE PRESSURE RATIO (CESIUM/STEAM)	70.6/9.7
NUMBER OF TURBINE STAGES (CESIUM/STEAM)	3/39

*WITH WEIGHT ALLOWANCE (APPROX. 30 PERCENT)

POWER CONVERSION (CONT.)	
NUMBER OF TURBINE REGEN BLEEDS (CESIUM/STEAM)	2/2
TURBINE EXTERNAL MOISTURE REMOVAL	CESIUM ONLY
BOILER PRESSURE RATIO (CESIUM/STEAM)	1.16/1.33
CESIUM TURBINE MASS FLOW - INLET (KG-SEC/LB-SEC)	142/312
CESIUM TURBINE MASS FLOW - OUTLET (KG-SEC/LB-SEC)	98/215
STEAM TURBINE MASS FLOW - INLET (KG-SEC/LB-SEC)	22/48.4
STEAM TURBINE MASS FLOW - OUTLET (KG-SEC/LB-SEC)	16.6/36.6
CESIUM PUMP POWER (HW_e)	0.32
WATER PUMP POWER - MAIN + BOOST (HW_e)	0.842
STEAM COMPRESSOR - GEN. COOLING (HW_e)	0.25
TURBINE SPEED CONTROL	INLET THROTTLE
TURBINE EXIT QUALITY (CESIUM/STEAM)	0.895/SUPERHEATED
CONCENTRATOR	
TYPE	CONTINUOUS, INFLATED
FOCAL LENGTH (APPROX)	0.6
CONCENTRATION RATIO (ACTUAL)	2250
COLLECTION EFFICIENCY (%)	64.9
COLLECTOR DIAMETER - 2 EACH (KM)	5.0
REFLECTOR MATERIAL	ALUMINIZED KAPTON
FILM STRESS (MN/M² (PSI)	2.07 (300)
POINTING ACCURACY (DEG)	0.1
DEFOCUSING RESPONSE (SEC)	10
INFLATION PRESSURE - N/M² (MICRONS) (PSF)	8.9×10^{-3} [2.4] (1.2×10^{-4})
ABSORBER	
TYPE	DISC/CPC SKIRT
OVERALL DIAMETER (M)	80
BOILER TUBE MATERIAL	T2M MOLY
PRESSURE DROP (%)	12
ABSORBER EFFICIENCY - (% AREA LOSS (%))	60
TUBE I.D. - CM (IN.)	0.76 (0.3)
TUBE LENGTH - M (FT)	1.08 (3.3)
SKIRT CAPTURE HALF-ANGLE (DEG)	45
RADIATOR *(REFERENCE ONLY -- PART OF THERMAL SUBSYSTEM)*	
TYPE	CONDENSING STEAM
CONSTRUCTION	HEATPIPE/FIN
TEMPERATURE, EFFECTIVE - °C (°F)	196 (385)

Table 2.2-12. Solar Thermal Point Design Mass Properties Summary (Cesium/Steam Rankine)

SUBSYSTEM	KG×10⁻⁶
COLLECTOR ARRAY	(18.016)
STRUCTURE AND MECHANISM	(1.661)
PRIMARY STRUCTURE	0.740
SECONDARY STRUCTURE	0.688
MECHANISM	0.233
ATTITUDE CONTROL	(0.095)
POWER SOURCE	(3.120)
SOLAR COLLECTOR	1.200
SOLAR ABSORBER	1.920
POWER DISTRIBUTION AND CONTROL	(4.304)
POWER CONDITIONING EQUIPMENT	(3.397)
TURBOMACHINES	1.160
PLUMBING, INSULATION	0.145
PUMPS, COMPRESSORS	0.145
CONDENSER	0.283
POWER LOOP FLUID	0.105
GENERATORS, WITH COOLING	1.300
ELECT. POWER CONDITIONING	0.259
POWER DISTRIBUTION	(0.907)
CONDUCTOR AND INSULATION	0.699
SLIP RINGS	0.208
THERMAL CONTROL	(8.786)
RADIATOR WITH PUMP	8.786
INFORMATION MANAGEMENT AND CONTROL	(0.050)
DATA PROCESSING	0.021
INSTRUMENTATION	0.029
ANTENNA SECTION	(14.204)
STRUCTURE AND MECHANISM	1.685
THERMAL CONTROL	1.408
MICROWAVE POWER	7.012
POWER DISTRIBUTION AND CONTROL	3.469
INFORMATION MANAGEMENT AND CONTROL	0.630
TOTAL SPS DRY WEIGHT	32.220
GROWTH (30%)	9.666
TOTAL SPS DRY WEIGHT, WITH GROWTH	(41.886)*

*31×10⁶ KG WITH DESIGN IMPROVEMENTS

Concentrator Design.

1. Use of 0.1 mil Mylar reflector film vs. 0.5 mil Kapton. Increases reflectivity, and reduces film mass, collector diameter, inflation pressure and makeup gas requirements.
2. Use of 0.1 mil FEP Teflon canopy film vs. 0.5 mil. Reduces film mass.

   Potential mass saving is ~0.9×10^6 kg per satellite.

Solar Absorber (Cesium Boiler).

1. Use of lightweight ceramic tubing when ceramic fabrication problems are solved. Reduces mass (vs. molybdenum) and permits higher outlet temperatures and cycle efficiency. Savings ~1.2×10^6 kg.
2. Transparent window over reflector skirt aperture to act as meteorite barrier and reduce reradiation losses. Savings ~0.9×10^6 kg (moly tubes), or ~0.25×10^6 kg (ceramic tubes).

Cesium Turbines.

1. Ceramic inlet manifolds, rotor discs and blades (assumes ceramic absorber also available). Permits 1649°C (3000°F) inlet temperature and 5 points increase in cycle efficiency. Savings ~2.35×10^6 kg.
2. Two additional expansion stages, exhausting at different reduced pressure levels to a compound condenser. Increases cycle efficiency ~5 points without increasing turbine diameter. Savings ~2.1×10^6 kg.

Electric Generator.

Use lightweight superconducting design cooled with liquid helium. Reduces generator system mass and provides higher voltage. Savings ~0.65×10^6 kg.

Power Distribution.

Use 200 kV-dc afforded by superconducting generator (vs. present 40 kV-dc) to reduce conductor mass. Assumes 200 kV Klystrons can be developed, or 40 kV Klystrons can be connected in series. Savings ~0.9×10^6 kg.

Radiator.

1. Reduce condensing temperature to 100°C (212°F). Reduces heat load and radiator mass. Increases cycle efficiency ~9 points. Savings ~1.8×10^6 kg.
2. Use condensing tube/fin radiator (vs. heat pipe/fin). Potential savings ~0.8×10^6 kg, or ~1.7×10^6 kg if compatible self-sealing additive developed.

Thermionic Topping Cycle

Operate thermioric diodes at 1965°C (3600°F) rejecting heat at 1260°C (2300°F) to cesium/steam Rankine cycle. Raises combined cycle efficiency ~8 points. Savings ~3×10^6 kg.

The above potential mass reductions are not directly additive, but can be handled as mass factors and multiplied in series. Certain of the design changes are mutually exclusive, but the most favorable combination of changes would result in a savings of ~9.5×10^6 kg or 52.7% of the non-rotating satellite mass (excludes antenna). Of this ideal amount, a savings of 8.4 kg or 46.6% of the non-rotating mass could probably be realized early in the SPS program, (excludes self-sealing radiator, high voltage Klystrons, and thermionic topping cycle). This is equivalent to a savings of 10.9×10^6 kg including the 30% growth allowance of Table 2.2-12, or a savings of 26% in the total satellite mass (rotating plus non-rotating).

2.2.12 COST CONSIDERATIONS

Although the solar thermal concept was not carried through into a detailed cost study, the following order-of-magnitude data was developed in the course of the point design.

1. Development/Verification - Considered to be less than that for the Apollo Program which was ~$40 billion in 1977 dollars. Equivalent to less than 0.3 mils/kW-hr over a 120 satellite program. Includes antenna and ground station but not transportation system.

2. Production Costs -

Power modules	-	~$100/kW* ($200/kg)
Solar concentrator (Mylar)	-	~$2.4/kW* ($20/kg)
Radiator	-	~$8.7/kW* ($10/kg)
Structure and mechanism	-	~$1.7/kW* ($10/kg)

   The total of these major items is equivalent to ~1.0 mils/kW-hr. Power distribution and antenna costs are approximately equal to those for the photovoltaic SPS.

3. Transportation and Construction Costs - Could be somewhat less than photovoltaic SPS due to LEO construction and LEO/GEO self-transport of solar thermal SPS.

4. Operations Costs - Considered ~1.5 times higher than photovoltaic concept due to power module maintenance requirements. Estimated at ~6 mils/kW-hr. Includes antenna and ground station.

2.2.13 ASSESSMENT OF SOLAR THERMAL CONCEPT

As discussed under subsystem analyses, there are no large state-of-the-art advancements required for development of a solar thermal SPS. With the many fall-back options available, overall development risk is considered "low-to-moderate", certainly no greater than that for the Apollo project in 1960. With proper modular design of equipment, the maintenance concepts proposed are considered realistic and practical. The main technical question is what the most cost-effective capacity utilization factor will be.

Everything considered, the overall merit of the solar thermal concept is not a question of technical feasibility, development risk, or resource availability, but one of cost-effectiveness relative to other energy conversion methods.

*At generator bus

REFERENCES

2.2-1. Amax Specialty Metals Corporation, *"Molybdenum Metal"*, 1960

2.2-2. J. B. Daniels, et. al, *"Preliminary Solar Sail Design and Fabrication Assessment"*, Sheldahl, Inc., Report 77-182, 22 June 1977, Prepared for Jet Propulsion Laboratory - CIT, under Contract 954721 (Subcontract under NASA Contract NAS7-100)

2.2-3. A. E. King, et. al, *"High Power Study Superconducting Generators"*, Westinghouse Aerospace Electrical Division Report AFAPL-TR-76-37, 1 March 1976, Contract F33615-75-C-2068, Air Force Aero Propulsion Lab., WPAFB

2.2-4. H. O. Blinn, et. al., *"Space Power Plant Study"*, Final Report NAS5-250, Westinghouse Electric Corporation Report WANL-PR-(B)-009, prepared for NASA Headquarters, December 31, 1963

2.2-5. W. D. Pouchot, et. al, *"Basic Investigation of Turbine Erosion Phenomena"*, Prepared by Westinghouse Electric Corporation, NASA Contractor Report CR-1830, November 1971

2.2-6. Kawecki Berylco Industries, Inc., *"Columbium Alloy SU-31"*, File Number 313-PD2A, Product Data (Metals and Alloys), No date

2.3 POWER DISTRIBUTION AND CONTROL SUBSYSTEM

The power distribution and control subsystem (PDS) receives power from the power conversion subsystem, and provides the regulation and switching required to deliver power for distribution to the satellite power users. During the ecliptic periods, batteries will be utilized to supply the minimum required power to the various subsystems. Figure 2.3-1 illustrates the major assemblies comprising the PDS. Functional requirements are shown in Table 2.3-1. The subsystem consists of main feeders, secondary feeders, tie bars, summing buses, voltage converters, switch gear, circuit breakers, manually operated switches, slip rings, brushes, and subsystem cabling. Batteries, battery chargers, and boost converters are included for eclipse operations.

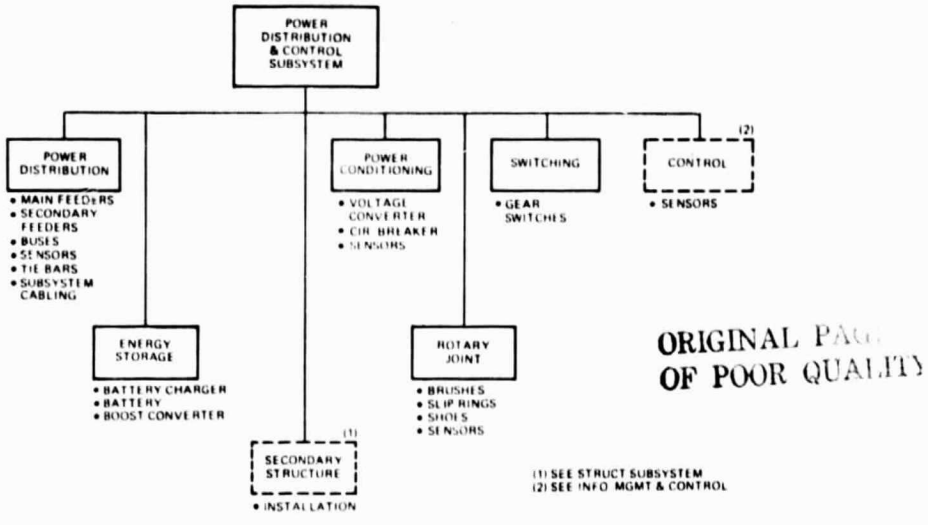

Figure 2.3-1. PDS Assembly Tree

Table 2.3-1. PDS Functional Requirements

LIFETIME	30 YEARS WITH MINIMUM PLANNED MAINTENANCE
OPERATIONS	GEOSYNCH ORBIT; 0° INCLIN, CIRCULAR (35,786 km ALTITUDE)
COMMERCIALIZATION	COMPATIBLE WITH U.S. UTILITY NETWORKS
OUTPUT POWER	STEADY-STATE OPERATION 42.5 kV @ 216 kA AT SLIP-RING INTERFACE; 5 GW AT UTILITY INTERFACE
WEIGHT GROWTH	30%
TOTAL WEIGHT	SATELLITE PDS APPROX .95 kg/kW
ENERGY STORAGE	BATTERIES INCLUDED TO SUPPORT ON-BOARD SATELLITE SYSTEM OPERATIONS ONLY DURING ECLIPTIC PERIODS (~1.7 MW-HRS)
FAILURE CRITERIA	NO SINGLE POINT FAILURE MAY CAUSE TOTAL LOSS OF SPS FUNCTIONS
DEVELOPMENT	EVOLUTIONARY WITH PROVISIONS FOR INCORPORATING LATER TECHNOLOGY
RESOURCES	MINIMUM USE OF CRITICAL RESOURCES
SUBSYSTEM CHECKOUT	CONTINUITY, INSULATION RESISTANCE, FUNCTIONAL SWITCHING OF SWITCH GEARS

The major requirements are to deliver power at specified voltages and levels on a continuous basis throughout the solar seasons for a duration of 30 years. To assure 5 GW at the utility interface, the solar array will generate and deliver 9.75 GW [end of life (EOL)] at the power distribution and control interfaces. Each solar array module is designed for 45.5 kV output. The total array produces 217,000 A. Power delivered to the klystrons (major power user) through power distribution is 8.69 GW, requiring 9.18 GW transferred across the rotary slip ring power interface.

Operations of the system are to be in geosynchronous orbit, and the ground rectenna power delivered at the utility interface compatible with U.S. utility networks. The design is to be such that no single point failure may cause total loss of SPS functions.

2.3.1 FUNCTIONAL DESCRIPTION

SPS power distribution interfaces are illustrated in Figure 2.3-2 for the solar photovoltaic point design concept. The secondary feeders transfer the power from the solar array to the main feeders. The power from main feeders to the summing bus is transferred via switch gears. On-array switching of submodules is used to maintain bus regulation. Mechanically operated breakers (MOB) are included for safety. The interconnection between slip rings and the summing buses is performed through tie bars. Klystron dc voltage conversion is performed by centralized converters (one for each brush assembly). The optimum number of converters is to be determined along with requirements for redundancy. The schematic shows one wing of the solar array only.

2.3.2 SIZING

A continuous review of subsystem efficiencies has been maintained in order to provide updated efficiency factors for sizing the SPS. The efficiencies of major components on the nonrotating solar array wing are shown in Figure 2.3-3. The major consideration for sizing the PDS is the power level (voltage and current) and line loss allowables. This subsystem was sized to handle EOL power levels of 9.75 GW at 45.5 kV.

2.3.3 POWER DISTRIBUTION

The power distribution subsystem utilizes flat aluminum (6101/T6) feeders. These flat conductors are not considered part of the main structure; they will normally be passively cooled by radiation to free space. Main feeders are sized to an average transmission efficiency of 94 percent (determined to be optimum on a cost basis).

2.3.4 POWER CONDITIONING

The power conditioning converts existing bus voltages to the subsystem voltage required for the various subsystem loads. Major requirements are shown in the table on Figure 2.3-2 (klystron requirements). Six basic voltages (40 kV, 32 kV, 24 kV, 12 kV, and 8 kV)—klystron body voltage (40 kV), mod anode voltage (20 kV) and low voltages for cathod heater (20 V), solenoid operation (20 V), computer (20 V) and retro-electronic (20 V)—are required

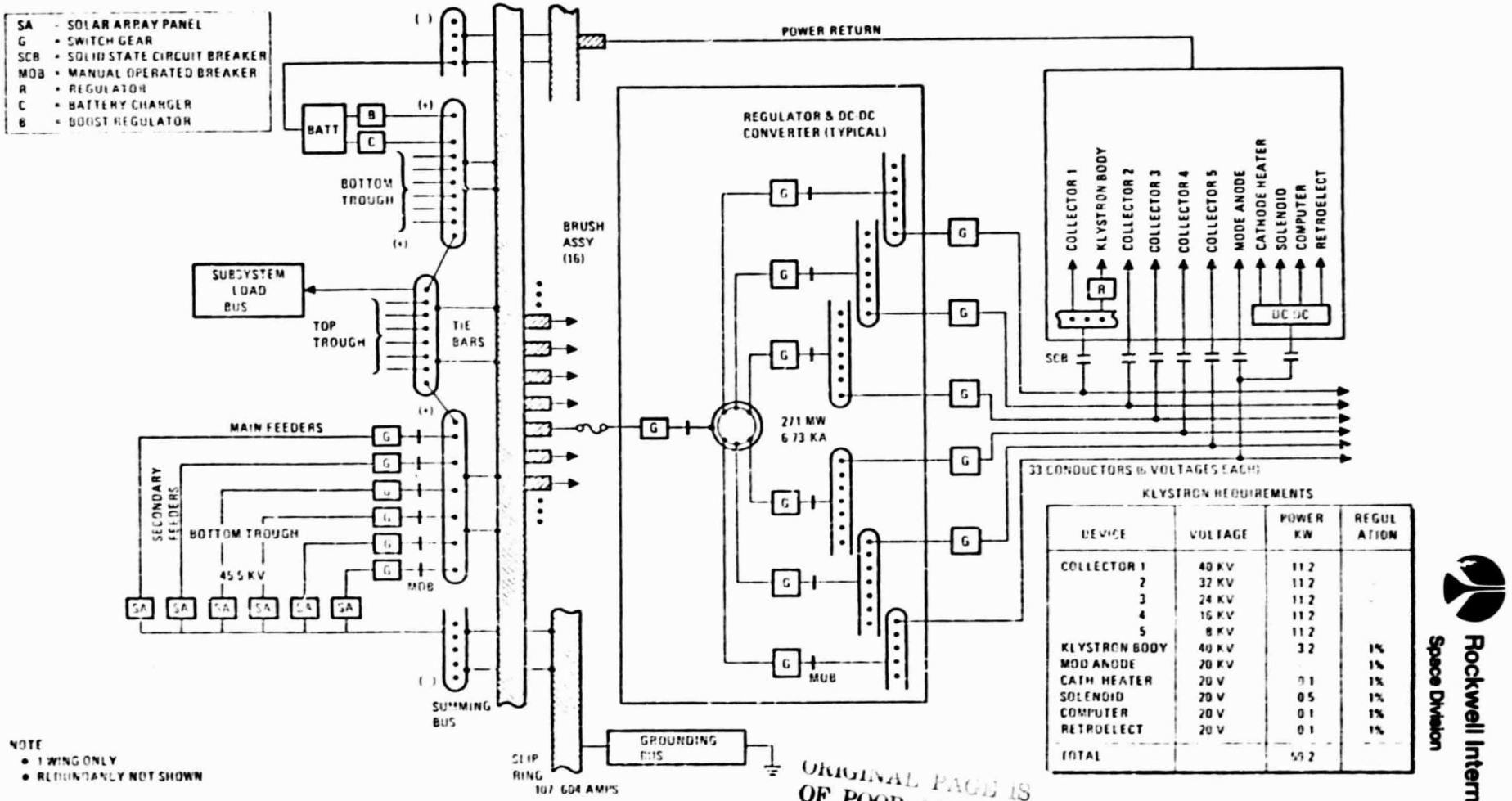

DEVICE	VOLTAGE	POWER KW	REGULATION
COLLECTOR 1	40 KV	11 2	
2	32 KV	11 2	
3	24 KV	11 2	
4	16 KV	11 2	
5	8 KV	11 2	
KLYSTRON BODY	40 KV	3 2	1%
MOD ANODE	20 KV		1%
CATH HEATER	20 V	0 1	1%
SOLENOID	20 V	0 5	1%
COMPUTER	20 V	0 1	1%
RETROELECT	20 V	0 1	1%
TOTAL		99 2	

Figure 2.3-2. PDS Simplified Block Diagram

to operate 135,864 klystrons. These voltages at the required power level are provided by centralized dc/dc converters as shown in Figure 2.3-2. The point design provides 32 converters, each sized for 271 megawatts (6.73 kA). The optimum number of converters will be selected after additional failure mode effects analysis.

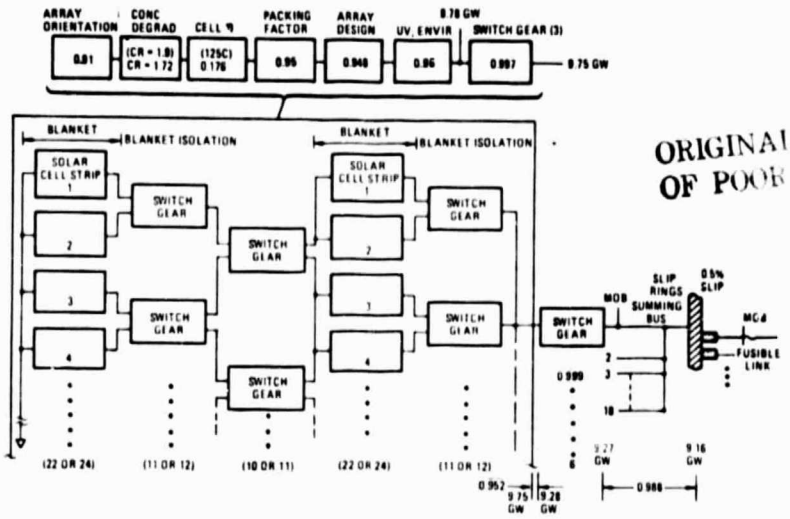

ORIGINAL PAGE IS OF POOR QUALITY

Figure 2.3-3. Solar Photovoltaic Nonrotating Sizing Model

2.3.5 SWITCHING

Switch gears are provided at each end of a string of solar cells for isolation and maintenance. Voltage regulation of the solar array power output, as well as beginning-of-life (BOL) excess power dissipation will be controlled by selective switching of isolation switch gears on array submodules. (NOTE: These switch gears are part of solar array assembly.) Optimum power output will be assured at all times by proper sizing and design of the submodules, their associated switch gear and IMCS control of the switching, in addition to control of the various loads. Voltages and currents being handled by the switch gears will be monitored by the IMCS to determine their status and to establish a need for the opening and closing of these switches.

A simplified computer module, shown in Figure 2.3-4, was formulated to perform a preliminary fault-isolation analysis. Two types of analysis were investigated: (1) short-circuit fault, and (2) loss of a solar array. In the short-circuit analysis (performed by Westinghouse), it was found that if one of the main feeders shorted, the short-circuit current was twice the normal current and the voltage at the loads decreased by 40 percent. If the short occurred at the load (klystron), the short-circuit current was three times the normal current. In the loss of an array (Rockwell analysis), it was found that the array closest to the faulted array would demand a power increase of 12.8 percent, while the array farthest from the faulted array demanded only an increase of 6.8 percent. For more uniform power demand of remaining array modules, regulation and control must be maintained. The point design achieves this by selectiving switching (by IMCS control) of solar array strings.

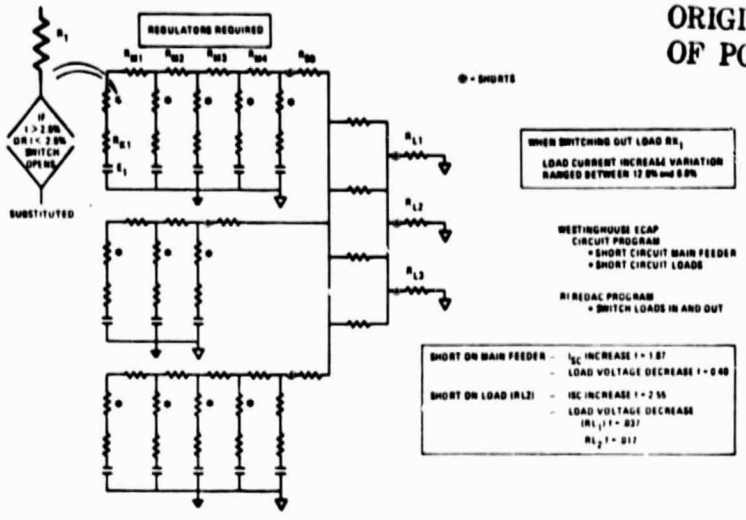

Figure 2.3-4. Preliminary Fault Isolation Analysis

2.3.6 ROTARY JOINT

The rotary joint is utilized to transfer energy through slip rings and brushes from the satellite fixed member to the satellite rotating member upon which the microwave antenna is located. The rotary joint assembly design characteristics are given in Table 2.3-2.

Table 2.3-2. Rotary Joint Design Characteristics

Total Assembly	
Operating voltage (kV)	45.5
Amps per ring assembly	109,000
Total mass (kg)	173,400
Slip Rings (4)	
Core	Aluminum
Cladding	Coin-silver
Core size (cm^2)	41.3 (cross section)
Diameter (km)	1.13
Length (km)	3.55
Shoe Brush (16/Slip Ring Assembly)	
Material	75% Mo Sz, 25 Mo + Ta
Shoe size	11.7 cm × 12.7 cm × 3 m
Current (A/cm^2)	7.75
Contact area (cm^2)	8.68
Quantity	64 brushes per shoe assy
Grounding	
Single point—copper bus (thermal isolated from structure)	

2.3.7 POWER DISTRIBUTION OF ANTENNA

A schematic of the power distribution or the rotating antenna is shown in Figure 2.3-5. Conductors from the brushes are tied to the dc/dc centralized converters through switch gears, to allow isolation when performing maintenance. Conductors are then tied between the voltage summing buses through switch gears for transmitting the required power to the klystrons. The centralized dc/dc converters (32 required) provide the necessary voltages to the klystrons.

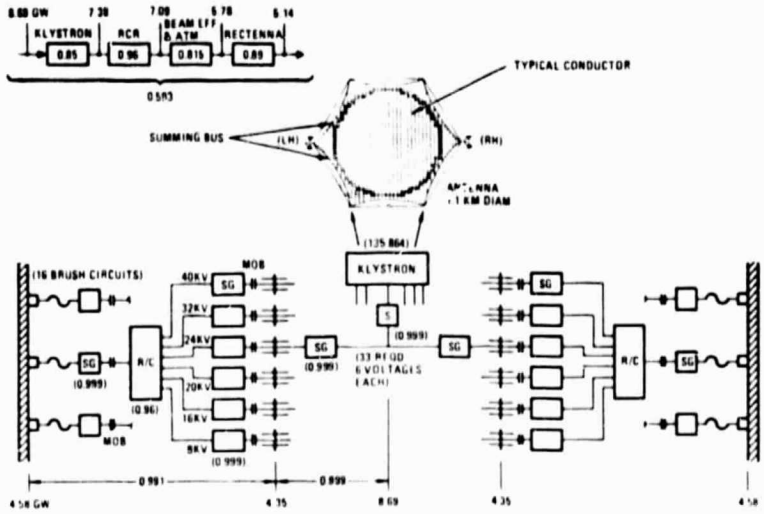

Figure 2.3-5. Rotating Antenna
Power Distribution Schematic

2.3.8 POWER DISTRIBUTION GROUND FACILITY

The power flow from the rectenna to the utility interface is shown in Figure 2.3-6. A control center is required to monitor and control the required

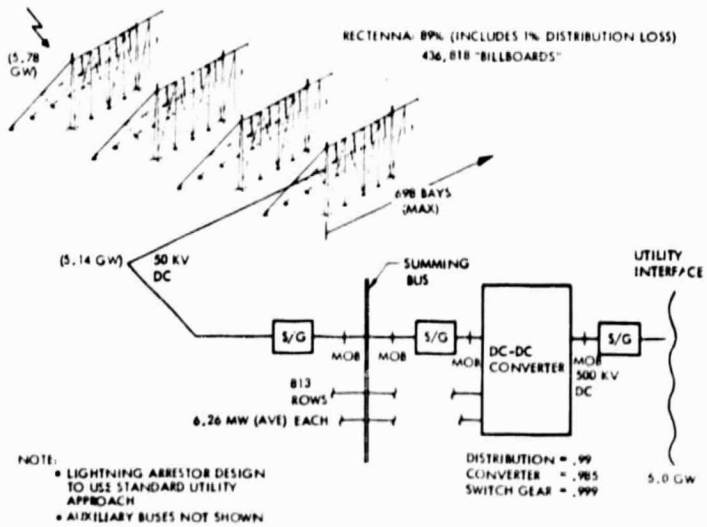

Figure 2.3-6. Power Distribution and Control Utility Interface

power to the utility grid. The control center also monitors the SPS power status at desired intervals. The power is collected by the rectenna, converted to 50 kV dc. The 50-kV dc is then converted to 500 kV dc through dc/dc converters, and then interfaced with the utility grid through switch gears. Switch gears are provided for isolation when performing maintenance. Lightning arrester provisions will be required. It is anticipated that standard utility design would be implemented.

The rectenna consists of 813 rows; the maximum power output from a row is 8.21 MW. Each row consists of standard module "billboards" approximately 14.7×12.2 m, producing 11.76 kW. There is a maximum of 698 bays in a row. Power from each row is controlled and transferred to a summing bus, and then transferred to dc/dc converters as shown in Figure 2.3-6. The rectenna is 89 percent efficient (including one percent distribution loss for diode interconnections). A total of 5.78 GW is inputed to the diode converters with 5.14 GW to the power distribution and control elements. A total of 5.0 GW is delivered at the utility interface.

2.3.9 ENERGY STORAGE

Batteries will be utilized during ecliptic periods to provide 1.7 MW/hour energy. The batteries will be a sodium chloride type and have a density of at least 200 Wh/kg.

2.3.10 POWER DISTRIBUTION AND CONTROL SUBSYSTEM CHARACTERISTICS

A weight breakdown for the PDC subsystem is shown in Table 2.3-3. The PDC accounts for 5.127×10^6 kg, approximately 14 percent of the total satellite mass.

Table 2.3-3. PDC Subsystem Mass Statement

Item	Mass 10^6 kg	Item	Mass 10^6 kg
Non-Rotating		Rotating	
Main feeders	0.342	Cable from rotator to antenna	0.636
Secondary feeders	0.045	Antenna tie bar	0.696
Summing bus	0.102	Antenna cables	0.132
Tie bar	0.162	Antenna module cable	0.031
Insulation	0.043	Switch gear	0.931
Switch gear	0.244	Rotary joint	0.139
Reg. and converter	0.009	DC/dc converter	0.704
Rotary joint	0.208	Insulation	0.20
AC thruster cabling	0.0053	Support structure	0.331
Battery	0.006		
Support structure	0.121		
Subtotal	(1.327)	Subtotal	(3.800)
Total PDC (1.327 + 3.800) = 5.127			

A tabulation of the PDS subsystem point design characteristics is given in Table 2.4-4. The power input from the solar array is 9.75 GW at an array output voltage of 45.5 kV. The klystrons require 8.69 GW input power at the required klystron operating voltages. This power is delivered from the array at an overall efficiency of 89.1 percent. A breakdown of this efficiency is given in the table along with other pertinent information.

Table 2.3-4. Power Distribution and Control Characteristics

INPUT POWER: 9.75 GW (ARRAY VOLTAGE 45.5 KV)		
OUTPUT POWER (TO KLYSTRONS): 8.69 GW		
OVERALL EFFICIENCY:	89.1% SATELLITE SYSTEM (86.4% INCLUDING GROUND)	
TRANSMISSION:	NON-ROTATING	• 94%
	ROTATING	• 99%
	GROUND	• 99%
SWITCHING/POWER CONVERSION:	NON-ROTATING	• 99.9% (EXCLUDING DC/DC FOR ACSK)
	ROTATING	• 95.7%
	GROUND	• 98%
TOTAL MASS:	5.12×10^6 KG	
VOLTAGE REGULATION:	ON-ARRAY SWITCHING (IMS CONTROL) REGULATOR/CONVERTER ± 1%	
TOTAL CURRENT:	215,208 AMPS (AT SLIP RINGS)	
CONDUCTORS:	Al 6101/T6 FLAT CABLE, 1 MM KAPTON INSULATION	
ENERGY STORAGE:	200 WH/KG (1.7 MW - HOURS) SODIUM CHLORIDE	
ROTATING JOINT:	SLIP RINGS (4) • Al CORE, COIN SILVER CLAD; 1.13 KV DIAM; 3.55 KM LENGTH; 41.3 CM^2 CORE CROSS SECTION	
	SHOE BRUSH ASSY (64) • 75% MoS_2, 25 Mo + Ta; 7.75 A/CM^2; 868 CM^2 CONTACT AREA PER SHOE ASSY; 64 BRUSHES PER SHOE ASSY	

2.4 STRUCTURAL SUBSYSTEM

This subsystem consists of the primary structure for the solar array, antenna, and rotary joint; secondary structure; and mechanisms. The primary structure assemblies are made up, basically, of the tribeam girders, tension cables, and joints. The fabrication and assembly of these structures are accomplished on orbit by beam machines and supporting auxiliary equipment.

2.4.1 NASTRAN COMPUTER SIMULATION

The characteristics of the structural subsystem are best understood by reviewing a mathematical simulation that was done using the NASTRAN computer program. Figure 2.4-1 shows the point design concept that was used in this simulation. A substructuring technique was used to develop the model. Three separate models were built and checked out individually; they were then combined in the proper quantities and orientations to form a skeleton of the point design structure.

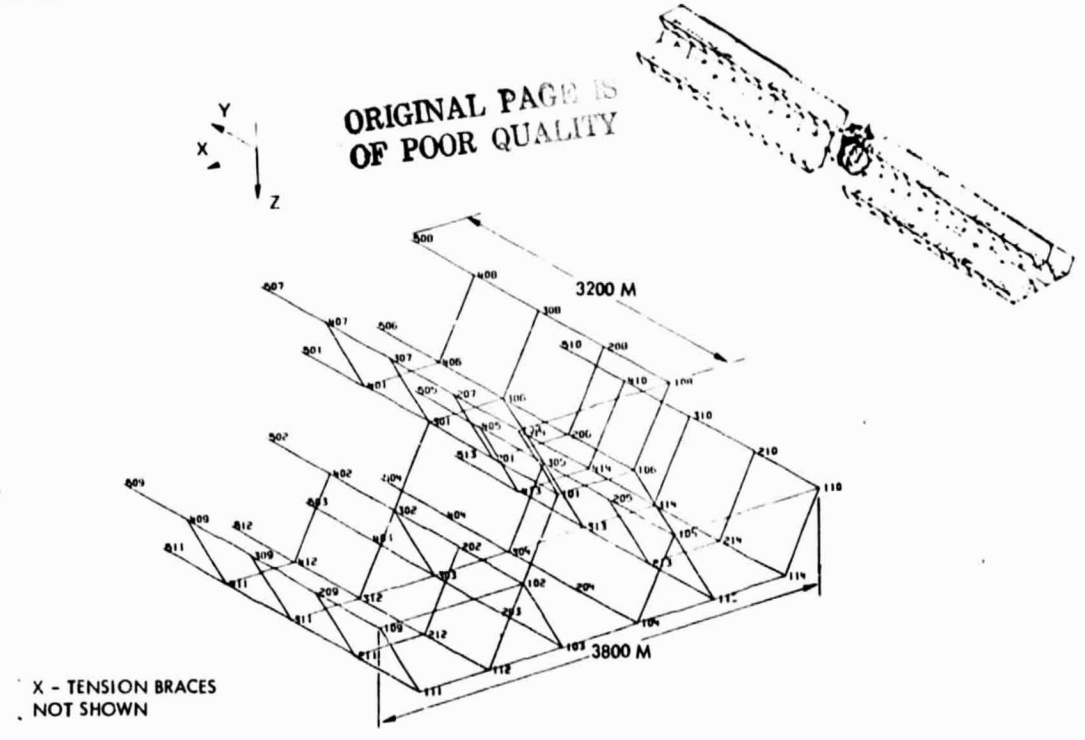

Figure 2.4-1. SPS NASTRAN Substructure Model No. 1

The first model was a module of the solar array wing on the CRT plot (Figure 2.4-1). The module is 3200 m in length and has a cross-section as illustrated in Figure 2.4-2. The module consists of a three-trough system made up of four 800-m bays. The lower troughs are 1250 m wide and the center or upper trough is 1350 m wide. Each trough bay (i.e., 800×1250 m or 1350 m) provides a picture frame construction for two aluminized kapton reflectors on the 60-degree faces and one solar cell blanket system on the trough base. A 25-m clearance is provided around both the reflectors and the solar cell

blankets to provide for attachment to the structural framework. Each 800-m frame is stabilized by X-tension ties which are not shown in Figure 2.4-1 for the sake of clarity. The troughs are attached to a hexagonal center structure that is continuous for the full length of the satellite. The troughs are positioned as shown in Figure 2.4-2 because (1) they provide a satellite structure depth consistent with results of the length/depth aspect ratio trade study, and (2) they support development of a satellite mass distribution which approaches mass balancing about the X and Z axes ($I_{xx} \approx I_{zz}$). Mass balancing is desirable because it minimizes propellants required to correct for sinusoidal gravity-gradient torques which occur twice each orbit.

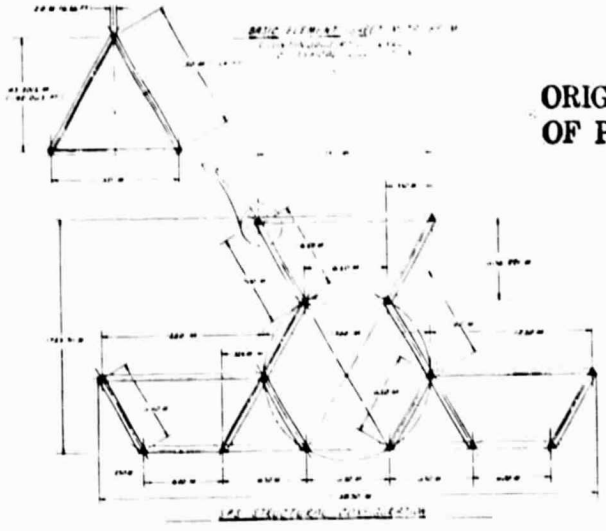

Figure 2.4-2. Satellite Point Design Structural Cross-Section

The first computer model (Figure 2.4-1) is repeated three times and connected end to end by the computer to form the 9600-m left solar array wing illustrated in the CRT plot of Figure 2.4-3. A mirror image is developed to form the right wing, Figure 2.4-4.

The second model is the satellite center section which is 2100 m long and consists of the solar array interior transverse closeout frames, the center hexagonal carry-through structure, the non-rotating portion of the rotary joint and required interface structure. A CRT plot of this model is presented in Figure 2.4-5. (NOTE: Again, X-tension ties are omitted for clarity.)

The third model, shown in Figure 2.4-6, includes the tension web, catenary rope and compression frame of the antenna structure, the rotating portion of the rotary joint, and required interface structure. All models were then combined by computer to form the skeleton point design structure, shown in Figure 2.4-7.

The complete model has been checked out and is now available for computing stresses and deflections of the structure due to forces, torques, and temperature gradients induced internally (e.g., reflector tensioning) and externally (e.g., gravity-gradient torques) on the satellite. These computations should

Figure 2.4-3. Left Solar Array Wing Structure Computer Model 1

Figure 2.4-4. Right Solar Array Wing Structure Computer Model 1

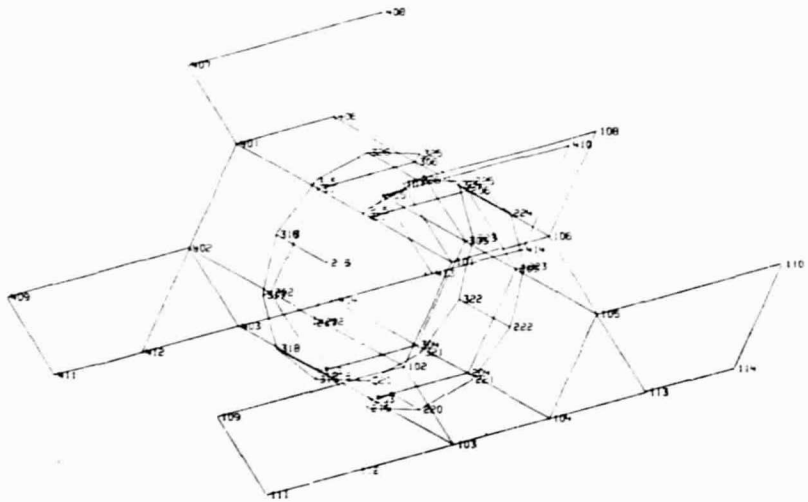

Figure 2.4-5. Substructure No. 2, Center Section

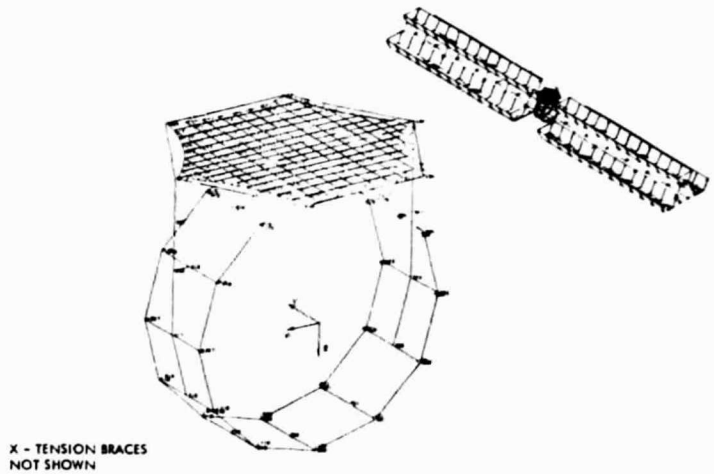

Figure 2.4-6. SPS NASTRAN Substructure Model No. 3

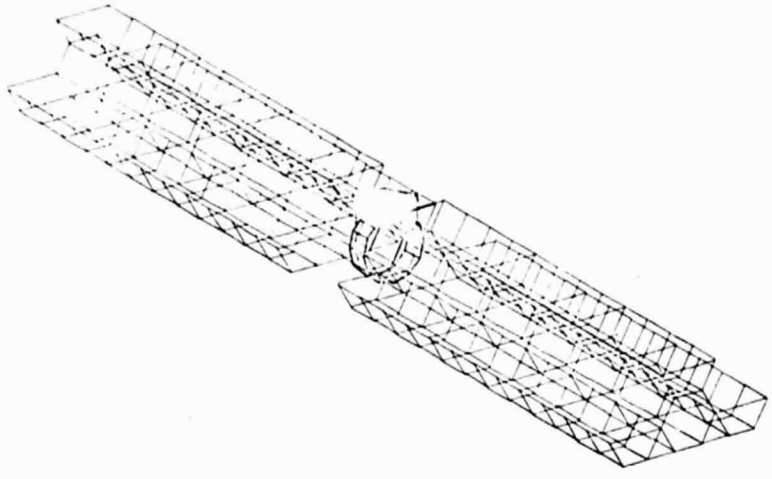

Figure 2.4-7. Combined Computer Models

be accomplished in future studies to improve the confidence level in the structure performance characteristics and mass properties estimates which are, at present, based on the results of preliminary sizing analysis.

2.4.2 TRIBEAM GIRDER

With the exception of the antenna structure, each line on Figure 2.4-7 represents a tribeam girder which is the basic structural element in the satellite. The general configuration and detailed breakout of this tribeam girder are illustrated in Figure 2.4-8.

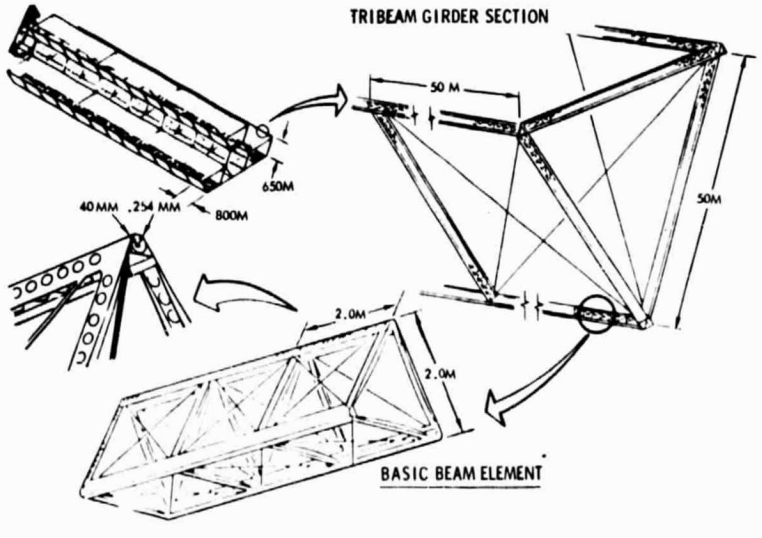

Figure 2.4-8. Photovoltaic Wing Structure Tiering

The girder is 50 m on a side, and each bay is 50 m in length, stabilized by X-tension ties. The three vertices, the transverse struts, are formed by basic beam elements fabricated on orbit by a beam machine. The basic beam element is 2 m on a side with transverse struts every 2 m and modified

triangular cap sections at the vertices. The cap sections, transverse struts, and X-tension braces are made from three sheets of 0.000254-m (10-mil) 2000 series aluminum, with approximately 88 percent cutouts, which is roll-formed, flanged, and welded by the beam machine to form a basic beam element 2 m on a side.

The worst-case environment for a tribeam girder within the solar array is determined by gravity-gradient torques and reflector tensioning. Figure 2.4-9 plots the point design gravity gradient torques as a function of the satellite

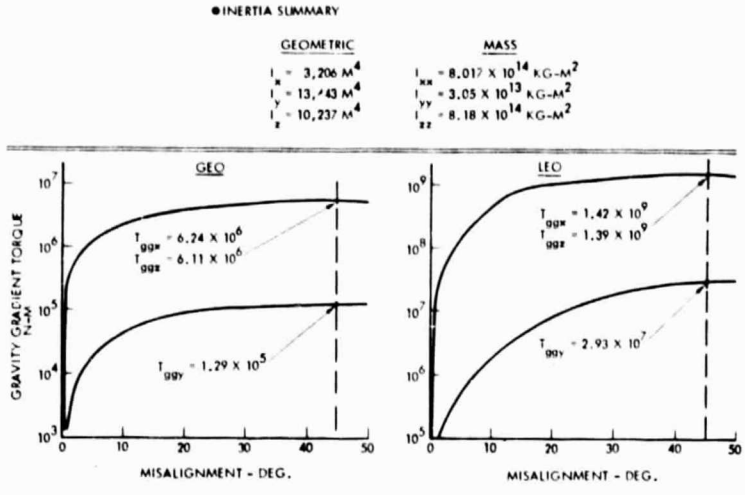

Figure 2.4-9. SPS Point Design Environmental Torques

long axis (Y-axis) misalignment for both GEO and LEO environments. The maximum value of Tggx = 6.24×10^6 n-m (GEO) was used to develop the bending moment and, in turn, the axial forces (P_X) on the tribeam depicted on Figure 2.4-10. These

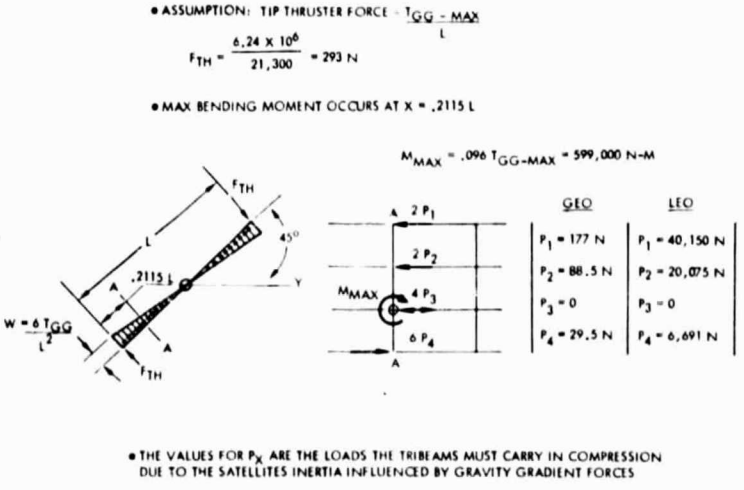

Figure 2.4-10. SPS Structural Element Sizing Analysis

compression forces, combined with reflector tensioning loads, can be applied to the free body of an 800-m tribeam girder as indicated in Figure 2.4-11, and a sizing analysis conducted.

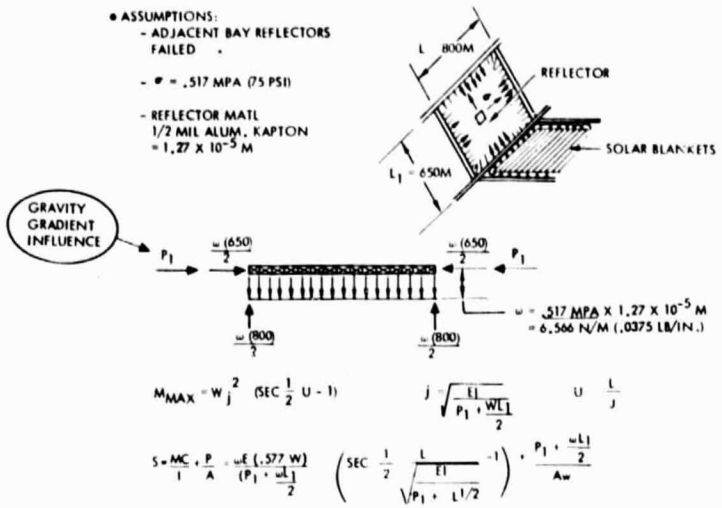

Figure 2.4-11. Compression Forces applied to Tribeam Girder

The pertinent physical properties of the tribeam girder basic beam element, cap section, and tension ties determined by this preliminary sizing analysis are listed in Table 2.4-1. The tribeam girder has a mass of 3.5 kg per meter of length.

Table 2.4-1. Solar Array and Rotary Joint Tribeam Girder Characteristics

ITEM NO.	PARAMETER	CAP SECTION	BASIC BEAM ELEMENT	TRI-BEAM GIRDER	TENSION TIE
1	A_{EM} = EFFECTIVE AREA FOR MASS CALCULATIONS IN M^2	0.035×10^{-3}	0.21×10^{-3}	0.21×10^{-3}	3.17×10^{-5}
2	A_{EI} = EFFECTIVE AREA FOR MOMENT-OF-INERTIA CALCULATIONS IN M^2	0.064×10^{-3}	0.19×10^{-3}	0.19×10^{-3}	3.17×10^{-5}
3	ρ = RADIUS OF GYRATION (M)	28.28×10^{-3}	820.78×10^{-3}	20.236	1.59×10^{-3}
4	I = GEOMETRIC MOMENT OF INERTIA (M^4)	5.1×10^{-8}	0.128×10^{-3}	237.5×10^{-3}	7.9×10^{-11}
5	E = MODULUS OF ELASTICITY - P_a (2)	6.895×10^{10}	6.895×10^{10}	6.895×10^{10}	6.895×10^{10}
6	α = COEFFICIENT OF THERMAL EXPANSION - M/M-°C	23.4×10^{-6}	23.4×10^{-6}	23.4×10^{-6}	23.4×10^{-6}
7	μ = POISSON'S RATIO	0.3	0.3	0.3	0.3
8	F_n = NATURAL FREQUENCY (Hz)	169.4	5.5	0.38 (1)	5.6×10^{-3}

(1) TRI-BEAM GIRDER LENGTH = 800 M
(2) MATERIAL IS 2000 SERIES STRUCTURAL ALUMINUM

2.4.3 ANTENNA STRUCTURE

The tension web compression frame antenna structure concept, shown in Figure 2.4-12, consists of three major elements (1) the tension web to which the dc-to-RF conversion and transmission hardware is attached, (2) a catenary

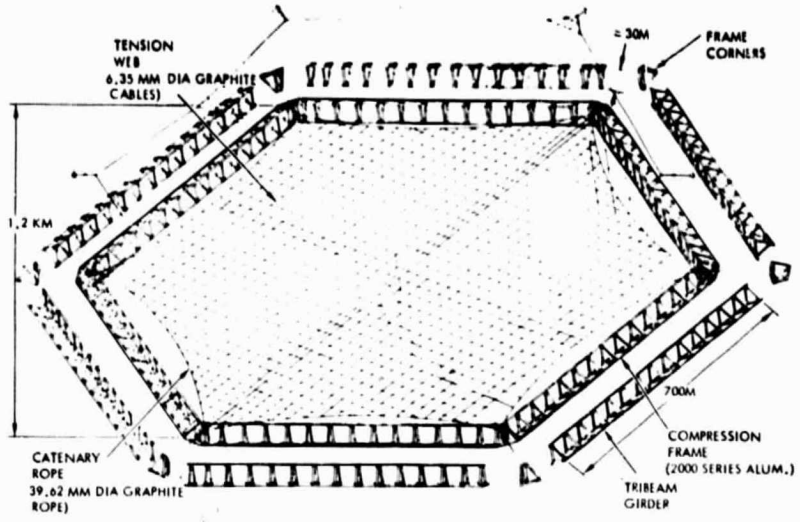

Figure 2.4-12. Microwave Antenna Structure Selected Design Concept

rope system which is attached to the perimeter of the tension web, and (3) a hexagonal compression frame. The tension web resists the lateral pressure loading described in Febure 2.4-13. The loading is transmitted to the vertices of the hexagonal compression frame via the catenary rope system. The compression frame members are loaded in pure compression and can be analyzed as columns. Three of the six catenary-to-compression-frame vertice attachments are fixed. The other three attachments at every other intersection have lateral adjustment jacks. The three fixed attachments describe a plane perpendicular to the desired

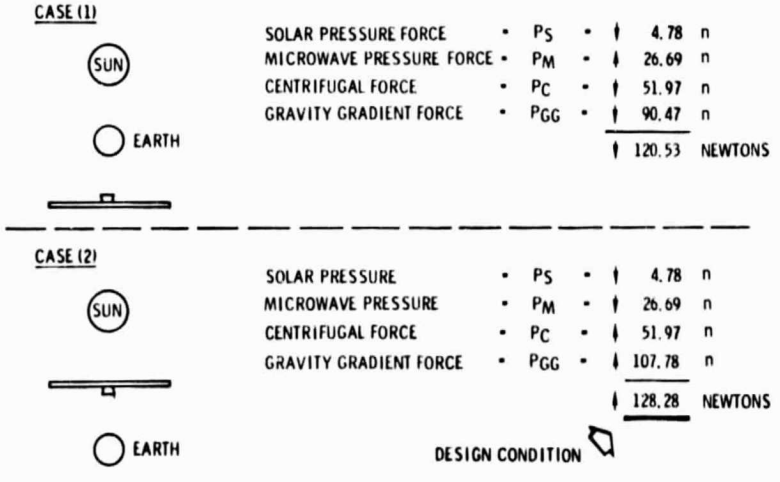

Figure 2.4-13. Microwave Antenna Structure Design Condition

boresight, and the adjustable attachments maintain the tension web as a flat surface. All six catenary rope/compression frame attachments have in-plane tensioning devices which maintain the tension web flat within the design limits. Antenna elevation (north-south) adjustments are accomplished by gimbals in the trunnion structure which attaches the antenna to the rotary joint. Azimuth adjustments are made by the rotary joint.

The basic design requirements for the compression frame tension web concept are as follows:

- 1-km-diameter surface (or equivalent)
- Web angular misalignment: ±0.08° under environmentally and operationally induced loads and temperatures
- Optimize for light weight
- Compatible with on-orbit fabrication and assembly
- Compatible with operational equipment
- Service life: >30 years

The antenna structure was subjected to a sizing analysis based on the environmentally and internally induced loads and the pressure forces indicated on Figure 2.4-13, as well as the design requirements listed above. This resulted in the physical properties for each of the three structural elements listed in Table 2.4-2. The tribeam girder material thickness is 4.36×10^{-4} m (0.17 in.) and its side dimension and bay length dimension are 30.57 m. The catenary cables and tension web cables are woven graphite, 0.0396 m (1.56 in.) and 0.0064 m (0.25 in.) in diameter, respectively.

Table 2.4-2. Antenna Structure Elements Physical and Mechanical Properties

ITEM NO.	PARAMETER	COMPRESSION FRAME			CATENARY CABLE	TENSION WEB CABLE
		CAP SECTION	BASIC BEAM ELEMENT	TRI-BEAM GIRDER		
1	A_{EM} = EFFECTIVE AREA FOR MASS CALC. (M^2)	0.05×10^{-3}	0.3×10^{-3}	1.8×10^{-3}	1.2×10^{-3}	3.167×10^{-5}
2	A_{EI} = EFFECTIVE AREA FOR MOMENT-OF-INERTIA CALCULATIONS (M^2)	0.09×10^{-3}	0.27×10^{-3}	0.81×10^{-3}	1.2×10^{-3}	3.167×10^{-5}
3	ρ = RADIUS OF GYRATION (M)	23.68×10^{-3}	0.47	12.48	1.58×10^{-5}	$1.53\ 10^{-11}$
4	I = GEOMETRY MOMENT OF INERTIA (M^4)	5.15×10^{-8}	0.6×10^{-4}	0.126	1.2×10^{-7}	7.9×10^{-11}
5	E = MODULUS OF ELASTICITY (P_a)	6.895×10^{10}	7.395×10^{10}	6.895×10^{10}	13.79×10^{10}	13.79×10^{10}
6	α = COEFFICIENT OF THERMAL EXPANSION (M/M-°C)	23.4×10^{-6}	23.4×10^{-6}	23.4×10^{-6}	0	0
7	μ = POISSON'S RATIO	0.3	0.3	0.3	TBD	TBD
8	MATERIAL	ALUMINUM	ALUMINUM	ALUMINUM	WOVEN GRAPHITE	WOVEN GRAPHITE

2.4.4 ROTARY JOINT

The rotary joint attached to the hexagonal center carry-through structure is illustrated in Figure 2.4-14. The joint consists of a double set of inner stationary and out-rotating rings. The rings are modified 50-m tribeam girders fabricated on orbit by beam machines. Rotary joint dimensions are noted in Figure 2.4-15. The power transfer slip rings, etc., are discussed in the Power Distribution section. This concept can be termed "large structure/large power transfer rotary joint" configuration.

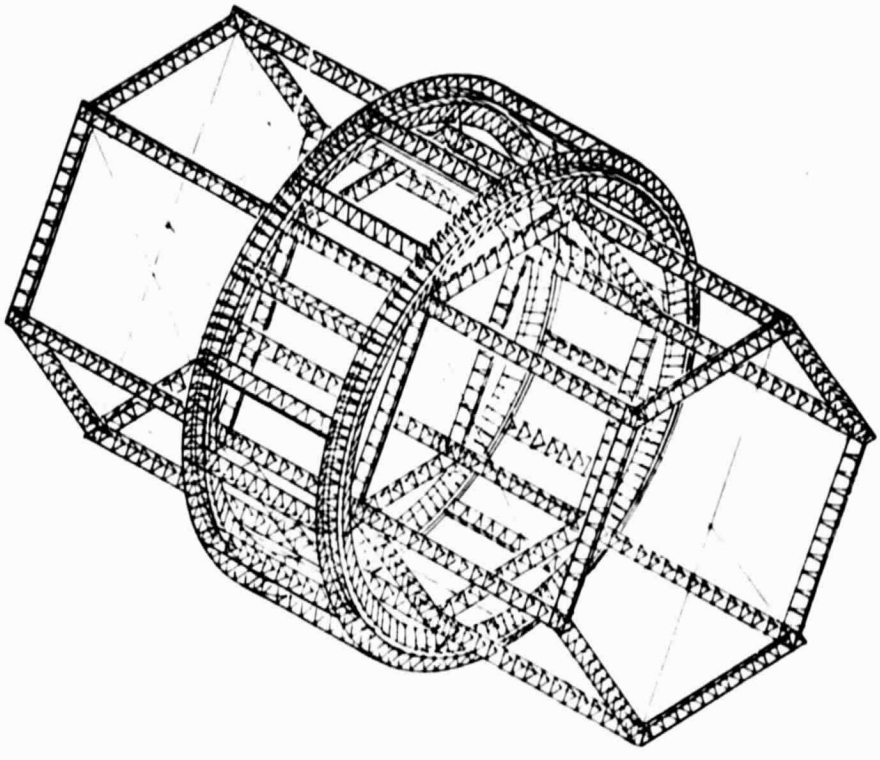

Figure 2.4-14. Rotary Joint Structural Concept

Alternate Rotary Joint - An alternate design has been developed by NASA/MSFC, which can be termed a "large structure/small power transfer" rotary joint concept. Although this concept was developed and sized for a different carry-through structure, it certainly could be adapted to the Rockwell point design and should be evaluated in future studies. The remaining paragraphs in this section present details of this alternate rotary joint concept.

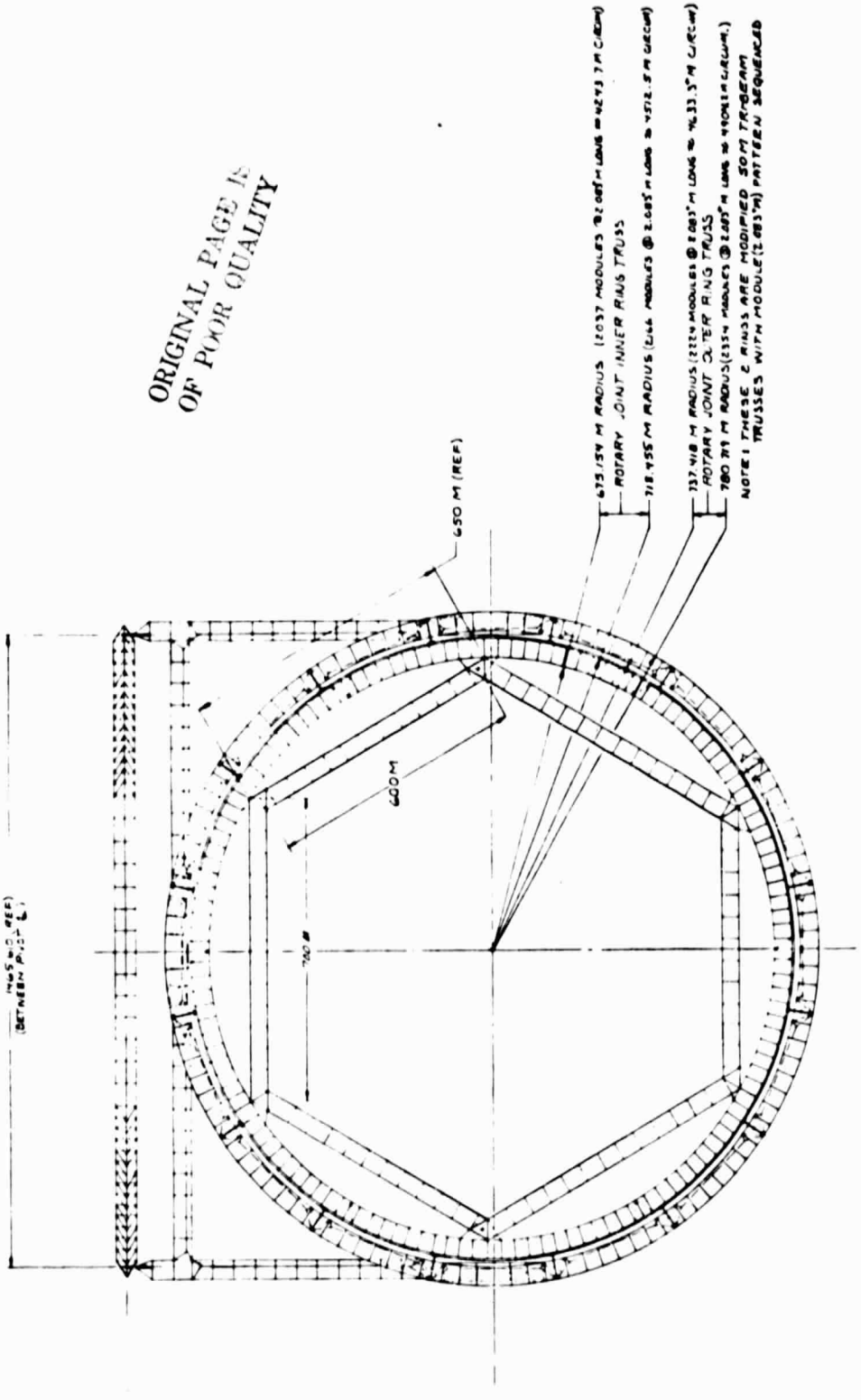

Figure 2.4-15. Rotary Joint Dimensions

The SPS carry-through structure is 1900 m long and includes a 1300 m long by 500-m-diameter rotating section (Figure 2.4-16) on which is mounted the microwave transmitting antenna. The rotating section incorporates two small coaxially located slip ring and brush assemblies which are secured by tensioning cables (not shown) and spider beams. The primary structural members of the

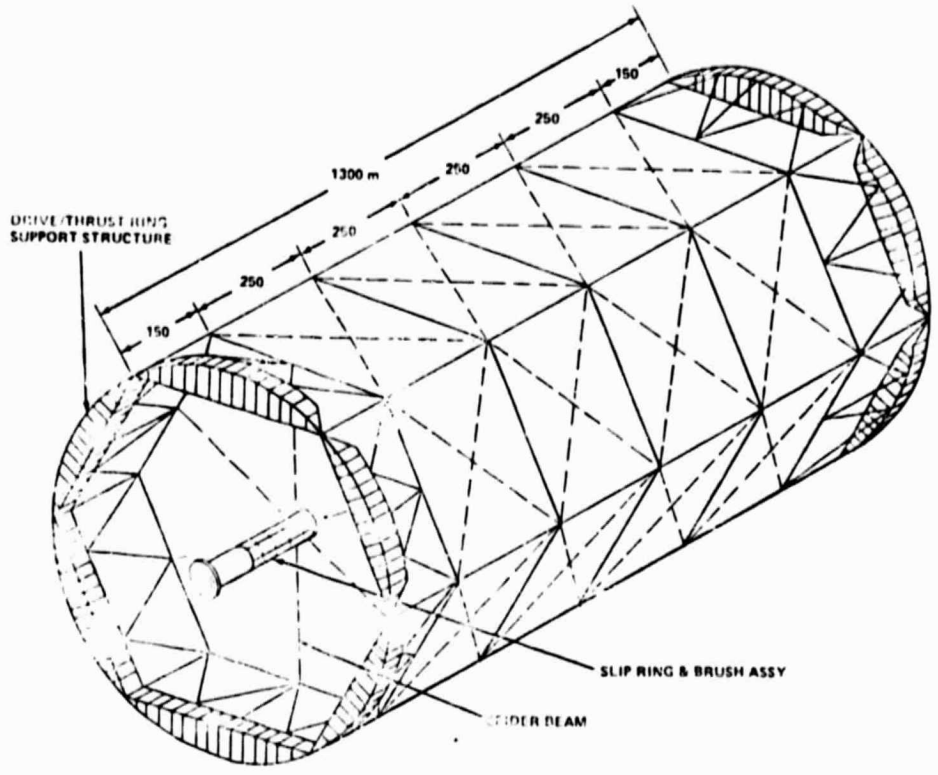

Figure 2.4-16. SPS Carry-Through Structure to Accommodate Slip Ring Concept

carry-through structure are aluminum beams and tensioning cables as in the solar array support wings. Rotation is provided by motorized rotary drive units which are uniformly attached to the fixed carry-through structure and engage the rotating structure through wheel assemblies interfacing with rotary drive rings. Loads are transmitted from the rotary drive assemblies to the rotary drive ring in the X-direction and in the tangential direction. Shear loads, or loads in the Y-Z plane, are transmitted from the stationary to the rotating carry-through structure by radial cables which attach to the stationary and rotating parts, respectively, of the small-diameter slip ring and brush assembly.

A functional schematic of the carry-through structure and slip ring is shown in Figure 2.4-17. This concept accomplishes two objectives: (1) it provides a smooth operating rotary joint for the antenna-mounted carry-through structure, and (2) it provides for a small-diameter slip ring and brush assembly which can be fabricated and checked out on earth and then transported to orbit by HLLV.

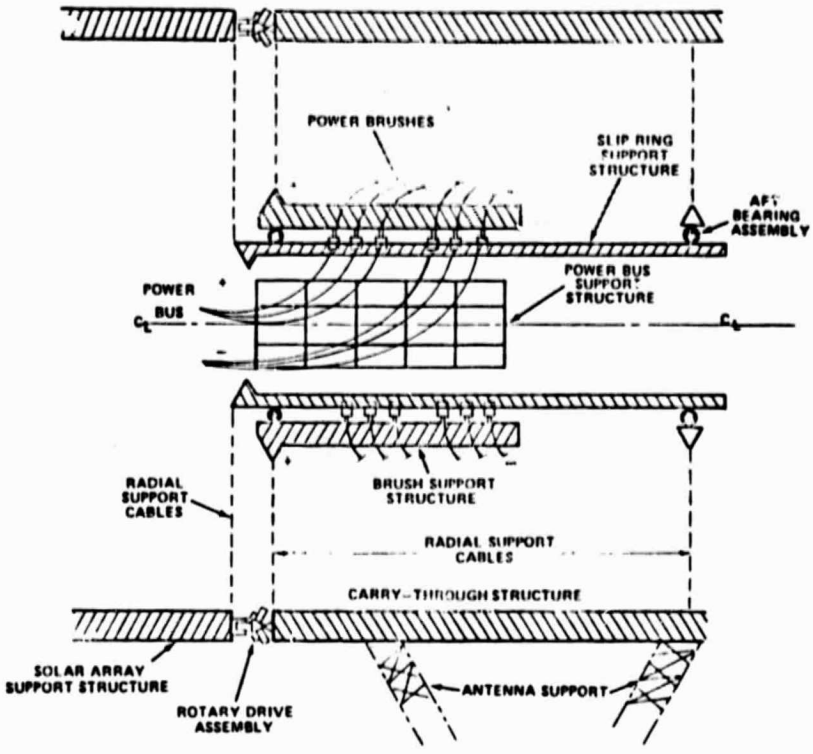

Figure 2.4-17. Carry-Through Structure and Slip Ring Functional Schematic

The rotary drive/bearing concept is designed to transmit loads across the rotating interface while maintaining a high degree of dimensional stability. The rotary drive is amounted to a drive ring support truss which, in turn, is mounted to a rotary drive primary truss that is backed up by an arrangement of kick trusses as shown in Figure 2.4-18. Kick loads react against spider beam members and at the joints typical of the one illustrated in the upper right corner of the figure. This provides a very still load path for loads transmitted through the drive ring. Two sets of radial tensioning cables are attached to the outer end of each of the two slip ring and brush assemblies. The inner set supports the rotating ring and brush assembly radially to the rotating carry-through structure. The outer set supports the stationary ring of the assembly radially to the stationary carry-through structure. These cables transmit the shear loads (or Y-Z plane loads) across the rotating joint. The slip ring and brush support assembly is approximately 150 m long and is supported on its inner end by tensioning cables which also take kick loads through the intersecting spider beams.

The SPS rotary drive assembly is shown in more detail in Figure 2.4-19. Each of the 12 rotary drive assemblies is attached to the stationary carry-through structure at one of the beam juncture assemblies. Two sets of three wheels on each assembly grip the triangular drive ring. The wheels are preloaded with sufficient gripping force to assure sufficient traction to the drive wheels under all loading conditions. One or two motorized drive wheels per drive assembly will be required. It is anticipated that the drive wheels will have a rubber-type tread; however metal-to-metal contact is not ruled out.

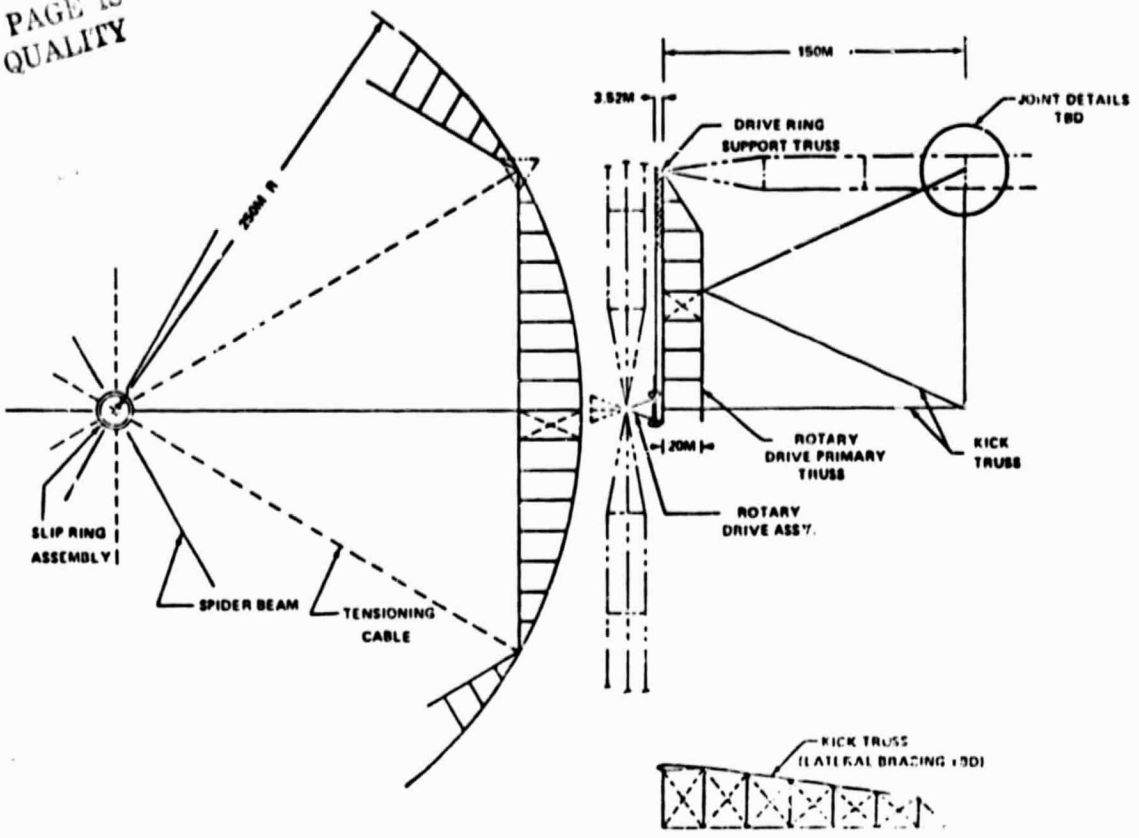

Figure 2.4-18. SPS Rotational Bearing Concept

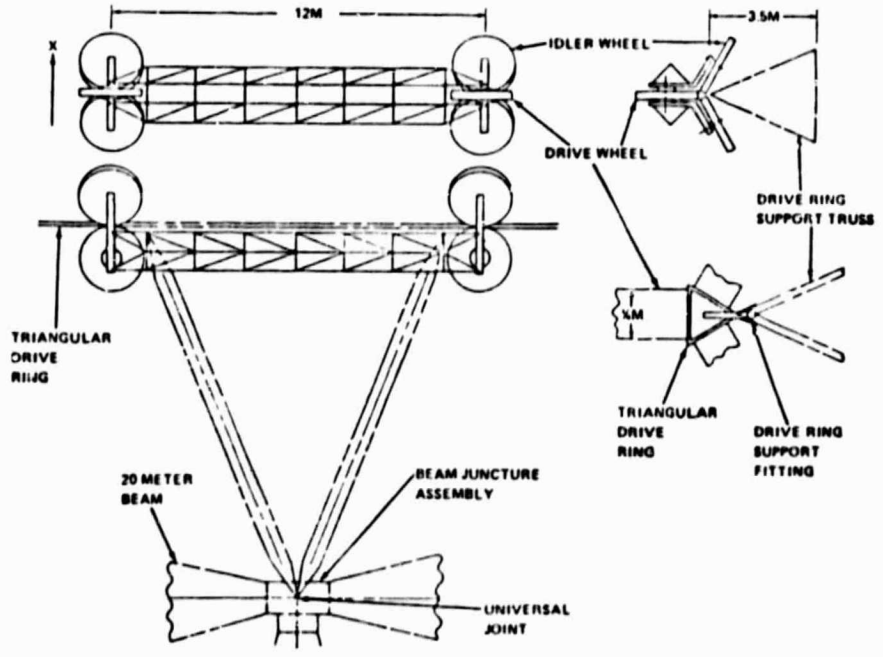

Figure 2.4-19. SPS Rotational Drive Assembly

Drive wheels should incorporate an override slip clutch to prevent lockup. The system should be designed for a fail-operational mode with the slip clutch turning on one of the drive wheels.

A modification of this rotary drive assembly would incorporate a third set of three wheels located midway between the two original sets. This additional set would be for driving purposes only, and would be so mounted as to transmit no kick loads to the drive ring. The outer two sets, having no drive requirements, would need much less preloading against the drive ring and would take kick loads only. This arrangement would lower the maximum load transmitted to the drive ring and reduce the ring weight.

The schematic shown in Figure 2.4-20 identifies primary structural elements for transferring loads across the rotary drive/bearing interface. Radial tensioning cables take the radial (shear) loads. Spider beam members transfer kick

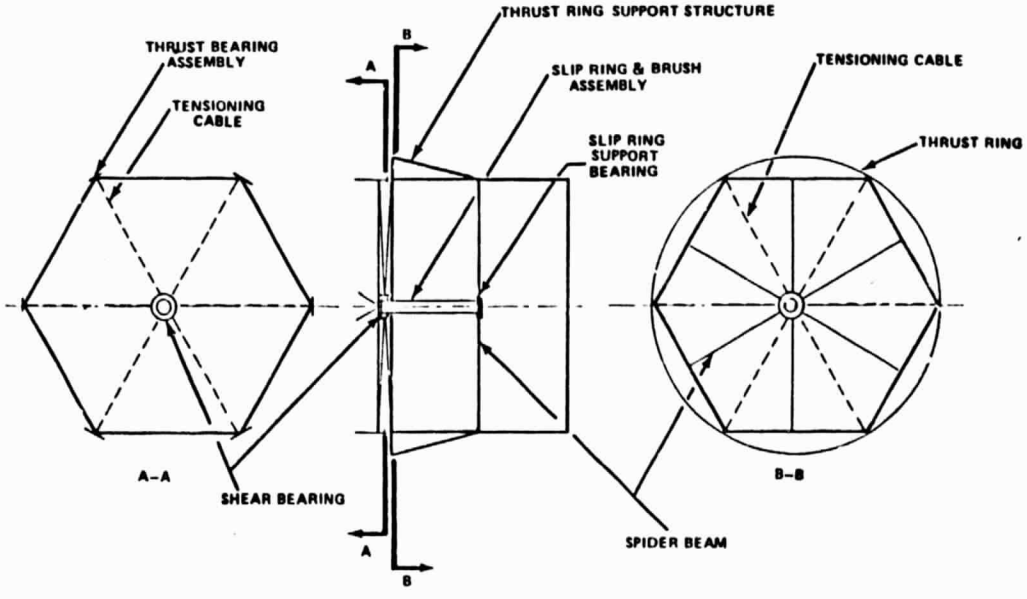

Figure 2.4-20. SPS Rotary Joint Concept to Accommodate Small Ring and Brush Assembly

loads from the thrust ring support structure to the radial tensioning cables (view B-B). Motorized rotary drive assemblies are attached to beam junctures of the nonrotating carry-through structure and rotate the drive ring of the rotating carry-through structure.

Additional details of the slip ring and brush concept are shown in Figure 2.4-21. This slip ring and brush concept has two primary functions: (1) to provide a means to electrically connect the rotating carry-through structure with the main power distribution buses, and (2) to transmit radial loads from the stationary carry-through structure to the rotating carry-through structure by means of an incorporated radial bearing concept. Radial loads are transmitted through support cables which radially support the concentric bearing rings. The concentric rings are interconnected by a bearing assembly which allows them to rotate with respect to one another. The outer rotating ring is

structured to the brush support assembly and the inner stationary ring is structured to the slip ring support structure. The power bus support structure reacts the force-field loads of the large power buses.

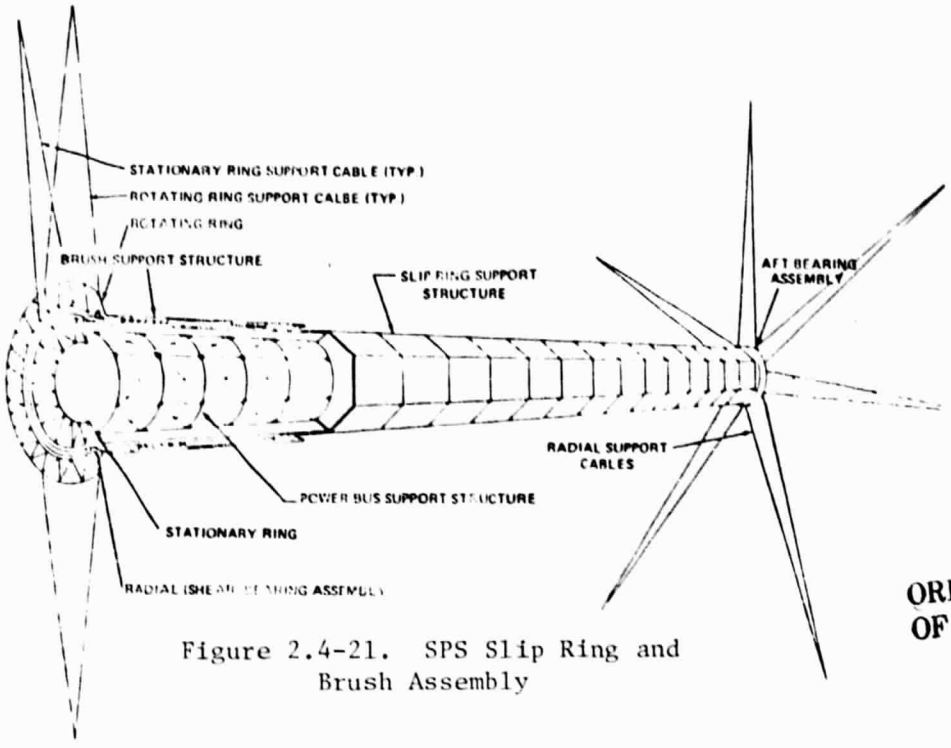

Figure 2.4-21. SPS Slip Ring and Brush Assembly

Another view of the slip ring and brush assembly is shown in Figure 2.4-22. The slip ring and brush assembly is supported by radial support cables at both

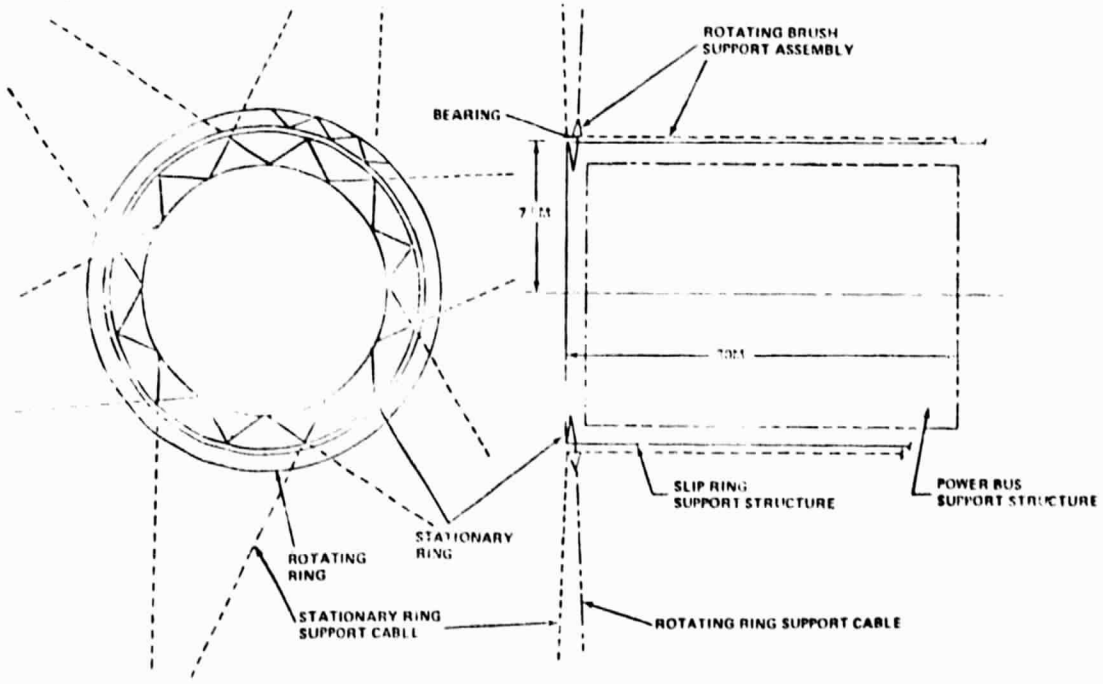

Figure 2.4-22. Slip Ring and Brush Concept

ends. However, the radial support cables are not shown on the left end. In this primary concept, the slip ring support structure extends the full length of the structure to connect with the aft bearing assembly which is radially supported by cables. An alternate embodiment in which the brush support structure would be extended to tie in with the aft support radial cables would eliminate the need for the aft bearing assembly. The power bus support structure is supported by a four-point support system designed to transmit inertial loads only.

2.4.5 JOINTS, MECHANISMS AND SECONDARY STRUCTURE

The joint concept for the point design is identical to that developed in the previous Rockwell/MSFC study.[1] Detailed joint design concepts should be developed in concert with the technology verification activity task titled "*Structural Design Criteria and Verification*" outlined in Volume VI of this report. Mechanisms and secondary structure were defined only to a depth necessary to develop preliminary mass estimates and are discussed in the end to end analysis covered in Volume V of this report.

---

[1] *Satellite Power System (SPS) Feasibility Study*, Rockwell International Contract NAS8-32161, SD 76-SP-0239-2, December 1976

2.5 ATTITUDE CONTROL AND STATIONKEEPING SUBSYSTEM (ACSS)

The ACSS functional requirements include the pointing and stabilization of the solar collector, the microwave antenna, and geosynchronous orbit stationkeeping for the overall spacecraft. The trade studies (Volume III) resulted in a relatively simple ACSS concept featuring argon ion electric thrusters for attitude control and stationkeeping, the Y-POP orientation (long axis perpendicular to the orbit plane) and partial inertia balancing of the spacecraft to minimize reaction control system (RCS) propellant consumption. An equatorial geosynchronous orbit (GEO) was selected over other alternative orbit inclinations to minimize the ground rectenna size (and cost) impact.

The ACSS dedicated subsystem elements are the RCS and the attitude reference determination system (ARDS). The principal features of these subsystem elements are summarized in Figures 2.5-1 and 2.5-2. The information management and control subsystem (IMCS) provides the interconnecting data paths for the ACSS components as well as the mini-processors for computation of the control algorithms. The mass properties and electrical power requirements of the ACSS are summarized in Tables 2.5-1 and 2.5-2. Passive figure control has been determined to be adequate for the CR = 2 collector. Active figure control is employed for the microwave antenna. This utilizes laser figure sensing and three actuation systems at alternate corners of the hexagonal antenna frame in order to maintain coplanarity of the antenna web to the three fixed attach points.

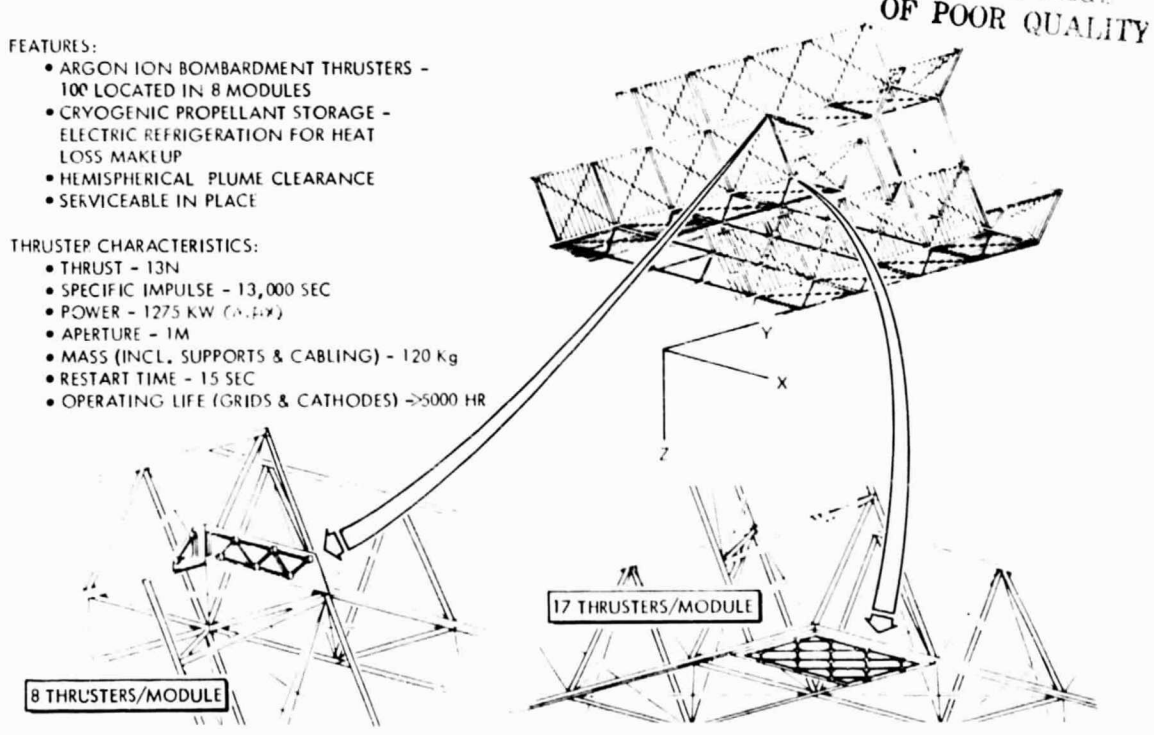

Figure 2.5-1. RCS Thruster Configuration

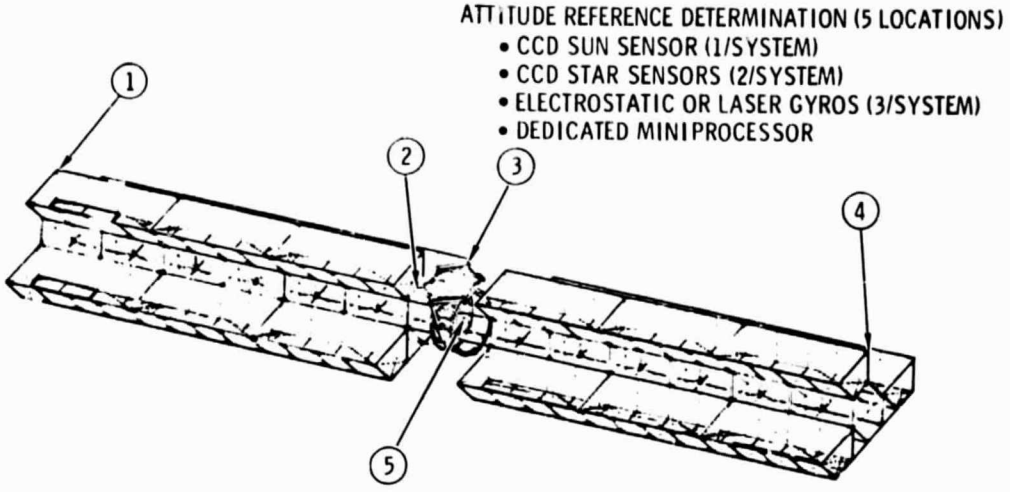

Figure 2.5-2. Attitude Reference Determination System Locations

Table 2.5-1. ACSS Mass Summary

Item	Mass ($\times 10^{+3}$ kg)
Attitude reference determination systems(5)	0.23
Thrusters - including support structure, 100 @ 120 kg/thruster	12.0
Tanks, lines, refrigeration	16.43
Power processing equipment	83.02
Argon propellant - annual requirement	93.26
Total (dry)	111.68
Total (with propellant)	204.94

Table 2.5-2. ACSS Electrical Power

Item	Power (~MW)	
	Average	Peak
Attitude reference determination system	*	*
Thrusters		
Solar/lunar perturbation (N-S)	4.36	8.72
Solar pressure perturbation (E-W)	32.27	32.27
Attitude control	0.26	0.52
Total	36.91	41.51

*Negligible

2.5.1 REACTION CONTROL SYSTEM

The RCS thruster configuration and thruster characteristics are shown in Figure 2.5-1. These thrusters are identical to those employed on the electric orbit transfer vehicle, except that they are operated in a throttled mode for ACSS application. The thruster configuration is similar on each corner of the spacecraft. The configuration minimizes contamination of reflectors and solar blankets due to ion engine sputtering. Eight thrusters (two in each corner) fire in the X-direction to provide yaw torques when N-S stationkeeping is not being performed. Twenty-four thrusters (six in each corner) fire in the Y-direction to provide N-S stationkeeping ΔV. During the N-S stationkeeping ΔV, these thrusters are throttled differentially to obtain yaw control torques. Sixty-eight thrusters (17 in each corner) fire in the -Z direction (directly toward the sun) to provide the solar pressure stationkeeping correction; this correction is performed continuously except when in the earth's shadow. Roll and pitch attitude control torques (about the X and Y axes) are obtained by differentially throttling these thrusters at each of the four corners.

The number of thrusters required to perform the various functions is summarized in Table 2.5-3. The number of thrusters which are added as spares to

Table 2.5-3. Summary of Thruster Requirements

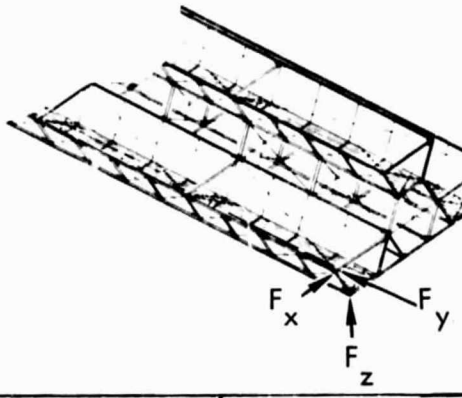

Function	Number of Thrusters Required/Corner		
	F_x	F_y	F_z
Attitude Control			
Roll (M_x) and Pitch (M_y)			1.7
Yaw (M_z)	0.2		
Stationkeeping			
Lunar/solar (N-S)		3.7	
Solar pressure (E-W)			6.0
Total required/corner*	1	4	8
Spares	1	2	9
Total/corner (with spares)	2	6	17
Total thrusters/spacecraft	100		
*Rounded up to even number			

accommodate the 5000-hour operating life of the thruster grids and random failures (assuming a 5-year MTBF) are also given. The system results in approximately 30 thrusters being operated on a time-averaged basis. The total number of thrusters including spares in the system is 100. The thruster configuration (Figure 2.5-1) has been designed with adequate spacing (10 m) to permit servicing (primarily grid replacement) of a thruster with a servicing cab while adjacent thrusters are operated.

The mass properties and power requirements of the RCS are given in Tables 2.5-1 and 2.5-2. The argon propellant is stored as a cryogen to prevent the large tank mass penalty that would result if the argon were stored as a gas. A small electric refrigeration system is located at each tank for heat loss makeup. Two argon tanks are provided at each of the eight thruster modules (total of 16 tanks) in order to prevent loss of function for single point failures. The tank outer diameters are 2.0 m for the upper (8-thruster) module and 2.6 m for the lower (17-thruster) module. The tank sizing is based on annual propellant resupply.

The annual propellant requirements for attitude control and stationkeeping are presented in Tables 2.5-4 and 2.5-5. Attitude control propellant contributions are itemized for the four sources of gravity-gradient torques depicted in Figure 2.5-3. This itemization was developed to clearly identify the more dominant factors influencing the propellant consumption in the two-body system (collector and antenna rotary joint bodies). The dominant propellant requirement arises from the collector body inertia unbalance. The mass distribution obtained from the point design cross section actually results in 66 percent inertia balancing (or 34% unbalanced). The data on Table 2.5-4 were developed using a Rockwell disturbance torque/RCS propellant consumption analysis program. It is noteworthy that the total propellant requirement is not the arithmetic sum of the four contributions taken individually. The microwave

Table 2.5-4. Attitude Control Propellant Requirements

TORQUE SOURCE	RCS PROPELLANT CONSUMPTION*	
	ANNUAL (~KG/YR)	OVER 30 YEARS (% OF S/C MASS)
1. NON-ROTATING SECTION (COLLECTOR) INERTIA UNBALANCE (34% OF MAX. POSSIBLE)	4240	0.44%
2. PRINCIPAL AXIS MISALIGNMENT (ϵ_p = 0.3°)	1360	0.14%
3. COLLECTOR MASS CENTER OFFSET FROM ROTARY JOINT ℄ (93 M)	542	0.057%
4. M.W. ANTENNA OFFSET POINTING (δ = 6°)	656	0.069%
NOMINAL CASE TOTAL (INCLUDES 1., 2., & 3. EFFECTS)	5540	0.580%
NOMINAL PLUS M.W. ANT. OFFSET (INCLUDES 1., 2., 3., & 4. EFFECTS)	5561	0.582%

* - Isp = 13,000 sec

Table 2.5-5. Stationkeeping RCS Propellant Requirements

FUNCTION	ΔV/YR. (~ M/SEC)	RCS PROPELLANT REQ'D* (KG/YR)	RCS PROPELLANT REQ'D* OVER 30 YR (% S/C MASS)
• EARTH TRIAXIALITY (E-W)	2.1	430	0.05
• SOLAR/LUNAR PERTURBATIONS (N-S)	53.3	11,000	1.25
• SOLAR PRESSURE PERTURBATION (E-W)	344.7	76,500	8.12
• DIURNAL PERTURBATIONS	NOT REQ'D	-	-
• M.W. ANTENNA RADIATION PRESSURE (E-W)	NEGLIGIBLE	-	-
• STATION CHANGE MANEUVERS (E-W) (6 @ 2 DEG./DAY = 34.2 m/sec)	1.1	235	0.03
TOTAL WITH COMPLETE SOLAR PRESSURE CORRECTION**	399.1	87,700	9.4

* - Isp = 13,000 sec, PHOTOVOLTAIC CONFIGURATION
** - ELIMINATED IF ± 3.1° LONGITUDE PERTURBATION IS ACCEPTABLE
*** - TOTALS ARE NOT ARITHMETIC SUM

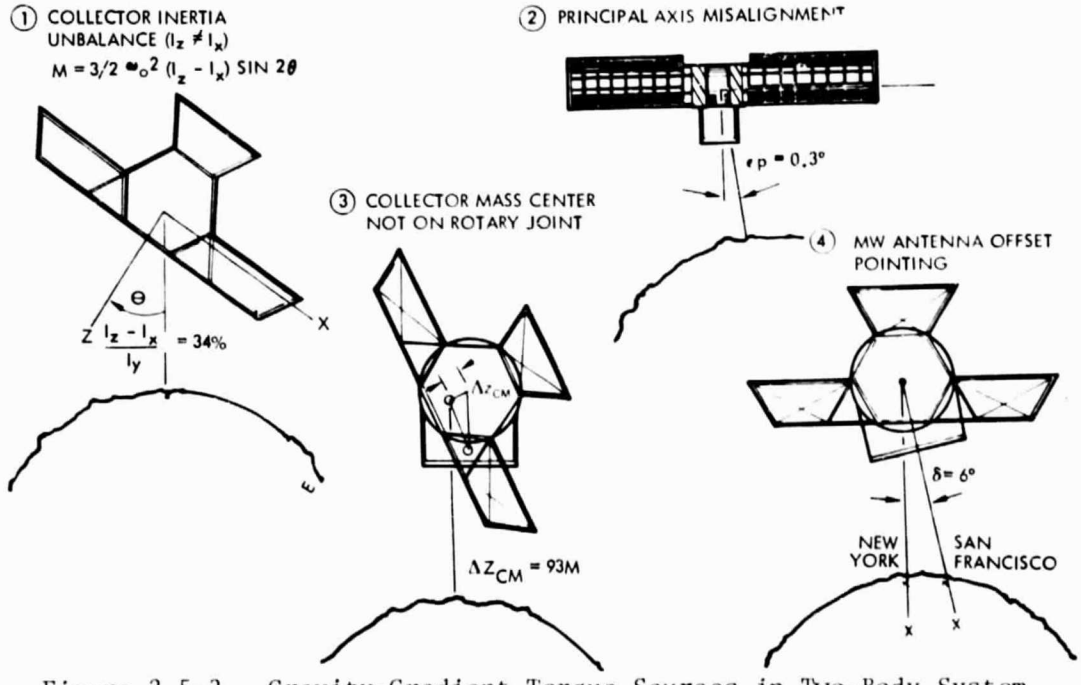

Figure 2.5-3. Gravity-Gradient Torque Sources in Two-Body System (Collector and Antenna Rotary Section Bodies)

offset pointing contribution is negligible. The nominal total is appreciably reduced from earlier trade study results due to:

- Increased specific impulse now estimated for the argon thrusters (5100 to 13,000 sec)
- Reduced principal axis misalignment (1.0° to 0.3°)
- Improved thruster moment-arm-to-inertia ratios

The dominant stationkeeping propellant requirement (Table 2.5-5) is the solar pressure correction. This correction can essentially be eliminated if a ±3.1° libration in longitude stationkeeping accuracy were acceptable. This, in turn, increases the space requirement of the SPS constellation in an already crowded geosynchronous orbit. Potential methods of reducing or eliminating this correction are discussed in greater detail in the ACSS trade study section of Volume II.

2.5.2 ATTITUDE REFERENCE DETERMINATION

There are five separate ARDS units on the spacecraft (Figure 2.5-2). The five units are located on the collector (3) and the microwave antenna (2) to permit accurate control in the presence of structural bending without the use of complex autocollimation equipment working across large expanses of structure and across the microwave antenna rotary joint. Each ARDS unit consists of strapdown sun, star, and gyro sensors operating in conjunction with a dedicated mini-processor (provided by the IMCS) to yield three-axis attitude state data with an accuracy better than 1 arc-minute. Charge-coupled device (CCD) sensors are selected for the sun and star sensors and are representative of the highly reliable, low-cost, sensor technology available in the near future. Electrostatic or laser gyros are representative of the gyro technology that may be commonplace in the SPS time frame.

2.5.3 CONTROL ALGORITHMS

On the basis of the control system/structural dynamic analysis presented in the ACSS trade study (Volume II), no major problems are anticipated in stabilizing structural bending. In order to minimize structural dynamic interaction with the control system, the following features appear to be desirable for incorporation in the control algorithms:

- Weighted averaging of the attitude data from the three ARD's located on the solar collector body is a powerful means of decoupling or stabilizing the bending.
- Bending-state observers (or estimators) are also a powerful method of accomplishing the same objective.
- The use of a "quasi linear" thrust command policy can minimize structural vibration excitation as well as permitting the attitude control system to actively damp modal bending. A means of achieving such a policy is illustrated in Figure 2.5-4.

- THROTTLING PLUS ON-OFF SWITCHING POLICY PRODUCES APPROXIMATE LINEAR TORQUES
- CAN TAKE ADVANTAGE OF BEST FEATURES OF LINEAR CONTROL

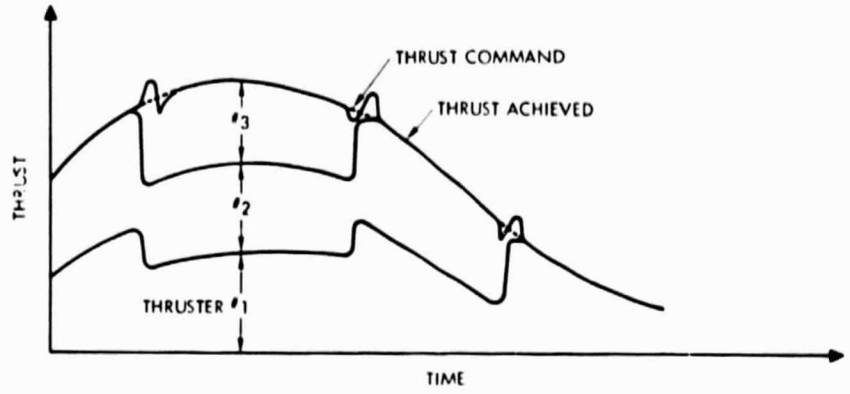

Figure 2.5-4. Quasi-Linear Thruster Control Policy

A statistical estimation scheme (Kalman filter) should be employed to provide optimal estimates of the principal axis of inertia orientation error. This parameter is observable and directly affects the RCS propellant consumption for roll and yaw control.

A relatively simple ACSS featuring argon ion electric thrusters for stationkeeping and attitude control torques has been defined. Reasonably small RCS propellant resupply requirements (and costs) are possible as a result of the Y-POP orientation (long axis perpendicular to the orbit plane) and the spacecraft design requirement for two-dimensional inertia balancing. Future analyses should address the means for reducing or eliminating the solar pressure stationkeeping correction since it dominates the RCS propellant resupply requirements (8 percent of spacecraft mass over 30 years).

2.6 MICROWAVE POWER TRANSMISSION SUBSYSTEM POINT DESIGN

The microwave power transmission subsystem (MPTS) for SPS basically consists of two very large antenna array assemblies. An antenna 1 km in diameter serves as the transmitting array. A large number of power modules with 50 kW klystrons are mounted on the array structure. The klystrons serve as dc-to-microwave power converters and the microwave energy is beamed to an antenna array located on the earth's surface.

The receiving array (rectenna) on the earth is 13 km × 10 km and consists of a large number of receiving subarray elements connected to diodes. This array is called the rectenna and converts the microwave power to dc for eventual transmission to the utility company. Table 2.6-1 provides a summary of the MPTS point design characteristics.

Table 2.6-1. Point Design Microwave Power Transmission System (MPTS) Characteristics

1. MPTS SYSTEM (GAUSSIAN BEAM)	
• FREQUENCY (GHz)	2.45
• MAXIMUM SATELLITE ARRAY POWER DENSITY (kW/cm^2)	21
• POWER DENSITY AT IONOSPHERE (mW/cm^2)	23
• MPTS EFFICIENCY (INCLUDES IONOSPHERE AND ATMOSPHERICS) (%)	59.3
• DC INPUT POWER TO MPTS FROM SOLAR ARRAY (GW)	8.61
• DC OUTPUT POWER TO UTILITY (GW)	5.0
2. SATELLITE MPTS ANTENNA ARRAY	
• SIZE (TRANSMITTING DIAMETER) (km)	1
- AREA (km^2)	102.6
• WEIGHT (kg)	10.034×10^6
• NUMBER OF MECHANICAL MODULES	777
• NUMBER OF SUBARRAYS	6,993
• NUMBER OF KLYSTRON POWER MODULES	135,864
• SATELLITE ANTENNA EFFICIENCY (%)	69.4
3. MPTS RECTENNA ARRAY	
• SIZE (km)	13×10
- TOTAL PANEL AREA (km^2)	66.97
- GROUND AREA (km^2)	94.74
• NUMBER OF BAYS	698
• NUMBER OF PANELS (BOW TIE)	395,296
• NUMBER OF DIODES	204,833,800
• RECTENNA EFFICIENCY (%)	88
• DC OUTPUT PER BAY (kV dc)	50
• DC OUTPUT TO UTILITY INTERFACE (kV dc)	500

2.6.1 MICROWAVE ANTENNA DESIGN CONFIGURATION

The design data and analytical results for the 1 km diameter microwave antenna for the SPS is presented below.

Subarray Description

The 50 kW klystrons, selected as power converters, are mounted in resonant cavity radiators (RCR) with their collectors protruding from the array

base as shown in Figures 2.6-1 and 2.6-2. This assembly is a power module. Its area varies so as to set the radiated power densities required over the array surface. There are ten density steps and corresponding module designs. These modules are assembled to form ten subarray types.

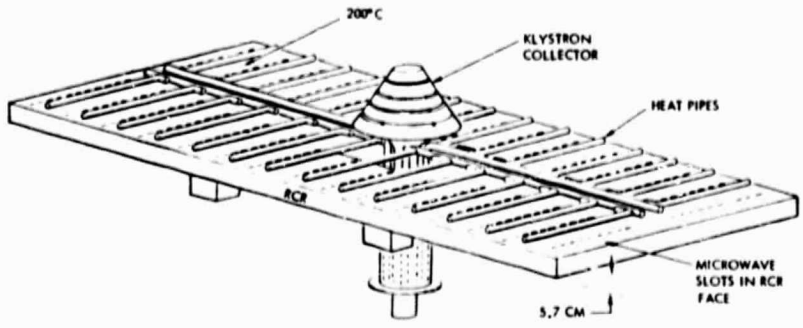

Figure 2.6-1. Radiating Face of Power Module

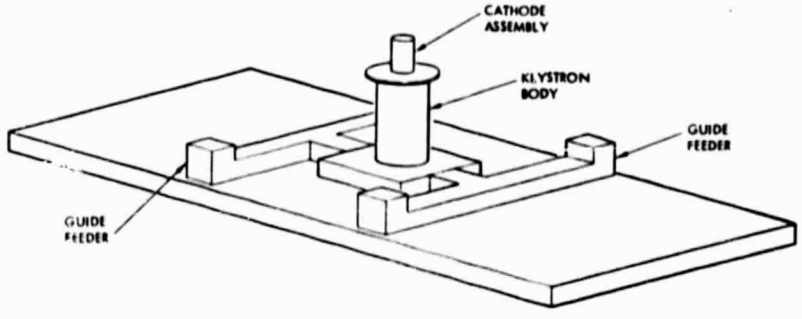

Figure 2.6-2. Back of Power Module

When the klystrons are removed from their wells, the subarray power modules can be stacked in a compact form for transport. The ten point-design subarray configurations and the dimensions of the stacked packages are shown in Figures 2.6-3, 2.6-4 and 2.6-5. The parameters associated with each subarray type are also given. The subarray coding is keyed to the coding of Figure 2.6-6 showing the total array. The planform of the point-design rectenna for 34° N latitude is given in Figure 2.6-7.

Subarray Configurations

The SPS spacecraft antenna is composed of subarrays. A subarray is defined as a portion of the total antenna array which has the same phase over its radiating surface. This definition will be modified in cases where the subarray beam is steered to point in the direction of the pilot beam as was proposed in the Eclectic-Phase-Control System. In that case, the center of the subarray has a phase, set by a single retroelectronics assembly. In addition, there is a phase variation across the array face used to steer the subarray antenna pattern.

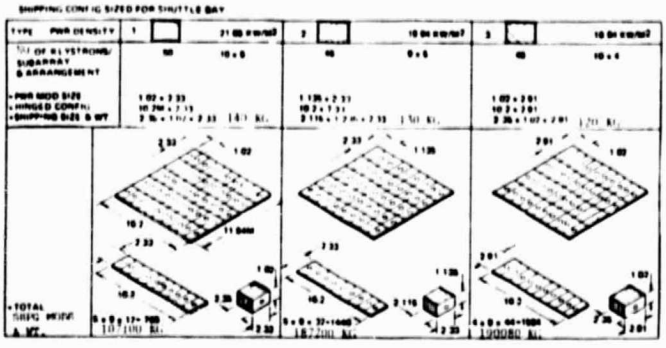

Figure 2.6-3. Standard Subarray Size - Block 1

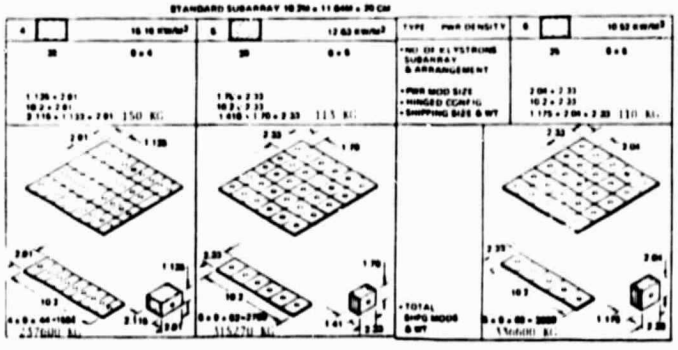

Figure 2.6-4. Standard Subarray Size - Block 2

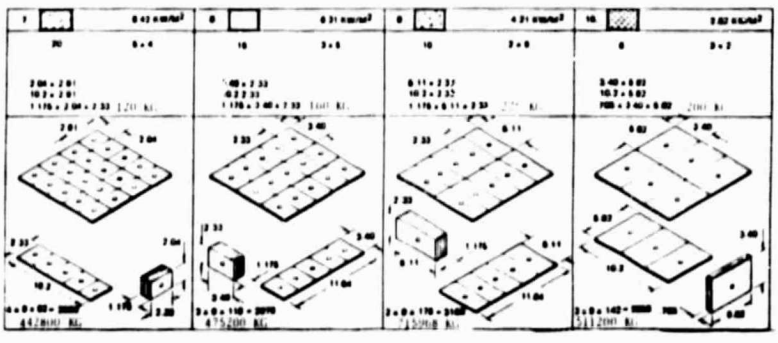

Figure 2.6-5. Standard Subarray Size - Block 3

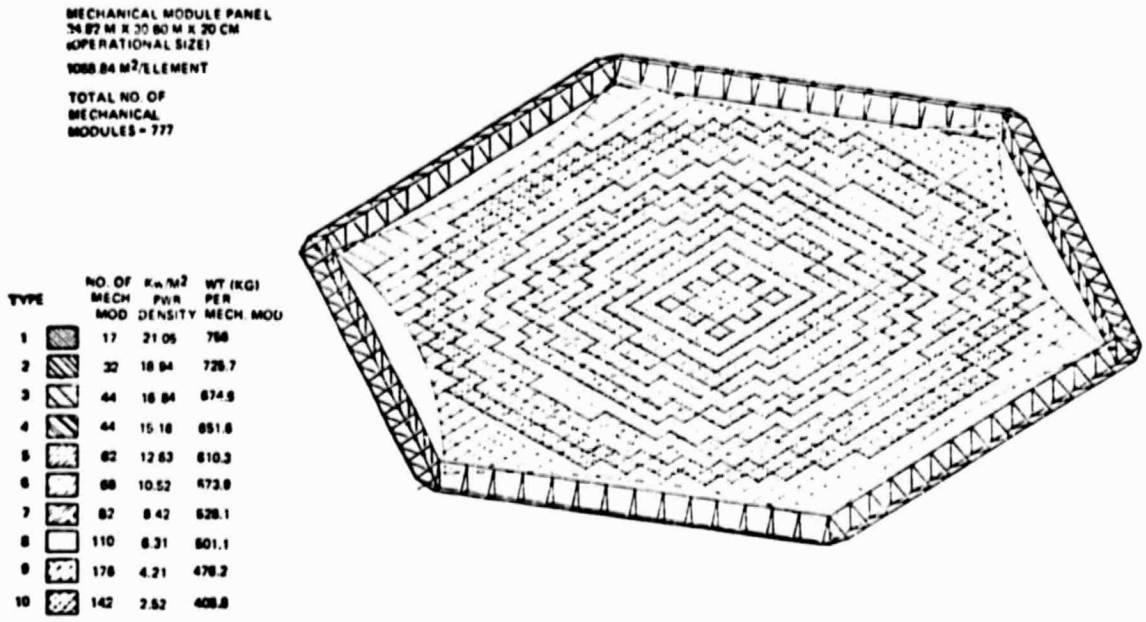

Figure 2.6-6. Gaussian Beam Microwave Antenna

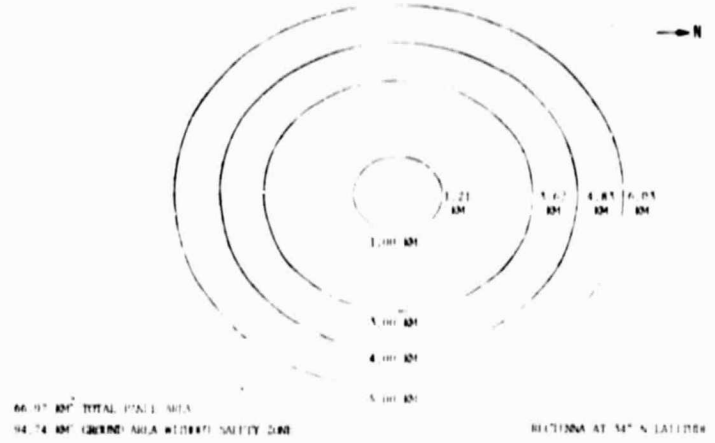

ORIGINAL PAGE IS
OF POOR QUALITY

Figure 2.6-7. Rectenna Array Layout
5 GW Gaussian Beam

The subarray size selected is 11.64×10.2 m. Sets of nine subarrays are then supported by a secondary structure to form a 34.92×30.6 m mechanical module. The module is supported by connections to the catenary tapes of the compression-frame/tension-web which forms the primary array structure.

In order to keep costs down and make fabrication easy it is desirable that the subarray radiators be made of metal. However, neither the total mechanical module nor the subarrays can be a single metal structure due to thermal effects. As an example, let the metal be aluminum with expansion coefficient of 2.5×10^{-5}/°C with an operating temperature range of 100°C.

Then the change in dimension for the mechanical module is 7.5 cm and for a subarray is 2.5 cm. The resulting deviation from uniform spacing of the radiating elements in the subarray surfaces is too great.

The subarrays are made up of power modules, each fed by a single microwave amplifier. These modules vary from about 1.0 m to 6.0 m on a side. The corresponding thermal dimension changes are ±0.13 cm to ±0.76 cm or ±0.010 λ to 0.062 λ around a design configuration. This is felt to be an upper limit on movement of the radiator elements. Therefore, the secondary support structure will be graphite-epon. Since the expansion coefficient of graphite-epon is an order of magnitude less than metals, only very small gaps between the mechanical modules are needed to accommodate thermal expansion. The gap size required is further reduced by the fact that the catenary tapes are Kevlar 49. This material has an expansion coefficient very similar to graphite-epon. Therefore, the center-to-center spacing of the mechanical modules hung from the catenaries varies with temperature so as to tend to hold the gap size constant.

The expansion coefficient of the plastic stripline panels proposed as the power modules when transistors are used as power converters will have expansion coefficients considerably higher than metals. Such panels therefore pose a dimension control problem which has not been solved. As mentioned earlier the primary radiating unit is the power module. A set of these modules are assembled to form a subarray. Each module has its own power amplifier or set of power amplifiers in the transistor case. However, all modules in a subarray have amplifiers which are driven from one retroelectronic circuit.

The power level of all module amplifiers is the same. The size of the module radiating surface is varied to vary the power density weighting over the total array area. For instance, if 50-kW klystrons are used and the weighting is Gaussian, the number of modules per 10×10-m subarray varies from 50 at the array center to 6 at the array edge. This is for the case of a 5-GW SPS system with a 1-km-diameter array. The module area then varies from 2.38 m^2 to 19.79 m^2. The layout of the ten subarray designs needed for a 10-step approximation to the Gaussian taper is shown in the section detailing the 5-GW microwave power transmission system (MPTS) point design.

Four different radiating structures which could be used in the power module design will be discussed in the remainder of this section. They differ radically in power level, thermal properties and fabrication techniques. Table 2.6-2 lists them along with some of their properties.

Aperture Illumination. The index of antenna performance of most interest is beam efficiency, η_b, which is the fraction of the total radiated power within the main beam. In the MPTS case, the rectenna fills the main beam. The optimum aperture illumination distribution is one which places the most power within this angle subtended by the rectenna. In the original Raytheon design it was noted that a truncated Gaussian amplitude distribution with uniform phase distribution provides a satisfactory approximation to an ideal distribution function. This truncated distribution is of the form

Table 2.6-2. Power Module Microwave Radiators

RADIATOR	VARIABLE AREA	VARIABLE POWER	SUBARRAY POINTING RANGE	THERMAL PROBLEMS
WAVEGUIDE	YES	NO	MODERATE, θ_1 LARGE, θ_2	MODERATE
RESONANT CAVITY RADIATOR	YES	NO	MODERATE, θ_1 & θ_2	MODERATE
DIPOLE ARRAY	NO	YES	LARGE, θ_1 & θ_2	EASY
CONICAL REFLECTOR	NO	YES	LOW, θ_1 & θ_2	HARD

$$f(\rho) = e^{-0.115\ (dB)\left(\frac{r}{r_o}\right)^2}$$

here r_o equals array radius, r = radial coordinate, and (dB) is the amount of taper from center to edge of the array in dB. Plots of the resulting antenna pattern and beam efficiency are shown in Figure 2.6-8 through 2.6-11. In these figures, the normalized angular parameter used is $\sqrt{A_T A_R}/\lambda D$, where A_T is transmitting array area, D is distance to measurement plane, λ is wavelength and A_R is the area of a disc whose radius subtends the pattern angle.

The taper was set by a permissible first sidelobe level of 10 dB. It may be seen from Figure 2.6-12 that the corresponding first sidelobe level may be about -23 dB. Figure 2.6-13 then shows equal beam efficiency contours plotted on a taper/beam-radius plane. For a 95% efficiency the minimum rectenna radius occurs for tapers of 10-15 dB. The least taper, 10 dB, is selected to minimize the power density at the array center needed to obtain the required total power. The corresponding rectenna radius is 5 km.

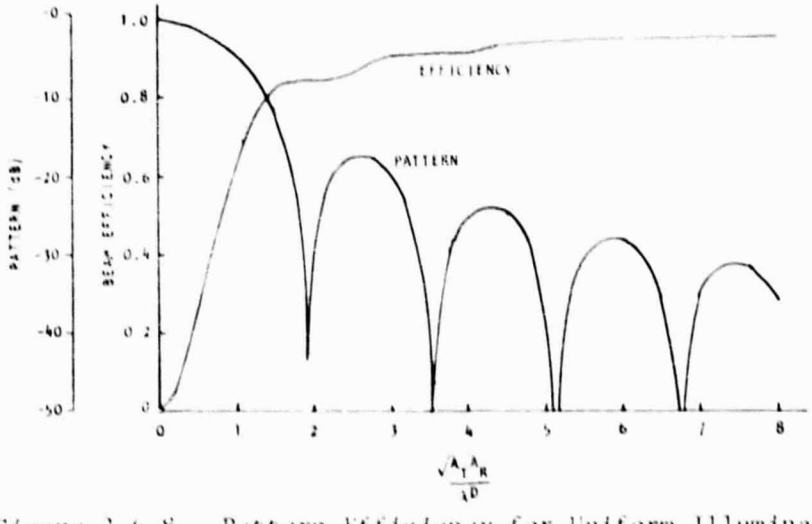

Figure 2.6-8. Pattern Efficiency for Uniform Illumination (0 dB Taper)

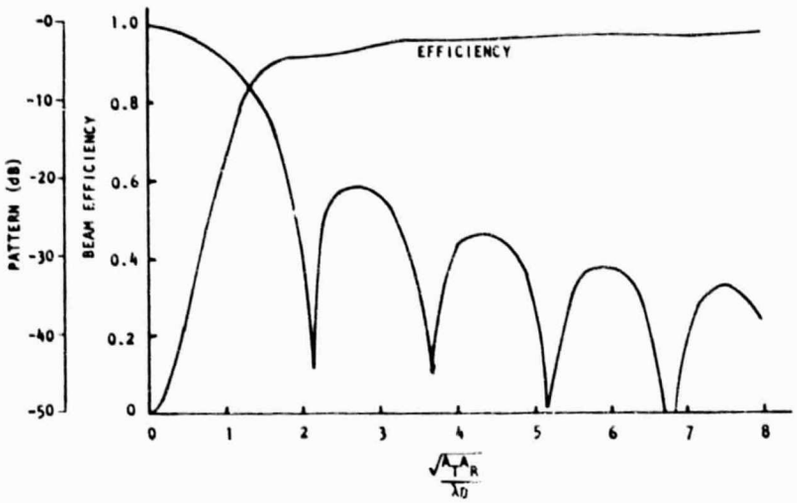

Figure 2.6-9.
Pattern Efficiency
for Uniform Illumination
(5 dB Taper)

Figure 2.6-10
Pattern Efficiency
for Uniform Illumination
(10 dB Taper)

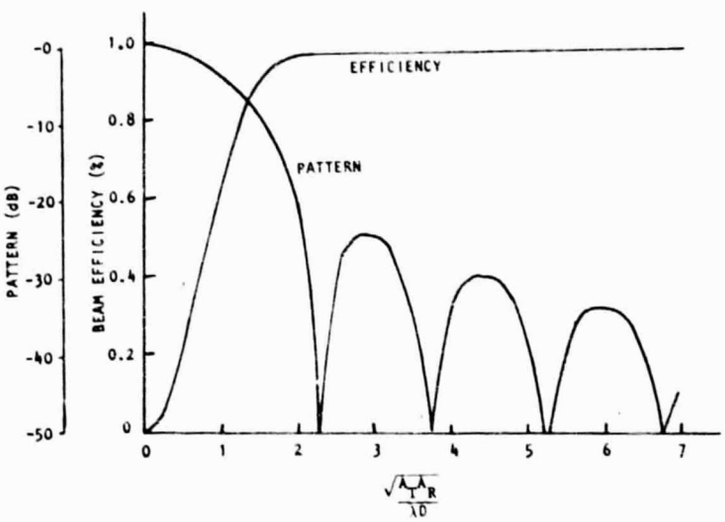

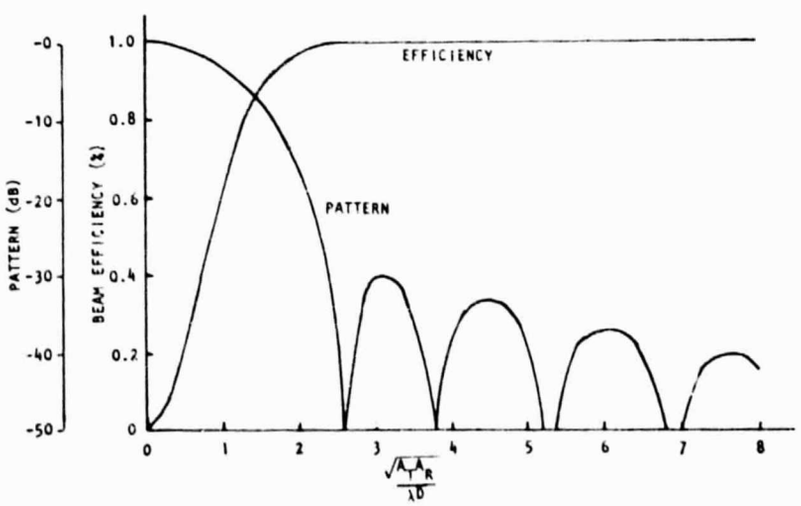

Figure 2.6-11.
Pattern Efficiency
for Uniform Illumination
(15 dB Taper)

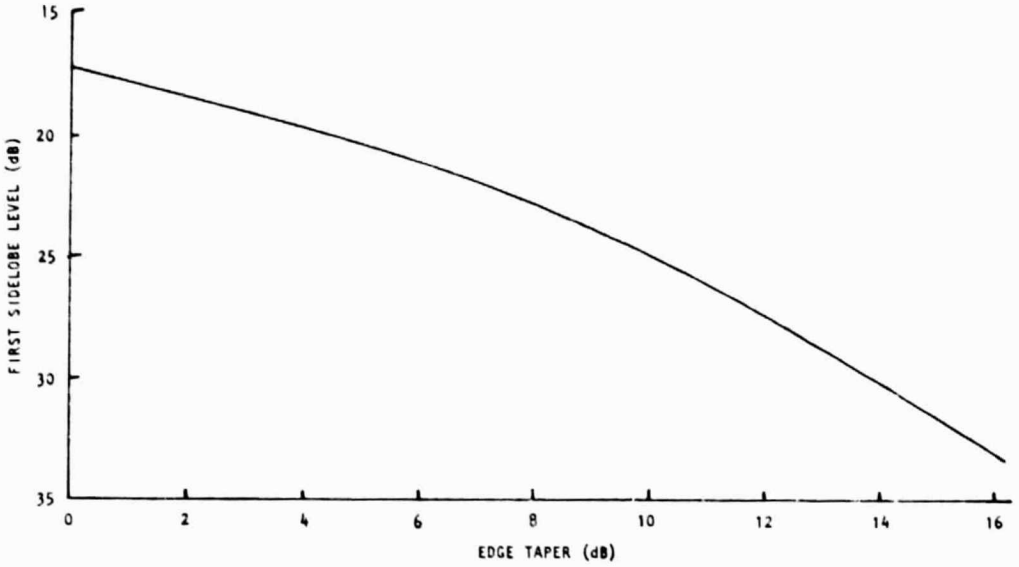

Figure 2.6-12. First Sidelobe Level Versus Truncated Gaussian Taper

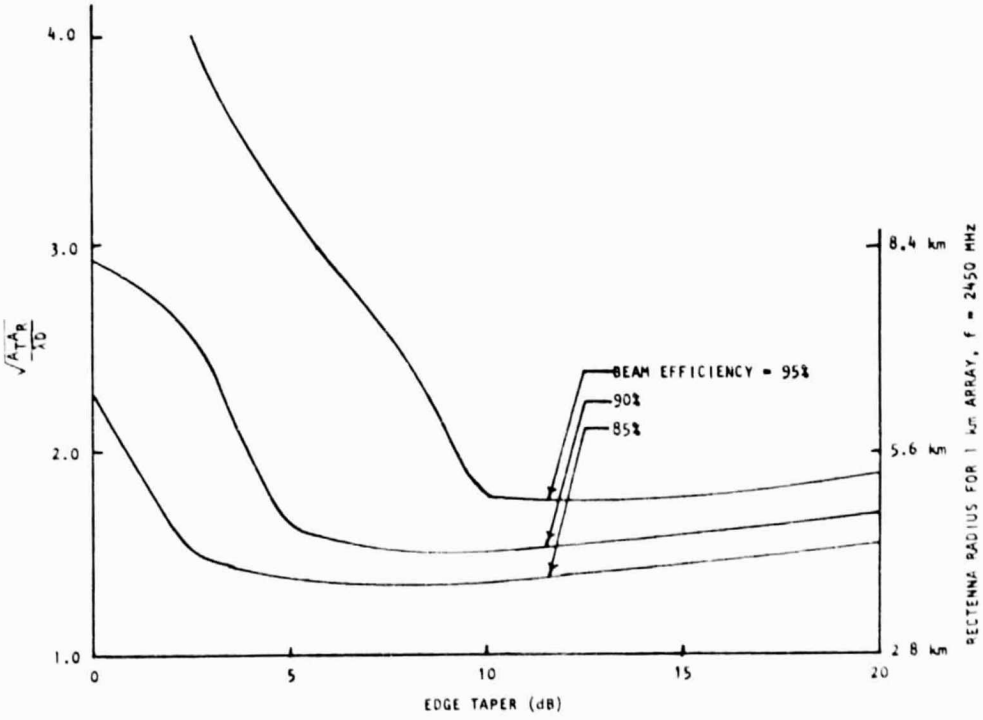

Figure 2.6-13. Antenna Sizes for Truncated Gaussian Tapers

In actuality, 95% beam efficiency will not be obtained due to phase errors over the array surface, quantization of the taper, and outage of power modules.

A ten-step quantization of the 10 dB taper was chose in agreement with the selection made in previous studies. A five-step taper would have given 1% less beam efficiency. Combining the effects of phase error, quantization and outage, Figure 2.6-14 shows the resulting beam efficiency versus radius. The results shown in Figure 2.6-14 represents the baseline configuration with a rectenna collection efficiency of 88% for a 5 km radius.

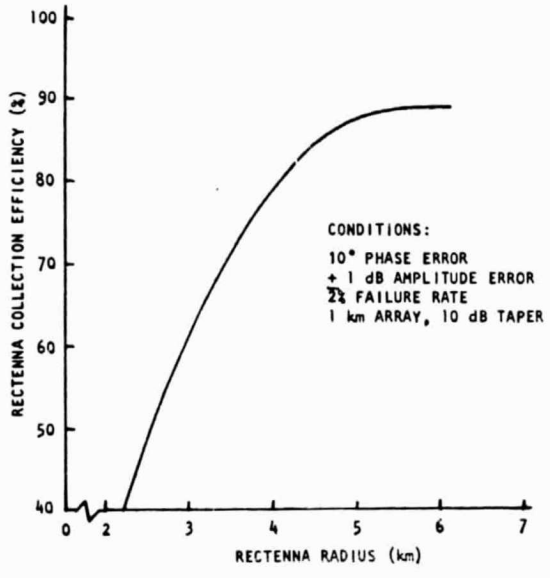

Figure 2.6-14. Rectenna Collection Efficiency for Baseline Configuration

Waveguide Radiators. The most obvious radiator structure is a waveguide. This radiator element was selected by Raytheon in the original MPTS concept. The slots radiating from the guide can be either staggered H-wall or inclined E-wall slots as shown in Figure 2.6-15. The staggered H-wall slot configuration is formed by placing sections of guide side-by-side in contact. It is therefore better structurally than the inclined E-wall configuration which would require auxiliary structure to support the guide.

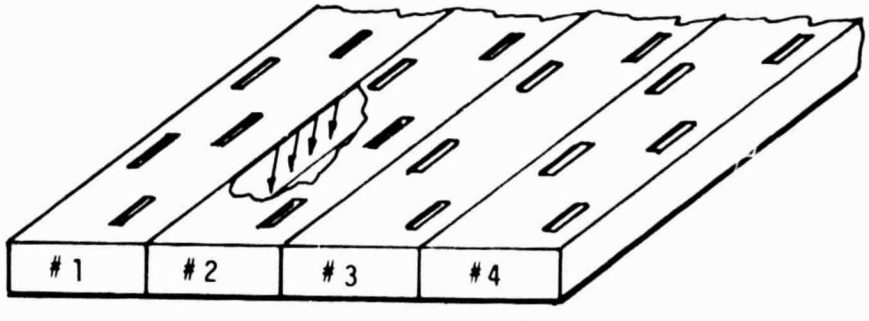

Figure 2.6-15. Waveguide Radiator Configuration

In the Raytheon case, one fifth the power fed into a radiator (1 kW) had to be extracted from the other end of the radiator to feed the next amplitron. This means that the guide must be used as traveling wave radiators. Now a traveling wave radiator cannot emit a beam normal to the radiator face without use of directional couplers. When the beam is at broadside (normal), the residual reflectors from the slots add in phase. This causes a high input VSWR which degrades match between source and load.

Coupling from a feeder guide into radiating guide stubs as shown in Figure 2.6-16 avoids this by dumping the radiator reflections in loads. However, this is too complicated a structure for this application.

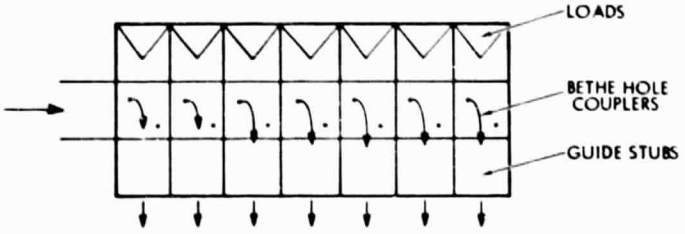

Figure 2.6-16. Line Source Using Directional Couplers

Therefore the array normal must point at the equator. For rectennas in northern latitudes, the beam will tilt away from the normal by 5-10°. If the guide runs are normal to the equatorial plane, the required beam tilt off broadside is obtained.

At the array center, the point-design power density is 21 kW/m^2. Therefore a 5 kW amplitron must feed an area of 1/4 m^2. Let the power module be one guide wide. This is 12 cm ≈ 1/8 m. The guide must then be 2 m long. The subarray then consists of 400 power modules. Five modules are stacked end-to-end to obtain the required 10 m subarray size in one direction. Eight such sets of 5 modules are stacked in the orthogonal direction to obtain the other 10 m subarray dimension. Ten power density levels are then obtained by increasing the module length from 2 m to 10 m in 0.9 m steps.

In the klystron case, the radiating guide sections can be standing-wave arrays. For a 50 kW klystron, the power module must have ten times the area of the amplitron power module (2.5 m^2), so it is ten guides wide or 10/8 m wide. Eight such modules side-by-side add up one 10 m subarray dimension. Again lengthening the module size in the direction of the guide runs from 2 m to 10 m in 10 steps provides the 10-step power density variation required. The ten guides are fed by a transverse standing wave feeder attached to the back of the guide as shown in Figure 2.6-17.

Resonant Cavity Radiators (RCR). The resonant cavity radiator is a modification of the basic slotted-guide radiator assembly. It is based on the observation that the traverse feeder forces loops in a standing wave field to appear at positions corresponding to the guide centers and nulls at positions corresponding to the guide walls. Therefore, if the guide walls are removed, we will still have the same field at the radiating slots as before and the radiated beam will be unperturbed.

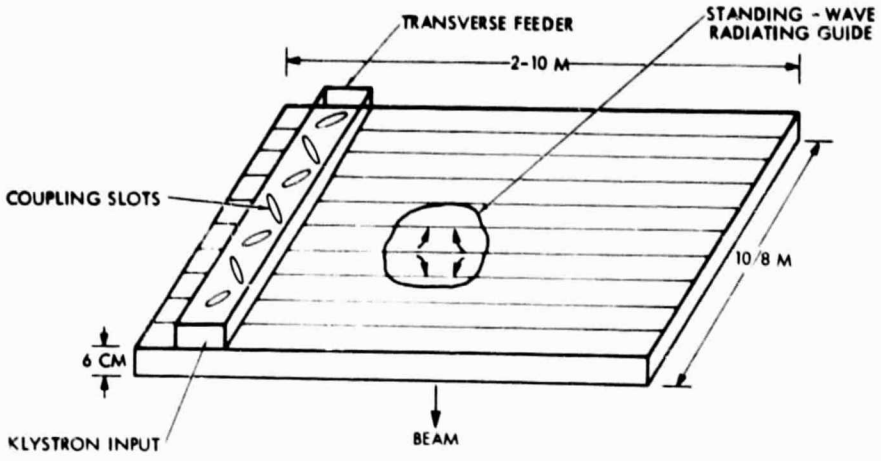

Figure 2.6-17. Klystron Power Module Guide Assembly

However, we have gained several advantages. First, the radiator is now a shallow box with slots formed in one face. This is an easier structure to fabricate than the guide assembly. As a matter of fact, if we wish, we can make the box up out of two nesting trays as shown in Figure 2.6-18. If tray lips are a quarter-wave high, they form a choke joint which produces a short at crack formed by the lips making the RCR electrically continuous.

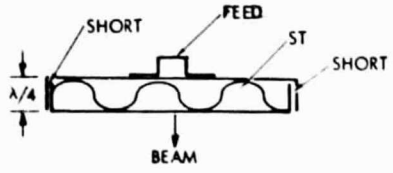

Figure 2.6-18. RCR Formed From Nested Trays

Next we have eliminated the weight of the guide walls. This is attractive since we are considering weight which must be transported to GEO.

Finally, we have decreased ohmic losses. The currents on the guide walls flow in opposite directions on the two sides of a partition. A portion of the topwalls of two adjacent guides are cutaway in Figure 2.6-17 to show these currents. When the walls are removed these currents cancel and the ohmic loss associated with these currents is eliminated.

The RCR is capable of supporting other modes than the T_{mo} mode. Such modes will radiate in off-boresight directions, causing null filling and higher sidelobes. However, Rockwell has developed special feed techniques which reduce higher order modes. To prove out these techniques a $TE_{7,0}$ RCR shown in Figure 2.6-19 was fabricated and tests were conducted. The RCR slots were cut to give uniform excitation, so its first sidelobes should be -13 dB. Figure 2.6-20 and 2.6-21 giving the measured pattern shows that the sidelobe level is about as predicted. No evidence of radiation by other modes in the directions where such radiation would be expected is found. Losses were of the order of 50%, rather than 3%. However, the RCR was

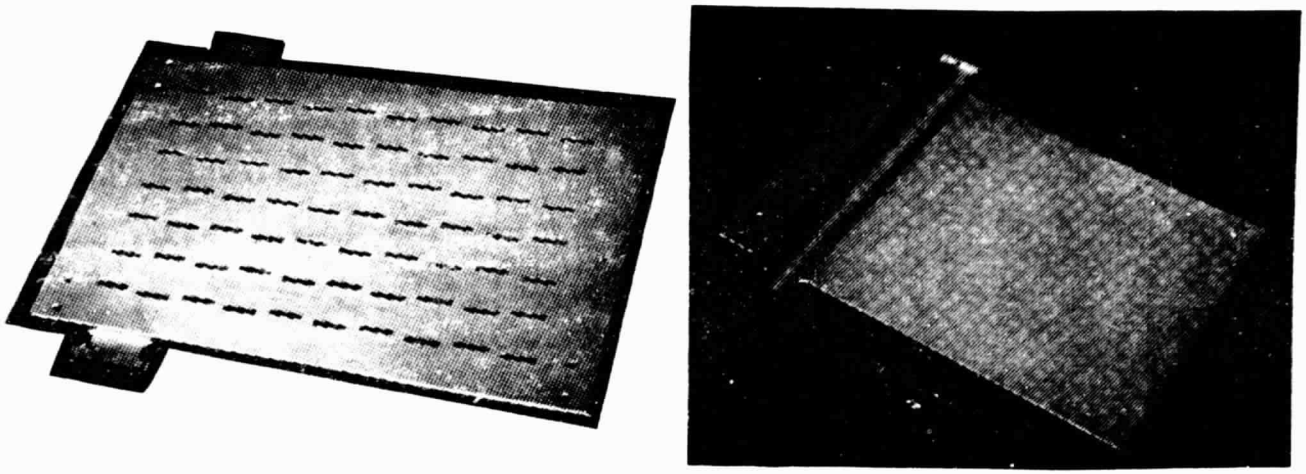

Figure 2.6-19. Experimental RCR

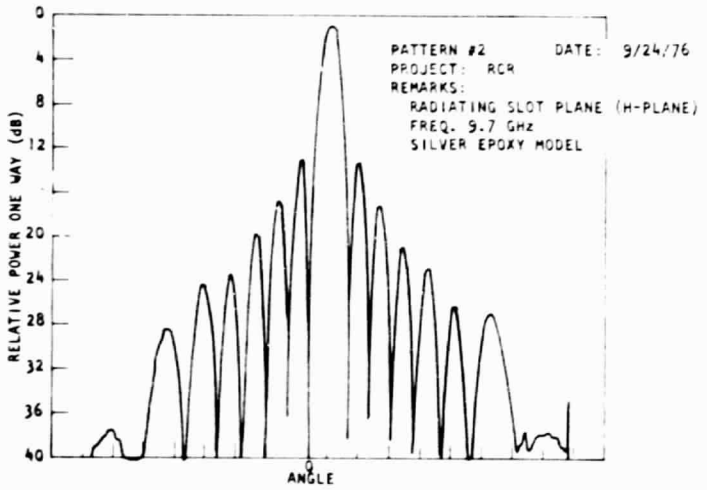

Figure 2.6-20. Radiating Slot Plane (H-Plane)

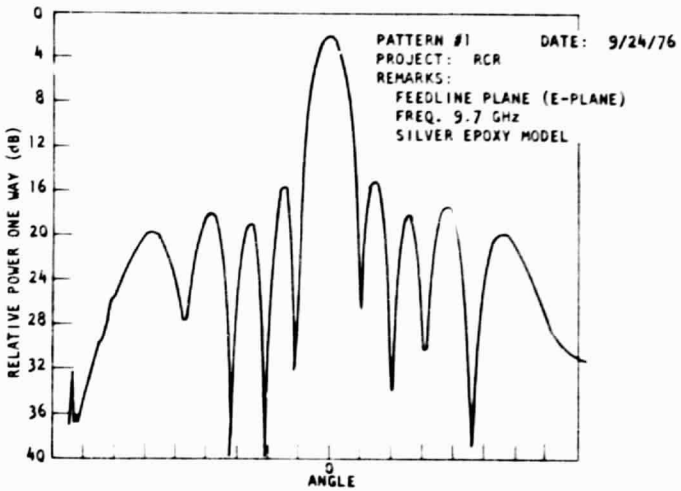

Figure 2.6-21. Feedline Plane (E-Plane)

assembled using conductive cement, which is very lossy. Efficiency verification tests are needed where the RCR is assembled by dip brazing or by use of choke joints in order to eliminate these losses. Verification of the theoretical loss calculations can then be carried out.

Reflector Array Configuration for SPS

An array of large reflector antennas has not heretofore been considered seriously for the Microwave Power Transmission System (MPTS) that forms the critical link in the Satellite Power System (SPS). The reason for this is due to the existence of grating lobes which can carry off power in unwanted directions. These lobes occur whenever radiating elements are arrayed with spacings that exceed one wavelength. In the case of an array of in-phase elements with spacing s, the main lobe occurs at broadside, i.e., at $\theta = 0$, where θ is measured from the array normal. Grating lobes will be formed at other angles for which $\sin\theta = m\lambda/s$ is satisfied, where m is any integer. When s/λ is large, it is clear that there will be many integer values of m (both positive and negative) for which the equation is satisfied. This problem does not arise for the slotted waveguide array that is usually considered for the MPTS because the spacing between slots is less than λ and the only permissible value of m is zero, corresponding to the main lobe.

An array of reflectors has certain potential advantages for use in the MPTS that are sufficient to warrant an investigation of the problem of grating lobe suppression. The two chief advantages are (i), considerably reduced weight and cost as compared t the slotted waveguide array, and (ii) the compatibility of a single reflector with a high gain klystron generator having high power output in the order of hundreds of kilowatts. The objective, then, is to suppress grating lobes in an array of reflectors to relatively low levels, and to confine them to a very few discrete directons in space.

The use of a hexagonal array of reflector elements (Figure 2.6-22) has been investigated as one means of controlling grating lobes because such arraying results in denser packing and therefore effectively closer spacing than can be had from a square array. This can be expected to result in a wider separation between adjacent grating lobes. The basic approach is thus to combine hexagonal arraying with the use of a reflector element that creates a sharp, narrow radiation pattern that will ensure that the grating lobes fall in locations where the reflector radiation is at a low level. Because the resultant radiation pattern, $F(\theta,\phi)$, is the product of the array factor, $A(\theta,\phi)$, and the element factor, $E(\theta,\phi)$, it is clear that if it were possible to cause the grating lobes due to $A(\theta,\phi)$ to fall in the nulls of the reflector pattern, $E(\theta,\phi)$, then the grating lobes would be entirely suppressed. This is not possible when reflectors with circular apertures are used, but a reasonable level of suppression can be attained.

To obtain a narrow element pattern from a reflector antenna requires that the aperture illumination created by the feed be nearly uniform, or even inversely tapered. The usual case, in which the illumination tapers from the center to a low level at the reflector rim, is inadmissible because it causes broadening of the pattern and wide separation between nulls. The approach therefore has included an investigation of an unfamiliar technique that is

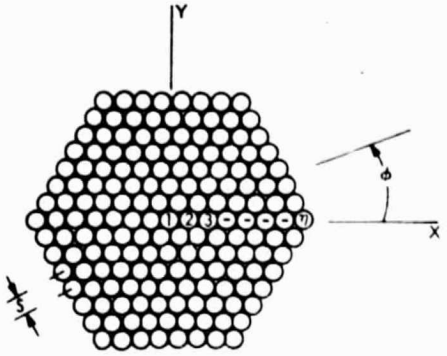

Figure 2.6-22. Geometry of a Hexagonal Array of Reflectors (Z Axis Normal to Array Plane)

known to create narrow radiation patterns in reflector antennas. It is based upon the use of a conical main reflector with a line source feed; it has been shown theoretically that an inverse illumination taper is possible by this means, with a concomitantly narrow pattern.

Analysis has shown that it is possible to design a waveguide-fed conical reflector with either a uniform or a highly inverse-tapered aperture distribution, the design of intermediate cases presents no problem. It is therefore concluded that a design can be found which will result in grating lobe suppression considerably better than the above two limiting cases. Suppression of all grating lobes to at least -28 to -30 dB levels appears possible.

In Figure 2.6-23, the line source is a rectangular waveguide with closely spaced (0.2 to 0.4 λ) transverse slots in each broadwall. It acts as an array of magnetic dipoles lying on the optical axis of the conical reflector and constitutes a nearly ideal linearly polarized feed. The guide must be fed at the end remote from the cone apex. One way to do this is shown in Figure 2.6-23 where the line source is flanked by a pair of feeder guides which carry power from one or a pair of high power klystrons located behind the reflector. The plot of attenuation constant in Figure 2.6-24 is based on an aperture diameter $D = 50\ \lambda$ and half-cone angle of 67.5° which results in a line source of length $L = 35\ \lambda$.

If used in the MPTS at a wavelength of 12 cm, the above reflector would have an aperture 6 meters in diameter; 169 of these dishes arrayed as in Figure 2.6-22 would form a single module in the SPS array, while a total of 169 modules, again arrayed hexagonally in n = 8 rings, would constitute the complete array. By tapering the power in the 8 modular rings in stepwise fashion, a good approximation to a Gaussian distribution can be achieved over the whole array. The total number of reflectors would be somewhat less than 169^2 due to overlap along the modular edges; say 25,000. To transmit a total power equal to 6 gigawatts then gives 240 kilowatts average power per reflector. The central module in the array might thus use two 500 kW klystrons per reflector while the outer modules, due to the Gaussian taper, might need only a single 100 kW klystron per reflector. An obvious problem area which has been ignored here is that of disposing of the waste heat from the high

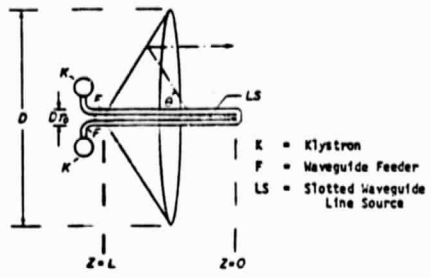

Figure 2.6-23. Conical Reflector with Line Feed

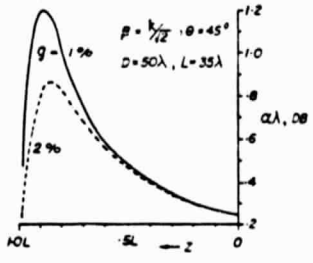

Figure 2.6-24. Attenuation Constant in Line Feed
(Uniform Aperture Distribution)

power klystrons. Conversely, the conical reflector has the very attractive potential for easy stowage and deployment because it is a developable surface. It may also lend itself to more precise figure control than would a conventional paraboloid.

It cannot be claimed that this approach is the ultimate answer to the SPS transmitting antenna problem. Nevertheless, it has been shown that grating lobes need not constitute an insurmountable objection to the use of a large array of reflectors as an alternative to the slotted waveguide array. The use of conical reflectors has some unique and attractive features that might lead to significant savings in weight and cost. For these reasons it may be that further study, with emphasis on the peculiar requirements of the SPS, is warranted.

Klystron Amplifiers

Klystrons have been proposed by Varian for the MPTS converters[1,2,3]. A total efficiency of 86% is predicted.[3] This is based on the performance of the VKS-7773, 50 kW, 2.45 GHz klystron previously built which obtained an efficiency of 74.4% without a depressed collector. Addition of a depressed collector with 55% beam power recovery efficiency plus other minor changes

[1]High Efficiency Klystron CW Amplifier for Space Applications, A. D. LaRue, February 1976, Company Report
[2]Personal Communication, A. LaRue to C. Tomita (11-24-76)
[3]A. LaRue, High Efficiency Klystron CW Amplifier for Space Power Applications, 1976 IEDM Tech. Digest

leads to an 80% efficiency. Taking into account cathode heater and solenoid power, a final efficiency of 85% is used in the point design calculations.

The major drawback to the use of klystrons is the large number of electrode voltages which are required. The depressed collector design selected by LaRue requires five unregulated voltages. In addition, two regulated power supplies are required to supply body current and establish the potential of the mod anode, which controls beam current. The present point design generates all these voltages from a single 40 kV bus by means of switching converters. It may be that the enormous number of switching regulators required by that design could be reduced by breaking the solar panels up into sections, each of which supplies a tube voltage. The present slip rings would have to be split up into several smaller slip rings in order to transfer the voltages from the solar panel to the array.

Power distribution losses would increase due to the lower voltages present on all but one of the multiple busses. However, this is probably more than balanced by elimination of losses in the switching converters currently estimated as 5%.

The VKS-7773 has both its body and collector liquid cooled. This is not an acceptable design for space applications. Mechanical pumps for moving coolant would not be reliable enough. The collector can be run very hot and radiate directly to space, if it is made of a refractory material. Figure 2.6-25 shows such a collector assembly made of pyrolytic graphite. The body cannot radiate directly to space as the collector can. The body cooling method most like the present tube design is the replacement of the glycol coolant loop which uses a mechanical pump with a NaK loop using an electromagnetic pump.

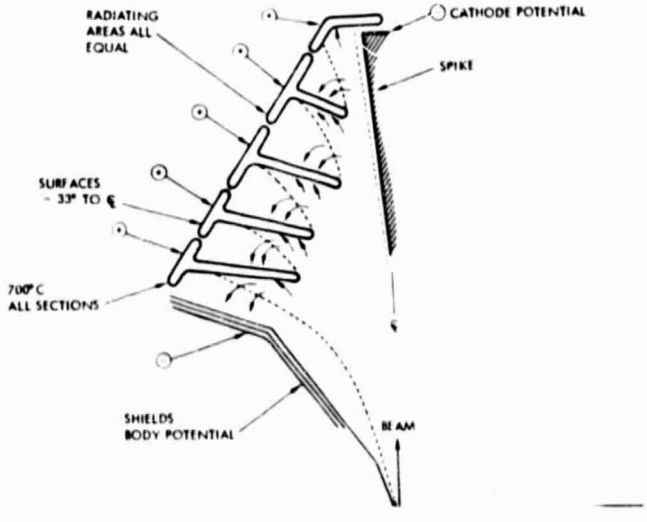

Figure 2.6-25. Collector Radiator

NaK is an acronym for a eutectic mixture of sodium and potassium. It melts at a temperature only slightly higher than the melting temperature of

ice. Since it is a good conductor, it can be pumped by passing a current through a pipe carrying the NaK in the presence of a magnetic field crossed with the current vector. Figure 2.6-26 shows that the NaK loop passes through the focusing solenoid in order to enter and leave the tube. Therefore current forced through the loop at those points is all that is needed to provide a pump with no moving parts except the fluid. The tube can be kept hot during eclipses by shutting off the pump.

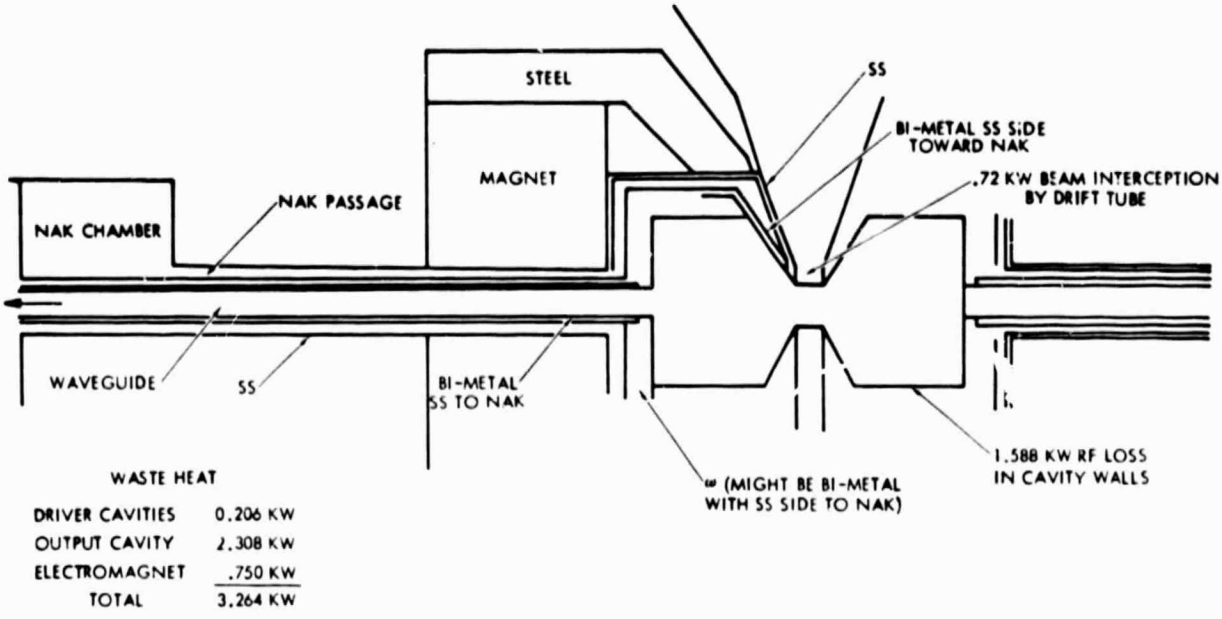

WASTE HEAT	
DRIVER CAVITIES	0.206 KW
OUTPUT CAVITY	2.308 KW
ELECTROMAGNET	.750 KW
TOTAL	3.264 KW

1. FOUR NAK CHAMBERS WHERE HEAT PIPES JOIN
2. TWO CHAMBERS FEED NAK THROUGH WAVEGUIDE COOLING PASSAGES TO AND FROM OUTPUT DRIFT TUBE
3. TWO CHAMBERS FEED NAK DOWN BODY - AND UP BODY

BODY TEMP °C		RADIATOR AREA M^2	RADIATOR TEMP °C
220		2.42 - 2.77	150
250		1.77 - 2.25	180
275		1.4 - 1.65	205
300	MAX	1.12 - 1.29	230

Figure 2.6-26. Klystron Output Cavity and Body Cooled by NaK Loop

An approach more in keeping with current space practice is the use of heat pipes embedded in the klystron body walls and output drift tube. The selected point design is based on this approach. In either case, the heat-carrying pipes leave the klystron and carry heat to a set of pipes lying between the microwave slot radiators of the RCR face. This permits the disposal of klystron body waste heat downward toward earth and away from the satellite. A thermal blanket on top of the RCR prevents heat from traveling upwards. This makes it possible to keep electronics on the array back at 60°C. It also prevents radiated body heat from heating the satellite

structure, slip rings and personnel working in this region.

It is especially important that the trunnion slip rings not be heated, since their performance drops drastically with temperature increase. This makes it necessary to radiate collector heat downward. This is done by inserting the klystron into a well as shown in Figure 2.6-27 in the center of the RCR. Its collector protrudes from the working face of the RCR so that it can radiate downward in the same direction the body heat is radiated.

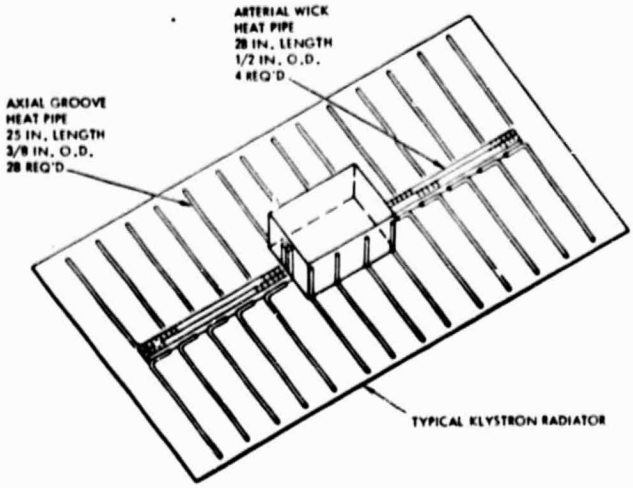

Figure 2.6-27. RCR Radiator Configuration

The klystron collectors block about 3% of the array surface. This causes the scattering of an additional 3% of the power out of the main beam, reducing estimated beam efficiency from 88% to 85%. However, it is necessary to accept this blockage in order to solve the thermal control problems.

In the array center there are 42 klystrons per 100 m^2 subarray. The radiator area per tube is then 2.38 m^2, if the microwave array structure is also used to radiate heat. The radiator temperature according to Figure 2.6-26 is then about 160-170°C, if a NaK loop is used. This is an allowable temprature for aluminum. If the tube body temperature is allowed to increase to its maximum permissible value of 300°C, the radiator area needed to radiate the 3.264 kW of waste heat is about 1.2 m^2. The actual area available (2.38 m^2) is twice as large. Therefore the power density in the center of the array could be doubled from 21 kW/m^2 to 42 kW/m^2, if desired. At these higher temperatures titanium would have to be used instead of aluminum in order to control creep.

When heat pipes are used, the array face temperature is somewhat higher, about 200°C for a power density of 21 kW/m^2. The maximum possible power density is also lower than with the NaK loop, about 30 kW/m^2 versus 42 kW/m^2 with the NaK loop. However, heat pipes are selected for the point design, shown in Figure 2.6-28 because there is more design experience available concerning their use in space. In Figure 2.6-29, the alternate configuration the klystron inverted with its cathode down and collector radiating upward toward the satellite is shown.

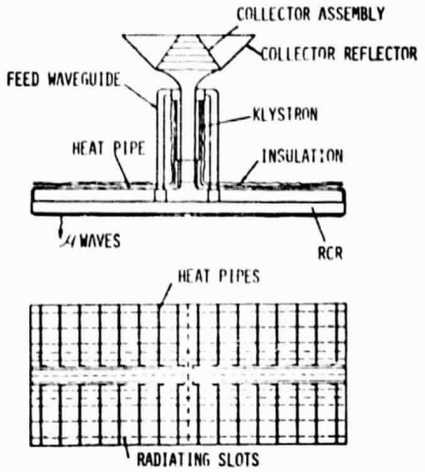

Figure 2.6-28. Power Module Design Concept

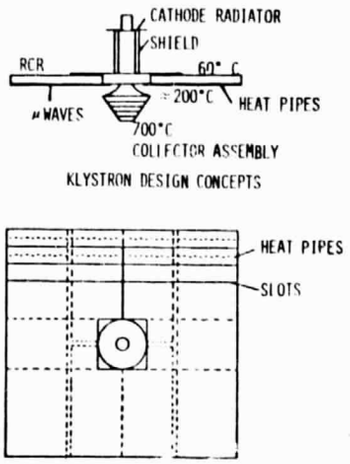

Figure 2.6-29. Heat Radiators on Array Face

Klystron component masses and total mass are tabulated below:

COMPONENTS	MASS (KG)
PPM Magnet	2.0
Magnetic Poles	6.5
Electromagnet	13.0
Collector Assembly	5.5
Collector Heat Shield	0.1
Body Heat Shield	0.8
Copper Cavities	0.4
Heat Pipes in Tube	2.1
Electron Gun	0.6
TOTAL	31.0 kG
Specific Mass	0.62 kG/kW

2.6.2 RECTENNA DESIGN

The analysis and performance data for the rectenna for a 5 GW SPS is presented below:

Rectenna/Array Sizing

The first task in designing the rectenna is the determination of its optimum size. This process will also yield the optimum size of the satellite array working with the rectenna, since there is a reciprocal relationship between these two arrays. Let R_B be the radius of the microwave beam entering the earth's atmosphere and R_A be the array radius. Then

$$R_B = k/R_A \qquad [k] = [R_A R_B] = [L^2] \tag{1}$$

where k is determined by the array weighting function, $\rho_A(R)$. The power transmitted by the array is

$$P_A = \int_0^{R_A} \int_0^{2\pi} \rho_A(R)\,dA = 2\pi \int_0^{R_A} \rho_A(R)(R\,dR) \tag{2}$$

Let $dA = 2\pi R_A^2 \frac{R}{R_A} d\frac{R}{R_A} = 2\pi R_A^2\, r\,dr$, $\rho_A(R) = \rho_A W_A(r)$, where r is a normalized radial coordinate, $W_A(r)$ a normalized weighting function, and ρ_A the permissable power density at the array center, so

$$P_A = 2\pi\rho_A R_A^2 \int_0^1 W_A(r)\,r\,dr = 2\pi F_A \rho_A R_A^2 \tag{3}$$

In a similar manner integrating over the circular beam entering the earth's atmosphere we obtain the beam power received by the rectenna

$$P_R = 2\pi\rho_B R_B^2 \int_0^1 W_B(r)\,r\,dr = 2\pi F_B \rho_B R_B^2 \tag{4}$$

where $W_B(r)$ is the normalized beam power density versus normalized radial distance from beam center, r, and ρ_B is permissable power density at beam center.

For a Gaussian beam with 10 dB taper

$R_A = 0.50$ km

$R_B = 5$ km

$P_R = 5.40 \times 10^6$ kW

$P_A = 6.14 \times 10^6$ kW

For a shaped beam with -25 dB sidelobes and 1 dB ripple across the beam the pertinent parameters must be obtained by graphic means from Figures 2.6-30, 2.6-31 and 2.6-32. We have

$$R_A = 1.12 \text{ km}$$

$$R_B = 4.02 \text{ km}$$

$$P_R = 7.03 \times 10^6 \text{ kW}$$

$$P_A = 7.73 \times 10^6 \text{ kW}$$

Microwave to dc Conversion Efficiency

In order to estimate the efficiency of such a rectenna let us assume that the arrays are approximated by circular discs of radius R. Assume that the feeders to the array elements run radially inward to a collection point at the disc center. For the time being, assume that the feeders are matched at each end so that they support a traveling wave and introduce an attenuation of α bels per unit length. The case of a resonant feeder system will be considered latter.

$$P_o = \int_o^R 10^{-\alpha r} dP = \int_o^R 10^{-\alpha r} (\rho dA) = 2\pi\rho \int_o^R r 10^{-\alpha r} dr \tag{5}$$

where ρ = incident power density, r = radial coordinate, dA = incremental area where the quantization of α due to the discrete power collection points at the array elements is neglected.

The power incident on the disc is

$$P_T = 2\pi\rho \int_o^R r dr = 2\pi\rho \left. \frac{r}{r} \right| \int_o^R = \pi\rho R^2 \tag{6}$$

So that the power out of the array becomes $\pi\rho R^2 = P_T$, if the feeder attenuation is zero or the disc is of incremental size.

Now Brown[1] states that the percentage loss in the diode rectifier circuit is very accurately given by the expression

$$(1-L) = B + \frac{A}{\sqrt{P_{in}}} \tag{7}$$

where A = 10.04 and B = 4.212 for the GaAs diodes mentioned earlier and P_{in} = power into the diode circuit = P_o (power out of array), L = percentage diode loss.

The DC power out is then

$$P_{DC} = P_o E_D = P_o (1-L) \tag{8}$$

[1]W. Brown, *Electronic and Mechanical Improvement of the Receiving Terminal of a Free-Space Power Transmission System*, NASA Report NASA-135194/PT-4964 (1 August 1977)

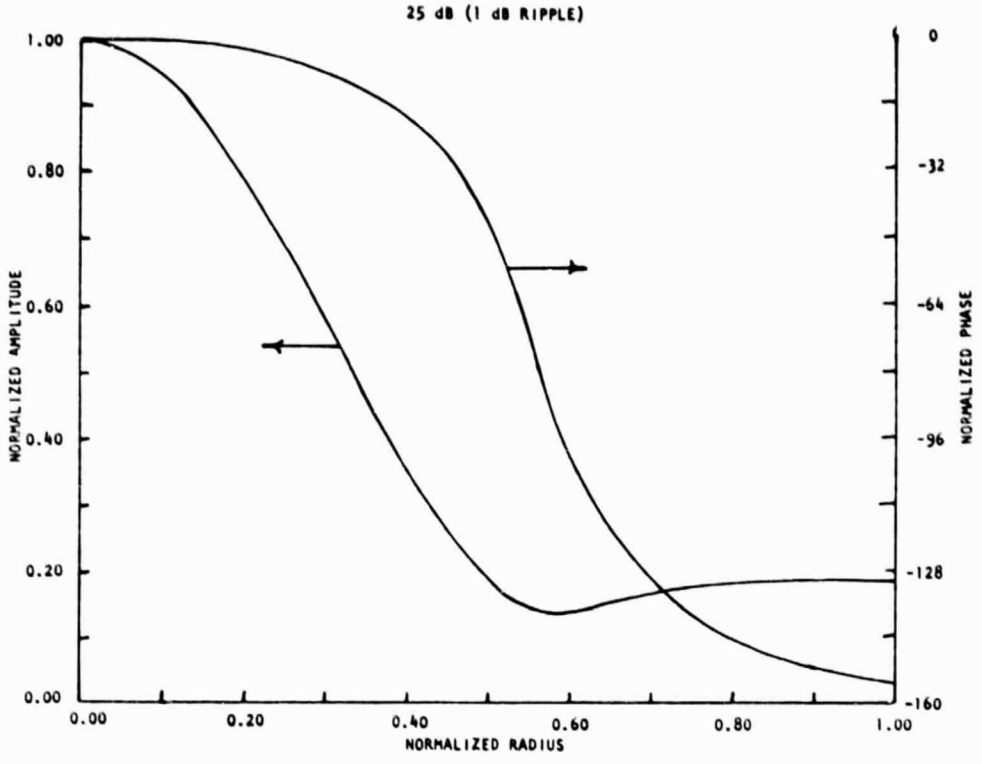

Figure 2.6-30. Array Excitation

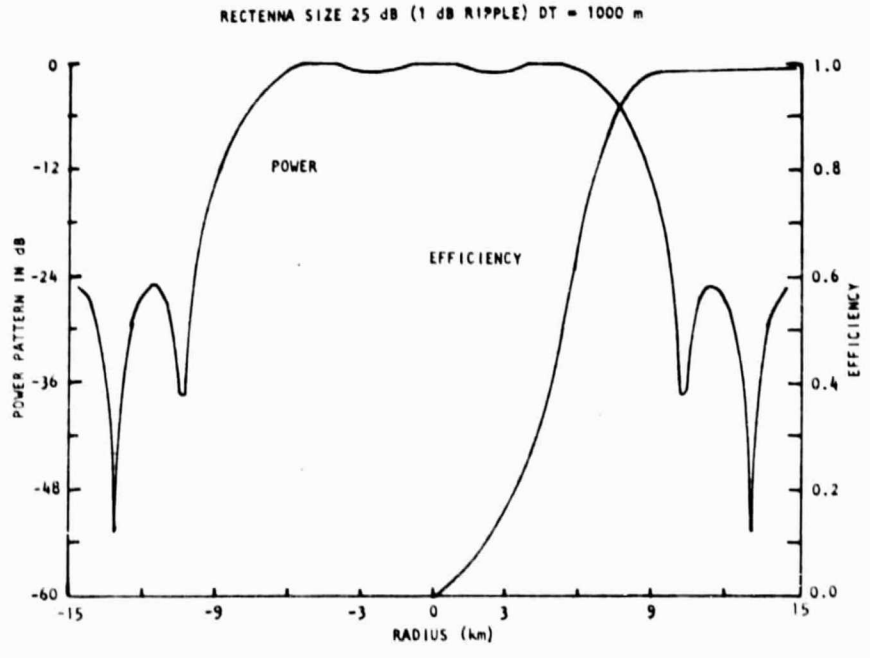

Figure 2.6-31. Beam Shape

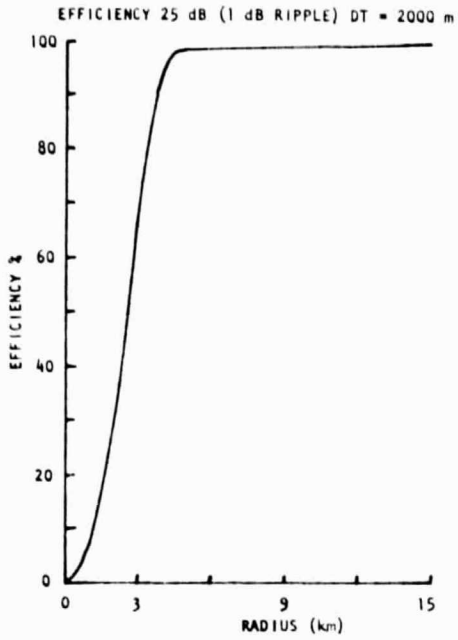

Figure 2.6-32. Beam Efficiency

as the array radius increases the efficiency at first rises due to the increased power applied to the diode. However, eventually P_o decreases due to the increasing attenuation introduced by the array feeders and the efficiency falls. There is therefore an optimum array radius giving maximum efficiency. This maximum depends on both α and ρ.

Obviously the rectenna will have considerable fewer diodes then the rectenna consisting of dipoles, each with its own diode rectifier. The reduction in number will be $(d\lambda)^2/A$, where d is the spacing of the dipoles and A is the array area. The above parameters were calculated for an attenuation varying from 0.005 to 0.03 dB/cm. These values were selected because they correspond to the attenuations of stripline panels of varying quality. All calculations were done for a Gaussian beam with peak intensity of 23 mW/cm^2 and diameter of 10 km (normal incidence beam from a 1 km transmitting array). The values of ρ at the rectenna are then well approximated by

$$\rho = \rho_{MAX\ C}^{-\frac{Z^2}{8}} \tag{9}$$

where Z is the rectenna radial coordinate in km.

Figure 2.6-33 is a typical plot of array efficiency versus radius at a distance of 4.25 km from the center of the rectenna. The plot is only carried out to a radius where the max is obtained.

Figure 2.6-34 is a typical plot of power applied to the rectifier versus rectenna radius. It is to be noted that the range of power is about 6 to 1 (42 to 7 W). This is somewhat smaller than the 20 to 1 range in the diode case. This helps in maintaining a constant generator impedance throughout

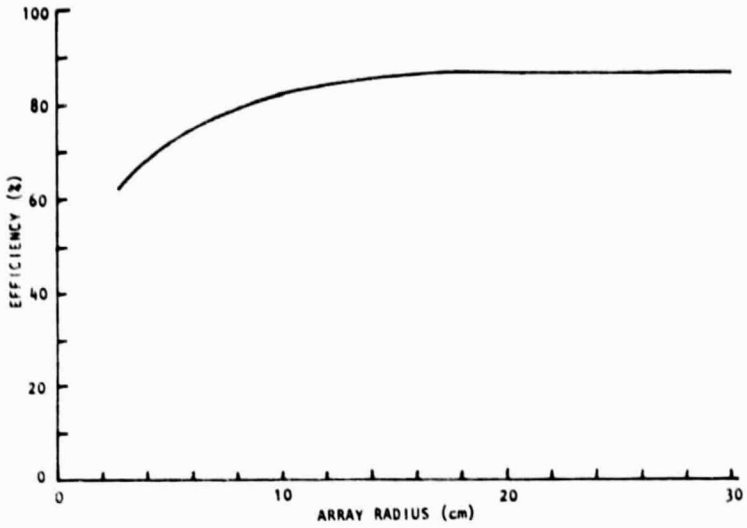

Figure 2.6-33. Typical Efficiency Versus Array Radius Plot (ρ = 2.4 mW/cm^2, α = 0.015 dB/cm)

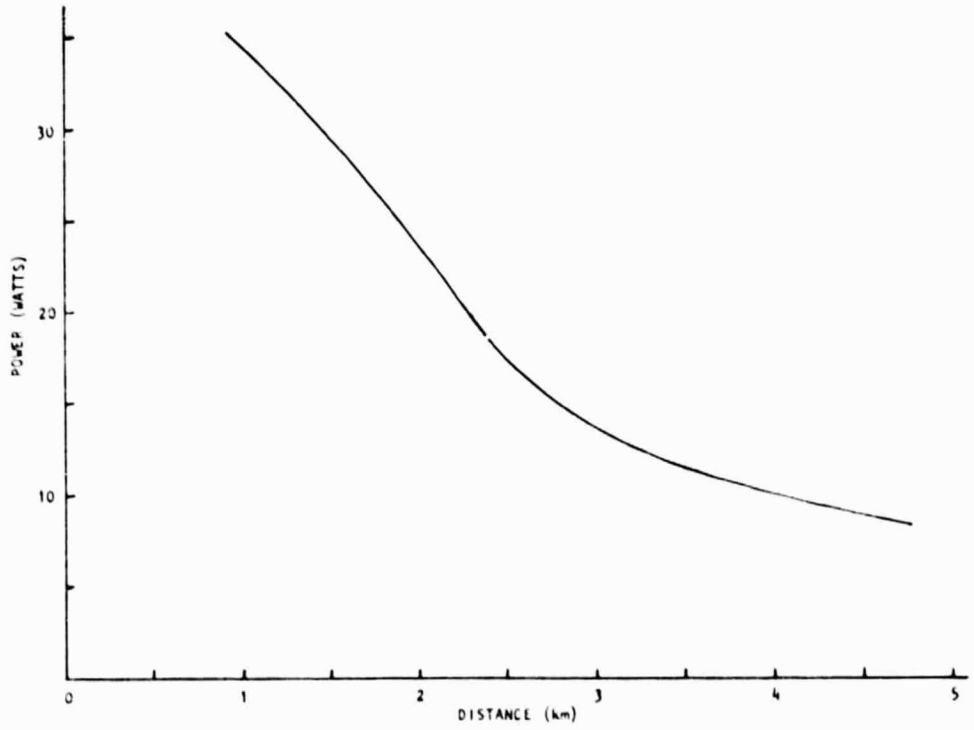

Figure 2.6-34. Rectifier Power Versus Rectenna Radius (α = .01 dB/cm)

the array. Use of push-pull rectifier circuits in the array center can reduce the power range by a factor of 2 to 21 W to 7W. Push-pull rectifiers will also reduce reradiated second harmonic power.

Figure 2.6-35 is a plot of array radius versus rectenna radius. It will be seen that at the edge of the rectenna the array beamwidth is about 10°, since the array diameter is about six wavelengths. Since the array is uniformly weighted its pattern is sin X/X. Let the pointing loss be Lp. Then for a deviation of the satellite from beam center of X

$$1 - Lp = \frac{G(X)}{G(0)} = \frac{\sin X}{X} \approx \frac{X - \frac{X^3}{6}}{X} = 1 - \frac{X^2}{6} \qquad (10)$$

and $X = \sqrt{6Lp}$. For $Lp = 10^{-2}$ $x = \sqrt{0.06} = 0.245$ radians. Since $X_{-3dB} = 1.9$ rad, the pointing error producing a pointing loss of 0.01 is 0.245/1.9 = 0.13 beamwidth. Figure 2.6-36 is a plot of the efficiency of the total rectenna versus attenuation. It will be noted that the target efficiency of 90% is reached at 0.01 dB/cm. Figure 2.6-37 shows the number of diodes required as a function of attenuation. In some ways Figure 2.6-38 is more meaningful. It shows the number of diodes required where there is one diode per dipole. This number is 1.57×10^{10} diodes. For α = 0.01 dB/cm only 2% as many diodes are required when the array technique is used. The savings is 15.4 billion diodes.

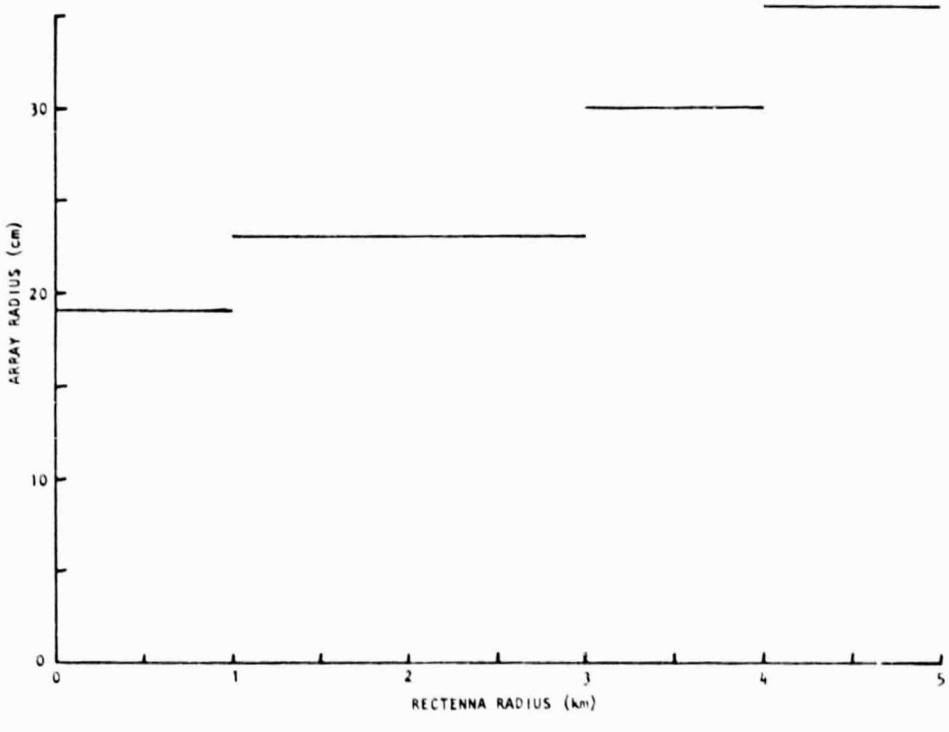

Figure 2.6-35. Array Radius Versus Rectenna Radius (α = .01 dB/cm)

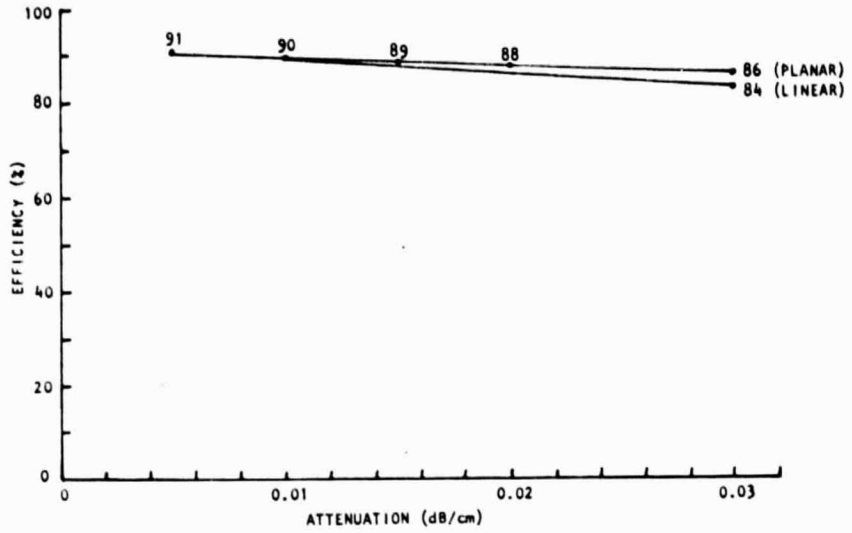

Figure 2.6-36. Rectenna Efficiency Versus Stripline Array Attenuation (ρ_{max} = 23 mW/cm^2)

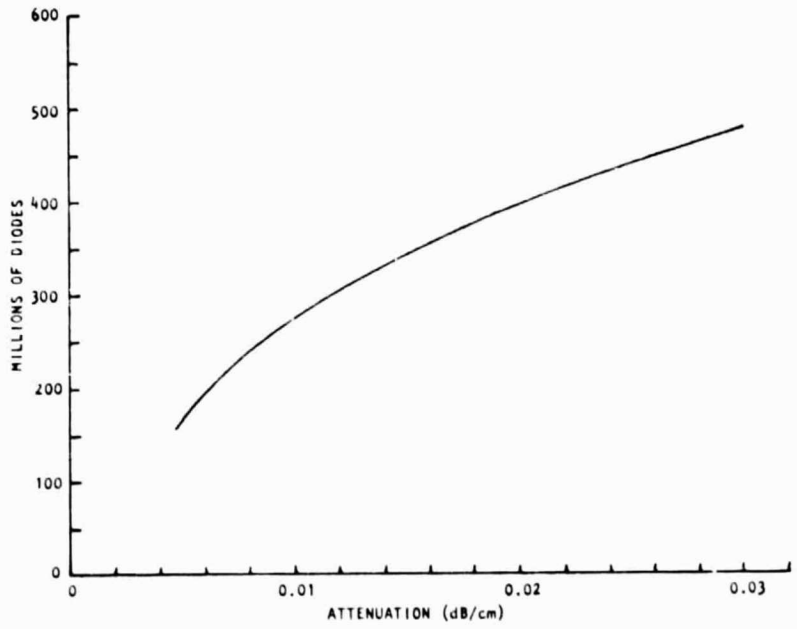

Figure 2.6-37. Number Diodes Required By Rectenna Versus Stripline Array Attenuation (Rectenna Radius = 5 km, ρ_{max} = 23 mW/cm^2) (Planar Case)

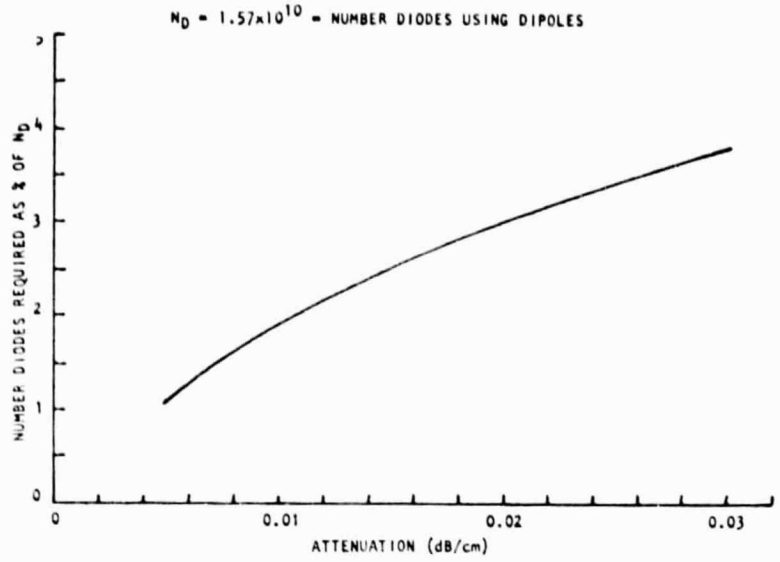

Figure 2.6-38. Percentage Diodes Required for Rectenna (Rectenna Radius = 5 km, ρ = 23 mW/cm^2)

Rectenna Rectifier Design

The rectenna consists of a set of antennas, each with its own diode rectifier, which absorb the power beam from the satellite array. The dc power from the diodes are then added in a collection network to form the output power delivered to the power grid.

The most recent analysis of the efficiency of the rectenna is by Brown.[1] Here the efficiency of Schottky barrier gallium arsenide diodes are analyzed by a computer program and compared with experimental results obtained with a Raytheon 40593-CPX1G diode developed for the SPS program. The results are shown in Figure 2.6-39. The computer orientation of this report makes it hard to see the factors that control the efficiency of the diode rectifier. Therefore Brown's program is useful in analyzing the rectifier, but hard to use in synthesizing the best configuration. Therefore an approximate analysis will be carried out in order to understand the rectifier better. The basic circuit is shown in Figure 2.6-40.

The antenna is represented by R_A and an ac voltage, V_A, in series induced by the power beam. The diode is represented by V_J, the built-in junction voltage, and R_D, the diode resistance. R_A is transformed to a new generator impedance by the network, so that $R_G = R_L$ and maximum power is transferred to the load.

[1]W. Brown, Electronic and Mechanical Improvement of the Receiving Terminal of a Free-Space Power Transmission System, NASA Report NASA-135194/PT-4964 (1 August 1977)

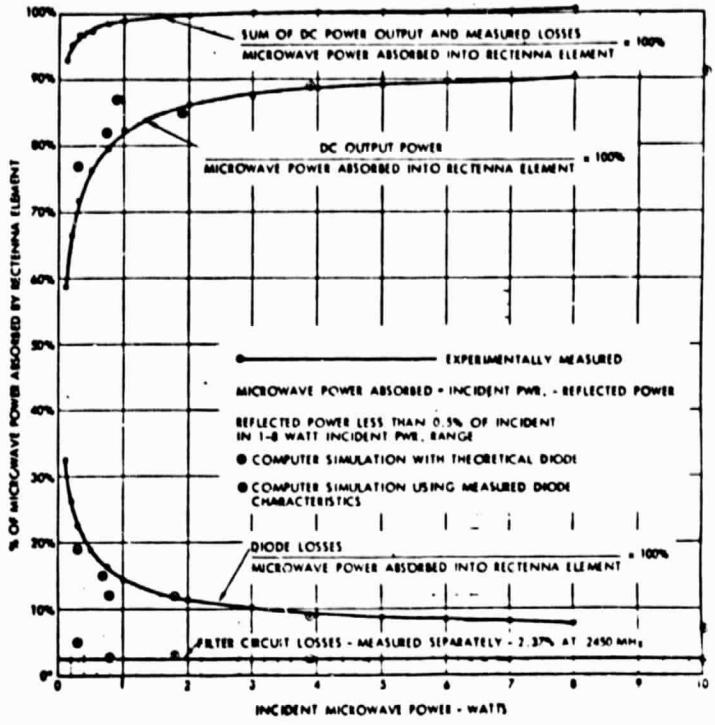

Figure 2.6-39. Microwave Performance - Computer Simulation

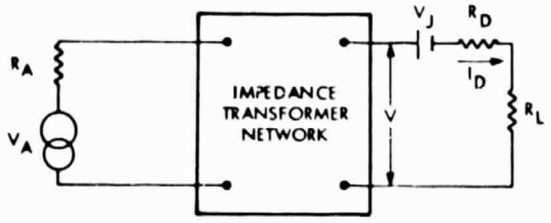

Figure 2.6-40. Rectenna Rectifier Circuit in Forward Conduction

There are also two other sources of loss besides mismatch loss. First, the voltage V is reduced by V_J. The power associated with this voltage reduction is reflected back to the generator and radiated. In addition with $V>V_J$ power is dissipated in the diode resistance R_D. We must set the diode parameters to minimize these losses. Past proposals have assumed that each diode is fed by a single dipole in the rectenna array. For the Gaussian 5 GW beam, the power densities of the incident beam vary from about 20 mW/cm^2 at the beam edge. Since a dipole receiving cross section is close to 50 cm^2, the corresponding collected powers vary from 1 watt to 50 milliwatts. Reference to Figure 2.6-39 shows that the efficiency of a rectifier using this diode vary from about 50% to 82% at these power levels. It is obvious that this diode has too low an impedance to be used at these power levels.

The analysis of diode performance just given indicates how diodes for lower power levels can be designed. However, it is also apparent that an optimum rectenna design should group the dipoles into small arrays so that the power levels applied to the diodes are raised. This will greatly decrease the number of rectifier circuits and diodes required and the amount of bus wiring required to collect the rectifier outputs. More rugged, higher power diodes also result from this move.

The use of subarrays can cause problems if they are too large and become too directional. Motion of the satellite due to imperfect station keeping can produce unacceptable losses due to movement of the satellite off the peak of the subarray beams. However, if the rectenna is operated in conjunction with a single satellite, the directions of arrival of the power beam will be restricted to a small solid angle. The solid angle dimensions are set by the satellite orbit and the stationkeeping scenario. The subarray can then be sized so that only a small budget loss results due to pointing error, say 1%. By tilting the subarrays to various directions this loss can be made constant over the solid angle. Diodes can then be designed to have optimum efficiency at the power levels produced by the subarray at each location within the rectenna. Even a very moderate amount of subarraying can dramatically decrease the number of rectifiers. For instance, subarrays three wavelengths on a side will reduce the number of rectifiers by an order of magnitude.

The total rectenna efficiency budget is given in Table 2.6-3.

Table 2.6-3. Rectenna Loss Budget

LOSS	TYPICAL VALUE %
POINTING, L_P	1.0
SUBARRAY, L_{SA}	0.5
DIODE, L_D	3.5
JUNCTION, L_J	3.5
CIRCUIT, L_C	1.5
MISMATCH, L_R	1.0
COLLECTION BUS LOSS, L_B	1.0
TOTAL LOSS, L_Σ	12%
RECTENNA EFFICIENCY	88%

Rectenna Panel Configuration

The rectenna can be made up of such panels having a width equal to the array diameters calculated and as long as possible. These panels are then mounted in frames which cross the rectenna area in an east-west direction. These frames are inclined so as to be normal to the incident radiation. The rectifier circuits are coupled into the back of panels. For a latitude of 30°, the high edge of the panel is about fifty feet above the ground. The overall arrangement is shown in Figures 2.6-41 and 2.6-42. Figure 2.6-43 shows the structure of stripline array with its bow tie receiving dipoles. Figure 2.6-44 shows an exploded view of the layers making up the stripline assembly. Figure 2.6-45 is a detail showing the tensioner for drawing tight the metal mesh on which the stripline assembly lies.

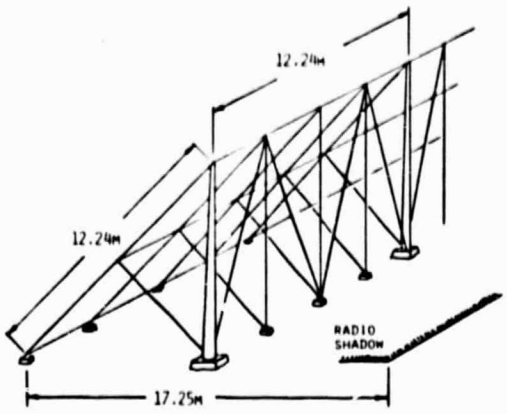

Figure 2.6-41. Rectenna Support Configuration
Metal/Dipole

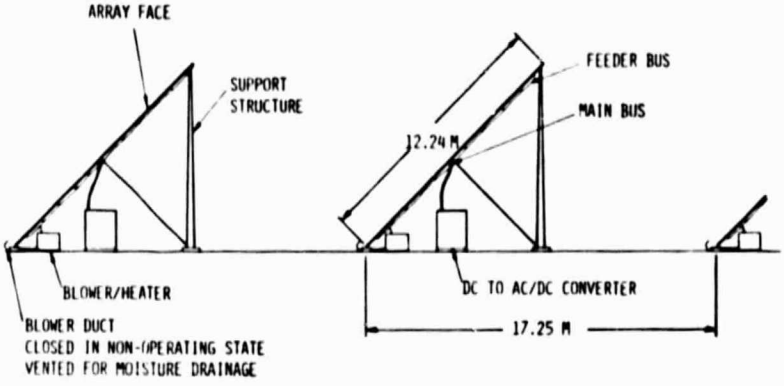

Figure 2.6-42. Rectenna-Elevation

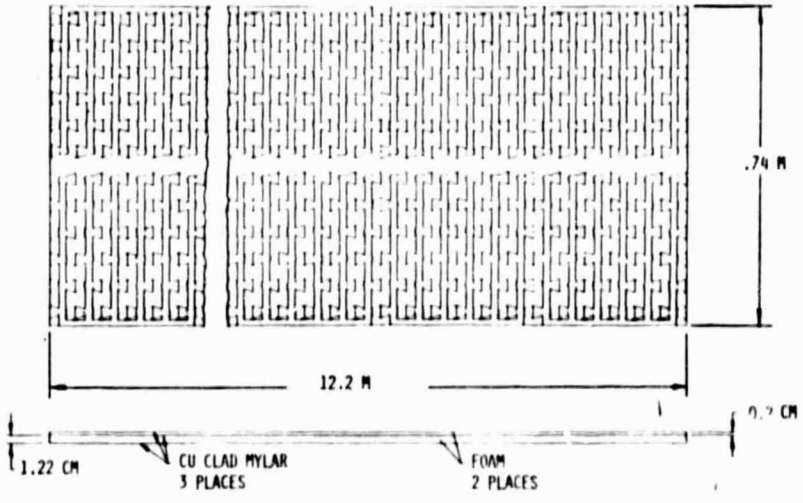

Figure 2.6-43. Rectenna Module
High Density Area

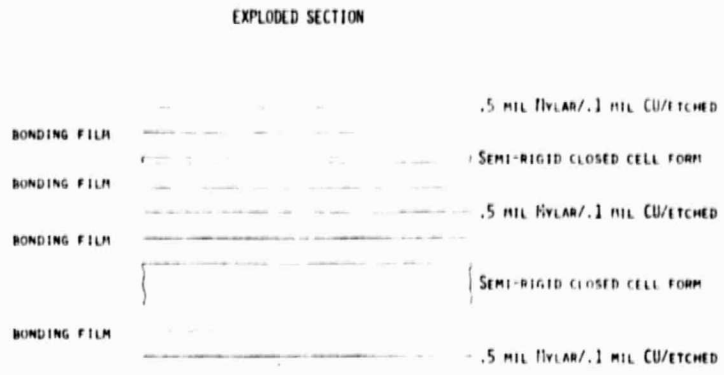

Figure 2.6-44. Rectenna
Bow Tie Dipole Panel

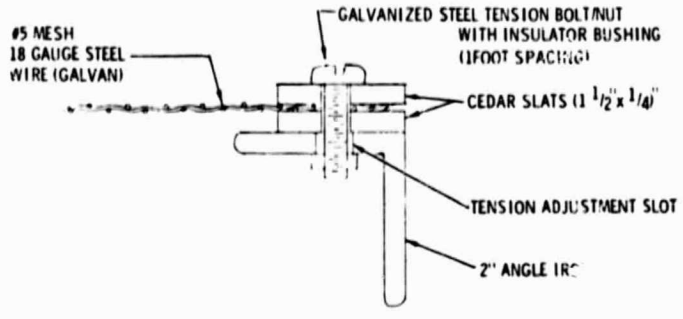

Figure 2.6-45. Rectenna Web Support
Mesh Tensioner Detail

The panels being tilted and non-wetting should not have an appreciable water film during rain. Snow and ice can be removed by blowing air over the panels and/or by vibrating them with vibrators attached to the back side of the panel. In case of sleet or rain which freezes on impact, the air blown on the panels can be heated in furnaces before being blown on the panels. The panel faces are not interrupted vertically to prevent trapping water at frame members.

Rectenna Power Collection

The individual rectifier outputs of a 30×30 m rectenna panel module must be connected to form the panel output. Such an arrangement is shown in Brown's report as Figure 2.6-46. Each rectifier circuit will be matched to its input from its stripline array for only one combination of input power and load resistance. This results because input power level affects the generator impedance of the rectifier.

By varying the number of diodes in parallel in each section, we can always produce a total panel load resistance which is constant. By varying the panel sizes the amount of power collected by a panel can be made the same from center to edge of the rectenna by varying the panel size. Therefore, the panel output voltages are the same and can be added in parallel.

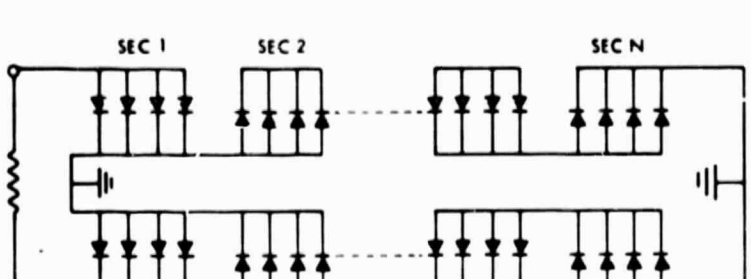

Figure 2.6-46. Series/Parallel Connection of Diode Rectifier Outputs to Form a Rectenna Panel Output

The bus connecting rectifiers can be sized to produce a given design loss between rectifiers and the panel board. Again following previous calculations we can set this loss at 1%. The overall rectenna efficiency is then conversion efficiency times aperture efficiency times bus efficiency times pointing efficiency. For a stripline loss of 0.01 dB/cm we have,

$$E_{\Sigma} = 0.90 \times 0.99 \times 0.99 \times 0.99 = 0.87$$

Computer Control of the MPTS Array

The total SPS computer control and information distribution system is reported in another portion of this study. This section will concentrate on a listing of the data from the subarrays which must be collected, coded and put on a data bus for transmission to a central computer. Likewise a list will be given of commands which come from the central computer. These commands are taken off a data bus, decoded and applied to the device indicated in the command list.

It is assumed that the subarray is an "intelligent terminal." A local microprocessor will first receive local data. Much of this data will not change by very much as long as the subarray is operating correctly. The microprocessor will periodically read this data on a short time scale. If it stays within a preset tolerance range and a preset rate-of-change tolerance, no data is put on the bus. If tolerances are exceeded, an immediate report is made to the central data processing station via the bus. In the case of data deviations which may indicate that equipment may be damaged the microprocessor may be programmed to take immediate action and then report. Indeed in the case of some critical events with short time constants, shutdown will be initiated by hard-wired paths and data reporting carried out after shutdown.

Data which stays within tolerance will be reported at much more infrequent intervals after averaging over this longer interval. Such data can be used to find secular changes in performance which indicate incipient failure. Such indications may be used to decide that unscheduled maintenance is needed. With proper array design, the subarray system will be accessible while the MPTS system is in operation. The maintenance is then carried out while the SPS is operating. This maintenance philosophy is the same as that used by the airlines. Airliners do not go out of commission for periodic maintenance.

Instead performance data is fed to a central computer at each airfield where the aircraft lands. On the basis of this data parts are sent to other airfields where the plane will appear at a later time and corresponding maintenance orders are issued. The airliner is thus being continuously maintained and repaired. It continues to fly indefinitely, unless there is a catastrophic failure. It is felt that study of these airline computerized maintenance systems would be of great help in setting up a similar system for SPS. The performance data list for the subarray and power module is presented in Table 2.6-4.

Table 2.6-4. Performance Data List

	PARAMETER	RPT PERIOD	LOCAL ACTION
SUBARRAY			
	PILOT BEAM SIG	1 DAY	SHUTDOWN
	REFERENCE SIG	1 DAY	SHUTDOWN
	PLL LOCK-IN	1 DAY	SHUTDOWN
	RETRO/COMMAND MODE		
	MONOPULSE $\Delta\phi$	1 MIN	SHUTDOWN
	MONOPULSE $\Delta\phi$	1 MIN	SHUTDOWN
	BEAM PROGRAMMER ϕ-GRADIENT	1 DAY	SHUTDOWN
	TRANSISTOR PREAMP OUTPUT	1 DAY	SHUTDOWN
PROGRAM MODULE			
	KLYSTRON DRIVE	1 DAY	HARD WIRED SHUTDOWN
	OUTPUT GUIDE ARC	-	HARD WIRED SHUTDOWN
	SOLENOID CURRENT	-	HARD WIRED SHUTDOWN
	PHASE ERROR SIG	1 DAY	SHUTDOWN
	BEAM CURRENT	1 DAY	
	COLLECTOR CURRENTS, 1-5	-	
	MOD ANODE CURRENT	1 DAY	
	BODY VOLTAGE	1 DAY	
	COLLECTOR VOLTAGES	1 DAY	
	BODY REGULATOR INPUT VOLTAGE		
	CATHODE HEATER VOLTAGE		
	CATHODE HEATER CURRENT		
	MOD ANODE VOLTAGE		
	SOLENOID TEMP		
	ARRAY FACE TEMP		
	REGULATOR TEMP		
	ARRAY BACK TEMP		
	COLLECTOR TEMP		
	OUTPUT DRIFT TUBE TEMP		
	HEAT PIPE TEMP		
	KLYSTRON PRESSURE		
	RCR PRESSURE		
	KLYSTRON POWER LEVEL		
	PPM MAGNET TEMP		
	SOLENOID VOLTAGE		
COMMAND PARAMETERS			
	KLYSTRON POWER LEVEL		
	COMMAND OR RETRO SUBARRAY PHASE		
	COMMAND OR SERVO SUBARRAY PHASE GRADIENT		
	PHASE COMMAND		
	PHASE GRADIENT COMMAND		
	BODY REGULATOR VOLTAGE		
	CATHODE HEATER ON-OFF		

2.6.3 ECLECTIC CONJUGATE - PHASE ARRAY SYSTEM

A composite phase-conjugating system is proposed which embodies most of the good features of the systems already proposed. An overall block diagram is given as Figure 2.6-47.

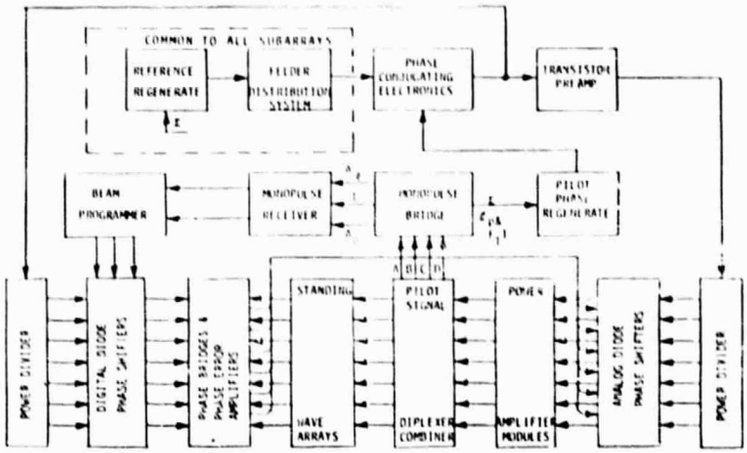

Figure 2.6-47. Phase Control (Electic)

Introduction

The reference phase distribution system is a modification of the system proposed by Seyl and Leopold of JSFC. It uses a group of traveling wave feeders which distribute the reference source to a set of array regions. These feeders are servoed to produce the same phase at all outputs by means of signals fed back to the feeder inputs. The amplifiers in a given region are excited by a local feeder distribution system using resonant feeder elements.

The pilot phase regeneration system is based on the JPL design. However, the transmitter signal is used as the local oscillator. This signal is of very high amplitude. It is feared that if it is not incorporated into the phase regeneration loop, it will produce so many spurious signals the design may fail. Elimination of transmitter phase noise forces us to a multiplier arrangement such as JPL used.

A pair of reference signals are used symmetrically placed around the operating frequency in order to eliminate ionospheric phase errors and errors due to filter detuning. The reference signal and the regenerated pilot are fed into the phase conjugating circuit shown in Figure 2.6-48, which was proposed in earlier Rockwell studies.

Note that the output is $(2f_r - f_p)$. This is of the correct form to produce phase conjugation. If $f_r = f_p$, $f_T = f_p$; this is the most desirable condition. The only drawback is possible leakage of the high power transmitted signal into the phase reference distribution system. This is controlled by distribution of a reference at a frequency of $f_r/2$ which is converted to f_r by doubling at the point of usage.

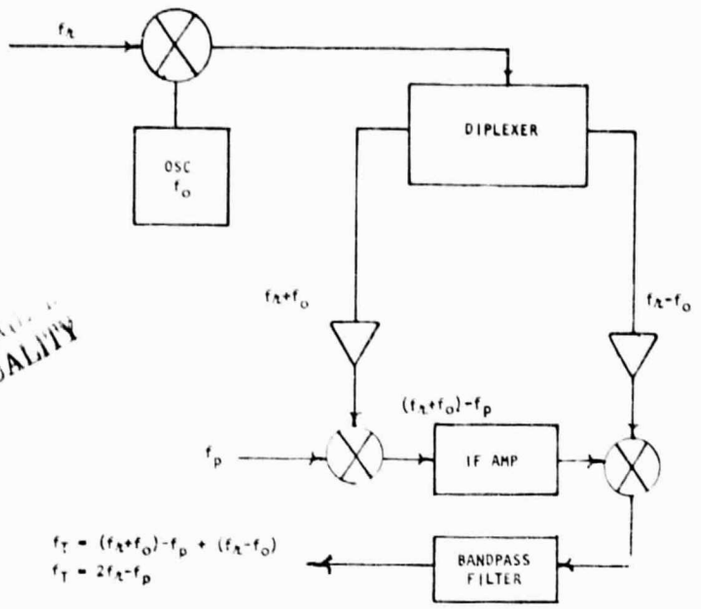

Figure 2.6-48. Phase Conjugating Electronics

The phase-conjugated signal, f_T, (which is what we wish to transmit) is fed to a transistor preamp and then to a power divider where the signal is distributed to the klystron amplifiers. The divider outputs are fed through analog phase shifters to the klystrons, where power generation occurs. The klystron outputs are used to drive the standing wave arrays which comprise the subarray.

The same subarray is receiving the pilot signals coming up from the earth station. Diplexers allow the klystron signals to flow into the standing wave radiators, while diverting the pilot signal coming from the cavity into a power combining network which feeds a monopulse bridge. Since the pilot signals are equally displaced from the transmitted signal, the 180° change in phase needed in the diplexer occurs for both pilots. Alternately the standing waveguide assembly or cavity can be fed from a separate feeder. The klystron signal at the bridge input is reduced by about 30 dB. The pilot signals are about 1 mW at this point. The pilot signals are then fed to a monopulse bridge. The sum signal is fed to the pilot phase regeneration circuitry. This sum signal and also the difference signals are fed to a monopulse receiver as shown in Figure 2.6-49. Just as in the pilot phase regeneration circuits, the transmitted signal is used as the local oscillator.

The monopulse receiver outputs ε_θ and ε_ϕ are a measure of the angular deviation of the direction of reception of the subarray from the direction of arrival of the pilot beam. The same signal f_T which was fed to the klystrons is fed to a second power divider. The outputs of this divider are fed through a set of phase shifters to an array of phase bridges.

The other set of inputs to these bridges is from taps which sample each klystron output in the standing wave radiators fed by the klystrons

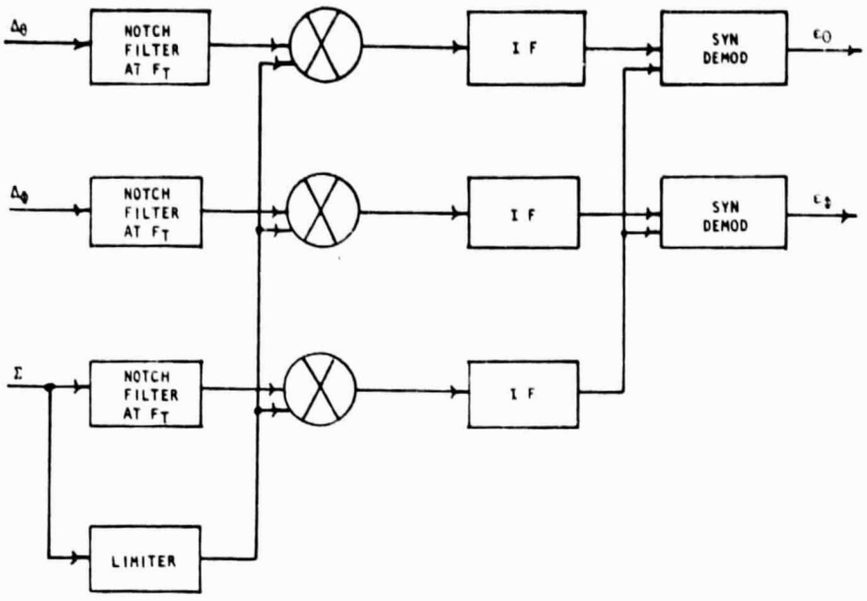

Figure 2.6-49. Monopulse Receiver

which comprise the subarray. These signals would be f_T, except that they have suffered phase shifts in the klystrons. They will be called f'_T. The first input to the phase bridges is f_T at the center bridge corresponding to the center of the subarray. The other members of this set are F_T shifted by the phase shifters so as to point the subarray pattern in the direction of arrival of the pilot beam. The phase shifters are set by a beam programmer which uses ε_θ and ε_ϕ from the monopulse receiver to make the correction. The phase bridge outputs are amplified and used to control the analog phase shifters at the klystron inputs. These servo loops then remove phase shift errors caused by the klystrons and introduce a phase gradient across the subarray face which corrects for subarray tilt.

At the edge of the array, subarrays will have only about six klystrons. As a result the subarray beam can only be steered about one beamwidth before the rms phase error of the subarray becomes too great. However, even angular control of one beamwidth greatly reduces the angular tolerances in mechanical orientation of the subarrays.

Reference Frequency Distribution

The basic organization of this distribution system is shown in Figure 2.6-50, taken from Seyl and Leopold in the JSFC SPS report. Since each region supplied by a primary feeder is fed directly from the phase reference system, there is no buildup of phase error due to repeated processing at the primary feeder output points. A feedback servo is used to hold the phase of the feeder outputs with respect to the source to a fixed value. This servo is shown in Figure 2.6-51.

The reference source is at half the actual reference frequency. This signal enters the feeder through a diode phase shifter and a circulator. After

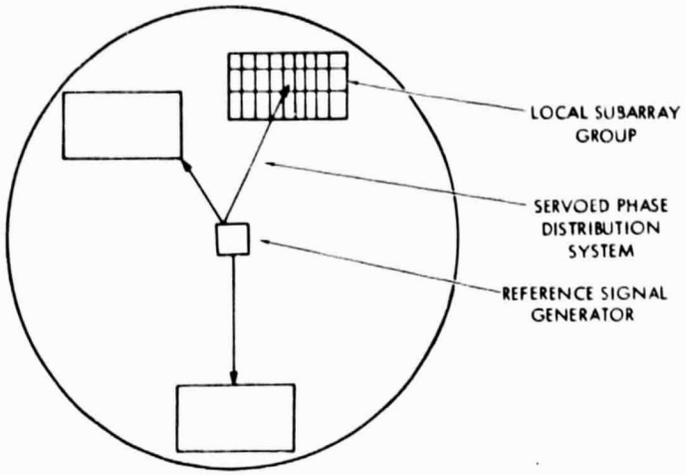

Figure 2.6-50. Array Reference Signal Distribution System

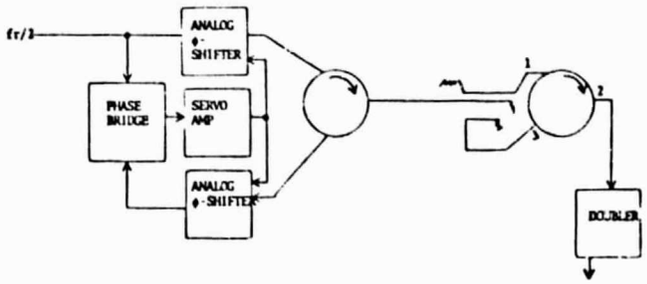

Figure 2.6-51. Reference Phase Distribution Servo

reflection from the short at the other end of the feeder, it arrives back at the input and directed by the circulator into the output port. It then passes through a second phase shifter to a phase bridge. The other input to the bridge is the original reference signal.

The phase bridge output is an error signal which changes the phase shifter settings until the input to the feeder and the reflected signal from the feeder are in phase. The path delay through the shifters and feeder is then an integral number of wavelengths, since the forward and backward path delays are of equal length. Since the forward and return paths are of equal length, the forward path is an integral number of halfwaves long. This forward-path signal is sampled by the directional coupler/circulator arrangement. At port 2 of the circulator part of the signal is reflected back to the central station and part is fed to the doubler. When the signal is doubled to form f_r in the harmonic multiplier driven by the probe the doubler output phase delay with respect to f_r at the source will be twice the phase delay of $f_r/2$ or an integral number of full wavelengths. Therefore, the phase of the doubler output is the same as the phase of the source.

Each coax feeder serves an array region which is small enough to use a phase distribution system based on resonant feeders. Such regions are

shown in Figure 2.6-50, designated as local subarray groups. The resonant feeder distribution concept depends on the fact that the phase at all points in a resonant cavity is approximately the same. The phase variation from point to point depends on the attenuation a wave experiences in traveling across the cavity. If the resonant feeder cavity is not too long, the cavity can be tapped along its length at the standing wave loops to obtain the reference phase. The accuracy with which the signals tapped from the feeder reproduce the reference phase depends on the total loss in the feeder.

If the resonant feeders are made of graphite-epox coated with metal or thin-wall invar, their thermal expansion coefficient can be of the order of 10^{-6} per °C or 10^{-4} for a 100°C change. The elongation is 2.4×10^{-3} m for a 25 m feeder. The corresponding change in electrical length at 2.45 GHz or 0.122 m wavelength is 7°. This small change will not destroy resonance, so it is felt that a servo to hold resonance is not required.

A servo to maintain resonance is required, if guide materials with larger expansion coefficients are used. An error signal for such a servo can be obtained by use of a loop and a dipole probe in the guide. At resonance, the electric and magnetic fields are in exact phase quadrature. These fields are sampled with a probe and a loop respectively and compared in a phase bridge to generate an off-resonance error signal. This signal can then be used to change the effective length of the line till it is exactly in resonance. Figure 2.6-52 shows such an arrangement.

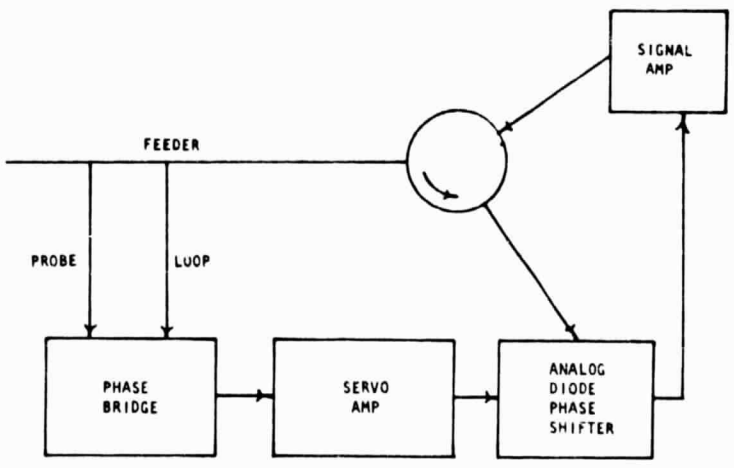

Figure 2.6-52. Electronic Servo Loop to Hold Feeder at Resonance

Since the signal is removed from the feeder and then reinserted, it can be amplified to make up for losses in the phase shift loop and some of the guide losses.

Pilot Signal Regeneration

The pilot signal required should be at the same frequency as the transmitted signal. However, it could not be detected in the presence of the very high power transmitted signal, if it were at the same frequency. Therefore,

it must be offset in frequency. It turns out that in order to control phase errors due to filtering and the ionosphere it is best to have two pilot signals displaced by equal amounts upward and downward from the transmitter frequency. Also since the transmitted signal is at such a high power level, transmitter phase noise can be the dominant noise in pilot signal reception, if the pilot regeneration system is not planned with this in mind. The transmitter signal can also cause spurious frequencies by beating with other signals which can cause trouble.

The solution appears to be to include the transmitter signal in the regeneration process in such a way it cannot cause harm, rather than suffer its presence as an extraneous signal. This is done in the regeneration circuit shown in Figure 2.6-53. Since the output of the frequency quadrupler is the basic quantity, any change in phase in the multiplier will be divided by four. The multiplier should be two halfwave rectifier frequency doublers, rather than high efficiency multipliers using snap-back diodes. This will reduce phase errors due to the multiplier.

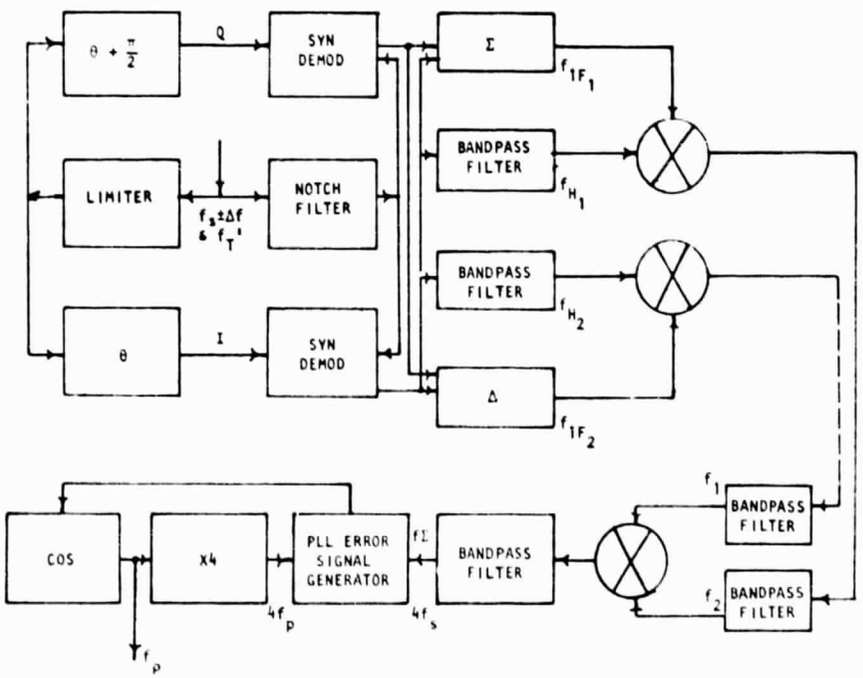

Figure 2.6-53. Pilot Signal Regeneration Circuit

2.7 THERMAL CONTROL SUBSYSTEM

The solar power satellite design is significantly influenced by thermal control considerations. The importance of this subsystem may extend well beyond the designation of specific thermal control components inasmuch as it is a major contributing element in the selection of structural configuration, power distribution network orientation, antenna power levels/layout, number of rotary joint slip rings, and rectenna design/location.

This description includes those aspects of the SPS point design for which the thermal control subsystem elements tend to stand alone. In other areas supported by thermal control, thermal response effects are incorporated into the individual study summary.

The thermal trades/definition documented here is presented relative to specific SPS system elements. It is sequenced according to power conversion, microwave antenna, rotary joint, and rectenna.

2.7.1 POWER CONVERSION - PHOTOVOLTAIC

A model of the photovoltaic baseline design was constructed to determine the adequacy of the design to meet blanket operating temperature specifications, and to identify the effect of coating optical properties on thermal gradients for incorporation in structural response analyses. The cross-sectional model of the baseline array is shown in Figure 2.7-1. Preliminary computations were

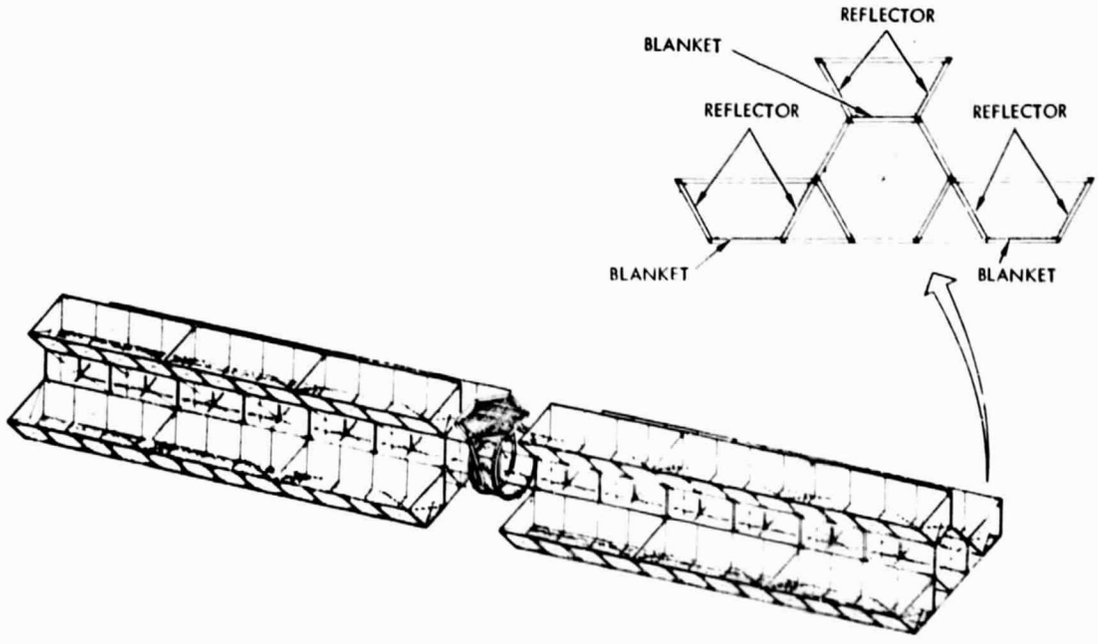

Figure 2.7-1. Photovoltaic Structure Model

based on the assumption that the basic aluminum material is anodized with $\alpha = 0.4$ and $\varepsilon = 0.8$ for absorptivity and emissivity values. Anodization can also be used to provide a higher α/ε ratio (≈ 1.0) if desired. Computed thermal

profiles are shown in Figure 2.7-2. The temperatures shown for the structure, blanket, and reflectors are based upon a solar constant of 1355 W/m^2. Optical properties for the solar cells and concentrators were based upon nominal inherent values for the materials of construction, i.e., selective coatings were not assumed. Also shown (Figure 2.7-2) are the temperature distributions for the original baseline configuration. Temperatures were also calculated for an uncoated aluminum structure. For this condition, α/ε can be as high as 10 to 15, although polishing would reduce this ratio to about 5. The temperatures

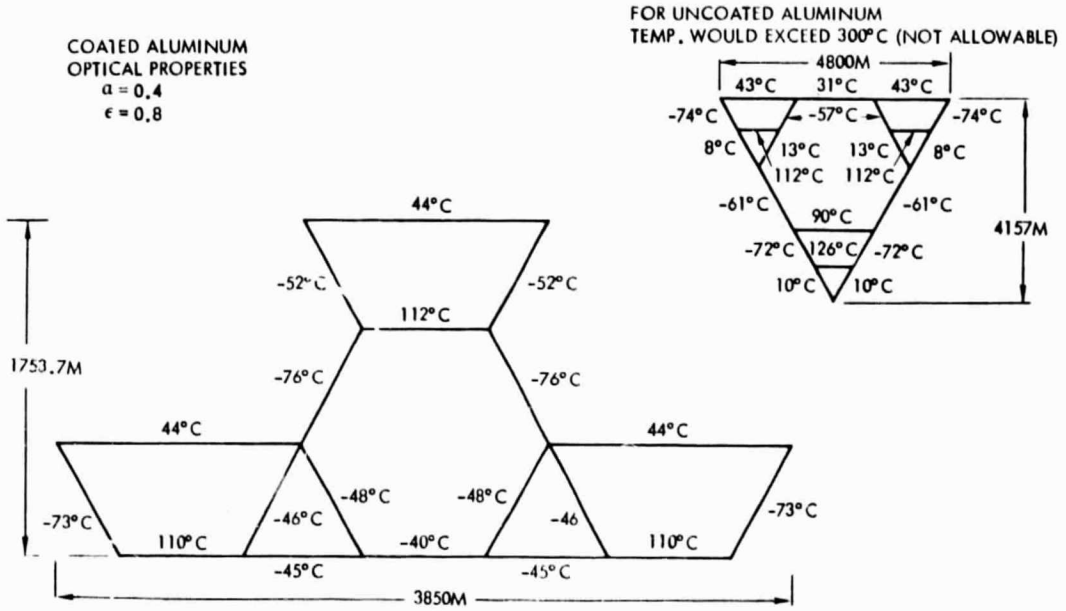

Figure 2.7-2. Photovoltaic Structural Configuration Temperatures

produced in the structure would exceed 300°C, which is well above allowable structural temperatures and thus the use of uncoated aluminum is unacceptable. There may be some concern over the use of anodization to provide desired optical properties due to possible degradation which might occur during reforming or joining operations in space. It appears that bending operations, such as brake forming, would affect the surface properties if the length change were significant. Degradation would result from cracking or crazing which would expose the underlying base material. The extent of emissivity reduction would also depend on the original thickness of the anodized film. Although some local hot spots could occur, it is not expected that the degree of additional heating would be excessive. Welding operations through an anodized layer are possible, but would likely result in poor attachment. Welding side to side would require an initial grinding or cutting operation. If the joining is end to end, a preliminary shearing step to remove the edges and expose the bare metal could be used.

The temperature of the solar blankets is 110°C to 112°C. As it is desired to operate at a temperature about 125°C to promote the GaAlAs self-annealing characteristic, some modification to the blanket design is required. Because of the temperature uniformity of the three blanket sections, any changes

introduced would be common to the array. This is an advantage over the previous baseline concept which would require selective alteration. The simplest approach is to reduce the rear surface emissivity from the design value of 0.68 to 0.36; this can be achieved at a negligible weight impact by the somewhat complex approach of vapor depositing a mosaic grid of several hundred angstroms of aluminum, or more simply by adding approximately 1/4 mil of Kapton (or Mylar) rear-surface-coated aluminum to the blanket. The required emissivity reduction would be moderated if self-annealing could be satisfied by periodic shutdown of individual bays to increase thermal loads through elimination of electrical conversion. Although not evaluated from a comprehensive system standpoint, the temperature could also be increased by raising the system geometric concentration ratio to 2.3 from 2.0; this would result if the concentrator angle was opened to 65 degrees. For the point design, the selected approach was to add the thin aluminized plastic layer.

2.7.2 POWER CONVERSION - SOLAR THERMAL

The baseline solar thermal Rankine cycle (cesium/steam) dissipates 9.35 GW of waste heat. An active radiator system was designed to reject this thermal load, following a series of analyses to identify optimal thermal control concepts.

Waste heat to be rejected and baseline system operating conditions, fin and heat pipe requirements are summarized in Table 2.7-1. It was assumed that the radiator can be continuously maintained edgewise to the sun and a coating of black anodize was selected for the aluminum fin material. The emissivity value of 0.9 was slightly above the current maximum obtained levels of 0.88, but it is expected that improved processing could increase the emmisivity. Alternately, a black paint with a higher emissivity could be substituted. The fin effectiveness of 0.8 is higher than the optimum value of 0.56 for tube/fin systems and results when plumbing weights are factored into the analysis. Radiator temperature was computed from the gradients occurring due to the interface requirements. The additional data presented were computed from the above values with subpanel size determined from volume constraints.

Table 2.7-1. Rankine System Radiator Requirements

HEAT REJECTION	9.35 GW
RADIATOR EMISSIVITY	0.9
FIN EFFECTIVENESS	0.8
RADIATOR TEMP (EFF.)	196°C
REQUIRED AREA (1 SIDE)	2.37×10^6 M^2 (2.55×10^7 FT^2)
SUBPANEL SIZE	20×20 M
NO. SUBPANELS REQUIRED	59,180
SUBPANELS/MODULE	29,590
FIN THICKNESS	0.254 CM (0.010 IN.)
TUBE SPACING	5.98 CM (2.35 IN.)
FIN LENGTH	2.99 CM (1.176 IN.)
HEAT PIPES REQUIRED	39,890,000

The most competitive forms of thermal control for this application are fully condensing and condensing/heat pipe systems. For the temperature regime and cycle design proposed, the obvious condensing fluid selection is water. Currently, the only heat pipe system which is off the shelf and reliable at 200°C is water/copper. The condensing tube alternative would use titanium tubes. It has been shown that the primary factors affecting selection are (1) substantial weight penalties for heat pipes to provide meteoroid protection (factor of two, compared to titanium) due to copper strength problems, and (2) the large number of valves (over 1 million) required for condensing tubes to provide 30-year life. Inasmuch as both alternatives are undesirable, heat pipe experts

at Rockwell, Hughes, and TRW were contacted to determine possible alternatives to copper as a container material. Two primary possibilities were identified. One was to use a copper liner encased in another material (which could be plated on the copper), such as stainless steel or aluminum. The other choice would be substitution for copper by another material. It was determined that this is probably limited to Monel (copper-nickel alloy), but that compatibility testing with water indicates that titanium is a feasible material.

One of the primary factors influencing radiator design is meteoroid protection. Accepted NASA damage correlations basically relate armor thickness to expected particle size, which is determined as a function of the product of vulnerable area and exposure time. The extrapolation of this relationship to radiator sizes and orbital lifetimes representative of SPS systems is of some concern because no experimental data exist to substantiate the models in this range. To illustrate the magnitude of shielding required, the variation of armor thickness with particle mass is presented for titanium alloy is shown in Figure 2.7-3. For particle sizes about 1 gram, the protection requirements increase at an extreme rate. Large area components that must be protected, such as radiator systems, will require armor and bumper shielding against impacts of this magnitude if strict enforcement of 30-year-life capability without maintenance is required.

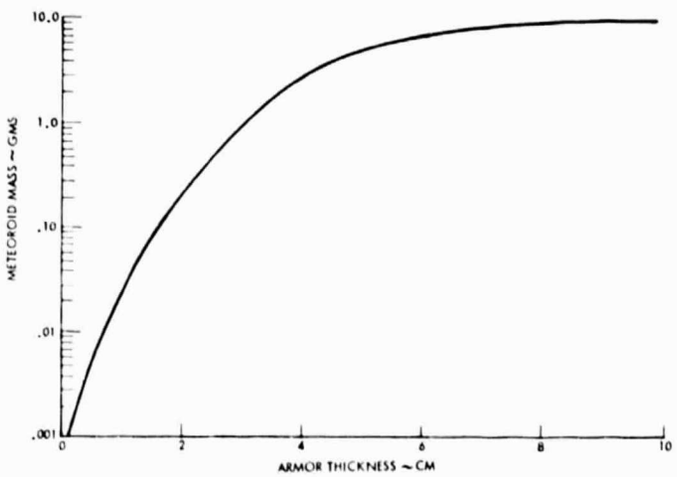

Figure 2.7-3. Titanium Tube Armor Requirements

Meteoroid protection analyses were performed for preliminary designs of both radiator systems. For the fully condensing system, optimization requires a tradeoff of armor, redundancy, and valving. From Figure 2.7-4, it is apparent that something on the order of 1 to 2 million valves is required to minimize system weight penalty. It should also be noted that redundant valves would also be required to satisfy long-life valve reliability considerations. An additional factor which must be evaluated is the placement and operational capability of associated electronics which might be exposed to the high-temperature radiator environment.

A similar analytical trade was performed to determine the desired redundancy level for the heat pipe radiator system (Figure 2.7-5). Redundancy was

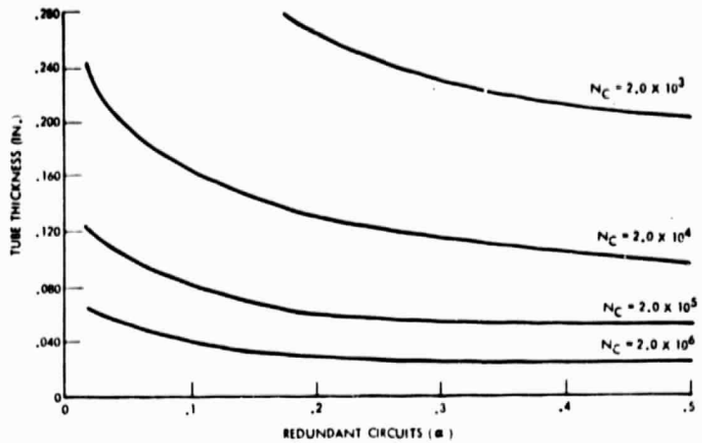

Figure 2.7-4. Armor Protection Requirements for Condensing Radiator System

factored simply by the addition of extra area, although some weight saving would result if the heat pipe spacing were reduced. In determining the effect of losing heat pipes through particle damage, it is important to note that even if the heat pipe is punctured the fin area remains and, consequently, the effect of a loss is really only some reduction in fin efficiency. Thus if, for instance, 10 percent of the heat pipes can be damaged, less than 5-percent redundancy is required in actuality.

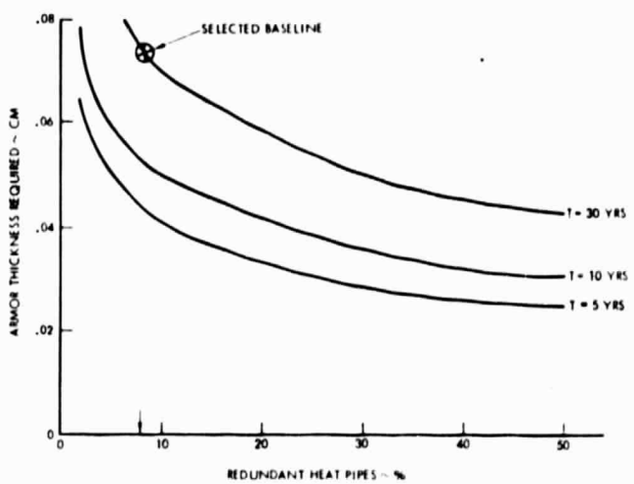

Figure 2.7-5. Heat Pipe Meteoroid Protection Requirements

The final radiator sizing was based upon the use of bumper/armor combinations where feasible, rather than sole use of armor; this results in substantial mass penalty reductions. At the conclusion of the analyses, it was determined that the weight of the competing systems was very similar and the heat pipe system was selected because of uncertainties related to valve performance/reliability/weight. The baseline point for the heat pipe design is also exhibited in Figure 2.7-5.

Specification of the heat pipes selected for the radiator is shown in Table 2.7-2. The use of an outer casing of aluminum is indicated to simplify attachment to aluminum fin and also for cost reasons. If startup after eclipse presents problems, an inert gas could be added to relieve this difficulty. This modification would be introduced if the initial low vapor pressure and interfacial thermal resistance at the condenser causes sonic or supersonic vapor velocities resulting in choked flow and large thermal gradients. The use of an inert, noncondensible gas would alleviate this problem because it has a higher pressure than the heat pipe fluid and, thus, only the vaporator heats up uniformly.

Table 2.7-2. Heat Pipe Specification

WORKING FLUID	WATER
MATERIAL	TITANIUM LINER (0.0127 CM)/ALUM. OUTER TUBE (0.0254 CM)
WICK	FLEXIBLE SCREEN
DIAMETER (I.D.)	0.9525 CM (0.375 IN.)
DIAMETER (O.D.)	1.0541 CM (0.415 IN.)
EVAPORATOR SECTION	12.45 CM
ADIABATIC SECTION	3.0 CM
CONDENSER SECTION	98.5 CM
Q_{MAX}	260 WATTS
QL_{MAX}	160 W-M (6300 W-IN.)
TUBE SPACING	2.53 DIAMETERS (BASED ON O.D.)

The radiator outline and representative details are presented in the Solar Thermal Power Conversion Subsystem section. System mass is comprised of the sum of the fin, heat pipe, fluid (water), piping, valves, and pump masses. The heat pipe totals include the contained fluid; the piping is the total for storage, mains, feeders, headers, manifolds, and through-pipes. The mass summary is presented in Table 2.7-3. Meteoroid protection includes armor and either single or double bumper (used to reduce mass penalties on the steam lines). The total system mass is 8.78×10^6 kg.

Table 2.7-3. Mass Summary

	MASS (KG)
FIN	1,804,000
HEAT PIPE (PLUS BUMPER)	5,069,100
FLUID INVENTORY	890,100
PIPING (PLUS BUMPER)	855,800
PUMPS	151,000
VALVES	16,200
TOTAL	8,786,200

The above mass represents modification of the earlier summary due to continued design refinement and the results of external studies which impacted heat pipe design. Vought Corporation conducted an in-house IR&D evaluation of the merits of condensing and heat pipe radiator systems, using baseline data provided by Rockwell that is almost identical to the final requirements (the

waste heat level was 9.56 GW). Although the Vought study only considered the radiator itself (mains, feeders, headers, and pumps were excluded), it provided some very complementary data for the final point design.

The results of the Vought condensing radiator trades are shown in Table 2.7-4. Two very interesting factors in this table are (1) the number of valves required is 1,690,288, and is close to that computed by Rockwell; and (2) the panel size optimizes at 11.8 feet (3.6 m) × 3.68 feet (1.12 m). The latter is different from the Rockwell subpanel size of 20×10 m, based upon transportation system capacity. The primary conclusions of this condensing tube optimization are (1) the selected configuration is very dependent on valve weight, which was assumed to be 2.727 kg/pair; and (2) the radiator mass is 15.69×10^6 lb (7.132×10^6 kg).

Table 2.7-4. Condensing Tube Near-Optimum Radiator Characteristics*

SYSTEM WEIGHT (MILLION LB)	15.69	TUBE DIAMETER (IN.)	0.07
NUMBER OF TUBES/VALVE	13	TUBE SPACING (IN.)	3.4
TUBE THICKNESS (IN.)	0.074	FLOW RATE PER TUBE (LB/HR)	4.14
PERCENT TUBE WEIGHT	32.4	PROB. OF NO MICROMETEOROID PENETRATION	0.82
PERCENT FIN WEIGHT	33.0		
PERCENT MANIFOLD WEIGHT	2.2	WEIGHT OF PANEL VALVES, 2 (LB)	6.0
PERCENT FLUID WEIGHT	0.1	EMISSIVITY	0.9
PERCENT VALVE WEIGHT	32.3	PANEL FIN EFFECTIVENESS	0.70
PRESSURE DROP (PSI)	20.0	T_{IN} (STEAM), °F	399.2
NUMBER OF PANELS	845,144	P_{IN} (STEAM), PSI	215.0
NUMBER OF VALVES	1,690,288	T_{OUT} (LIQUID), °F	363.0
PANEL LENGTH (FT)	11.8	P_{OUT} (LIQUID), PSI	195.0
PANEL WIDTH (FT)	3.68	VAPOR MANIFOLD DIA. (IN.)	0.187
RADIATOR AREA (MILLION FT²)	36.7	LIQUID MANIFOLD DIA. (IN.)	0.075

*SOURCE: VOUGHT CORPORATION

The results of the Vought heat pipe radiator trade are presented in Table 2.7-5. The Vought analyses contradict the earlier assumption that the system should utilize advanced, high-capacity heat pipes to minimize weight. They show that small-diameter, short heat pipes are most desirable. Using the Vought results, Rockwell has modified its earlier baseline design and, as shown in Table 2.7-2, the current water heat pipe is 0.9525 cm (3/8 in.) I.D., with a 1-m condenser section. The Vought system also optimizes at a subpanel size of 20×0.43 m and requires 720,000 valves. This conclusion is again based upon a valve weight of 2.727 kg/pair.

The Vought analyses conclude that the minimum heat pipe radiator weight is 8.2×10^6 kg (18.1×10^6 lb). Although this is greater than the summary for the fully condensing system, it still requires a very large number of valves which Rockwell feels is undesirable. The Rockwell design selected involves wrapping the heat pipes around the through-pipes to promote heat transfer and eliminate the extreme through-pipe armor requirement, which represents a substantial savings and leads to fewer valves.

In summary, the contributions of Vought Corporation to the SPS radiator point design are appreciated; two primary areas of investigation are recommended that could lead to further radiator reductions—(1) better characterization of micrometeoroid effects for very large, extended life systems, and (2) improved prediction techniques of valve performance and mass for SPS system flow regimes.

Table 2.7-5. Heat Pipe Radiator Trades*

HEAT PIPE DIA (IN.)	0.625	0.500	0.375
TUBE SPACING (IN.)	3.00	3.0	3.0
FIN THICKNESS (IN.)	0.01	0.01	0.01
HEAT PIPE LENGTH (FT)	1.41	1.41	1.41
HEAT PIPE TUBE THICKNESS (IN.)	0.028	0.027	0.026
THROUGH-PIPE DIA. (IN.)	0.344	0.344	0.344
THROUGH-PIPE TUBE THICKNESS (IN.)	0.110	0.110	0.110
MANIFOLD LENGTH (FT)	65.5	65.5	65.5
PANEL PRESSURE DROP (PSIA)	20.0	20.0	20.0
PANEL FLOW RATE (LB/HR)	121.6	121.6	121.6
PANEL LENGTH (FT)	65.5	65.5	65.5
PANEL WIDTH (FT)	1.41	1.41	1.41
NO. HEAT PIPES PER PANEL	262	262	262
AVG FIN EFFECTIVENESS	0.75	0.75	0.75
AVG RADIATING TEMP (°F)	379.3	379.3	379.3
EMISSIVITY	0.9	0.9	0.9
NO. SIDES RADIATING	2	2	2
NO. PANELS/VALVE	1	1	1
HEAT PIPE MICROMETEOROID PROB.	0.80	0.82	0.85
MANIFOLD MICROMETEOROID PROB.	0.95	0.95	0.95
WEIGHT (LB × 10^6)	23.15	20.57	18.10
AREA (ONE SIDE) × 10^6 FT^2	34.37	33.85	33.10
NO. PANELS × 10^6	0.373	0.368	0.360
NO. VALVES × 10^6	0.746	0.736	0.720
NO. HEAT PIPES × 10^6	97.73	96.42	94.32
T_{IN}, °F (°C)		399.2 (204)	
T_{OUT}, °F (°C)		363.2 (184)	
P_{IN} (PSIA)		215	
ΔP (PSIA)		20.0	

*SOURCE: VOUGHT CORPORATION

2.7.3 MICROWAVE ANTENNA

Thermal control of the microwave antenna includes protection of the klystrons and associated electronics, the antenna structure, and consideration of the impact of antenna thermal response on the rotary joint.

The antenna structure configuration can experience minimal distortions/deflections due to imposed thermal gradients/stresses. A thermal model of the hexagonal frame/web structure was developed for variable solar orientations to determine peak operating temperatures and thermal gradients, and to support dynamic structural response computations. The model, shown in Figure 2.7-6, assumed that the earth side of the web could be treated as an isothermal section at T = 200°C, and the space side of the web could be fixed at an isothermal temperature of 60°C. This represents a simplification because the hot side of the web will vary with time due to solar loading and will vary with distance from the center due to RCR density and size variation. There may also be some influence by the higher temperature collector radiators (≈700°C) on structural temperature. The space side of the antenna changes temperature with sun loading also, and will probably operate between 0°C and 60°C (effective temperature).

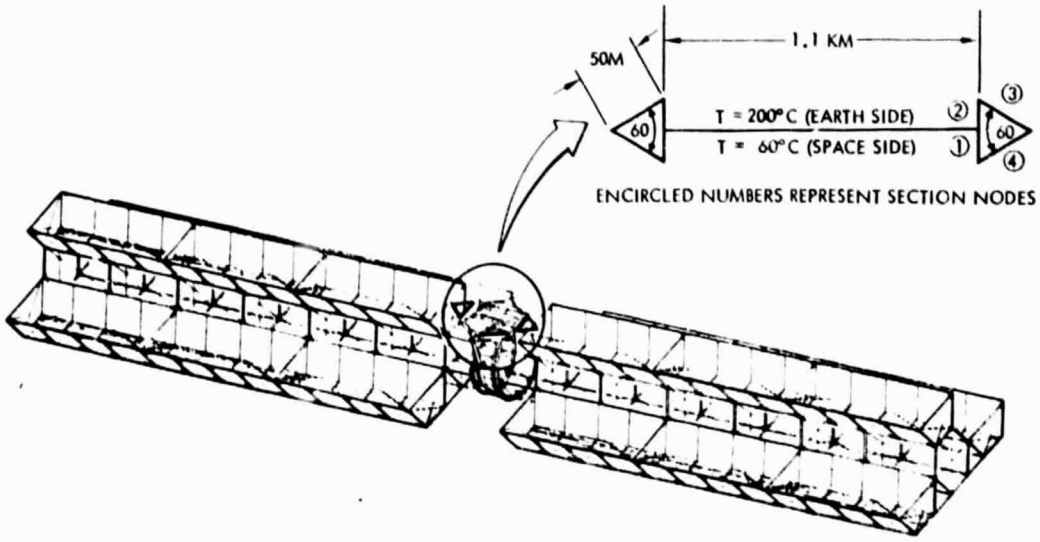

Figure 2.7-6. Antenna Frame/Web Model

Nodal points were selected as shown (Figure 2.7-6), and a thermal analysis was conducted assuming that each section can be represented as a uniform node at a single temperature. View factors to space and from element to element were determined from an exact representation of the section by using the CONFAC computer code.

Due to variation in solar incidence during each orbit, the sections of the frame will experience time-varying temperature. Temperature profiles are shown in Figure 2.7-7 for a typical orbit representing the response of a low α/ε

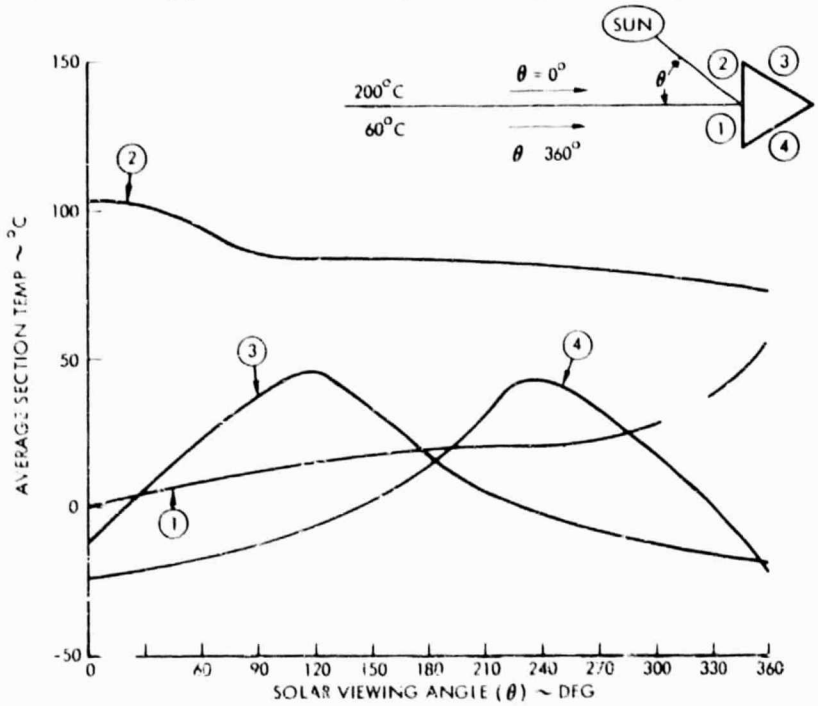

Figure 2.7-7. Frame Temperature Variation with Solar Orientation (BOL)

anodize structural coating and, in Figure 2.7-8, for a degraded coating condition. (It could also represent a "dark" or high α/ε anodize structural coating.) For an eclipse condition, the minimum temperature levels and thermal profiles would markedly change. Temperature gradients during construction would also influence the structural design.

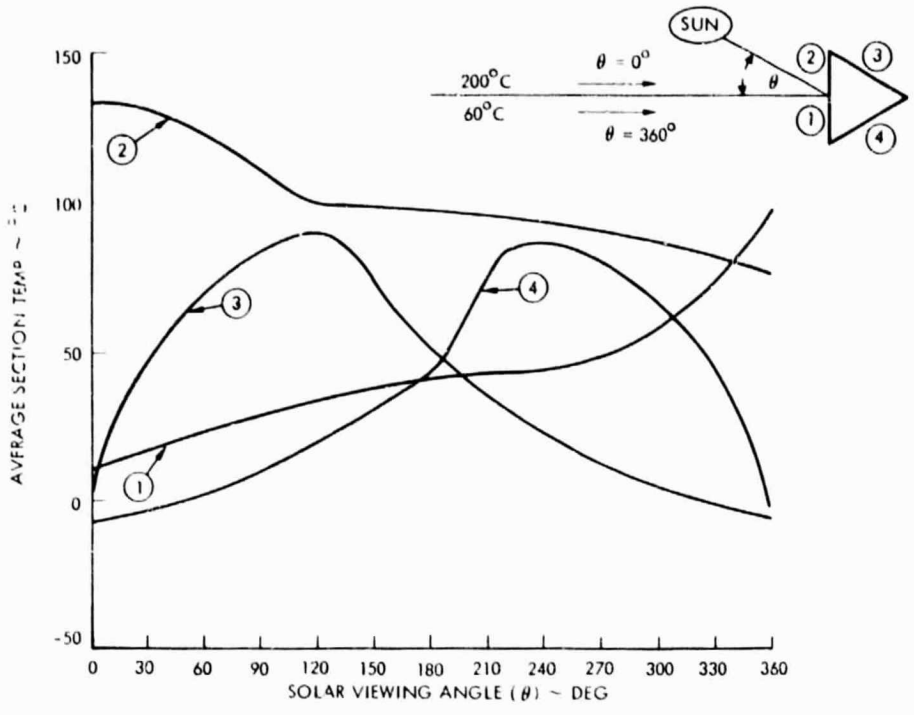

Figure 2.7-8. Frame Temperature Variation with Solar Orientation (EOL)

A thermal control design was developed for the klystron tubes is dissipate the waste heat levels and minimize interactions with the antenna structure and rotary joint. The thermal rejection requirement includes a cavity heat load of 3.267 kW and a collector heat load of 7.454 kW. It was determined that a heat pipe radiator for the cavity tube would provide a high-confidence/low-mass system. The relative orientation of the slots and the heat pipes in the baseline RCR is shown in Figure 2.7-9, along with the relative location of the insulation and electronics. An alternate configuration in which the collector radiates heat toward space is illustrated alongside the baseline design. This latter concept was proposed to eliminate the necessity of passing the klystron through the RCR, which reduces beam efficiency by 3 percent. However, this design has the disadvantages of (1) requiring a thermal shield to isolate the electronics from the collector, (2) substantial heating of the rotary joint structure by the collector waste heat (above 370°C), and (3) decreased accessibility of the antenna for maintenance operations. Because of these negative aspects, the initial configuration was retained for the baseline design.

The RCR design as shown (Figure 2.7-9), is representative of a unit near the center of the antenna. Modules will vary in size and heat pipe spacing/number throughout the antenna. A top view exhibiting relative orientation of the klystron pipes is presented in Figure 2.7-10. The heat pipes all use water

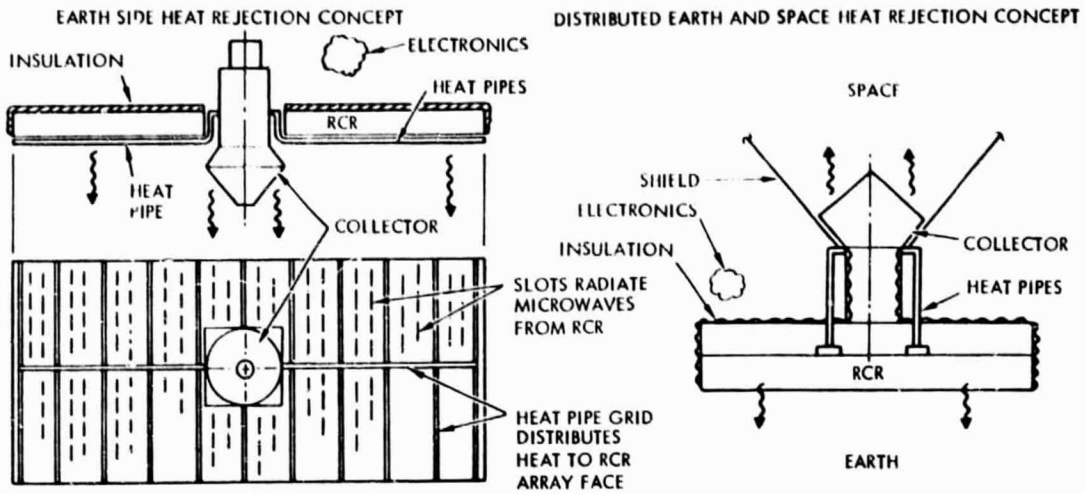

Figure 2.7-9. Klystron/RCR Configuration

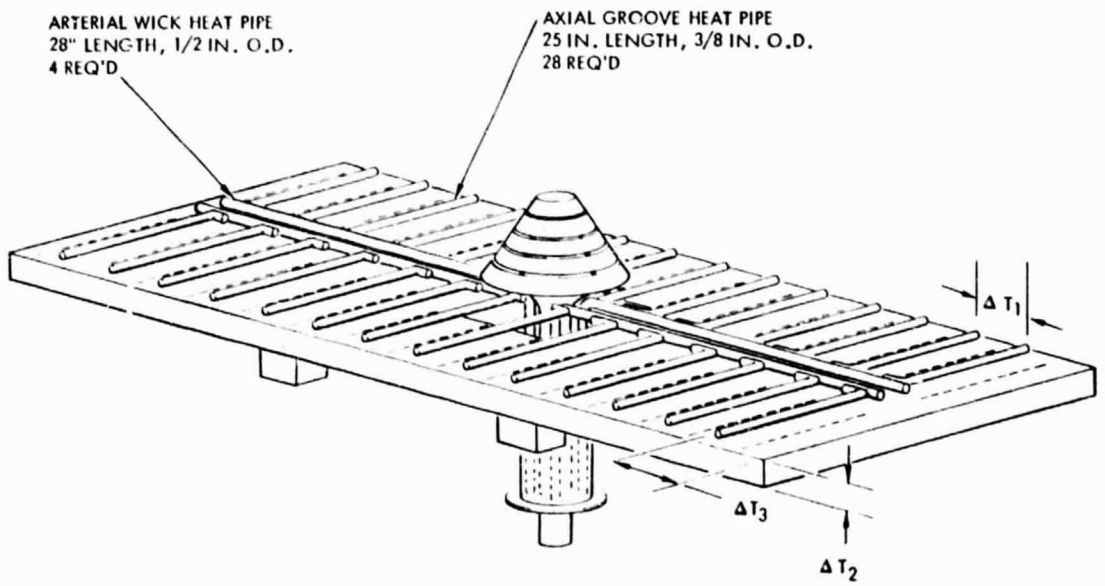

Figure 2.7-10. Klystron Radiator Configuration

as a working fluid encased in a copper liner. The outer tube is aluminum to eliminate the single-point contact of dissimilar metals. The spacing of the axial groove heat pipes is 11.4 cm. Any one of the arterial wicked pipes can fail and the system will still reject the incident heat load and maintain allowable temperature limits, although the structural response for this mode must be evaluated. There are four of these arterial wick pipes, each 1/2 inch O.D.; and 28 axial groove pipes, each 3/8 inch O.D. The layout of the pipes is dictated by the microwave slots which will not permit a more optimal radial distribution. Total mass of this subsystem is 6.18 kg.

Thermal distortions may occur as a result of various temperature gradients occurring in the RCR as shown in Figure 2.7-11. The temperature drop across the fin length will be about 40°C. Thermal gradients from one face of the RCR to the other face are shown as a function of internal emissivity. The value of 0.9 corresponds to the use of a high emissivity coating (e.g., black anodize) and the lower limit of 0.1 is representative of bare aluminum. Gradients at the end of the RCR depend upon the fraction of the surface that is used for radiator, and the view factor variation to the collector radiator. The value shown (63°C) is an average value for the high-density portion of the antenna.

ΔT_1 • TEMP DROP BETWEEN HEAT PIPES

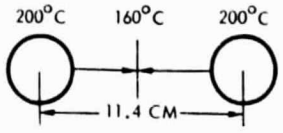

ΔT_2 • TEMP DROP FROM TOP OF RADIATOR TO BOTTOM OF RADIATOR

EMISSIVITY OF OPPOSITE SURFACE	ϵ	ΔT °C
	0.9	3°
	0.5	5°
	0.1	21°

ΔT_3 • TEMP DROP FROM END OF HEAT PIPES TO END OF KLYSTRON RCR = 200°C ⟶ 137°C

Figure 2.7-11. Related Design Configurations

Distortions/stresses in the power module must be analyzed to determine if the transmission efficiency losses can be restricted to an allowable level for the current design. If this is not possible, several alternatives are available. These include substitution of *Lockalloy R* (a beryllium-aluminum alloy which is currently rather expensive, but could conceivably come down substantially in cost, or mild steel which is relatively heavy). Some form of advanced composites could also prove applicable.

The collector radiator (Figure 2.7-12) is required to dissipate the 7.5 kW of waste heat dissipated due to beam inefficiencies. The pyrolytic graphite structure must have a relatively high fin efficiency to maintain local temperature below 700°C. If required, radiation shields can be used to isolate the collector from the cavity radiator. This would reduce the effective rejection capability and require higher temperature operation on thicker fins. The effect of fin efficiency on radiator temperature is shown in Figure 2.7-13. It can be seen that the minimum possible operating temperature is only slightly below 700°C. This assumes that the waste heat distribution can be controlled and is rejected equally from the radiator segments.

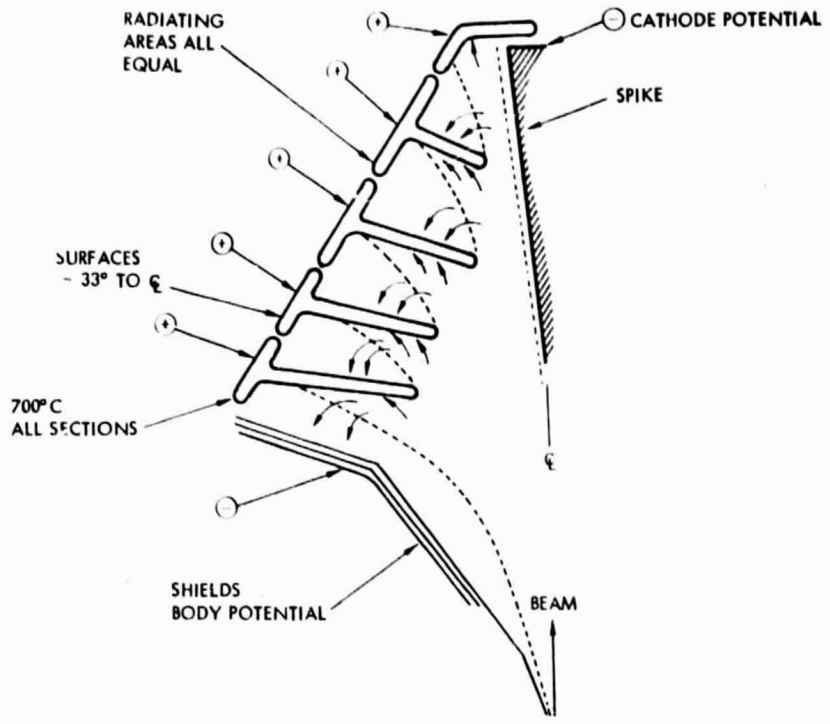

Figure 2.7-12. Collector Radiator

- ASSUME RAD FIN IS PYROLYTIC GRAPHITE
- COLLECTOR AREA IS 0.173 M^2

  (8 IN. HIGH CONE, r_1 = 7 IN., r_2 = 1.75 IN.)

  ASSUME ALL SECTIONS EQUAL

  ASSUME $\alpha = \epsilon = 0.9$

  ASSUME SOLAR FLUX (EFF) = 35 WATTS

FIN EFFICIENCY η	TEMP ^{o}C	
1.0	687	
0.9	712	← BASELINE DESIGN
0.8	742	
0.7	776	
0.6	818	
0.5	868	
0.4	934	

Figure 2.7-13. Collector Radiator Analysis

Insulation is required for the back surface of the cavity radiator to restrict waste heat leaks which could increase temperature of the electronics to unacceptable levels. This insulation must be coated externally with low α/ε materials to limit the absorbed solar flux to which the surface is exposed during part of the orbit. Although many materials with low absorptivity/emissivity ratios are available, they typically experience substantial degradation as a function of solar exposure time. To limit the rear surface to 60°C (maximum allowable temperature of electronics), it is seen in Figure 2.7-14 that the maximum α/ε ratio is about 0.5, which is below values typically obtained for extended-life inexpensive insulations. If refurbishment of degraded blanket is not possible, the electronics could be protected by isolation in finned containers or by use of active cooling. Alternatively, advanced blankets using more expensive external surfaces (e.g., quartz microsheet) could be applied at some cost penalty.

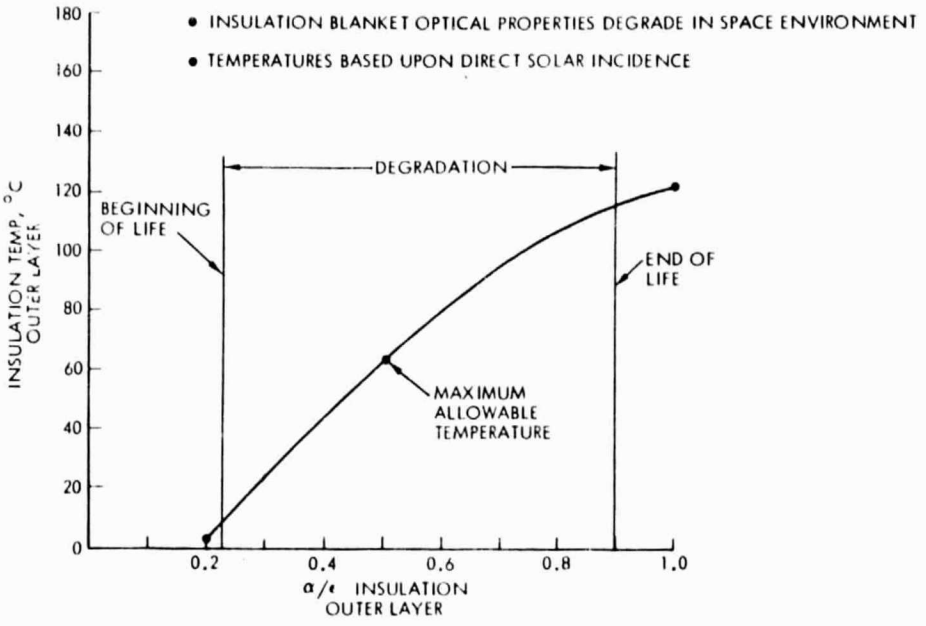

Figure 2.7-14. Rear Surface Cavity Radiator Thermal Response

2.7.4 ROTARY JOINT

The orientation of the rotary joint relative to the photovoltaic structure and the antenna is shown in Figure 2.7-15. Proximity to the space-facing side of the antenna substantially influences both the antenna design and the rotary joint thermal environment. Temperature levels for the slip rings and brush boxes were computed for the design configuration. The slip rings were assumed to be aluminum-core/coin-silver cladding of 1.1 km diameter, and I-beam shape with a current/wing design value of 112,500 A.

The temperatures shown in Figure 2.7-16 represent average values for the inner slip ring based on a voltage loop of 20 V across the slip ring-brush interface. For aluminum, the maximum allowable operating temperature is about 150°C. To provide assurance of structural integrity, it is necessary to

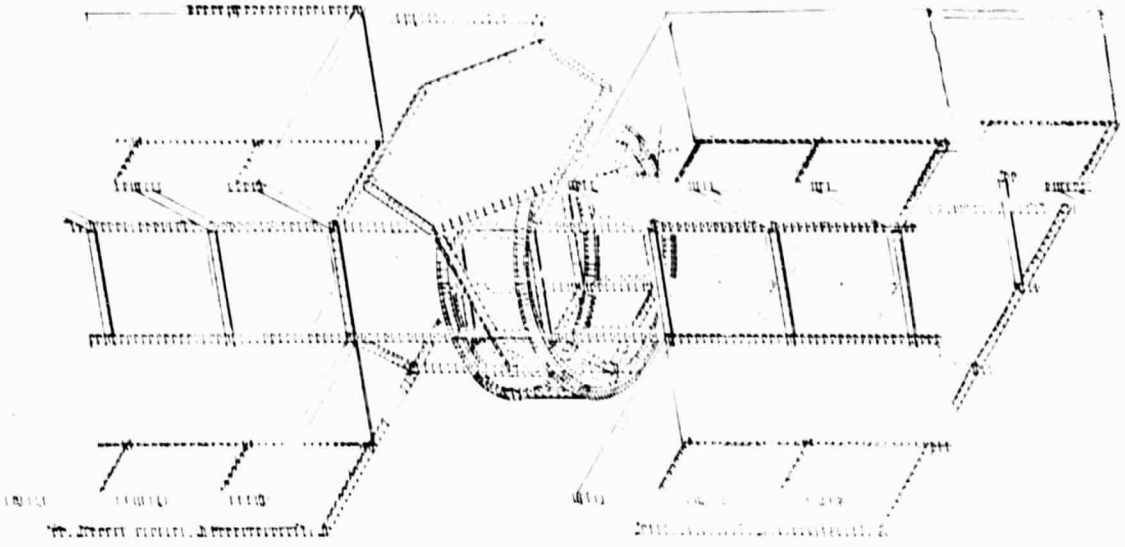

Figure 2.7-15. Rotary Joint Installation

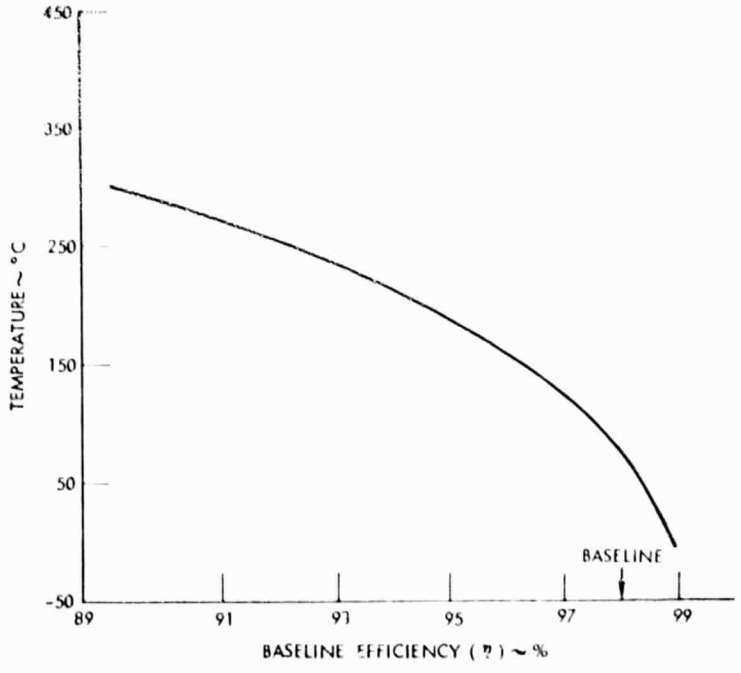

Figure 2.7-16. Slip Ring Temperature Variation with Efficiency

demonstrate that excessive stresses do not result from the thermal gradients developed in the rings. Both rings were thermally modeled to include the effects of electrical inefficiencies, antenna interactions, and solar heating. Temperature levels are shown in Figure 2.7-17. The outer ring can reach a higher temperature because it shields the inner ring from the sun. Brush assembly temperatures will approximate the slip ring values due to conduction across the contact area. Additional electrical losses are relatively negligible. During eclipse, the klystrons must be kept warm and thus some relatively large gradients may occur because radiation from the antenna is the sole heating source.

- INNER RING 65°C TO 115°C
- OUTER RING 65°C TO 130°C
- BRUSH ASSEMBLY TEMPERATURES SIMILAR TO SLIP RING VALUES
- FOR ALTERNATE KLYSTRON DESIGN RING TEMPERATURE CAN EXCEED 370°C
- ECLIPSE PROFILES NOT YET DETERMINED - MAY BE VERY SEVERE

Figure 2.7-17. Rotary Joint Temperature Gradients

2.7.5 RECTENNA

The rectenna configuration used to develop a thermal model to predict local temperature profiles is shown in Figure 2.7-18. Optical properties for the panel elements are based on those of mylar for the thicknesses shown on the module. Rectenna thermal model development included consideration of solar heating, local air convection, and waste heat arising from microwave conversion inefficienecies.

Temperature profiles are shown in Figure 2.7-19 for the rectenna panels in the high-density region. During the daylight hours, air convection tends to cool the panels and at night it acts as a heating source. The effect of air convection on the gradients is substantial, as evidenced by the large difference from the root to the end which arises due to transition from laminar to turbulent flow. Ground temperatures will typically be within 6°C of the module levels and will be somewhat warmer than the evening levels and cooler than the daytime values. For different climates (wind, overcast sky, air temperature) the temperatures will vary. In outer regions of the rectenna, the waste heat arising from conversion inefficiences will be reduced—but this is a small fraction of the total heat load and will not greatly influence panel temperature levels. The thermal environments computed for the current rectenna configuration do not differ greatly from earlier analyses and it is expected that influences on the microclimate would be relatively unchanged from current predictions.

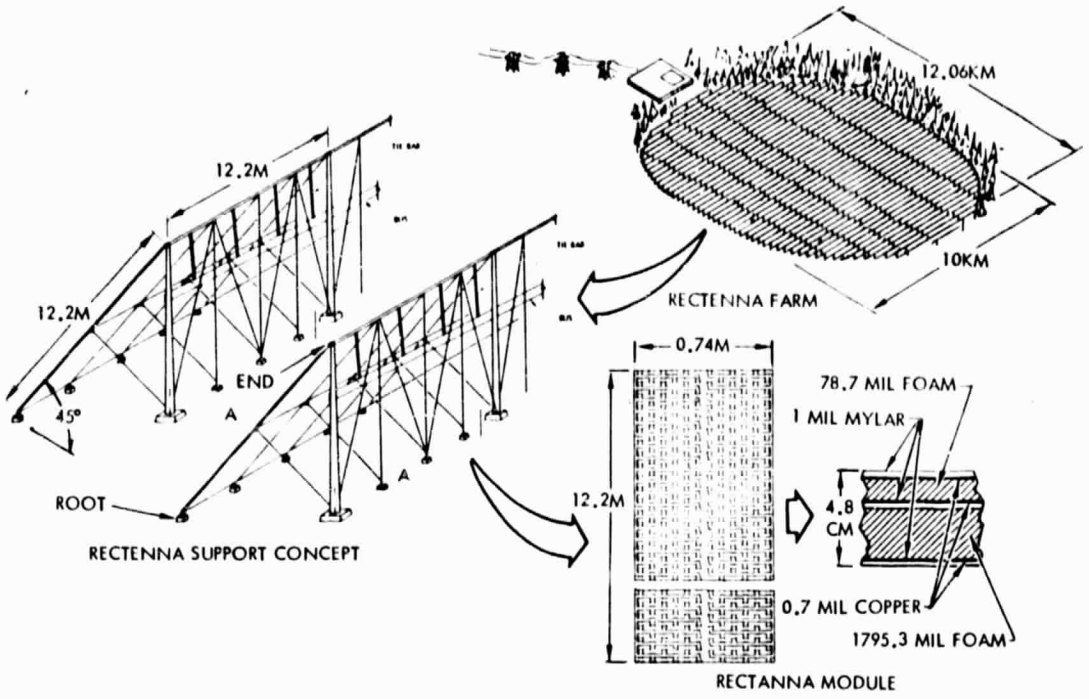

Figure 2.7-18. Microwave Transmission Subsytem—Rectenna

	DAY (PEAK SUN)	NIGHT
ROOT	56°C (132°F)	-17°C (2°F)
END	33°C (92°F)	18°C (64°F)

AIR TEMPERATURE = 27°C (80°F)

- CONDUCTION IN RECTENNA PANEL NEGLECTED
- ALL COMPUTATIONS BASED UPON STEADY STATE EQUILIBRIUM; GROUND HEAT SINK EFFECT NOT INCLUDED

Figure 2.7-19. Rectenna Panel Temperatures, High-Density Microwave Region

2.8 INFORMATION MANAGEMENT AND CONTROL SUBSYSTEM

2.8.1 INTRODUCTION

Initial and preliminary analyses and trades (Reference 1,2) have been performed to establish a basis for the selection of a baseline design for the SPS Information Management and Control Subsystem (IMCS). These analyses and trades have been performed by IBM under a subcontract from Rockwell and have pointed to a distributed data processing system as the favored approach. In the distributed system a hierarchy of remote micro-, mini-, supervisory and master computers is combined into an integrated processing system. Concurrent data bus analyses have favored an inter-computer communications network which utilizes a fiber optics technology. As stated in the opening sentence, these conclusions are very preliminary because much work remains to be performed in: 1) projecting technology and related technology characteristics to the late 1980's and early 1990's and 2) defining requirements for the IMCS. However, the projections and data available today are adequate to warrant the selected approaches for baseline configuration and study.

2.8.2 DESIGN APPROACH

The IMCS design selected for the baseline study is shown in top level block diagram in Figure 2.8-1. This diagram illustrates a simplex (non-redundant) system. A candidate spatial distribution for the distributed system for a two trough photovoltaic configuration is shown in Figure 2.8-2. Local computer centers are envisioned to be located at stations about 1/3 and 2/3 along each wing and at the wing end sections. Section 6 left and 6 right (each sing is divided into 600 meter sections and numbered 1 to 21) would house processing centers for thermal and power controls. The wing end sections would house attitude control support centers. Processing support to structure alignment, microwave antenna beam pointing control, and additional attitude control functions would be housed in the center section.

Three levels of data processing are illustrated in Figure 2.8-1: Master, Supervisory, and Remote. Subtiered to this hierarchy are microprocessors, Remote Acquisition and Control Units (RAC), and Submultiplexors (SM). Microprocessors as stand-alone processors have only been identified for the microwave antenna beam pointing function. The processing approach for this function is illustrated in Figure 2.8-3. A typical processing system to support other subsystems is shown in Figure 2.8-4 for the power distribution subsystem.

The distributed system was selected because of its strong evaluation in the area of software complexity, performance (lower MIPs), reliability, and safety. These are further discussed in Reference 1 and will not be repeated

---

1. *Satellite Power System, Satellite Information Management and Control Subsystem (IMCS), Central versus Distributed Processing Trades,* 1 August 1977, IBM Federal Systems Division

2. *Satellite Power System, Satellite Information Management and Control Subsystem (IMCS), Data Bus Trades,* 26 July 1977, IBM Federal Systems Division.

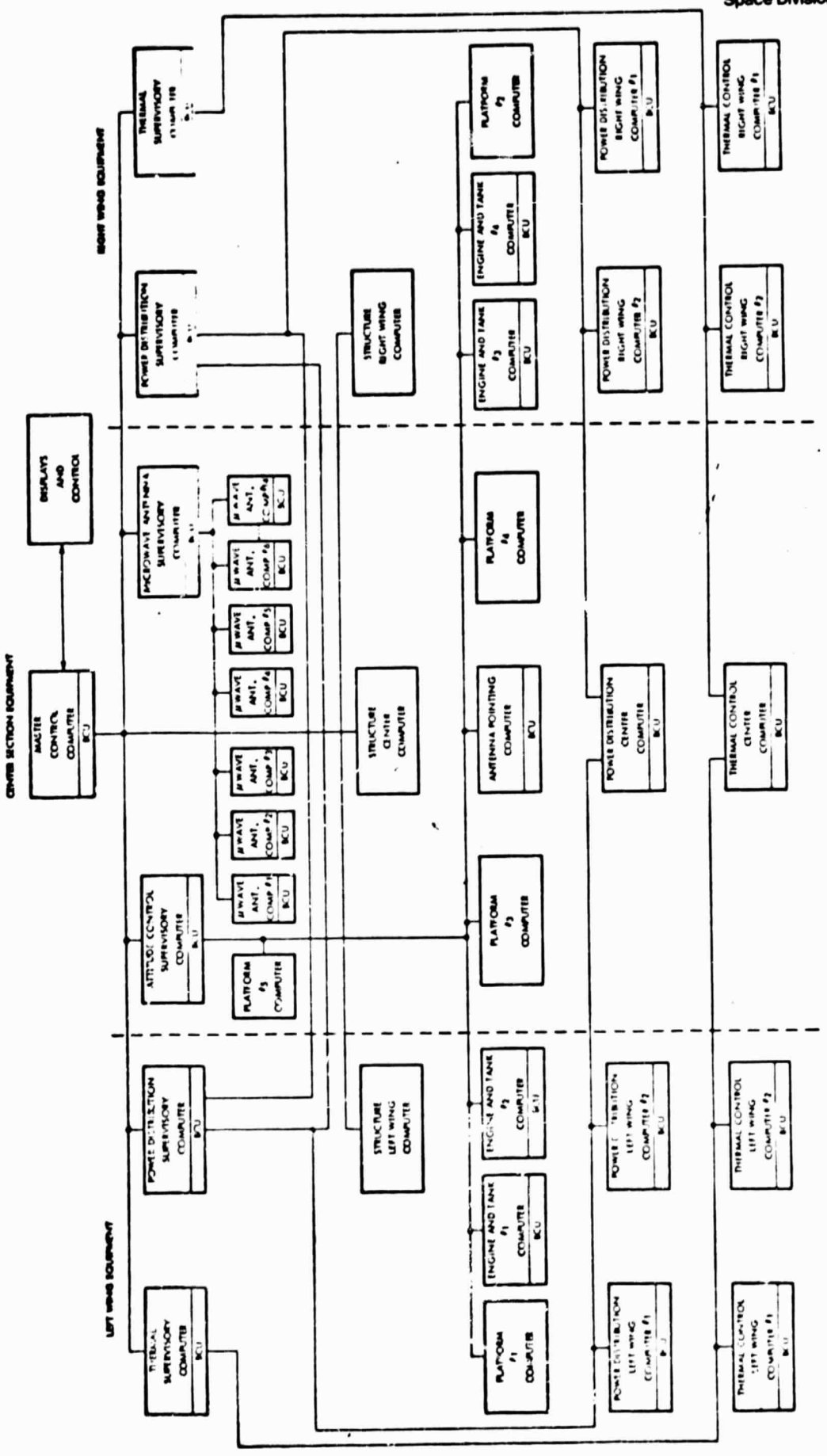

Figure 2.8-1. SPS IMCS Top-Level Block Diagram

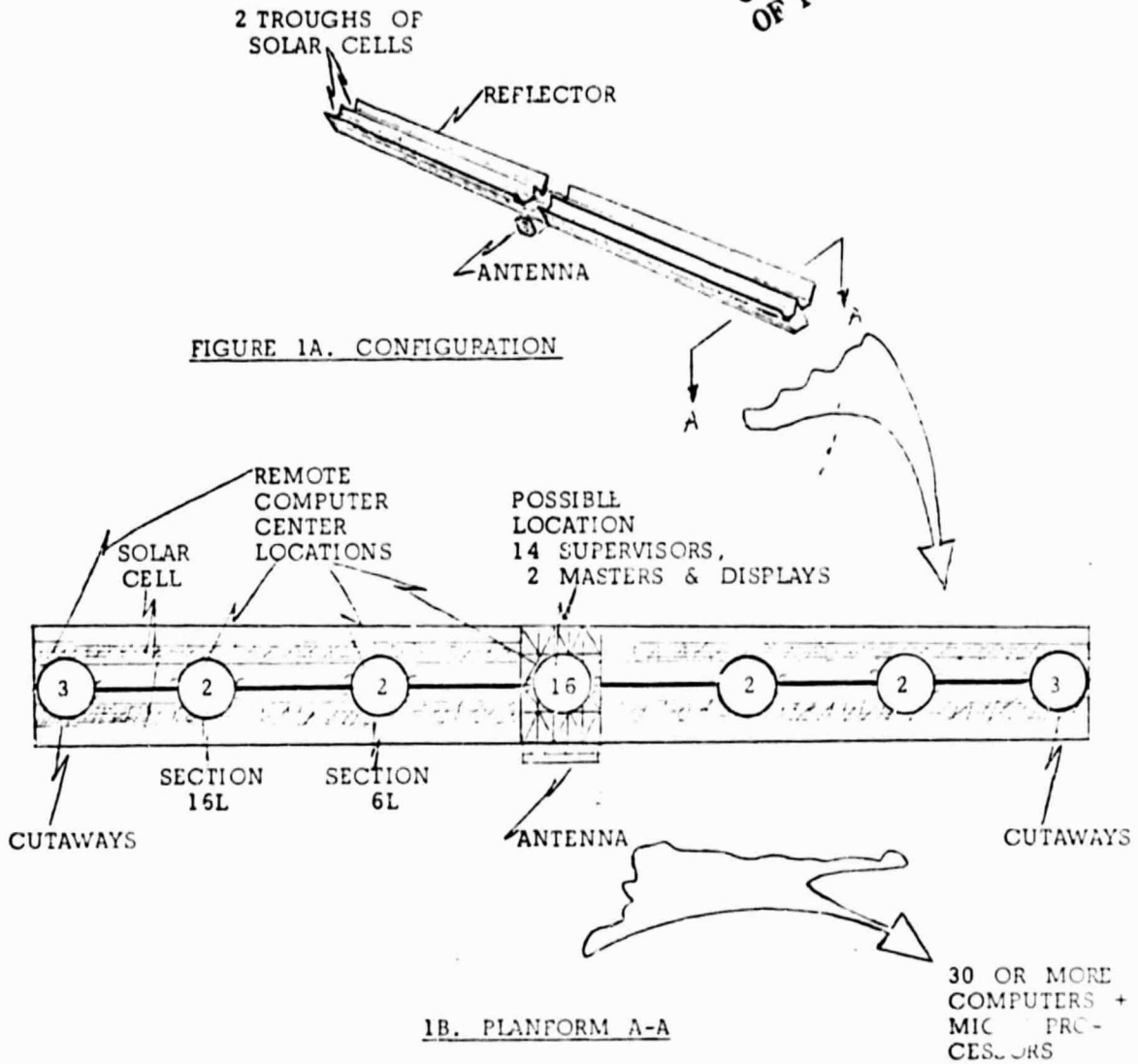

FIGURE 1A. CONFIGURATION

1B. PLANFORM A-A

Figure 2.8-2. Distributed Computer Concept

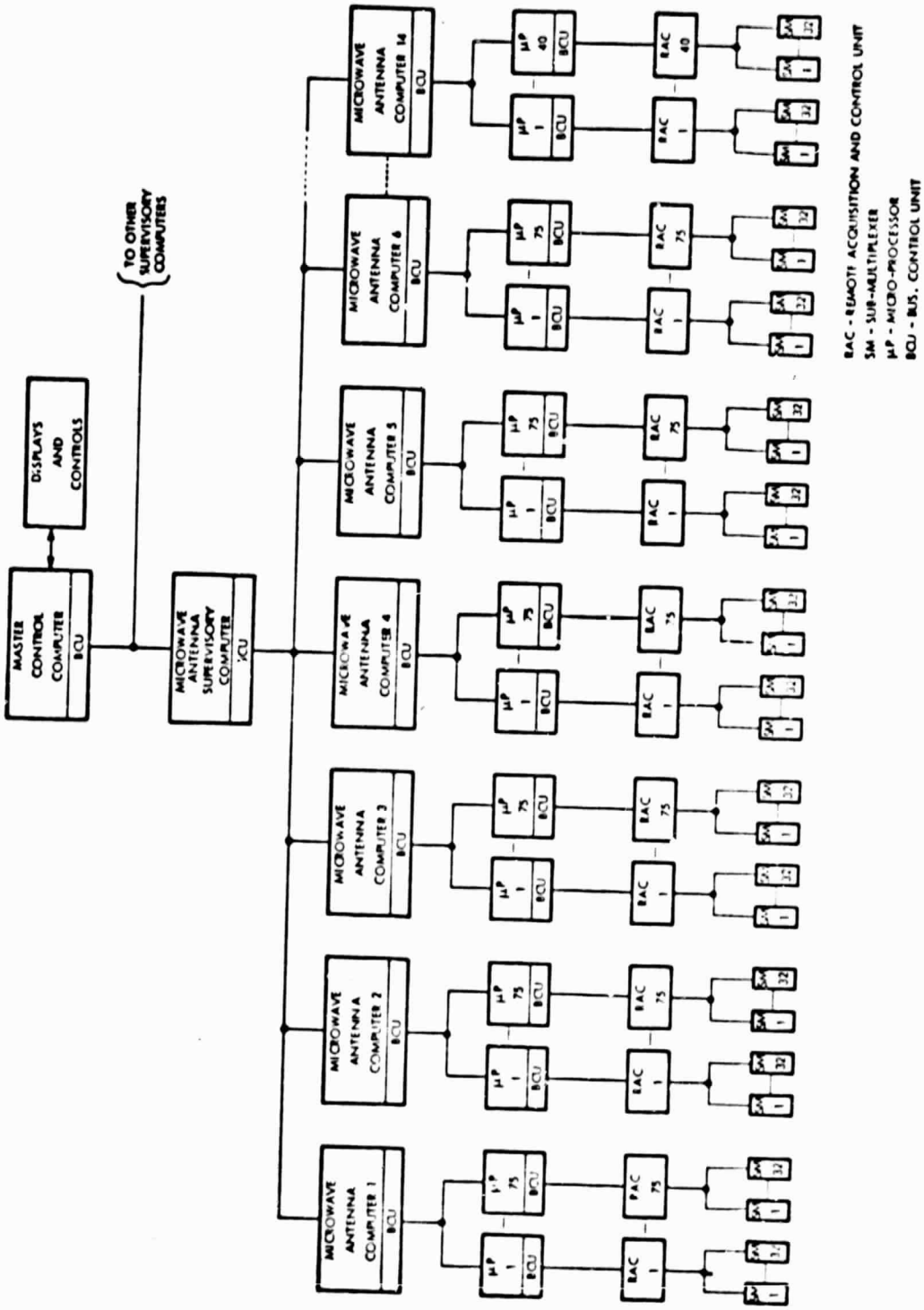

Figure 2.8-3. IMCS - Microwave Antenna

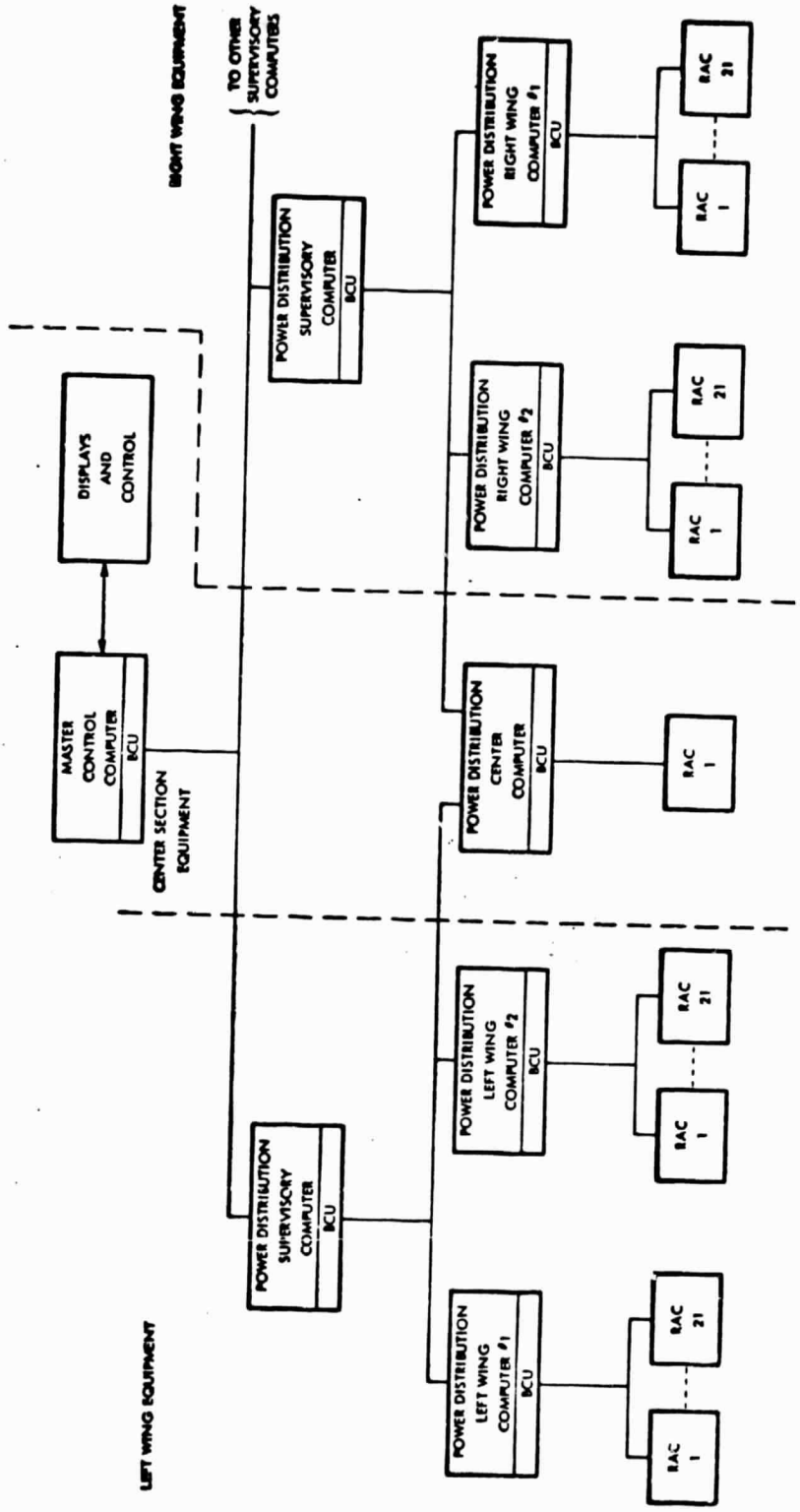

Figure 2.8-4. IMCS - Power Distribution

C-3

here. Inherent in the low MIPs requirement is the spreading of computational loads so that any given computer cap probably be quite low in performance, e.g., <1.0 to 2.5 MIPS. This concept begins with the lowest system element, the submultiplexor, which services many sensors and incorporates a small microprocessor for limit checking, local thresholding, alarming, and control. The SM sends its outputs to RACs which might service 10 to 30 SMs. The RAC may also incorporate a microprocessor sized to its computational load. The baseline system utilizes 684 RACs and 17.180 SMs.

By concentrating computational capability at the "User" location, constant and immediate attention can be given to anomalies and other discrepancies which may arise. Out of tolerance or other unusual situations can be flagged for attention of the remote, supervisory or master control computers. These upper level computers function primarily to maintain control of the multiplicity of lower level processors and also to analyze out of tolerance situations for corrective action or reporting to ground and/or satellite master display and control stations.

Assumed characteristics of the processing elements used in the baseline system are given in Table 2.8-1. A summary of the equipment components together with the baseline system weight, power and volume characteristics are given in Table 2.8-2 and 2.8-3 respectively.

A fiber optics data bus concept has been selected for the data interconnection paths between the various system computers and between computers and their RACs. It is now anticipated that wire interconnections will be adequate at the lower levels where shorter run distances prevail and locations are remote with respect to high EMI levels.

Fiber optics technology was chosen for the data bus because of its low susceptibility to electromagnetic interference, low weight, low losses, and projected low cost. Typical projected characteristics of 1 channel/1 fiber optics (Corning Glass) are as follows:

- 200 to 1500 μm outside diameter (OD) depending on sheathing thickness, such as ethylene vinyl acetate, and core fiber diameter, which is typically less than 62 to 85 μm.
- 0.14 kg/km
- <3 to 6 dB/km line loss.

Table 2.8-1. Assumed Equipment Characteristics

COMPUTERS	WT (KG)	PWR (KW)	VOL (M^3)	SPEED (BIPS)
• MASTER CENTROL COMPUTER FOR SATELLITE	500	2	0.4	1-5
• GENERAL PURPOSE FOR DISTRIBUTED SYSTEM	14	0.07	0.01	0.025
• ANTENNA MICROPROCESSORS	5	0.02	0.003	0.05
• DATA BUS CONTROL UNIT (BCU)	5	0.02	0.005	0.001
• RAC W/MICROPROCESSOR	5	0.02	0.005	0.001
• SM W/MICROPROCESSOR	3	0.01	0.003	0.001

Table 2.8-2. IMCS Hardware Summary

HARDWARE ELEMENT	FUNCTION							
	MASTER CONTROL COMPUTER	DISPLAY AND CONTROL	SUPER-VISORY COMPUTER	REMOTE COMPUTER	MICRO-PROC.	BUS CONTROL UNIT	REMOTE ACQUIS. AND CONTROL	SUB-MUX
SATELLITE CONTROL	2	1	-	-	-	2	-	-
THERMAL CONTROL	-	-	2	5	-	7	85	1,352
STRUCT. ALIGN.	-	-	-	3	-	3	-	-
ATTITUDE CONTROL	-	-	1	10	-	11	28	148
POWER DISTRIB.	-	-	2	5	-	7	85	-
MICROWAVE ANTENNA CONTROL	-	-	1	14	777	792	787	29,500
TOTAL	2	1	6	37	777	822	985	31,000

Table 2.8-3. IMCS Weight, Power, Volume Summary

NON ROTATING

HARDWARE ELEMENT	QUANTITY	UNIT MASS (Kg)	TOTAL MASS (Kg)	UNIT POWER (KW)	TOTAL POWER (KW)	UNIT VOLUME (m^3)	TOTAL VOLUME (m^3)
MASTER CONTROL COMPUTER	2	500	1,000	2	4	0.4	0.8
DISPLAY & CONTROL SET	1	200	200	0.9	0.9	0.72	0.72
SUPERVISORY COMPUTER	5	14	70	0.07	0.35	0.01	0.05
REMOTE COMPUTER	23	14	322	0.07	1.61	0.01	0.23
MICRO PROCESSOR	-	5	-	0.02	-	0.003	-
BUS CONTROL UNIT	30	5	150	0.02	0.6	0.005	0.15
REMOTE ACQUISITION & CONTROL	198	5	990	0.02	3.96	0.005	0.99
SUB MULTIPLEXOR	1,500	3	4,500	0.01	15.0	0.003	4.5
SUBTOTAL			7,232		26.42		7.44

ROTATING

MASTER CONTROL COMPUTER	-	500	-	2	-	0.4	-
DISPLAY & CONTROL SET	-	200	-	0.9	-	0.72	-
SUPERVISORY COMPUTER	1	14	14	0.07	0.07	0.01	0.01
REMOTE COMPUTER	14	14	196	0.07	0.98	0.01	0.14
MICRO PROCESSOR	777	5	3,885	0.02	15.54	0.003	2.331
BUS CONTROL UNIT	792	5	3,960	0.02	15.84	0.005	3.96
REMOTE ACQUISITION & CONTROL	787	5	3,935	0.02	15.74	0.005	3.935
SUB MULTIPLEXOR	29,500	3	88,500	0.01	295.0	0.003	88.5
SUBTOTAL			100,440		343.17		98.876
TOTAL			108,000		369.6		106.3

CABLE

NON ROTATING-WIRE (22GA)	1,200 KM	12.0/KM	14,000			2×10^{-5}/KM	0.48
FIBER OPTICS	90 KM	0.14/KM	12			2×10^{-6}/KM	
ROTATING-WIRE	23,000 KM		279,000				
FIBER OPTICS	350 KM		50				
TOTAL			293,000				0.48

3.0 MASS PROPERTIES

The detailed mass properties of two selected point design concepts, the GaAlAs solar cell concept and the cesium steam Rankine solar thermal concept are presented in this section. Tabular data indicating mass changes in the design configuration from the mid-term design to the final point design configuration are presented. The results of a computer program tabulation for determining the center of gravity and the moments of inertia for the photovoltaic configuration is included in the data.

3.1 GaAlAs PHOTOVOLTAIC POWER CONVERSION SUBSYSTEM

3.1.1 MASS PROPERTIES STATUS

The mass of the current SPS versus mid-term mass are shown in Table 3.1-1. Current SPS point design configuration mass estimates, based on Figure 2.1-1, have resulted in a gross weight increase of 8.56% over the mid-term configuration. It will be noted that there was a reduction in the collector array mass which helped to reduce the overall SPS mass increase which was caused by sizable increases in the antenna subsystem (primarily in the power distribution and control). Table 3.1-2 explains the reasons for these mass changes.

3.1.2 BASIS FOR CURRENT MASS ESTIMATES

The design of the primary structure is based on the utilization of a 10-mil aluminum material for use in the fabrication of the tribeams. The structural beams consists of 50-meters-on-a-side triangular sections and has specific mass of 4.766 kg/m of length. Secondary structure consists essentially of equipment supports, tensioning devices, standoffs and catenary membranes for attachment of solar blankets and reflectors. The antenna design is based on tension webs of 14-mil graphite epoxy supported by an 0.0805-m-diameter (3.17 in.) Kevlar catenary rope which, in turn, is supported by the compression frame which is constructed of the standard 50-m beams. Mechanism mass include rotary joint actuation plus antenna array actuation system.

Attitude control system mass includes the mass of 720 ion thrusters, power processors, and associated argon and tankage plus plumbing for the SPS.

The required solar cell blanket area for the SPS is 30.6 km^2 and has a specific mass of 0.2525 kg/m^2. The solar reflector area for the point design is 61.2 km^2 of 1/2-mil kapton and has a specific mass of 0.018 kg/m^2. The solar cell blankets and refulctors are mounted on the basic structure.

Power conditioning equipment mass includes the masses of the switch gear, regulators, converters and batteries in the collector array section, and switch gear and dc/dc converters in the antenna section. The aluminum conductors and insulation (electrical) mass was based on an environmental

Table 3.1-1. Mass Statement - Photovoltaic Power Conversion Mid-Term and Current

SUBSYSTEM	MASS, KG×10⁻⁶ MID-TERM CONFIG 2F-3	ΔMASS	CURRENT 77016-16
COLLECTOR ARRAY			
STRUCTURE AND MECHANISMS	(3.993)	-0.216	(3.777)
PRIMARY STRUCTURE	3.640	-0.784	2.856
SECONDARY STRUCTURE	0.343	+0.345	0.688
MECHANISM	0.010	+0.223	0.233
ATTITUDE CONTROL	(0.212)	-0.117	(0.095)
POWER SOURCE	(8.042)	+0.789	(8.831)
SOLAR BLANKETS	5.990	+1.732	7.722
SOLAR REFLECTORS	2.052	-0.944	1.108
POWER DISTRIBUTION AND CONTROL	(3.218)	-2.052	(1.166)
POWER CONDITIONING EQUIPMENT	(0.387)	-0.128	(0.259)
POWER DISTRIBUTION	(2.831)	-1.924	(0.907)
CONDUCTORS AND INSULATION	2.670	-1.971	0.699
SLIP RINGS	0.161	+0.047	0.208
INFORMATION MANAGEMENT AND CONTROL	(-)	+0.050	(0.050)
DATA PROCESSING	-		0.021
INSTRUMENTATION	-		0.029
TOTAL ARRAY, DRY	15.465	-1.546	13.919
ANTENNA SECTION			
STRUCTURE AND MECHANISM	(0.268)	+1.417	(1.685)
PRIMARY STRUCTURE	0.091	+0.317	0.408
SECONDARY STRUCTURE	0.167	+0.913	0.890
ANTENNA			0.190
MECHANISMS	0.010	+0.187	0.197
THERMAL CONTROL	(0.200)	+1.208	(1.408)
KLYSTRON COOLING	-		0.851
INSULATION	-		0.557
MICROWAVE POWER	(9.230)	-2.218	(7.012)
KLYSTRONS	5.690	-1.440	4.250
ATT. SEN., ELECTRONICS & PHASE CONT.	-	+0.142	0.142
WAVEGUIDES	3.540	-0.920	2.620
POWER DISTRIBUTION AND CONTROL	(0.096)	+3.373	(3.469)
POWER CONDITIONING EQUIPMENT	-	+1.635	(1.635)
POWER DISTRIBUTION	(0.096)	+1.738	(1.834)
CONDUCTOR AND INSULATION	0.084	+1.611	1.695
SLIP RING BRUSHES	0.012	+0.127	0.139
INFORMATION MANAGEMENT AND CONTROL	(0.240)	+0.390	(0.630)
DATA PROCESSING	0.240	+0.140	0.380
INSTRUMENTATION	-	+0.250	0.250
TOTAL ANTENNA SECTION	10.034	+4.170	14.204
TOTAL - SPS, DRY	25.499	+2.624	28.123
GROWTH (30%)	8.115	+0.322	8.437
TOTAL SPS, DRY, WITH GROWTH	33.614	+2.946	36.560
PROPELLANT PER YEAR	0.100	-0.060	0.040
TOTAL SPS, GROSS WITH GROWTH	33.714	+2.886	36.600

Table 3.1-2. Reasons for Changes - Mid-Term to Current

CHANGE	REASON	ΔMASS KG×10^{-6}
	COLLECTOR ARRAY	
1	PRIMARY STRUCTURE - COMPLETE NEW CALCULATION OF PRESENT CONFIGURATION WITH A L/W OF 5.53 VS. 9.52 FOR THE 2F-3 CONFIGURATION RESULTED IN THIS WEIGHT REDUCTION.	-0.784
2	SECONDARY STRUCTURE - A REASSESSMENT OF IDENTIFIABLE EQUIPMENT SUPPORTS RESULTED IN THIS WEIGHT INCREASE.	+0.345
3	MECHANISMS - MECHANISM WEIGHT HAS BEEN TAKEN AS A FUNCTION OF THE ROTATING ANTENNA SECTION MASS. SINCE ROTATING ANTENNA MASS HAS INCREASED, MECHANISM ALSO INCREASES.	+0.223
4	ATTITUDE CONTROL - THIS WEIGHT REDUCTION REFLECTS NEW ESTIMATES.	-0.117
5	SOLAR BLANKETS - INCREASE RESULTS FROM CHANGING REQUIRED CELL AREA FROM 23.76 KM^2 TO 30.6 KM^2, PLUS CARRYING CELL UNIT WEIGHT TO FOUR PLACES.	+1.732
6	SOLAR REFLECTORS - REDUCTION RESULTS FROM CHANGING THE AREA FROM 116.766 KM^2 TO 61.2 KM^2.	-0.944
7	POWER CONDITIONING EQUIP - REDUCTION IS PRIMARILY THE RESULT OF TRANSFER OF EQUIPMENT TO THE ANTENNA SECTION.	-0.128
8	CONDUCTOR AND INSULATION - REDUCTION WAS DUE TO SOME SHORTER RUNS, BUT PRINCIPALLY DUE TO TEMPERATURE REDUCTION FROM 50-70°C TO -18°C.	-1.971
9	SLIP RINGS - INCREASE DUE TO COMPLETE NEW WEIGHT CALCULATION.	+0.047
10	INFORMATION MANAGEMENT AND CONTROL - INCREASE (ADDITION) REFLECTS INADVERTENT OMISSIONS IN THE MID-TERM DATA.	+0.050
	ANTENNA SECTION	
11	PRIMARY STRUCTURE - INCREASE REFLECTS A COMPLETE NEW ESTIMATE.	+0.317
12	SECONDARY STRUCTURE AND ANTENNA STRUCTURE - INCREASE IS IN EQUIPMENT SUPPORTS WHICH ARE CONSIDERED TO HAVE BEEN OPTIMISTIC IN THE ORIGINAL ESTIMATES.	+0.913
13	MECHANISMS - INCREASE FOR ANTENNA ACTUATION MECHANISM WAS ALSO BASED ON WHAT IS CONSIDERED AN OPTIMISTIC ESTIMATE PREVIOUSLY.	+0.187
14	THERMAL CONTROL - INCREASE IS RESULT OF A BETTER DEFINITION OF THE KLYSTRON AND EQUIPMENT COOLING SYSTEM.	+1.208
15	KLYSTRONS - THIS REDUCTION IS PER A/N DATA	-1.440
16	MISC. EQUIP. (ELECTRONICS, PHASE CONT. & ATT. SENSORS) - THIS INCREASE (ADDITION) IS ALSO DUE TO A/N DATA.	+0.142
17	WAVEGUIDES - REDUCTION DUE TO A/N REVISED DATA.	-0.920
18	POWER CONDITIONING EQUIPMENT - INCREASE REFLECTS INADVERTENT OMISSIONS IN THE PREVIOUS ESTIMATE.	+1.635
19	CONDUCTOR & INSULATION - INCREASE DUE TO MORE REFINED ANALYSIS OF REQUIREMENTS ON THE ANTENNA SECTION.	+1.611
20	SLIP RING BRUSHES - INCREASE DUE TO RE-ESTIMATE.	+0.127
21	INFORMATION MANAGEMENT AND CONTROL - INCREASE DUE TO MORE DETAILED ACCOUNTING OF REQUIREMENTS OF DATA MANAGEMENT EQUIPMENT, CABLE, AND INSTRUMENTATION SENSORS.	+0.390
22	GROWTH - INCREASE RESULTS FROM THE HIGHER CURRENT WEIGHT WITH A 30% GROWTH IN LIEU OF THE 31.7% GROWTH IN THE ORIGINAL ESTIMATES.	+0.322
23	PROPELLANT PER YEAR - REDUCTION DUE TO BETTER DEFINED REQUIREMENTS.	-0.060

operating temperature of -18°C on the collector array and 70° to 85° on the antenna section. The mass of the four slip rings includes the mass of the plated aluminum slip rings and the pickoff brushes.

Microwave power consists of klystrons, waveguides, phase control, and associated electronics. The mass of the microwave subsystem was calculated by the Autonetics Division of Rockwell.

Thermal control mass is based on the mass of the heat pipes for cooling the klystrons plus insulating panels for the associated equipment.

The information management and control subsystem is divided into data processing and instrumentation. The subsystem mass includes the mass of computers, microprocessors, sub-multiplexer, cable, fiber optics, etc., in the data subsystem, and 4.9×10^6 sensors and associated cables in the instrumentation subsystem.

Mass growth is based on 30% of the SPS dry weight, all detail weight, c.g., and inertia computations were determined utilizing the Rockwell 260 computer program. A summary printout of the total SPS computer data is presented in Table 3.1-3, which shows the weight; X, Y, and Z centers of gravity; mass moment; and products of inertia. The numbers directly below the moments of inertia are the products of inertia I_{xy}, I_{xz}, and I_{yz}, respectively. Figure 3.1-1 illustrates the axis system used for the center-of-gravity and inertia computations.

A summary of the SPS photovoltaic mass properties is presented in Table 3.1-4.

Table 3.1-3. Mass Properties Summary - SPS Baseline, CR-2
(1-11-78 Status)

WEIGHT (KG)	S M	OPERAT CODE CENTER OF GRAVITY X - CG (METERS)	DESCRIPTION OF COMPONENTS Y - CG (METERS)	Z - CG (METERS)	SH A FA X	MOMENTS OF INERTIA IXX (KG - M**4)	IYY (KG - M**4)	IZZ (KG - M**4)	BEGINING X STATION (METERS)
TOTAL SPS DRY (WITH GROWTH)									
TOTAL SPS DRY (LESS GROWTH)									
		C O	COLLECTOR ARRAY TOTAL						
1.3919E+07	0	1.3139E+01	0.0	1.0367E+02	21	5.9795E+14	2.2062E+13	6.0747E+14	0.0
		P O							
0.0	0	0.0	0.0	0.0	21	1.6543E+12	-1.6951E+10	0.0	0.0
		O O	ANTENNA SECT TOTAL						
1.4204E+07	0	0.0	0.0	7.3470E+02	21	2.1370E+12	2.7169E+12	2.4318E+12	0.0
		P O							
0.0	0	0.0	0.0	0.0	21	0.0	0.0	0.0	0.0
TOTAL-SPS DRY (LESS GROWTH)									
		*** FIRST LEVEL TOTALS ***							
2.8123E+07		6.5030E+00	0.0	4.2238E+02		6.0288E+14	2.7578E+13	6.0991E+14	
						1.6543E+12	-7.7214E+10	0.0	

Table 3.1-3. Mass Properties Summary - SPS Baseline, CR-2 (1-11-78 Status) Cont.

WEIGHT (KG)	S M	OPERAT CODE	DESCRIPTION OF COMPONENTS		SH A FA X	MOMENTS OF INERTIA IXX (KG - M**M)	IYY (KG - M**M)	IZZ (KG - M**M)	BEGINING X STATION (METERS)
		CENTER OF GRAVITY X - CG (METERS)	Y - CG (METERS)	Z - CG (METERS)					
PROPELLANT									
		0 0	1 YEAR SUPPLY ARGON						
1.0000E+04	0	1.2500E+03	1.0650E+04	0.0	20	0.0	0.0	0.0	0.0
		C 0	1 YEAR SUPPLY ARGON						
1.0000E+04	0	-1.2500E+03	1.0650E+04	0.0	20	0.0	0.0	0.0	0.0
		C 0	1 YEAR SUPPLY ARGON						
1.0000E+04	0	1.2500E+03	-1.0650E+04	0.0	20	0.0	0.0	0.0	0.0
		5 0	1 YEAR SUPPLY ARGON						
1.0000E+04	0	-1.2500E+03	-1.0650E+04	0.0	20	0.0	0.0	0.0	0.0
TOTAL-PROPELLANT PER YEAR									
TOTAL-SPS GROSS (WITH GROWTH)									
		*** FIRST LEVEL TOTALS ***							
4.0000E+04		0.0	0.0	0.0		4.5352E+12	6.2472E+10	4.5977E+12	
						0.0	0.0	0.0	
		*** SECOND LEVEL TOTALS ***							
4.0000E+04		0.0	0.0	0.0		4.5352E+12	6.2472E+10	4.5977E+12	
						0.0	0.0	0.0	
		*** THIRD LEVEL TOTALS ***							
3.3600E+07		6.5112E+00	0.0	4.2118E+02		6.0742E+14	2.7648E+13	6.1450E+14	
						1.6543E+12	-7.7105E+10	0.0	

Table 3.1-3. Mass Properties Summary - SPS Baseline, CR-2
(1-11-78 Status) Cont.

WEIGHT (KG)	S M	OPERAT CODE	DESCRIPTION OF COMPONENTS			SH A FA X	MOMENTS OF INERTIA			BEGINING X STATION
		CENTER OF GRAVITY					IXX	IYY	IZZ	
		X - CG (METERS)	Y - CG (METERS)	Z - CG (METERS)			(KG - M*M)	(KG - M*M)	(KG - M*M)	(METERS)
GROWTH										
		3.0	GROWTH (30%)							
8.4372E+06	0	6.5695E+00	0.0	4.1918E+02	21		0.0	0.0	0.0	0.0
TOTAL-GROWTH										
TOTAL-SPS DRY (WITH GROWTH)										
		*** FIRST LEVEL TOTALS ***								
8.4372E+06		6.5695E+00	0.0	4.1918E+02			5.9493E-04	0.0	8.7255E-05	
							0.0	1.1424E-06	0.0	
		*** SECOND LEVEL TOTALS ***								
3.6560E+07		6.5183E+00	0.0	4.2164E+02			6.0238E+14	2.7578E+13	6.0991E+14	
							1.6543E+12	-7.7215E+10	0.0	

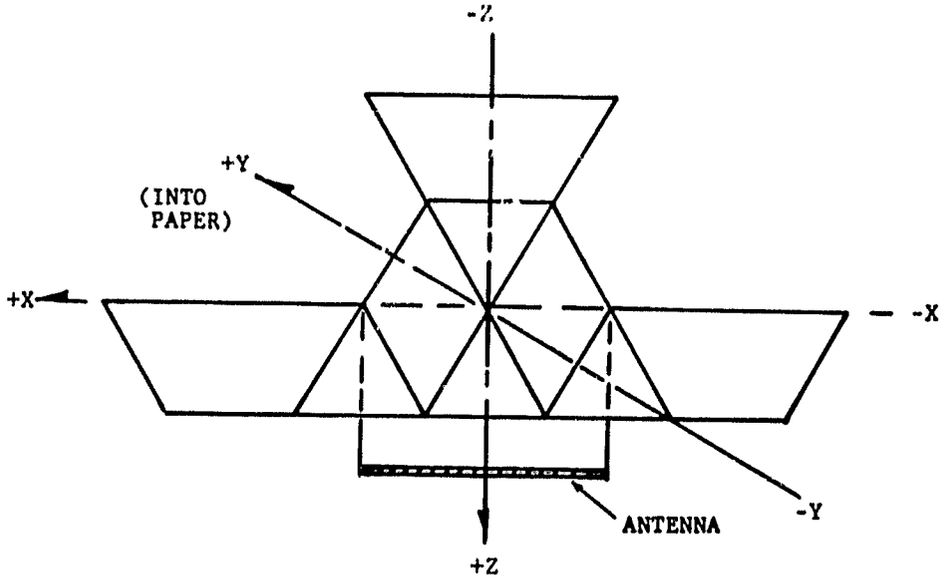

Figure 3.1-1. Axis System for Mass Properties

Table 3.1-4. Mass Properties Summary

	COLLECTOR ARRAY SECTION	ANTENNA SECTION	TOTAL SPS WITH GROWTH & PROPELLANT
MASS (kg)	13.919×10^{4}	14.204×10^{4}	36.600×10^{4}
X (m)	13.14	0	6.51
Y (m)	0	0	0
Z (m)	103.67	734.70	421.18
I_x (kg m^2)	5.979×10^{14}	2.137×10^{12}	6.074×10^{14}
I_y (kg m^2)	2.206×10^{13}	2.717×10^{12}	2.765×10^{13}
I_z (kg m^2)	6.075×10^{14}	2.432×10^{12}	6.145×10^{14}
I_{xy} (kg m^2)	1.654×10^{12}	0	1.654×10^{12}
I_{xz} (kg m^2)	-1.895×10^{10}	0	-7.711×10^{10}
I_{yz} (kg m^2)	0	0	0

3.2 CESIUM-STEAM RANKINE SOLAR THERMAL POWER CONVERSION SUBSYSTEM

3.2.1 MASS PROPERTIES STATUS

The mass of the solar thermal power conversion subsystem point design SPS versus the mid-term and third-quarter masses is shown in Table 3.2-1. Current masses are based on Figures 2.2-3 and 2.2-10 and have resulted in a 4.53% reduction over the third-quarter mass, and an increase of 21.16% over the mid-term status. The major reasons for the changes from the mid-term to the current masses are presented in Table 3.2-2.

3.2.2 BASIS FOR CURRENT MASS ESTIMATES

The design of the primary structure is based on the utilization of a 10-mil aluminum material for use in the fabrication of the tribeams. The structural beams consists of 50-meters-on-a-side triangular sections and has specific mass of 4.776 kg/m of length. Secondary structure consists essentially of equipment supports, tensioning devices, standoffs and catenary membranes for attachment of the solar blankets and reflectors. The antenna design is based on tension webs of 14-mil graphite epoxy supported by an 0.0805-m-diameter (3.17 in.) Kevlar catenary rope which, in turn, is supported by the compression frame which is constructed of the standard 50-meter beams. Mechanism mass include rotary joint actuation plus antenna array actuation system.

Attitude control system mass includes the mass of 720 ion thrusters, power processors, and associated argon and tankage plus plumbing for the SPS.

The solar collector mass includes the mass of the 1/2-mil Kapton for both top and bottom paraboloid surfaces having a 5000-m-diameter, and also includes the mass of the supporting ring and cables. Solar absorber and thermal power conditioning equipment (turbomachines, condenser, generators, etc.) masses are based on in-house estimates from layout drawings and vendor data. The mass of the electrical power conditioning equipment has been taken as identical to the photovoltaic power conversion subsystem. The aluminum conductors and insulation (electrical) mass was based on an environmental operating temperature of -18°C on the collector array and 79° to 85° on the antenna section. The mass of the four slip rings includes the mass of the plated aluminum slip rings and the pickoff brushes.

Radiator mass is based on a total radiative surface area of 9.48 km^2 (four surfaces).

The mass of the information management and control subsystem was assumed identical to that of the photovoltaic concept and the mass of the antenna section is identical to the photovoltaic configuration and reference is made to that section for the mass.

Table 3.2-1. Mass Statement - Solar Thermal Power Conversion Mid-Term and Current

SUBSYSTEM	MASS, KG×10⁻⁶		
	MID-TERM DWG 77016-10	THIRD-QUARTER	CURRENT
COLLECTOR ARRAY			
STRUCTURE AND MECHANISM	(1.931)	(2.320)	(1.661)
PRIMARY STRUCTURE	0.782	0.740	0.740
SECONDARY STRUCTURE	0.833	1.041	0.688
MECHANISM	0.316	0.539	0.233
ATTITUDE CONTROL	(0.200)	(0.095)	(0.095)
POWER SOURCE	(1.020)	(2.800)	(3.120)
SOLAR COLLECTOR	0.850	1.200	1.200
SOLAR ABSORBER	0.170	1.600	1.920
POWER DISTRIBUTION AND CONTROL	(5.601)	(6.517)	(4.304)
POWER CONDITIONING EQUIPMENT	(4.339)	(4.418)	(3.397)
TURBOMACHINES	0.800	0.800	1.160
PLUMBING, INSULATION (FORM. REGEN.)	0.080	0.080	0.145
PUMPS, COMPRESSORS	0	0	0.145
CONDENSER	0.450	0.450	0.283
POWER LOOP FLUID	0.070	0.070	0.105
GENERATORS, WITH COOLING	1.100	1.100	1.300
ELECT. POWER CONDITIONING	1.839	1.918	0.259
POWER DISTRIBUTION	(1.262)	(2.099)	(0.907)
CONDUCTOR & INSULATION	1.101	1.891	0.699
SLIP RINGS	0.161	0.208	0.208
THERMAL CONTROL	(7.500)	(8.500)	(8.786)
RADIATOR, WITH PUMP	7.500	8.500	8.786
INFORMATION MANAGEMENT AND CONTROL	(-)	(0.049)	(0.050)
DATA PROCESSING	-	0.021	0.021
INSTRUMENTATION	-	0.028	0.029
TOTAL ARRAY, DRY	16.252	20.281	18.016
ANTENNA SECTION			
STRUCTURE AND MECHANISM	(0.268)	(2.217)	(1.685)
PRIMARY STRUCTURE	0.091	0.408	0.408
SECONDARY STRUCTURE	0.167	1.422	0.890
ANTENNA		0.190	0.190
MECHANISM	0.010	0.197	0.197
THERMAL CONTROL	(0.200)	(1.490)	(1.408)
KLYSTRON COOLING	0.200	0.851	0.851
INSULATION		0.639	0.557
MICROWAVE POWER	(9.230)	(7.012)	(7.012)
KLYSTRONS	5.690	4.250	4.250
ATT. SENSORS, ELECTRONICS & PHASE CONT.	-	0.142	0.142
WAVEGUIDE	3.540	2.620	2.620
POWER DISTRIBUTION AND CONTROL	(0.096)	(2.340)	(3.469)
POWER CONDITIONING EQUIPMENT	(0)	(0.953)	(1.635)
POWER DISTRIBUTION	(0.096)	(1.087)	(1.834)
CONDUCTORS & INSULATION	0.084	0.948	1.695
SLIP RING BRUSHES	0.012	0.139	0.139
INFORMATION MANAGEMENT & CONTROL	(0.240)	(0.631)	(0.630)
DATA PROCESSING	0.240	0.380	0.380
INSTRUMENTATION	-	0.251	0.250
TOTAL, ANTENNA SECTION	10.034	13.390	14.204
TOTAL, SPS (DRY)	26.286	33.671	32.220
GROWTH (30%)	8.219	10.113	9.666
TOTAL - SPS (DRY), WITH GROWTH	34.505	43.787	41.586
PROPELLANT PER YEAR	0.100	0.140	0.040
TOTAL - SPS (GROSS) WITH GROWTH	34.605	43.824	41.926

Table 3.2-2. Reasons for Changes - Mid-Term to Current

CHANGE	REASON	ΔMASS KG×10⁻⁶
	COLLECTOR ARRAY	
1	PRIMARY STRUCTURE - COMPLETE NEW DESIGN ANALYSIS RESULTED IN WEIGHT REDUCTION.	-0.042
2	SECONDARY STRUCTURE - A REASSESSMENT OF IDENTIFIABLE EQUIPMENT SUPPORTS RESULTED IN THE WEIGHT REDUCTION.	-0.145
3	MECHANISMS - REDUCTION IS RESULT OF RE-ESTIMATE OF THIS ITEM ON THE PHOTOVOLTAIC CONFIGURATION.	-0.083
4	ATTITUDE CONTROL - REDUCTION REFLECTS NEW ESTIMATES.	-0.105
5	SOLAR COLLECTOR - INCREASE REFLECTS A SIZE INCREASE FROM 3048-M DIAMETER to 5000-M DIAMETER.	+0.350
6	SOLAR ABSORBER - MOST OF INCREASE CAUSED BY ADDITION OF METEOROID ARMOR PROTECTION (+1.430); REMAINDER OF INCREASE RESULTED FROM ADDED INSULATION.	+1.750
7	TURBOMACHINES - INCREASE WAS NECESSARY FOR ADDED PLUMBING AND PUMPS.	+0.360
8	PLUMBING, INSULATION (FORM, REGENERATOR) - INCREASE ALSO DUE TO ADDED REQUIREMENTS.	+0.065
9	PUMPS AND COMPRESSORS - INCREASE ALSO DUE TO ADDED REQUIREMENTS.	+0.145
10	CONDENSER - REDUCTION DUE TO REFINED REQUIREMENTS DEFINITION.	-0.167
11	POWER LOOP FLUID - INCREASE DUE TO REFINED REQUIREMENTS DEFINITION.	+0.035
12	GENERATORS, WITH COOLING - INCREASE DUE TO GENERATOR SIZE INCREASE.	+0.200
13	ELECTRICAL POWER CONDITIONING - REDUCTION DUE PRINCIPALLY TO TRANSFER OF ITEMS FROM THE COLLECTOR ARRAY TO THE ANTENNA SECTION.	-1.580
14	CONDUCTOR AND INSULATION - REDUCTION DUE TO TEMPERATURE REDUCTION FROM 50°C TO 70°C TO -18°C.	-0.402
15	SLIP RINGS - THIS INCREASE WAS DUE TO COMPLETE NEW WEIGHT CALCULATION.	+0.047
16	RADIATOR, WITH PUMP - MOST OF THIS WEIGHT INCREASE (+1.000) WAS DUE TO ADDED METEOROID ARMOR PROTECTION; THE REMAINING INCREASE (0.286) WAS DUE TO HEAT PIPE LENGTH INCREASE.	+1.286
	ANTENNA SECTION	+4.170
	THE CHANGES MAKING UP THIS INCREASE ARE IDENTICIAL TO THE PHOTOVOLTAIC CONCEPT AND ARE LISTED IN DETAIL IN THE SECTION ON THE PHOTOVOLTAIC MASS.	
	GROWTH (TOTAL SPS)	+1.447
	THIS INCREASE, BASED ON 30% GROWTH IN THE DRY WEIGHT, RESULTS FROM THE CURRENT INCREASED SPS MASS.	
	PROPELLANT PER YEAR	-0.060
	THIS REDUCTION IS DUE TO BETTER DEFINED REQUIREMENTS.	

4.0 GROUND RECEIVING

The siting analysis for the ground receiving rectenna has been performed in detail by the NASA George C. Marshall Space Flight Center and is documented in the report, "*Candidate locations for the SPS Rectifying Antennas*", NASA Technical Memorandum, NASA TM-78146, November 1977. The rectenna subsystems performance has previously been described and documented in Section 2.6 of this volume. The support subsystems for the rectenna are briefly described and presented in Section 5.0 of this volume.

5.0 SUPPORT SYSTEMS

The support systems are comprised of those elements required to construct, operate, and maintain the SPS system. They include ground facilities (material handling and launch operations), LEO and GEO bases, and the ground and space transportation systems required for satellite and rectenna construction and maintenance. The HLLV's are utilized to carry material and personnel to LEO. COTV's and POTV's carry material and crews respectively from LEO to GEO, while small, transport vehicles are utilized at both LEO and GEO for local cargo transfer and inter-facility movement. The characteristics of these elements are summarized here and detailed descriptions are given in Volume V.

5.1 ORBITAL SUPPORT SYSTEMS

The major elements of the orbital support systems are orbital transportation, satellite and construction base, operations and maintenance base, and LEO base. A description and listing of the characteristics of the orbital support system elements are presented in the following subsections.

5.1.1 SATELLITE CONSTRUCTION BASE

Construction of the satellites takes place in GEO at its designated operational longitude. Construction is accomplished almost entirely from the single assembly and fabrication fixture shown in the upper left of Figure 5.1-1. A crew size requirement of 680 has been estimated for accomplishing the construction in the scheduled time. The crew and their facilities are divided equally and are located on each side of the hex portion of the fixture as shown. One of these 320 men facilities, shown in the upper center of the figure, consists of 7 three-module crew habitability complexes plus 2 base management modules, 2 pressurized storage modules and solar array power modules.

The modules of the crew habitability complex are described in more detail in the lower right of Figure 5.1-1. Each complex is composed of two of the crew hab modules, each of which provide staterooms, personal hygiene facilities and support subsystems for 24 crew members; and one crew support module which provides galley, recreational and medical facilities and subsystems for the 48 crew members of the two crew hab modules. The base management modules house the communications and control systems for the base and the construction facility. The pressurized storage modules include work-shops for maintenance of construction facility elements and satellite hardware as required.

Seven of the modules (indicated by the dashed lines) are hardened against solar flare radiation and serve as temporary quarters for the entire crew when the base is subjected to that environment.

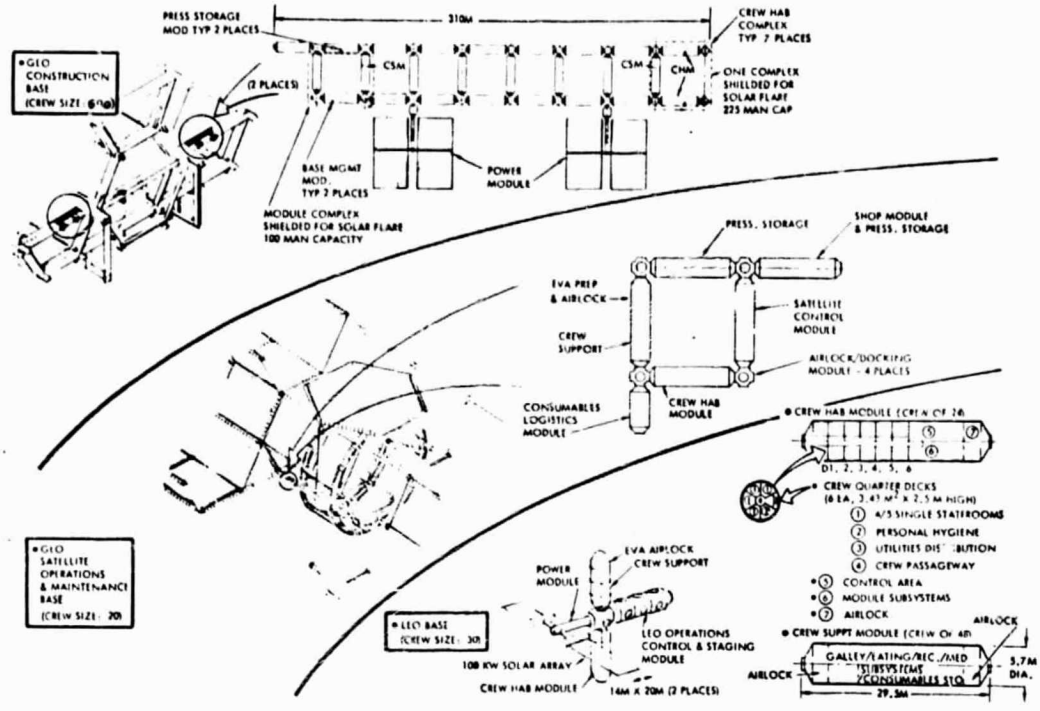

Figure 5.1-1. Orbital Base Concepts

5.1.2 OPERATIONS AND MAINTENANCE BASE

Shown in the center panel of Figure 5.1-1 is the permanent operations and maintenance base which is installed on each satellite prior to completion of construction. It is located near the center of the satellite for best access to all parts of the satellite and is installed subsequent to completion of the center structure as described in the discussion of the construction schedule. A maintenance crew requirement of 20 has been estimated. The functions of the five modules which comprise the base are identified in the figure. The crew hab module internal configuration is the same as for the construction base. The crew support module also has the same internal function as for the construction base but occupies only 1/2 of the module, the other 1/2 being an integrated multi-crew member EVA preparation and airlock station.

All base modules are of the dimensions shown for the crew support module at the lower left of Figure 5.1-1. Module size and mass are designed for compatibility with HLLV cargo carrying capability.

5.1.3 LEO BASE

The LEO base personnel provide supervisory activities for transfer of up and down payloads between the HLLV and the OTVs, and perform the scheduled maintenance required by the COTV (changeout of thruster screens and argon propellant tanks). It has one crew hab and one crew support module of the same configurations as the GEO construction base except that six of the 30

staterooms required are located in the crew support module. Direct transfer of crew and equipment between the HLLV and the OTV's are planned; however, multiple docking ports and excess subsystems capacity and power are provided for emergency staging support.

5.1.4 ORBITAL TRANSPORTATION

The orbital transportation system concept for support of satellite construction and operational maintenance consists of:

- A horizontal take-off and landing winged, single stage to orbit heavy lift launch vehicle (SSTO-HLLV), which transports materials and personnel from earth to a 300 nmi equatorial LEO (Figure 5.1-2). It has cargo bay dimensions of 6×6×30 m and carries a 91,000 kg payload.
- An electric powered, ion propelled, cargo orbital transfer vehicle (COTV), Figure 5.1-3, which carries a payload of approximately 3.9×10^6 kg between LEO and GEO. The COTV is constructed in space with maintenance being accomplished in LEO.
- A chemically powered personnel orbital transfer vehicle (POTV), Figure 5.1-4, which transports personnel between LEO and GEO. It has two (common/chemical) stages each of which has a mass of 91,000 kg and carries a payload of 91,000 kg. The operation of the HLLV in conjunction with the COTV is illustrated in Figure 5.1-5.
- A small intra-orbit transfer vehicle (IOTV) which transfers cargo between the HLLV and COTV, and between the COTV and the GEO construction base.
- The space operations scenario is more fully described in Section 9.2 of Volume V.

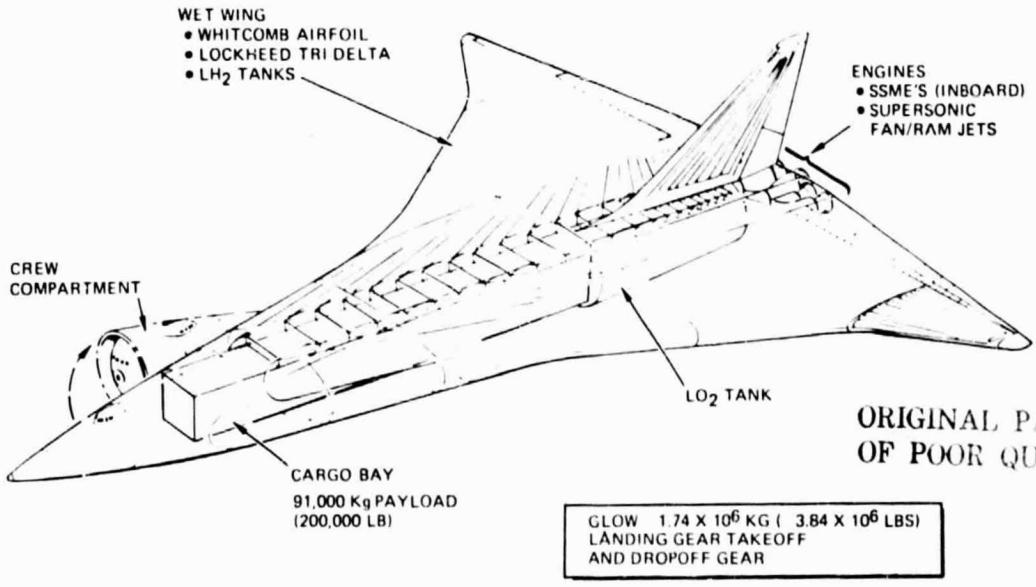

Figure 5.1-2. Air-Augmented HTO-SSTO Concept

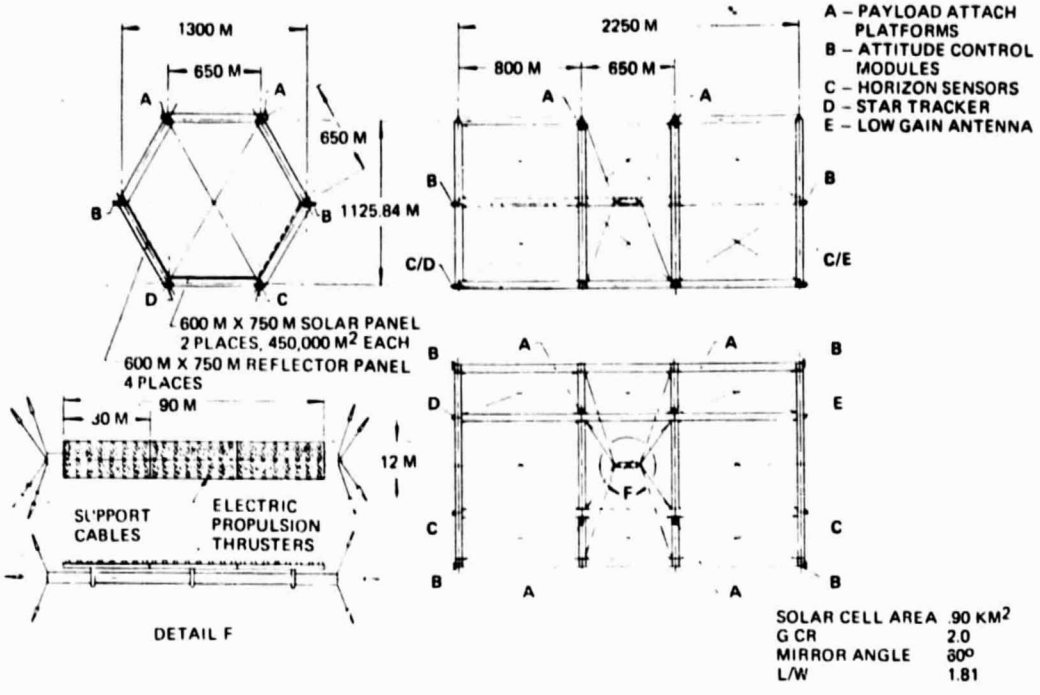

Figure 5.1-3. Electric OTV Concept

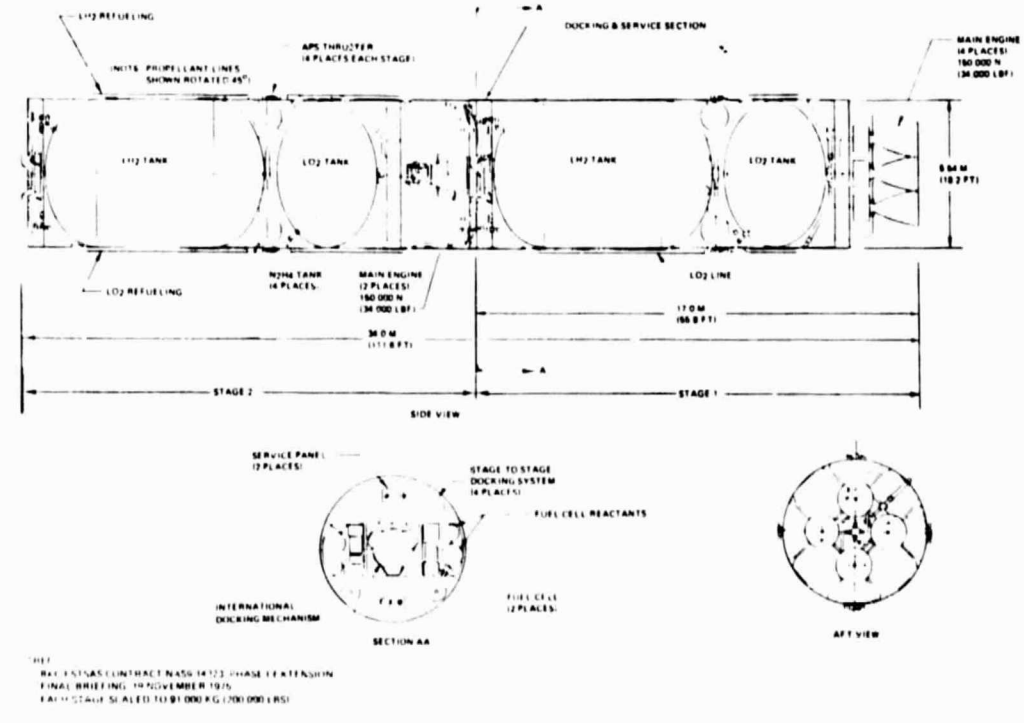

Figure 5.1-4. Common Stage LO_2/LH_2 OTV Concept*

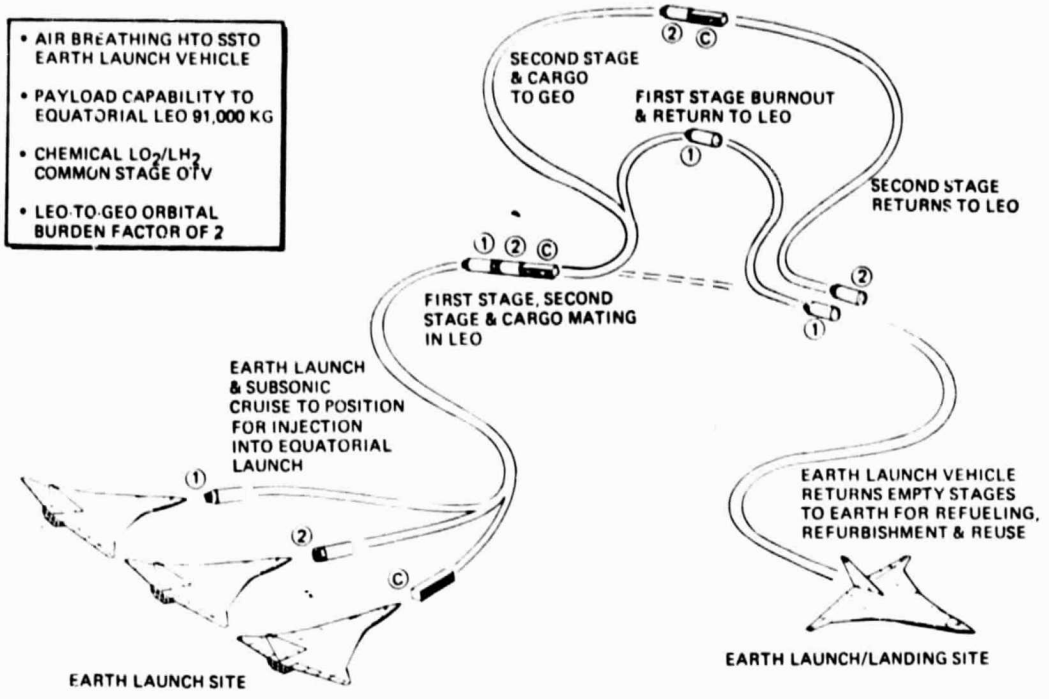

Figure 5.1-5. Cargo Delivery Concept for GEO Construction of SPS Large Common Stage OTV

5.2 GROUND OPERATIONS

The major elements of ground operations consists of launch site requirements and operations - facilities and the rectenna construction and logistics. A brief description of these ground operations are presented in the following subsections.

5.2.1 LAUNCH SITE REQUIREMENTS AND OPERATIONS - FACILITIES

Launch base facilities must provide for (1) receiving, storage, and processing of material and propellants, (2) storage of ELV's sufficient for initial operations, (3) refurbishment and checkout of returning ELV's, and (4) personnel handling and administration. Figure 5.2-1 depicts the facilities which must be provided and indicates the interfacility relationship for material and personnel processing.

Incoming material (rail, air, etc.) is offloaded, subjected to receiving inspection, taken up on the computerized inventory control system, and then stored in the appropriate warehouse facility as shown in Figure 5.2-1. Some of the material will be processed through a subassembly buildup facility prior to storage. This material includes the basic metal stock required to fabricate and assemble microwave waveguide subarrays, totaling 6993 per SPS. It is estimated that 15,000 square meters of floor space will be required for subarray fabrication. Section 9.6 of Volume V defines transportation and storage requirements in more detail.

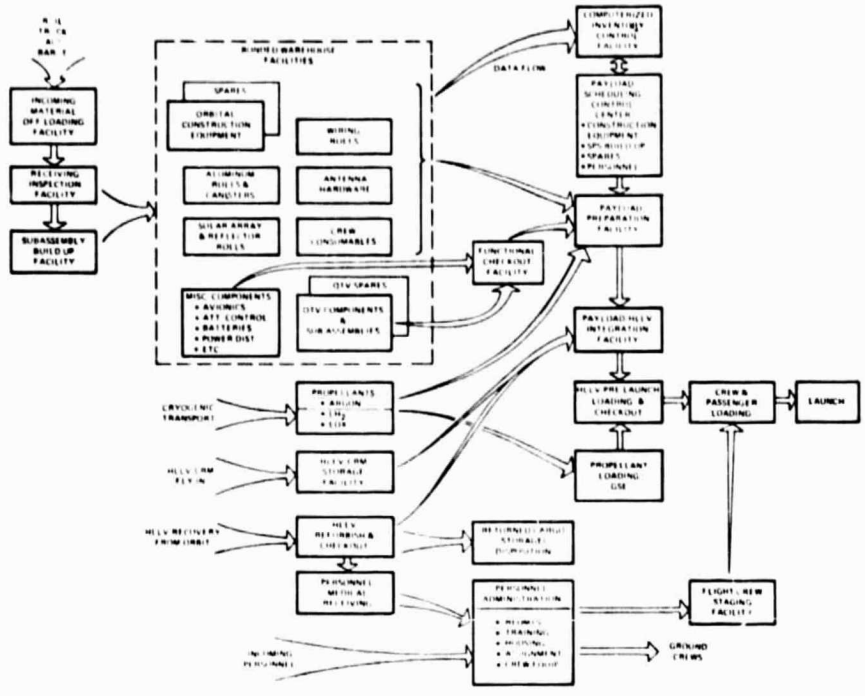

Figure 5.2-1. Launch Site Logistics

Bonded warehousing must be provided for SPS construction material and spares and for COTV construction material. An initial requirement of about 145,000 square meters of floor space, ultimately increasing to 170,000 square meters, has been established.

When scheduled by the Payload Scheduling Control Center, material (construction material, consumables and spares as required) is transferred to the payload preparation facility for packaging and arranging into payload units on 6×30 meter pallets. Electronic modules and other selected components will be functionally tested prior to packaging. The packaged payloads are then transported to and loaded on the HLLV prior to propellant loading and final HLLV checkout. Personnel comprising part of a payload will enter their crew module in the payload bay shortly before launch.

The propellant storage facilities must provide for cryogenic storage of HLLV propellants and for argon which will be shipped to low earth orbit for COTV utilization. See Volume V, Section 9.5 for additional details regarding propellant requirements.

Since initial HLLV flight requirements are substantial (approximately 550 flights during the first year), a fleet build-up will be required prior to initiation of the orbital phase of the program. A facility to store "mothballed" HLLV's during the build-up period must be provided, either at the launch site or elsewhere. It is probable that this facility could also serve as a refurbishment area for HLLV's returning from orbit.

Personnel administration and planning is a vital element in the overall base function. Incoming personnel must be trained and assigned to either flight or ground crews. Personnel returning from 90 days in orbit must undergo medical processing and then be reassigned to ground activities for a TBD period before returning to orbit. The continuous growth in number of both base personnel and space crews throughout the 30 year program precipitates the requirement for extensive facilities for medical, housing, training, and administration.

Finally, provision must be made for processing and disposing of large amounts of packaging materials, and failed and damaged hardware which will be returned from orbit by the HLLV's.

5.2.2 RECTENNA CONSTRUCTION AND LOGISTICS

A rectenna will be required for each operational satellite. Approximately 15 months is required to prepare the site and construct the rectenna. Since this exceeds the time allocated for satellite construction, a number of rectennas must be in the construction phase at any one time.

The support systems required for construction of the rectenna are anticipated to be much greater magnitude than those required for operational maintenance and are therefore of primary concern because of the large mass of construction materials required. (Each rectenna requires approximately 1800×10^6 kg of concrete, 900×10^6 kg of galvanized steel, and 350×10^6 kg of miscellaneous material; this equates to about 420 truck trips per day which must be processed at the site and which requires some 20 unloading docks.) On-site assembly of the 436,818 rectenna panels presents the major construction time challenge. The large number dictates the need for multiple, semi-automated assembly equipments. The concept shown in Figure 5.2-2 fulfills that requirement. It is essentially a mobile construction jig which is assembled on-site and can be disassembled for transport to another rectenna site. The concept shown is initially loaded with materials for assembly of 10 rectenna panels. Since each rectenna panel weighs 2080 kilograms (4576 lbs), then a single flat-bed truck trip can deliver the 10 sets of rectenna panel materials. As each rectenna panel is completed, it is lifted from the construction jig by a truck crane (see insert on Figure) and set on concrete piers.

Operational maintenance will require special designed equipment for removal, repair and replacement of faulty panels; however, unique logistics problems associated with transport of operational spares to the individual rectenna sites is foreseen. For additional detail see Volume V, Section 9.9.

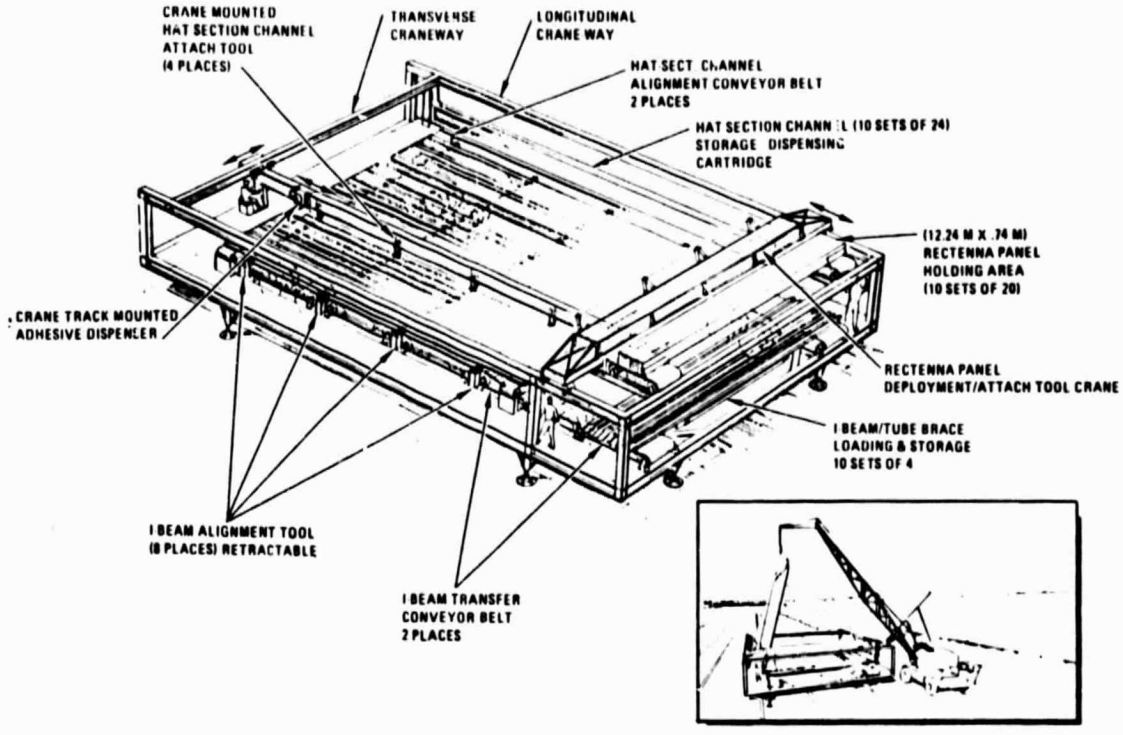

Figure 5.2-2. Rectenna Panel Assembly Concept